ABSTRACT

Title of dissertation: NUMERICAL SIMULATION AND VALIDATION OF HELICOPTER BLADE-VORTEX INTERACTION USING COUPLED CFD/CSD AND THREE LEVELS OF AERODYNAMIC MODELING

Mathieu Amiraux, Doctor of Philosophy, 2014

Dissertation directed by: Professor James D. Baeder
Department of Aerospace Engineering

Rotorcraft Blade-Vortex Interaction (BVI) remains one of the most challenging flow phenomenon to simulate numerically. Over the past decade, the HART-II rotor test and its extensive experimental dataset has been a major database for validation of CFD codes. Its strong BVI signature, with high levels of intrusive noise and vibrations, makes it a difficult test for computational methods. The main challenge is to accurately capture and preserve the vortices which interact with the rotor, while predicting correct blade deformations and loading. This doctoral dissertation presents the application of a coupled CFD/CSD methodology to the problem of helicopter BVI and compares three levels of fidelity for aerodynamic modeling: a hybrid lifting-line/free-wake (wake coupling) method, with modified compressible unsteady model; a hybrid URANS/free-wake method; and a URANS-based wake capturing method, using multiple overset meshes to capture the entire flow field. To further increase numerical correlation, three helicopter fuselage models are implemented in the framework. The first is a high resolution 3D GPU panel code; the second is an

immersed boundary based method, with 3D elliptic grid adaption; the last one uses a body-fitted, curvilinear fuselage mesh.

The main contribution of this work is the implementation and systematic comparison of multiple numerical methods to perform BVI modeling. The trade-offs between solution accuracy and computational cost are highlighted for the different approaches. Various improvements have been made to each code to enhance physical fidelity, while advanced technologies, such as GPU computing, have been employed to increase efficiency. The resulting numerical setup covers all aspects of the simulation creating a truly multi-fidelity and multi-physics framework.

Overall, the wake capturing approach showed the best BVI phasing correlation and good blade deflection predictions, with slightly under-predicted aerodynamic loading magnitudes. However, it proved to be much more expensive than the other two methods. Wake coupling with RANS solver had very good loading magnitude predictions, and therefore good acoustic intensities, with acceptable computational cost. The lifting-line based technique often had over-predicted aerodynamic levels, due to the degree of empiricism of the model, but its very short run-times, thanks to GPU technology, makes it a very attractive approach.

NUMERICAL SIMULATION AND VALIDATION OF HELICOPTER BLADE-VORTEX INTERACTION USING COUPLED CFD/CSD AND THREE LEVELS OF AERODYNAMIC MODELING

by

Mathieu Amiraux

Dissertation submitted to the Faculty of the Graduate School of the
University of Maryland, College Park in partial fulfillment
of the requirements for the degree of
Doctor of Philosophy
2014

Advisory Committee:
Dr. James D. Baeder, Chair/Adviser
Dr. Inderjit Chopra
Dr. Anya Jones
Dr. Amir Riaz
Dr. James Duncan, Dean's Representative

Acknowledgments

First, I would like to thank my adviser, Dr. James D. Baeder, for his guidance and support throughout the course of my master and doctoral work. When I arrived in the US for Graduate School, I had limited knowledge in aerodynamics, coming from a mechanical engineering background, and no prior understanding of CFD. He led me in the right direction and let me join his research group. His calm and kind leadership has been key to providing me with a peaceful but focused research environment, in which I was able to grow. He was always open to new ideas, letting me develop and explore various computational paths.

I am also grateful to the members of my dissertation committee, who took the time to review my work and bring me valuable feedback. Dr. Inderjit Chopra was always available and resourceful for any rotorcraft related questions. I also learned a lot from Dr. Amir Riaz and his Viscous Flow class. I appreciate that Dr. Anya Jones and Dr. James Duncan agreed to serve on my dissertation committee, as well as for my comprehensive exam.

In addition, I want to thank other professors and scholars from whom I have had the privilege to learn: Dr. V. T. Nagaraj for many rotorcraft related topics, Dr. Fredric H. Schmitz, Dr. Sudarshan Koushik, and Dr. Gaurav Gopalan in acoustics; Kumar Ravichandran in structural dynamics and UMARC; Dr. Shreyas Ananthan, Dr. Vinod Lakshminarayan, Dr. Shivaji Medida, and Dr. Sebastian Thomas in CFD.

Finally, I would like to recognize my group mates and friends at UMD: Taran,

Nishan, Camli, Ben, Juergen, Teju, Ananth, Debo, Barath, Yashwanth, Pranay, as well as many others. They have been a great source of help in my research, while bringing me fun and relaxing times outside. And a very special thought for Yadviga.

Dedication

This dissertation is dedicated to my dad,

for his constant support and words of wisdom.

Table of Contents

List of Tables

List of Figures

Nomenclature

AR	Rotor aspect ratio
c	Blade chord [m]
$C_m M^2$	Non-dimensional pitching moment coefficient
	Scaled by local Mach number squared
$C_n M^2$	Non-dimensional normal force coefficient
	Scaled by local Mach number squared
C_T	Non-dimensional thrust coefficient
e	Energy
$\mathbf{F}$, $\mathbf{G}$, $\mathbf{H}$	Flux vectors
M	Mach number
M_{tip}	Tip Mach number
M_{TR}	Trace Mach number
p	Pressure [Pa]
Pr	Prandtl number
$\mathbf{Q}$	Vector of conserved variables
r	non-dimensional radial distance or spanwise location
R	Rotor radius [m]
Re	Reynolds number
r_c	Vortex core radius
u, v, w	Cartesian flow velocity components
	Axial, lead-lag, flap displacements
V_{infty}	Freestream velocity $[m.s^{-1}]$
V_{tip}	Blade tip speed $[m.s^{-1}]$
x, y, z	Cartesian coordinates
$/rev$	Per rotor revolution

Symbols

α	Shaft tilt angle, positive nose-up [degree]; Angle of attack
Γ	Vortex strength or circulation
λ	Rotor inflow
μ	Advance ratio
Ω	Blade rotational speed $[rad.s^{-1}]$
ϕ	Wake age [degree]
Φ	Torsional displacement
Φ_{HHC}	Phase of the 3/rev HHC pitch input [degree]
ψ	Azimuth angle [degree]
ρ	Flow density
θ_0	Collective pitch angle [degree]
θ_{1C}	Lateral cyclic pitch angle [degree]
θ_{1S}	Longitudinal cyclic pitch angle [degree]
θ_{HHC}	Magnitude of the 3/rev HHC pitch input [degree]

Abbreviations

AFDD	AeroFlightDynamics Directorate
AHS	American Helicopter Society
BL	Baseline case
BPF	Blade Passage Frequency
BTD	Blade Tip Deflection
BVI	Blade-Vortex Interaction
BVISPL	BVI Sound Pressure Level [dB]
CFD	Computational Fluid Dynamics
CPU	Central Processing Unit
CSD	Computational Structural Dynamics
CRWENO	Compact-Reconstruction Weighted Essentially Non-Oscillatory
DNS	Direct Numerical Simulation
FMM	Fast Multipole Method
GPU	Graphics Processing Unit
HART	Higher harmonic control Aeroacoustic Rotor Test
HHC	Higher-Harmonic Control
IBC	Immersed Boundary Condition
IHC	Implicit Hole Cutting
LDV	Laser Doppler Velocimetry
LES	Large Eddy Simulation
LLS	Laser Light Sheet
MN	Minimum Noise case
MUSCL	Monotone Upstream-centered Schemes for Conservation Laws
MV	Minimum Vibration case
PIV	Particle Image Velocimetry
RANS	Reynolds-Averaged Navier-Stokes
SA	Spalart-Allmaras
SPL	Sound Pressure Level [dB]
SPR	Stereo Pattern Recognition
UMD	University of Maryland
URANS	Unsteady Reynolds-Averaged Navier-Stokes
VTG	Vortex Tracking Grid
WENO	Weighted Essentially Non-Oscillatory

Chapter 1

Introduction

1.1 Helicopter Blade-Vortex Interaction

Helicopters, and rotorcrafts in general, are proven machines that have shown great success in achieving missions that most other types of vehicles, especially fixed-wing aircrafts, are not capable of. Since the first viable helicopter flight in the late 1930s, considerable improvements having been made to help these extraordinary devices achieve higher speeds and travel greater distances, while, at the same time, making them safer and more reliable. However, in today's world, a helicopter remains easily recognizable by its acoustic signature. Although there are multiple sources of this undesirable noise, as can be seen on Fig. 1.1, a particular one stands out as the most intrusive. It is the sound that arises from the interaction of helicopter blades and the different vortical structures shed into the surrounding flow field. Therefore, it is called Blade-Vortex Interaction (BVI) noise.

1.1.1 BVI Physics

Rotorcraft BVI typically appears during low speed descending flight conditions, as well as during some maneuver trajectories. The idea is that, under these flight conditions, the vortex system trailed by the different blades stays close to the plane of the rotor, as the amount of flow coming through the rotor, the inflow, is

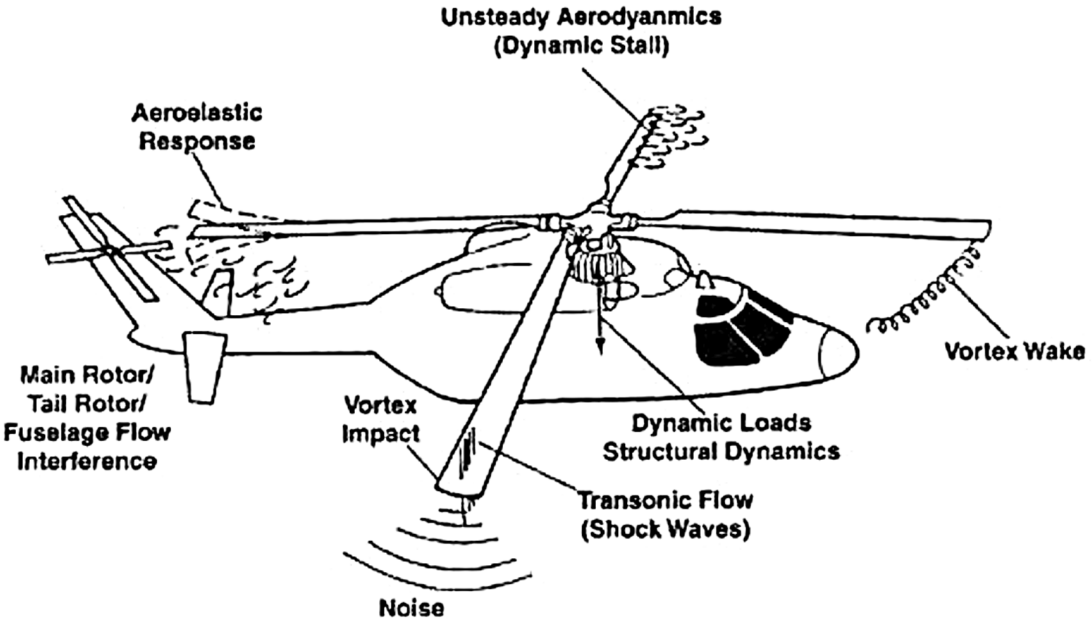

Figure 1.1: The different sources of helicopter noise (Ref. [22])

reduced and comes close to zero. Figure 1.2 is a simple representation of a helicopter in low speed descent where the blade tip vortices are pushed back up into the plane of the rotor.

As a result, the vortices come in close proximity, or even intersect, the different blades as they rotate. This leads to strong and impulsive induced velocities at the

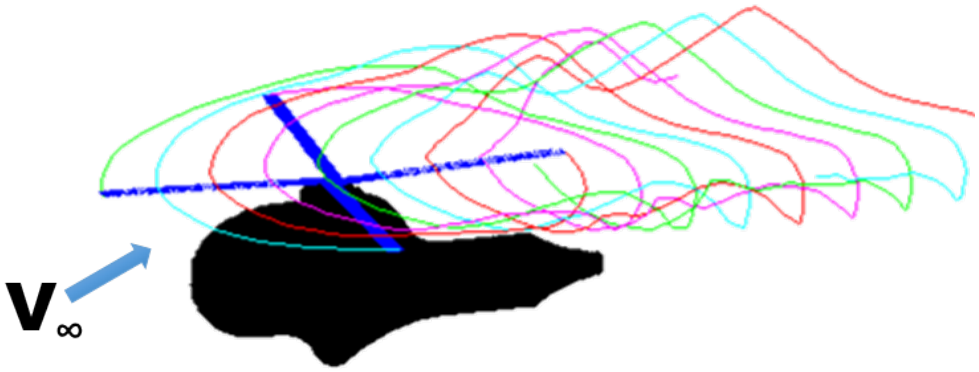

Figure 1.2: Representation of a helicopter in low speed descent experiencing BVI

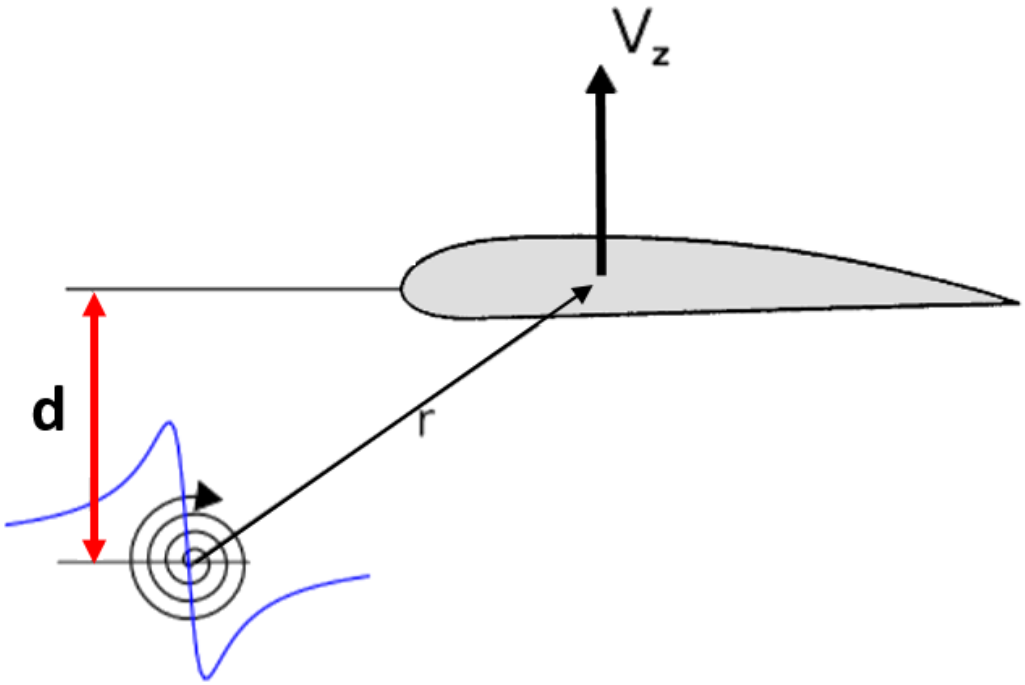

Figure 1.3: 2D representation of a vortex interacting with an airfoil (Ref. [24])

blades, which modify the effective angles of attack of each airfoil section along the blade span, and lead to sharp and rapid changes in surface pressure. This phenomenon is schematized in Fig 1.3. As will be seen, BVI events are strongest in the first and fourth quadrants of the rotor disk. This interaction is the cause of the impulsive and highly directional nature of BVI noise.

Many factors influence the strength of BVI. The most important ones are:

- Miss-distance: This is the distance between the blade and the center line of the vortex; the lower the distance, the stronger the interaction. It is the parameter Z_c in Fig. 1.3. It depends on the flight conditions (advance ratio, shaft tilt), as well as the blade position at the time of interaction. This highlights the need for accurate blade deflection predictions, and particularly blade flapping

for good miss-distance estimation.

- Interaction angle: This is the angle between the blade leading edge and the center line of the vortex; the more parallel they are ($\gamma \simeq 0$), the stronger the interaction. It is the parameter γ in Fig. 1.5. As will be shown, this interaction angle is lower in the first and fourth quadrants. This also depends on the flight conditions and blade deflections, mostly blade lead-lag this time.

- Strength of the vortex at time of interaction: The stronger the vortex, the stronger the interaction. This mainly depends the blade loading and tip Mach number.

- Core radius of the vortex at time of interaction: The tighter the vortex, the stronger the interaction. This depends on how much the vortex has diffused before the interaction.

1.1.2 BVI modeling: wake models

To qualitatively capture BVI, different techniques exist. The main requirement is to have a mean of representing the vortex system trailed by rotor blades as they rotate. Simplified wake models can give meaningful information about the location and number of blade-vortex encounters. Figure 1.4 shows the BVI pattern of a 4-bladed rotor at two advance ratios. At the higher advance ratio, there are less BVI encounters as the wake is convected downstream faster.

This method models the wake as Lagrangian vortex filaments which only convect with the freestream in two dimensions (no vertical change). An improvement

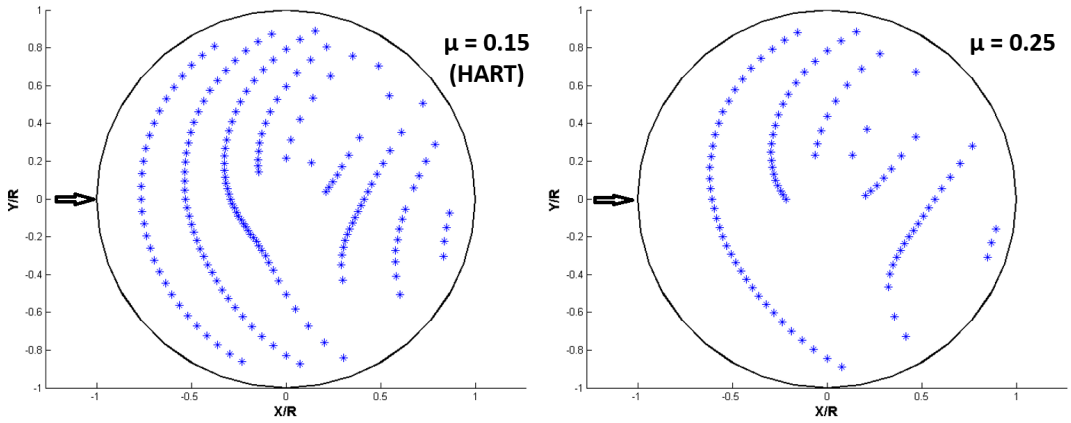

Figure 1.4: Localization of BVI for a 4-bladed rotor at two advance ratios

over this formulation is to give the filaments vertical freedom. This can be done using the advance ratio and shaft tilt angle: $Z_{wake} = \mu \sin(\alpha) t$, where t represents the time. Adding the rotor inflow, which can be obtain by solving the inflow equation, further improves the model. This model is called "Rigid Wake" model and the vortex markers coordinates follow these equations:

$$\left| \begin{array}{c} x = r\cos(\psi - \phi) + \mu_x \phi + \lambda_x \phi \\ y = r\sin(\psi - \phi) + \mu_y \phi + \lambda_y \phi \\ z = z_0 + \mu_z \phi - \lambda_z \phi \end{array} \right|$$

Inflow equation:

$$\lambda = \mu \tan(\alpha) + \lambda_i = \mu \tan(\alpha) + \frac{C_T}{2\sqrt{\mu^2 + \lambda^2}}$$

Here, r is the spanwise location, ψ is the reference blade azimuth, ϕ is the wake age, μ is the advance ratio, λ is the rotor inflow, α is the shaft tilt angle.

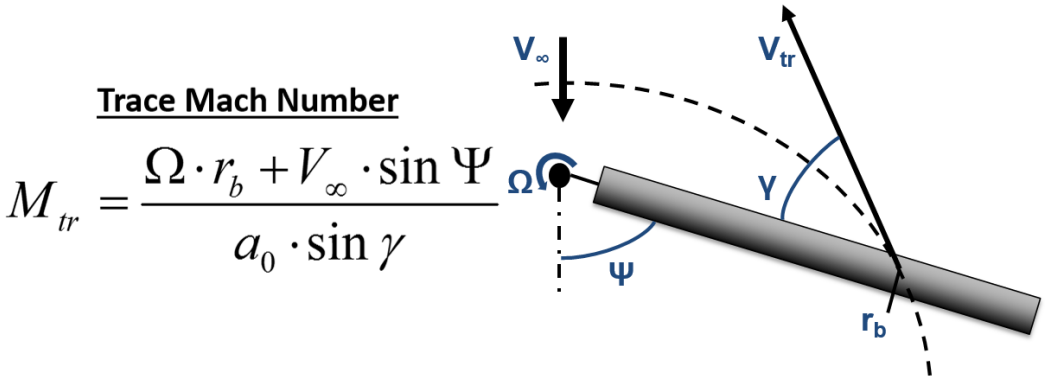

Figure 1.5: Trace Mach Number and parameters

More advanced wake models, such as the one by Beddoes (Ref. [13]), include more wake distortion, using the wake skew angle, for a more realistic wake geometry. All these models do not include the effect of the mutual influence of the vortex filaments, although Beddoes modification is an attempt to take it into account. Free-wake models, which will be described in more depth later, do include the mutual interaction of filaments using the Biot-Savart law.

1.1.3 Trace Mach Number

The Trace Mach number (M_{TR}) is a useful metric to compute the strength of BVI. It is a function of the rotor rotational speed and azimuth angle, the freestream velocity and speed of sound, the spanwise location of the BVI encounter and the interaction angle. Figure 1.5 shows the formula for M_{TR} and the different parameters involved. Figure 1.6 is a visual representation of M_{TR} at two azimuthal locations.

As can be seen, the strongest interactions occur for azimuths around 50 ° and 300 °. Figure 1.7 shows M_{TR} and γ as a function of the rotor azimuth. These plots

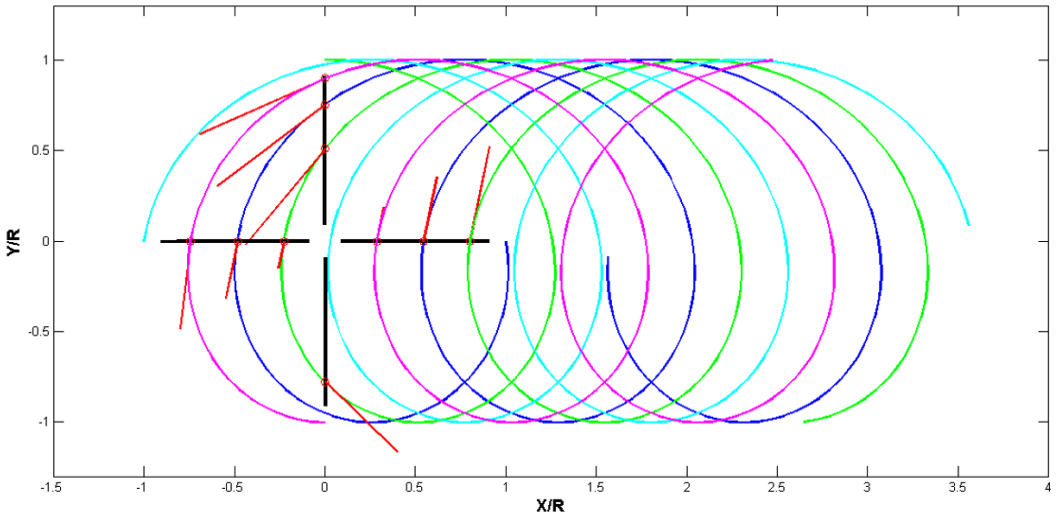

(a) $\psi = 0.0$ °

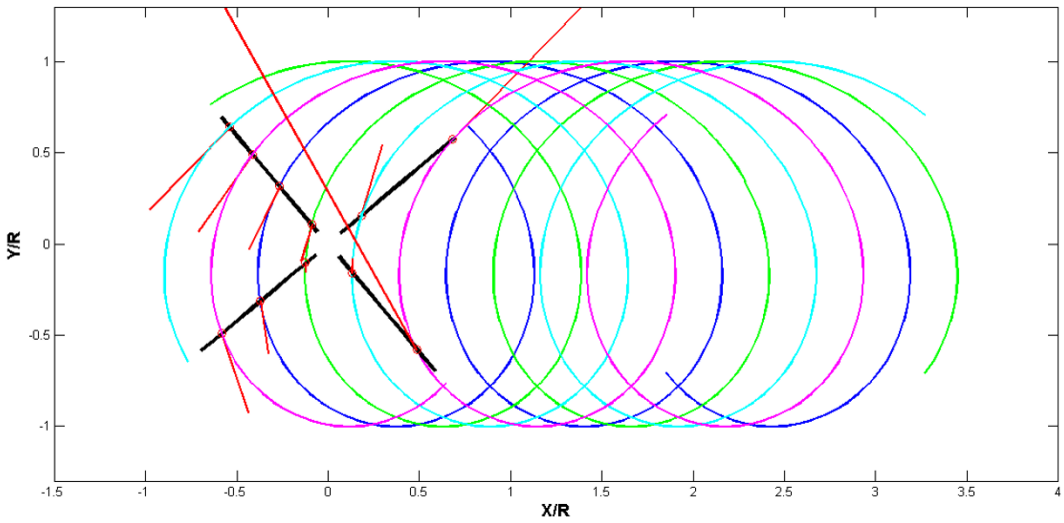

(b) $\psi = 50.$ °

Figure 1.6: Visual representation of M_{TR} at two azimuthal locations

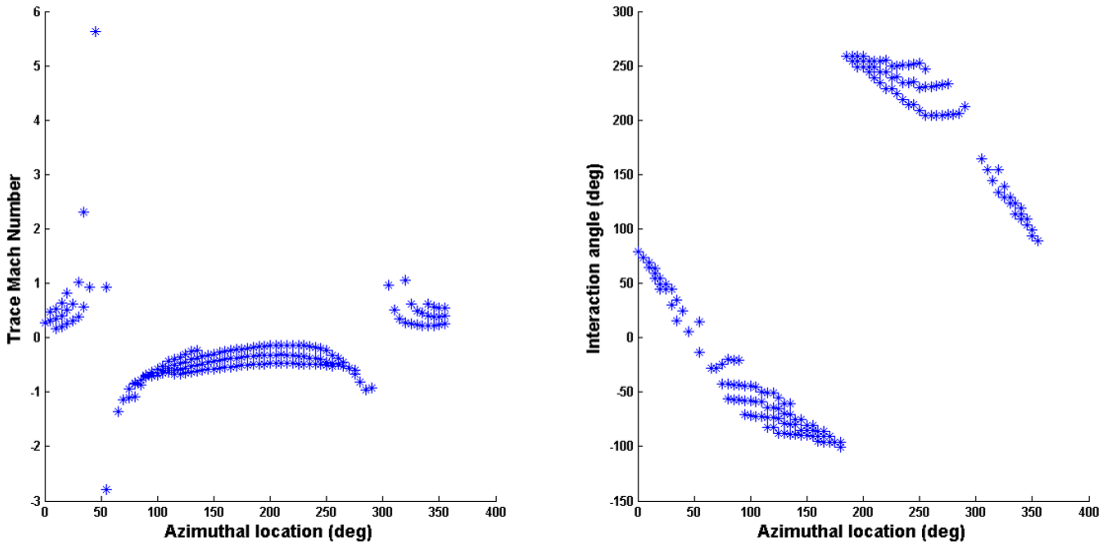

Figure 1.7: M_{TR} and γ as a function of ψ

confirm that M_{TR} is largest in the first quadrant, the advancing side of the rotor, and in the fourth quadrant, the retreating side. Around these locations, the vortices are almost parallel to the leading edge of the blades ($\gamma = 0\ ^\circ - 180\ ^\circ$). It can also be seen that multiple BVI events can occur at a given azimuthal location.

As was explained above, the close proximity of a vortex with a blade at the time of BVI leads to strong impulsive blade loading. A typical BVI loading signature is plotted on Fig. 1.8, along with a contour plot of its time derivative. Evidence of BVI on the advancing and retreating sides is displayed in these figures, as spikes can be observed on the advancing and retreating sides of the rotor disk. It should be noted that interactions with root vortices that develop behind the rotor hub also appear.

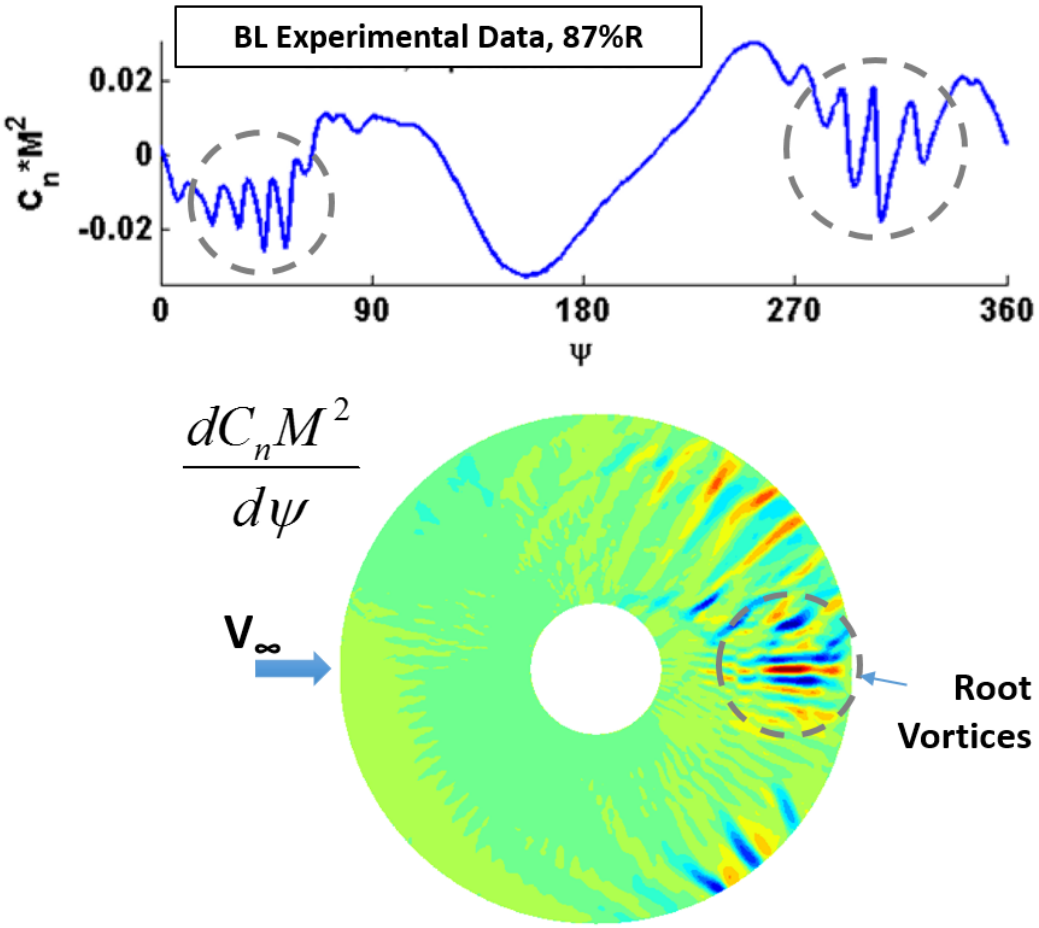

Figure 1.8: Typical BVI signature: normal force and its time derivative

1.2 The HART International Program

To further understand Blade-Vortex Interaction, many experimental tests have been conducted. Among the most notable ones is the HART program. HART stands for Higher harmonic control Aeroacoustic Rotor Test. It is an international program started in 1994 between USA, Germany, the Netherlands, and France. Its first aim was to understand rotor BVI noise generation and reduction mechanisms through the use of Higher-Harmonic blade-pitch Control (HHC). The second goal was to investigate the numerical capabilities of modern flow solvers to accurately simulate helicopter BVI. Two wind tunnel testing campaigns were conducted, the first one in 1994, the second one in 2001. The outcome of this program was one of the most comprehensive experimental and numerical rotor aeroelastic and aeroacoustic database, comparable to the UH-60A Airloads Program. The different participants to the wind tunnel tests were: the US Army AeroFlightDynamics Directorate (AFDD) and NASA Langley in the US, DLR in Germany, ONERA in France, and DNW in the Netherlands. Excellent international cooperation was achieved, bringing the expertise and financial resources of renowned organizations together. Many more research groups later took part in the numerical studies that followed each test, including universities from the US (University of Maryland, Georgia Tech) and Korea (Konkuk University), JAXA in Japan. More than a hundred HART-related publications were published over the years.

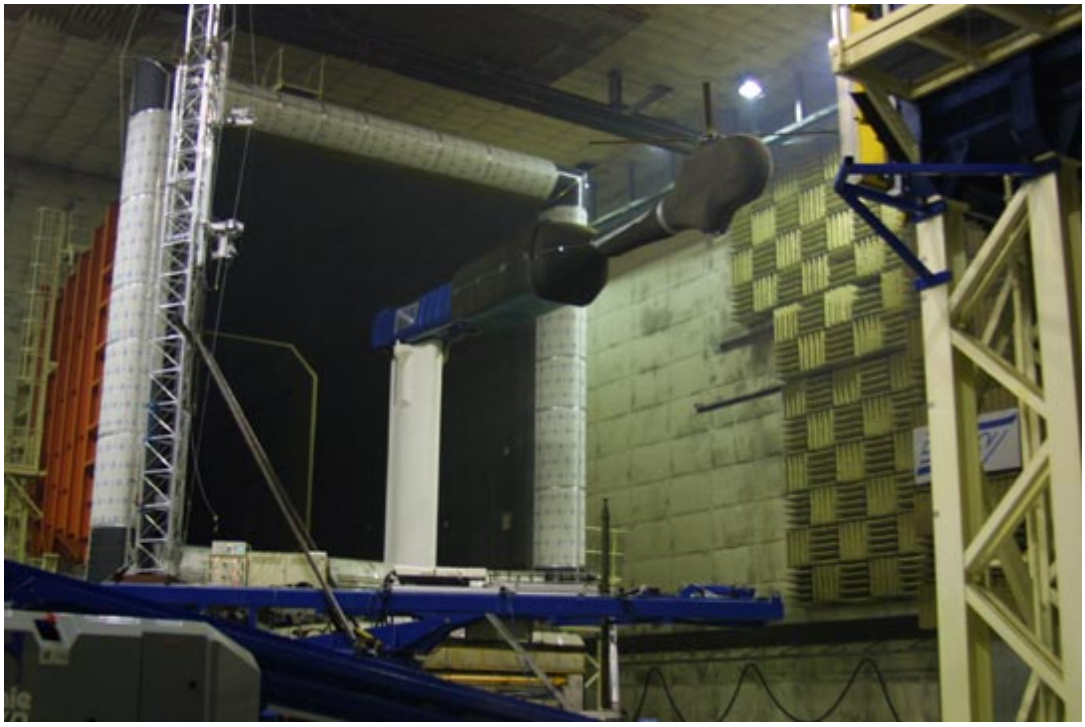

Figure 1.9: HART-II rotor and fuselage model in the LLF-DNW wind tunnel (Ref. [1])

1.2.1 Wind Tunnel Tests

Both HART-I and HART-II wind tunnel tests were carried out in the Large Low-Speed German-Dutch Wind tunnel (DNW), which has a 8×6 m^2 (26.2×19.6 ft^2) open jet cross section (Fig. 1.9). It is the largest acoustic wind tunnel in the world.

While AFDD had the overall program responsibility, the different tasks were divided between all organizations according to their respective domain of expertize. All participants provided preliminary analytical predictions to help in the wind tunnel setup and optimal positioning of the different sensors. NASA coordinated this effort. Many measurements were made using state-of-the-art experimental techniques and hardware, all of which was overseen by DLR. Blade airloads and structural

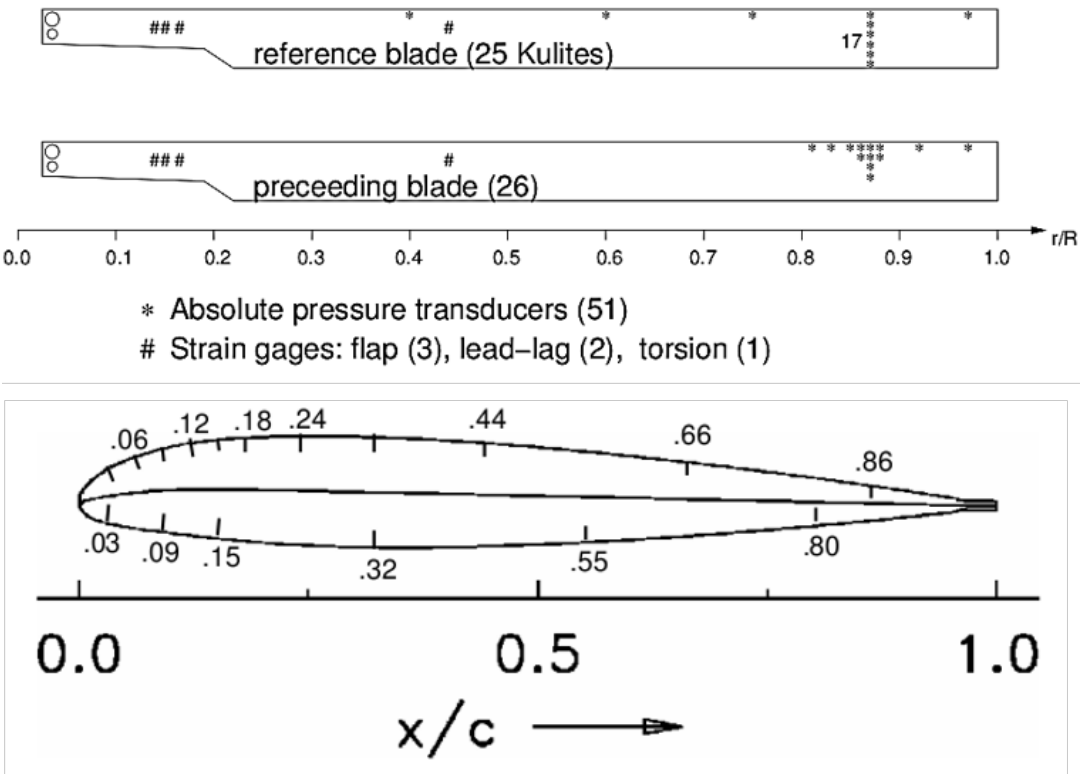

Figure 1.10: HART-II blade instrumentation (Ref. [1])

forces were obtained using fully instrumented rotor blades with absolute pressure transducers and strain gages. Fifty one Kulites were used (25 on the reference blade and 26 on the preceding blade), with chordwise distribution at 87% radius for aerodynamic loading and leading edge distribution for BVI location measurements. Three strain gages were used in flap, two in lead-lag, and one in torsion. Figure 1.10 shows the location of the different blade sensors.

Blade deflections were measured using Stereo Pattern Recognition (SPR) and Blade Tip Deflection (BTD) techniques. They are 3D reconstruction methods using visible markers and stereo camera images. Thirty six markers per blade were used, as well as 4 markers on the fuselage to locate the hub center. The SPR system had 4 camera on the ground while BTD had 2 cameras focused on the blade tip for flap,

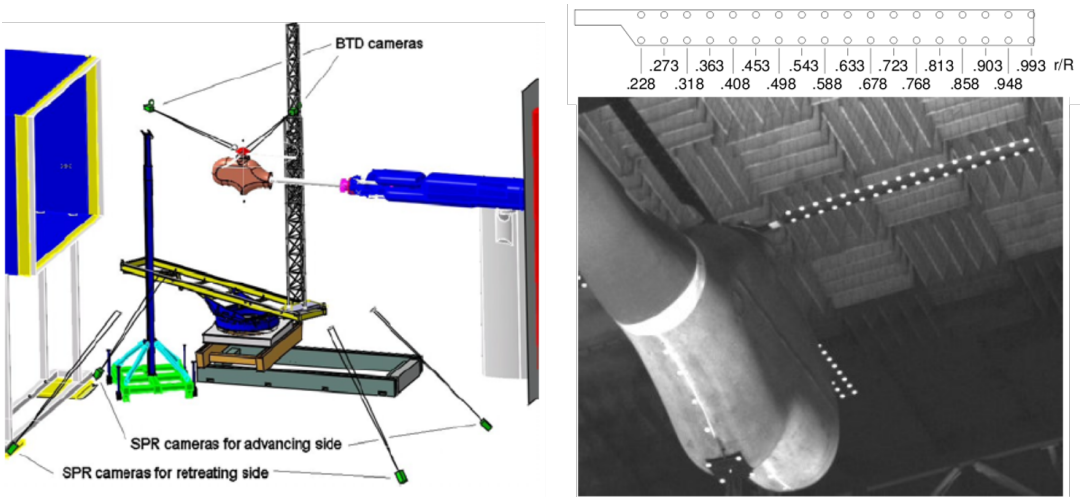

Figure 1.11: SPR/BTD system in the DNW wind tunnel (Ref. [1])

lead-lag, and torsion analysis, as shown on Fig. 1.11.

Rotor balance was also obtained using pitch sensors, torque meters, and force transducers. The wake geometry was captured by Laser Light Sheet (LLS) and 3-Component Particle Image Velocimetry (PIV) systems. Three double pulse lasers and five digital cameras were used (HART-II) with a common traversing system. Figure 1.12 shows this setup.

Finally, acoustic noise levels acquisition was done using a total of 18 microphones, 13 of which were positioned on an array located 1.1 radius below the rotor, moving 2 radii for and aft of the hub center. Figure 1.13 is a schematic representation of this system. A hundred revolutions were captured at a frequency of 2048/rev for each test condition.

HART-I was performed in June 1994 with 22 days of wind tunnel testing. However, shortcomings were observed, such as the limited wake measurements and the low resolutions of certain measurements. On the numerical side, limitations

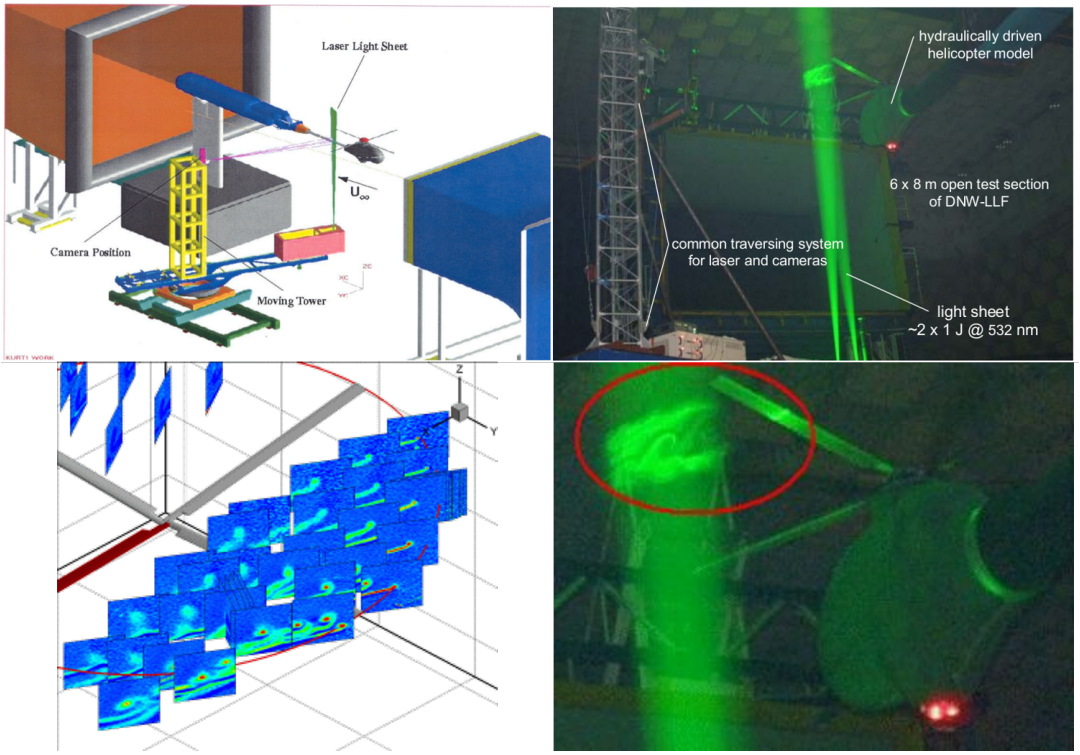

Figure 1.12: PIV system in the DNW wind tunnel (Ref. [1])

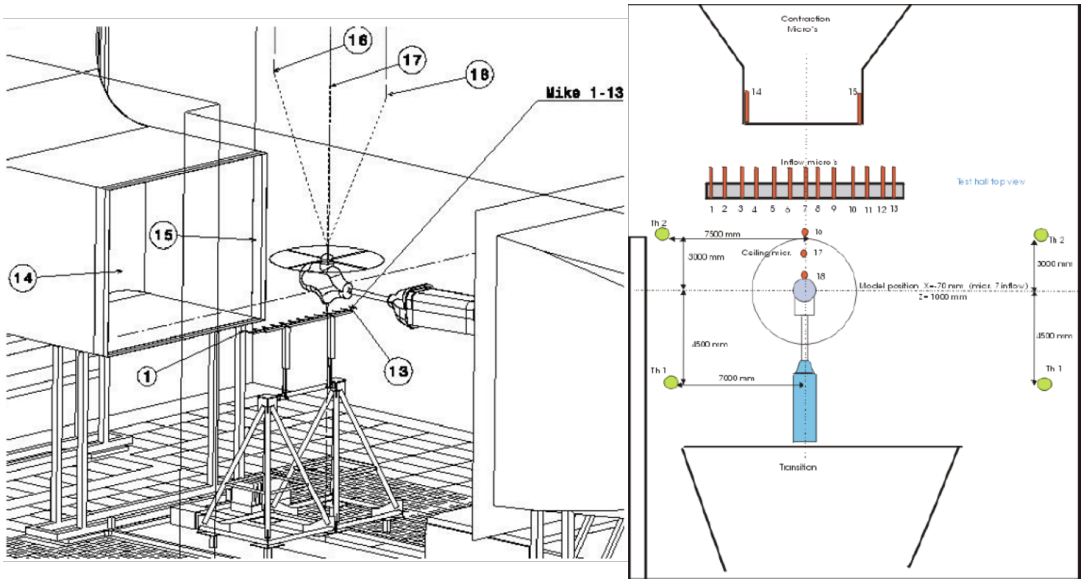

Figure 1.13: Microphones in the DNW wind tunnel (Ref. [1])

in the predictive capabilities of fluid and structural solvers were seen (airloads, wake geometry, blade deflections). Therefore, it was decided to carry out a second wind tunnel test, HART-II, a few years later in October 2001, as technologies had matured. The more robust and detailed 3C-PIV system replaced Laser Doppler Velocimetry (LDV) measurements for a more complete investigation of the wake system over the entire rotor disk: tip vortex trajectory, wake development, aging process, vortex core size and strength. LDV only gives conditionally averaged data whereas PIV provides instantaneous velocity vectors.

1.2.2 The HART Rotor and Fuselage

The HART-II rotor is a 40% Mach-scaled model of the BO-105 rotor (Eurocopter). It is a 4-bladed, hingeless rotor with a 2 *meter* radius (R) and 0.121 *meter* chord (c), leading to an aspect ratio (AR) of 16.5289. The blades have a rectangular planform and a negative linear twist of -8 *degrees*. 2.5 *degrees* of precone is used as well as a root cut-out of 22% of the rotor radius. The airfoil is the cambered NACA23012 which has a 12% thickness-to-chord ratio. It was modified to match the full scale rotor by adding a 5 *mm* trailing edge tab (Fig. 1.10). The rotor was driven and controlled by complex hydraulic actuators, with full swashplate motion, as seen in Fig. 1.14. For the HART-II wind tunnel testing, a generic helicopter fuselage, as seen in Fig. 1.15, was used to roughly simulate the effects of such a structure on the flow field and have a more realistic simulation of BVI. As will be seen in later chapters, including a mean of modeling such effects in CFD is one of

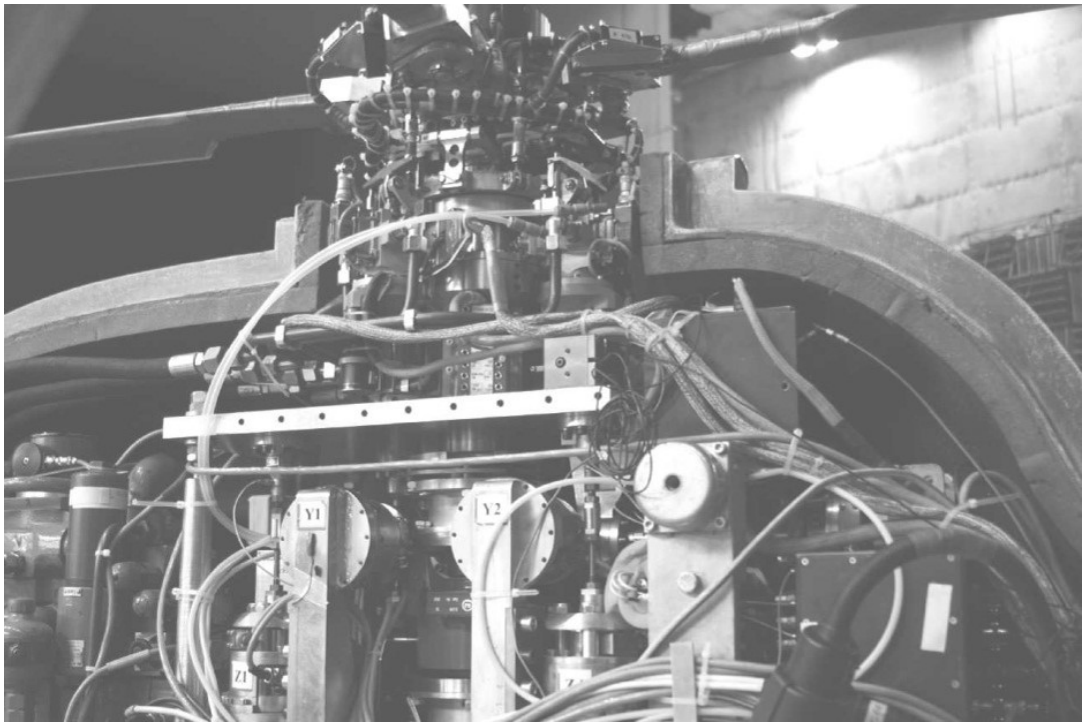

Figure 1.14: HART-II rotor hydraulic system (Ref. [1])

the key to achieving higher levels of fidelity.

1.2.3 Higher-Harmonic Control

As mentioned above, one of the goal of this study was to measure the impact of HHC on BVI and rotor noise and vibrations. Therefore, HHC inputs were superimposed as additional pitching in the swashplate motion. It is a precisely sized and phased 3/rev additional blade root pitch input. The total blade pitching motion follows this equation:

$$\theta = \theta_0 + \theta_{1C}\cos(\psi) + \theta_{1S}\sin(\psi) + \theta_{HHC}\sin(3\psi - \Phi_{HHC})$$

In this equation, θ_0 is the collective pitch angle, θ_{1C} is the lateral cyclic pitch angle, θ_{1S} is the longitudinal cyclic pitch angle, θ_{HHC} and Φ_{HHC} are the magnitude

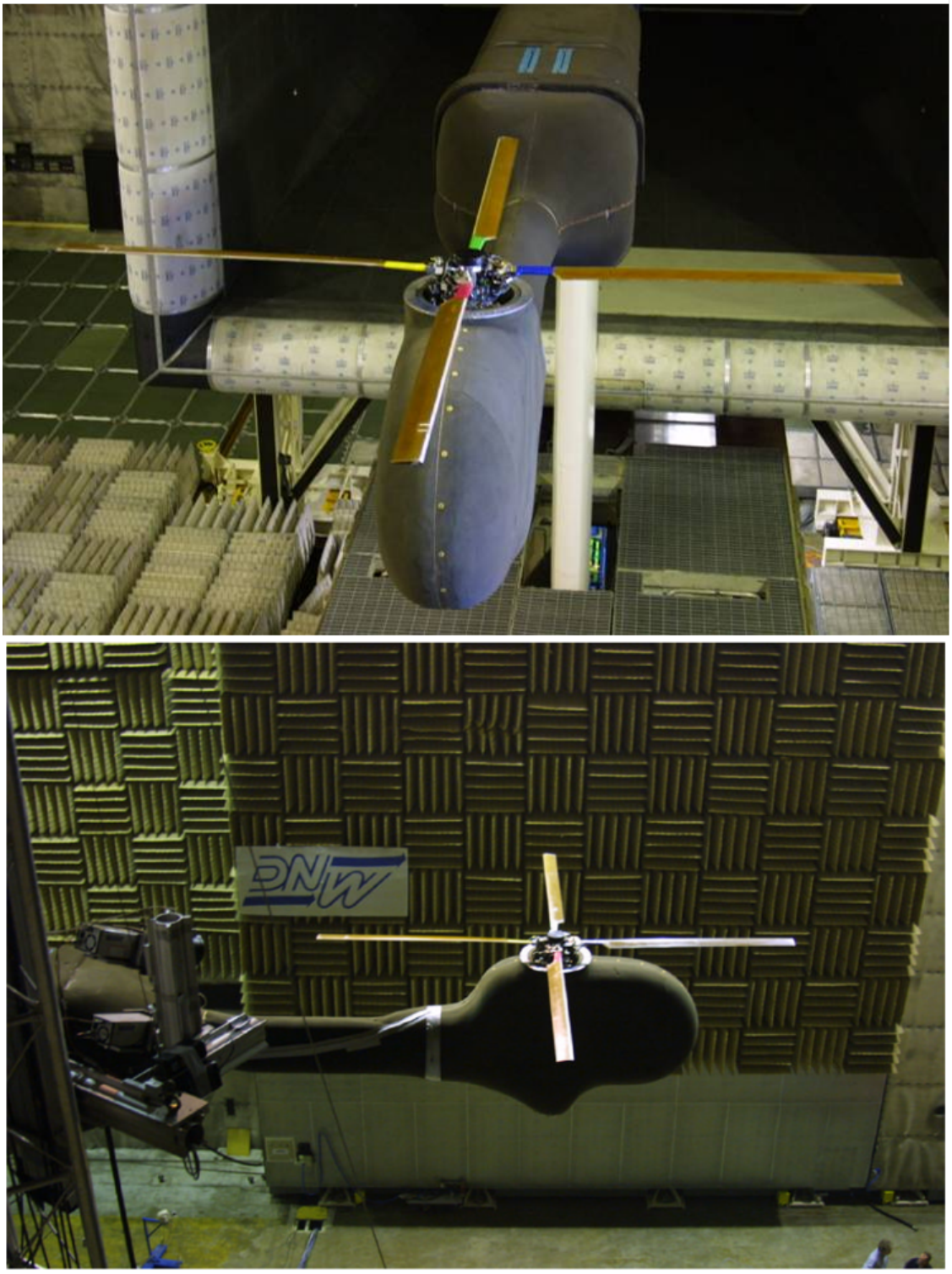

Figure 1.15: The HART-II rotor and its fuselage in the DNW wind tunnel (Ref. [1])

Case	Amplitude	Phase
Baseline (BL)	0.0 °	0.0 °
Minimum Noise (MN)	0.81 °	300 °
Minimum Vibration (MV)	0.79 °	180 °

Table 1.1: 3/rev HHC blade root pitch amplitude and phase of the three cases.

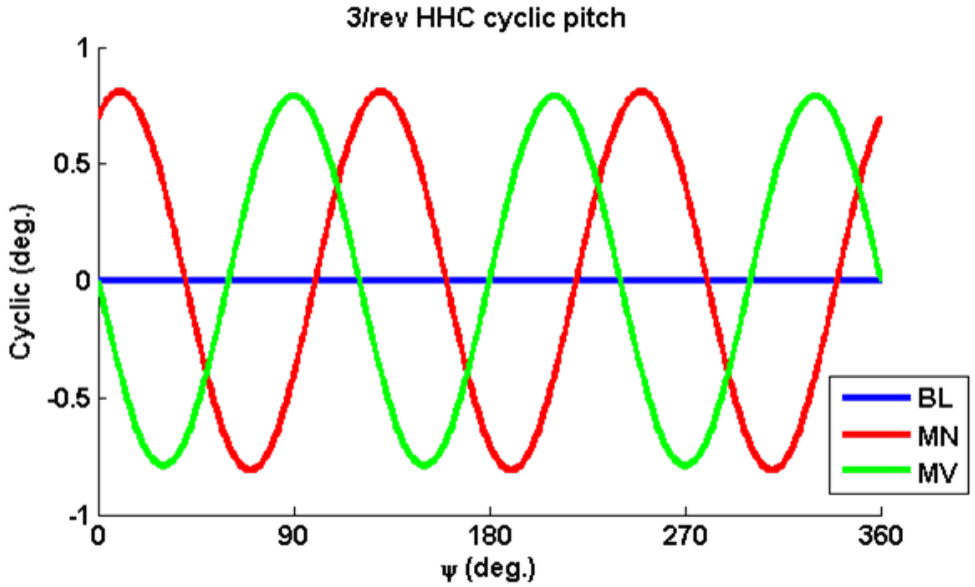

Figure 1.16: 3/rev HHC pitch signal of the Minimum Noise and Minimum Vibration cases

and phase of the 3/rev HHC signal, and ψ is the blade azimuth angle. Three different flight conditions were studied: Baseline (BL), Minimum Noise (MN), and Minimum Vibration (MV). Their respective value of HHC pitch amplitude and phase are shown in Table 1.2.3. The Baseline case (BL) does not have any HHC. Figure 1.16 shows this higher harmonics pitching input signal. To try to understand the influence of HHC on BVI, both in terms of noise and vibration, numerical results obtained in this doctoral work are used. They will be presented in greater details, along with the numerical implementation of the codes, in later chapters. The main effect of HHC is to modify the loading pattern around the rotor disk. Figure. 1.17

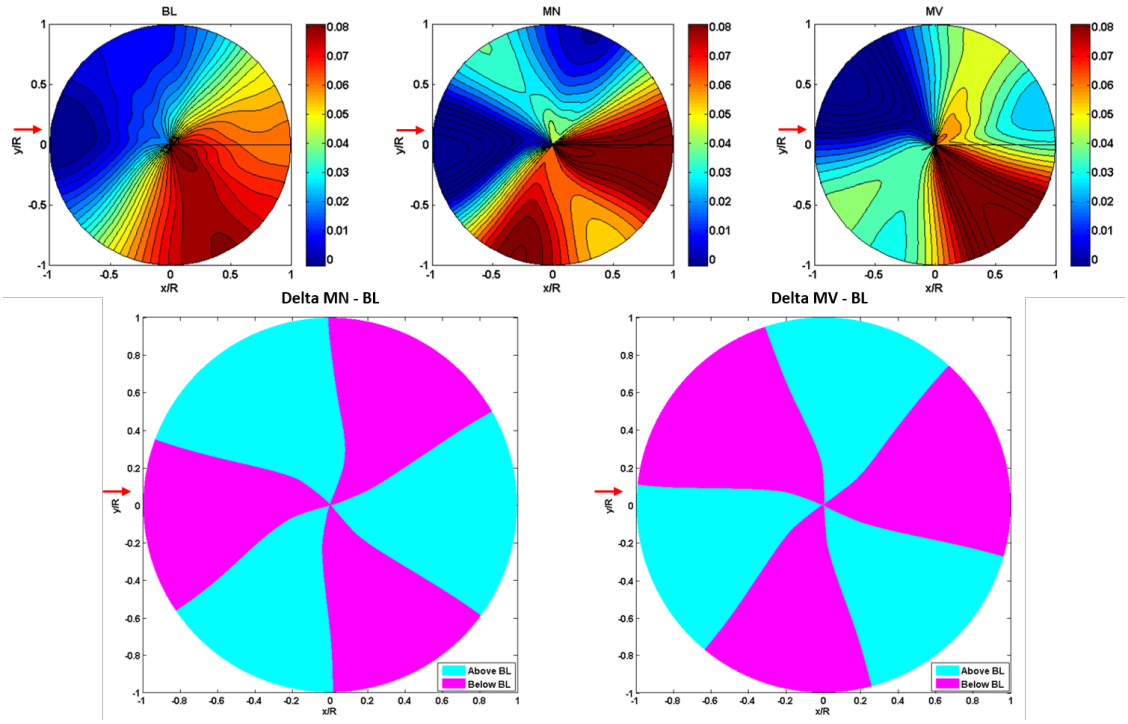

Figure 1.17: Total blade twist contours for the three HART-II conditions and delta with the baseline case.

shows the total blade twist, which is the combination of the built-in linear twist, the pitching motion due to the control angles and HHC, and the elastic response of the blade. The strong 3/rev signal due to HHC is displayed for the minimum noise and minimum vibration cases, and is especially evident in the delta plots, which show the azimuths where the blade pitch is above or below that of the baseline case. Due to its particular phasing, the minimum noise case has higher blade angles than the baseline case in the 2^{nd} and 3^{rd} quadrants. This translates to higher loading at those locations, as seen on Fig. 1.18. This loading pattern greatly affects the wake strength and geometry. In the minimum noise case, the tip vortices released in regions of higher normal force have higher vorticity magnitudes, which means that their mutual influence is greater. This can be seen in Fig. 1.19 where top

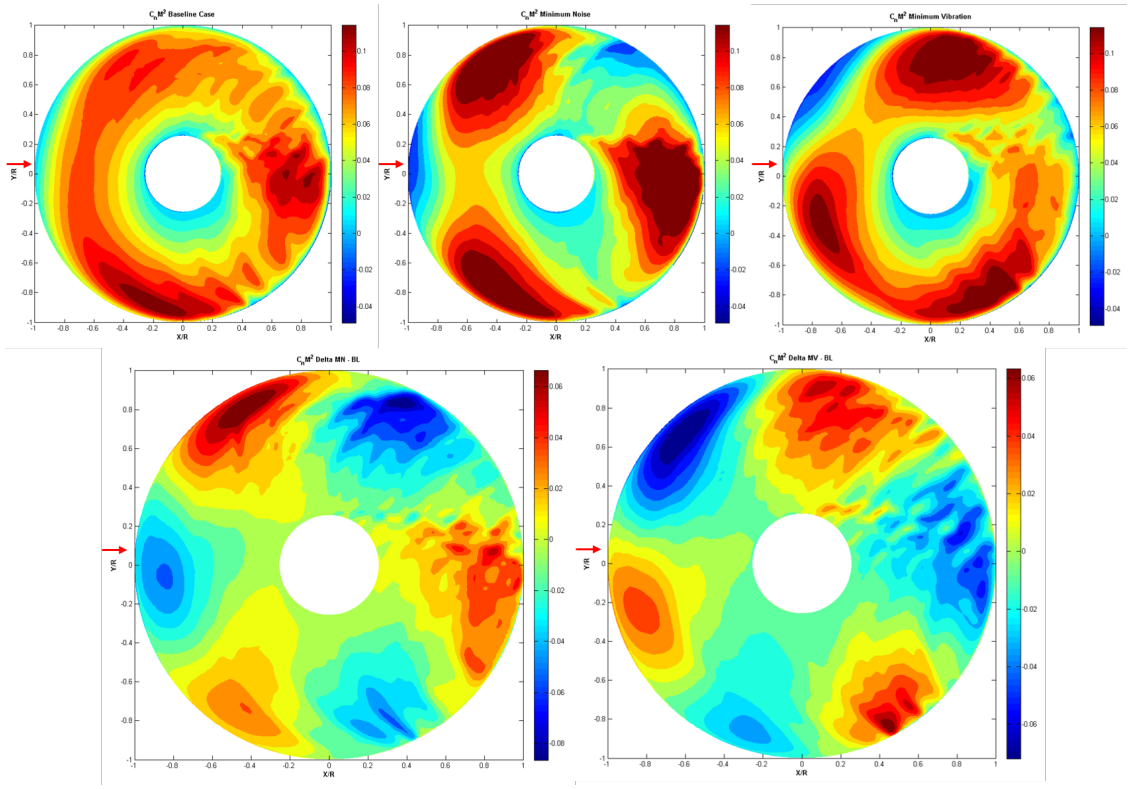

Figure 1.18: Blade normal force coefficient contours for the three HART-II cases and delta with the baseline case.

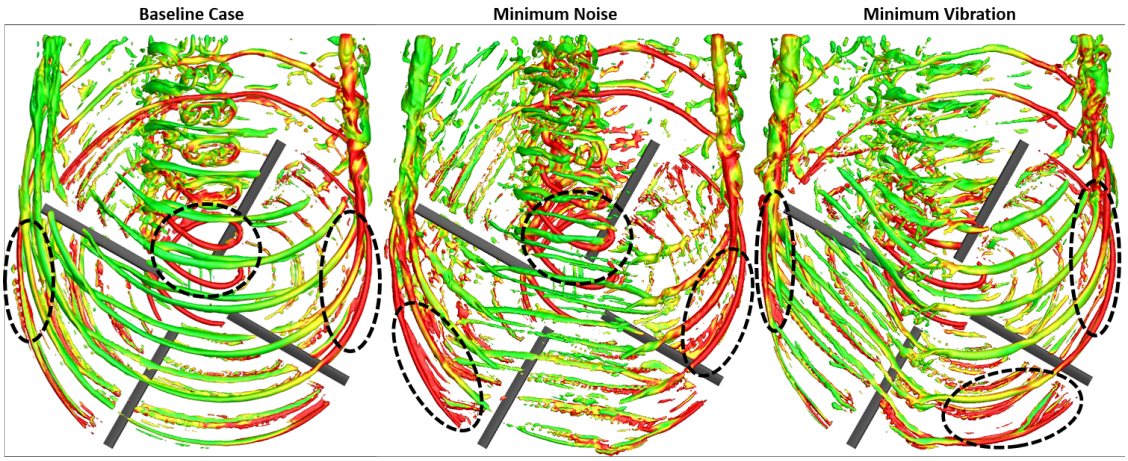

Figure 1.19: Iso-surfaces of Q-criterion for the three HART-II cases, top view.

views of the wake geometries for the three cases are plotted and colored by vorticity magnitude. At the front of the MN rotor, the younger, and stronger, tip vortices push older vortices down to a point where they will cross the plane of rotation of the blades, as seen on Fig. 1.20 which is a contour plot of vorticity magnitude on a longitudinal plane of the advancing side. This could seem to be an adverse effect, as stronger vortices come to interact with the blades, creating BVI. However, in the 2^{nd} and 3^{rd} quadrants, the interaction angle is large as the blades and vortices are not parallel, which means that BVI noise remains acceptable. This interaction helps diffuse and burst the vortices which create the strongest BVI in the 1^{st} quadrant of the baseline case. As will be seen later, the noise levels generated by the minimum noise case are lower, and a shift in the noise pattern towards the front of the rotor can be observed, due to the shift in loading pattern. For the minimum vibration case, the effect is different: the lower blade loading in the 2^{nd} quadrant leads to the formation of weaker and smaller vortices. However, more individual vortices can be seen as they do not combine under their own mutual influence. Although this

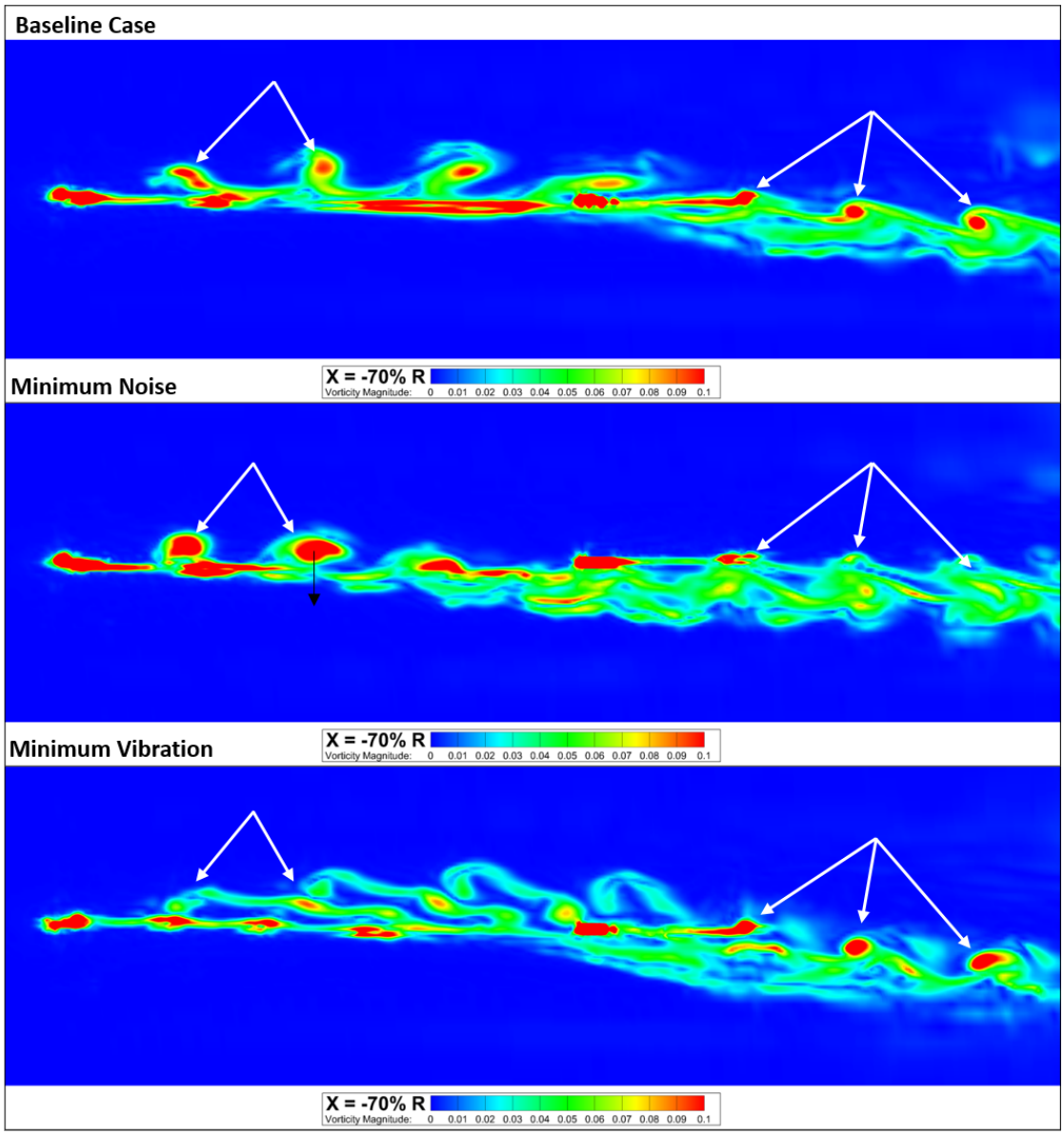

Figure 1.20: Contours of vorticity magnitude on a longitudinal plane on the advancing side for the three HART-II cases.

creates higher levels of noise, as more BVI events occur, their individual strength is lower, which reduces the blade response and therefore the amount of vibration in the system.

Another effect of HHC on the rotor blades is to modify their position in space as they rotate. In addition to altering their pitching motion, variations in lead-lag and flapping displacements are introduced, with a certain amount of phase delay. This can have a great impact on rotor noise and vibrations as the driving mechanisms of BVI can be aggravated. For example, the miss-distance can be increased if using adequate higher harmonic magnitude and phase to increase the flapping deflection of the blades at the time of the strongest interaction. Similarly, lead-lag deflections can be used to change the interaction angle. Figure 1.21 shows the flapping response of the blades around the rotor disk for the three HART-II conditions. The influence of the minimum noise and minimum vibration HHC over the baseline case can be seen. Looking more closely at a particular BVI event on the advancing side, Fig. 1.22 summarizes the effects explained above. The blade shown is at 60° azimuth. In the baseline case, the blade is seen hitting a strong vortex. In the minimum noise case, the blade is higher and the vortices are lower and much weaker, as they have been diffused in the 2^{nd} quadrant. In the minimum vibration case, the blade is lower and interacts with more vortices, but they are smaller and weaker ones.

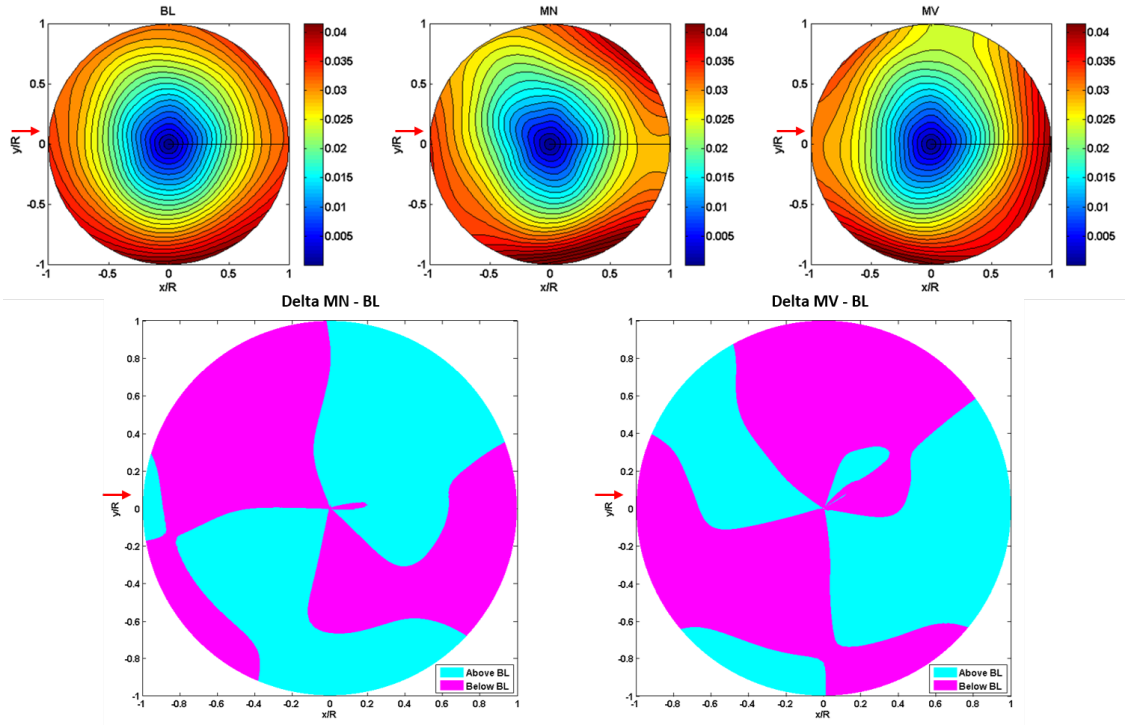

Figure 1.21: Blade flapping contours for the three HART-II conditions and delta with the baseline case (100 Z/R).

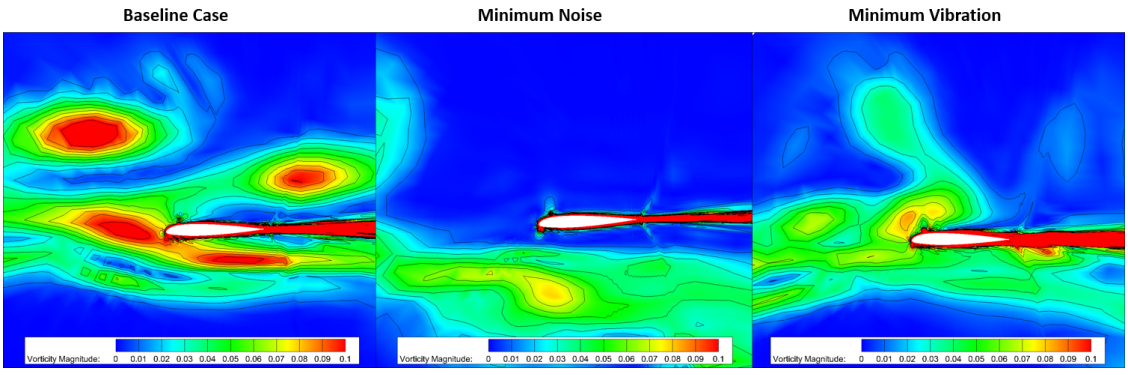

Figure 1.22: Vorticity magnitude cross-sections on the advancing side for the three HART-II cases.

1.2.4 The HART Flight Condition

The wind tunnel was setup to create a low speed descending flight condition. The advance ratio was set to 0.15 ($\mu = V_\infty/V_{tip} = V_\infty/(R\Omega)$). Note that a $cos(\alpha)$ factor can appear in some definitions depending on the convention. A range of shaft tilt angles (α) were tested in the wind tunnel (from $-6.9\,^\circ$ to $11.4\,^\circ$). $\alpha = 5.3\,^\circ$, corrected to $4.5\,^\circ$ to account for wind tunnel effects, was chosen for most numerical simulations, as it showed the most intense BVI signature. This nose-up shaft tilt attitude simulates a descent flight condition, as it creates a reduced rotor inflow. The tip Mach number M_{tip} was set to 0.6387 and the thrust coefficient C_T to 0.00457. These parameters were specifically chosen to create strong BVI both on the advancing and retreating sides of the rotor disk, as the wake is blown back into the plane of the rotor. As will be seen later, this leads to high levels of intrusive noise and vibrations. More details about the HART experimental testing can be found in Ref. [1] and on Fig. 1.23.

1.3 HART-II Numerical Simulations

Over the years, the HART-II experimental data has been extensively used to validate and test many different numerical approaches. Various CFD methods have been used, with different levels of numerical and physical assumptions, and either using prescribed blade motion or with coupling to a structural solver. From a numerical stand point, the main difficulty in accurately capturing BVI resides in the ability of the solver to capture and preserve the rotor wake, especially the tip

Characteristic	Symbol	Value
Rotor geometry:		
Rotor radius	R	2 m
Blade chord	c	0.121 m
Number of blades	N_b	4
Rotor solidity	σ	0.077
Non-dim. root cutout	r_a	0.22
Non-dim. zero twist radius	r_{tw}	0.75
Blade linear twist per span	Θ_{tw}	$-8°$
Airfoil (trailing edge tab)		NACA23012
Wind tunnel data:		
Cross-section		8 m $\times$ 6 m
Air pressure	p_∞	100.97 kPa
Air temperature	T_∞	17.3°C
Air density	ρ_∞	1.2055 kg/m^3
Speed of sound	a_∞	341.7 m/s
Wind speed	V_∞	32.9 m/s
Mach number	M_∞	0.0963
Hub centre dist. to nozzle	x_{hub}/R	3.5
Hub pos. up of centreline	z_{hub}/R	0.4575
Mic. array below centreline	z_{mic}/R	-0.65
Operational data (BL case):		
Rotational speed	Ω	109.12 rad/s
Hover blade tip Mach no.	M_h	0.639
Rotor shaft angle of attack	α_S	5.3°
Wind tunnel interference angle	$\Delta\alpha_S$	$-0.8°$
Advance ratio	μ	0.151
Rotor thrust	T	3300 N
Thrust coefficient	C_T	0.00457
Rotor loading coefficient	C_T/σ	0.0594
Rolling moment	M_x	20 Nm
Pitching moment	M_y	-20 Nm
Rotor power	P	18.3 kW
Collective control at r_{tw}	Θ_{75}	3.8°
Lateral cyclic control	Θ_C	1.92°
Longitudinal cyclic control	Θ_S	$-1.34°$
Mean steady el. tip twist	Θ_{el}	$-1.09°$

Figure 1.23: The HART-II rotor in numbers (Ref. [1])

and root vortices. These vortical structures must have the correct strength and size when released into the flow field to yield acceptable results. Then, they must not be over-diffused through out the course of their evolution, so that their strength and size, at the time of interaction with rotor blades, is satisfactory. Doing so requires the use of advanced numerical techniques, some of which are highlighted below.

In 2005, Lim et al (Ref. [29]) investigated the need for free-wake models to include multiple trailed vortices to improve lift prediction in case of strong BVI. They applied their model to the HART-I, HART-II, and UH-60 rotors and compared with available experimental data. They tried different combination of trailed vortex bundles. The main finding was that modeling a root vortex, in addition to the typical tip vortex, leads to improved lift correlations. In addition, letting the tip vortex release point move to a more inboard location helps $C_n M^2$ predictions. This is due to the formation of dual tip vortices in case of negative lift. This modeling technique is used in the free-wake solver developed at UMD. They also noted that simulating multiple trailed vortices increased the 3/rev lift correlation compared to the more traditional roll-up wake model.

In 2006, Sim et al (Ref. [30]) used a wake capturing approach with loosely coupled structural dynamics (OVERFLOW-2 + CAMRAD-II) to simulate the HART-II rotor. They saw a notable improvement over the use of a lifting-line / free-wake approach, although computational limitations and coarse grid spacing led to under-predicted BVI loads and noise.

The same year, Dietz et al (Ref. [31]) tried to overcome this issue by using Vortex-adapted Chimera grids in their simulation. The idea was to locally refine

the grid region around vortices using vortex conforming overset meshes to avoid excessive numerical diffusion of the wake and under-predicting BVI airloads. These additional vortex grids followed an analytical tip vortex model. While their method was promising, the use of an inviscid solver with only a second order accurate space-marching scheme was not enough to accurately capture some of the features of the HART-II rotor.

In 2007, van der Wall et al (Ref. [34]) presented results from DLR's high resolution comprehensive code applied to the HART-II case. This code includes a lifting-line based aerodynamic model for near-field solution, a prescribed wake approach for the far-field, a structural solver for blade deflection and trim, and an acoustic solver for noise radiation. They showed that good qualitative and quantitative results could be achieved as long as unsteady airloads, fully elastic blades, and an improved wake model was used in the simulation.

In 2009, Kelly et al (Ref. [32]) investigated the potential benefit of using a lifting-chord formulation over the more common lifting-line approach for high frequency BVI airloads. These blade loading models were used as source to a Vorticity Transport Model, which is known to accurately represent rotor wake structures. They showed good improvement in lift amplitude and phase, as the lifting-line approach usually yields over-prediction. This is especially true for blades interacting with vortices that are much smaller than their chord.

The same year, Yu et al (Ref. [35]) modeled the HART-II rotor using unstructured deforming meshes and a viscous flow solver. Experimental prescribed blade deflections were used and proved to be critical, compared to a rigid rotor simulation,

to accurately predict BVI loads, especially torsional motion. Solution-adaptive mesh refinement was used to better capture tip vortices and provided better magnitude predictions of high frequency loads.

In 2010, Anusonti-Inthra (Ref. [33]) used a loosely coupled CFD/PVTM/CSD approach to simulate different flight conditions, including that of the HART-II rotor. The Particle Vortex Transport Method (PVTM), which accounts for vortex stretching and diffusion, was applied to the far-field region and used the near-field vorticity from the CFD solver as source. Accurate wake predictions were obtained and the expected flow featured were reasonably well captured, including the effect of negative blade lift. However, under-prediction in blade loads was generally observed.

In 2010 and 2011, two papers (Ref. [36] - Ref. [37]) were published on the importance of including a fuselage model in BVI numerical simulations. Both did so by embedding a specific fuselage mesh into a wake capturing overset grid topology. Simpler models, such as analytical formulations derived from potential flow theory were also used (Ref.[2]). The main influence of such a model came through better wake position predictions, due to the upwash and downwash seen fore and aft of the HART-II fuselage. Improvements were also observed in the phasing of the low and high frequency blade lift and in the trim angles.

At University of Maryland (UMD), Gopalan et al published in 2006 preliminary results for the HART-II rotor. They used a wake coupling approach with the Navier-Stokes solver SUmb from Stanford University (Ref. [18]). Their primary focus was on BVI acoustics.

The most recent numerical results from the different organizations taking part

Partner	CFD Code	CSD Code
U.S. Army Aero-flightdynamics Dir.	OVERFLOW	CAMRAD-II
U.S. Army Aero-flightdynamics Dir.	NSU3D-SAMARC	RCAS
NASA-Langley	OVERFLOW	CAMRAD-II
NASA-Langley	FUN3D	CAMRAD-II
Georgia Institute of Technology	FUN3D	DYMORE-4
Georgia Institute of Technology	GENCAS	DYMORE-2
Konkuk University	KFLOW	CAMRAD-II
University of Maryland	TURNS	UMARC
German Aerospace Center	2D semi-empirical	S4

Figure 1.24: List of the different CFD and CSD codes used by the various HART-II partners

in the HART-II project were published at the 2012 Forum of the American Helicopter Society (AHS) (Ref. [2] - Ref. [3]). In the first reference, van der Wall et al compared results using comprehensive analysis, while in the second reference, Smith et al used fully coupled RANS-based CFD with CSD. The numerical solvers employed by the different collaborators are listed in Fig. 1.24. Figure 1.25 shows representative views of some of the numerical approaches and setups used, whether it is structured or unstructured, Eulerian or Lagrangian. The main objectives of these papers were to survey today's "State-of-the-Art" numerical capabilities and to define the minimum levels of modeling required to accurately predict helicopter BVI. The most important elements were: fully elastic blades model, unsteady aerodynamics, fine discretization in time and space, and the inclusion of fuselage effects into the simulation.

While this is just a short summary of some of the numerical work done around the HART-II project, the diversity and number of methods seen here clearly high-

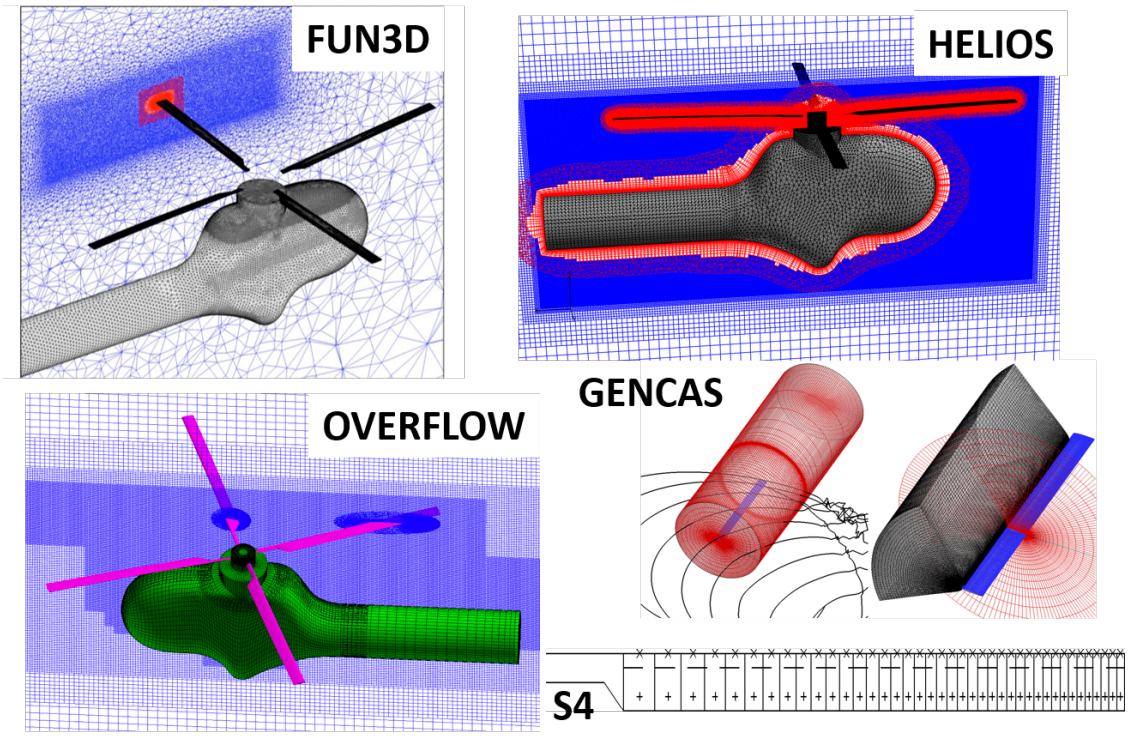

Figure 1.25: Approach and setup used by some of the HART-II partners (Ref. [3])

lights the great interest and value of this program. Both Eulerian and Lagrangian solvers were applied, inviscid or viscous simulations conducted, structured or unstructured meshes employed, and diverse combinations of them for the different flow domains. This has been a tremendous effort that has lead the field of CFD forward for over a decade.

1.4 Objectives of the Thesis

As was seen in the previous section, numerous numerical methods have been used over the years to simulate the HART-II rotor, and, in general, rotorcraft BVI. In an attempt to pursue this on going effort, the main objective of this thesis is to implement a numerical framework capable of accurately simulating BVI. Taking into

account some of the remarks and findings made by other research teams, the required components to carry out such simulations have been developed or improved. These include flow solvers to predict blade airloads, a mean of calculating rotor blade deflections from these airloads, a way of representing the rotor wake and trailed vortices precisely, and an acoustic code to compute BVI noise. It should be noted that experimental prescribed blade motions can be used in place of the structural solver. In addition, this must be done with numerical efficiency in mind and using reasonable computational resources. Therefore, GPU computing was used for some of the numerical solvers developed, which greatly reduced the simulation times.

The second objective of this thesis is to validate the different codes using the HART-II experimental database. All three conditions are simulated: Baseline, Minimum Noise, Minimum Vibration. The solution accuracy is examined by looking at data like blade airloads, blade motion predictions, rotor trim quantities, wake geometry, and noise signature. These results are also compared to other numerical simulations made by research teams from around the world, through the publication of collaborative papers (Ref. [2], Ref. [3]).

The third objective of this thesis is to compare and evaluate different approaches to BVI modeling. Although some attempts were made to compare the diverse flow solvers and CFD/CSD methods applied to the HART-II rotor by different research groups, it seems that a more consistent and systematic approach is necessary to understand the effect of different levels of modeling. Therefore, the framework developed through the course of this doctoral work includes different aerodynamic solvers, both for the near-field and far-field flow domains, that can

be changed and compared. This makes assessing the accuracy and computational efficiency of specific modeling techniques easy.

Another objective of this thesis is to develop and compare different ways of including fuselage effects into a CFD simulation. As was shown by other research groups, fuselage modeling is necessary in order to obtain adequate BVI simulation results. Therefore, three different techniques have been implemented and put into contrast, both in terms of solution improvement over previous simulations and in terms of computational efficiency.

1.5 Contributions of the Thesis

The main contribution of this thesis is the combination and systematic comparison of a broad range of CFD methods applied to the problem of rotorcraft BVI. All aspects of the simulation were covered creating a multi-fidelity and multi-physic framework including: finite element structural dynamics, multiple Lagrangian and Eulerian flow solvers, acoustics modeling, and advanced meshing tools. By making incremental changes in the numerical complexity and level of physics captured, a deeper understanding of the required components for simulating BVI was achieved. In addition, it was possible to highlight the trade offs that exist between achieving higher solution accuracy and keeping the computational costs to a minimum. Furthermore, the development of novel and advanced fuselage modeling techniques was carried out and proved to be a key factor in achieving better BVI predictions. Finally, the use of modern computing technologies such as GPUs allowed for great

improvements in code efficiency.

1.6 Organization of the Thesis

The first part of the thesis is dedicated to the detailed description of the various numerical solvers used in this research. Starting with comprehensive analysis, which includes a simple aerodynamic model, a structural solver, and an algorithm to perform rotor trim, multiple improvements are introduced including: advanced linearized aerodynamic, free-wake model, RANS-based methods. Then, the coupling strategy employed in the framework is highlighted. Parametric studies conducted to determined optimal numerical parameters are presented next. In the following chapter, fuselage modeling and the three methods developed are explained. Validation cases are also shown to access their accuracy and performance. Finally, HART-II numerical results are presented. These include comparison of blade airloads, deflections and structural moments, rotor trim, wake geometry, and acoustics levels.

Chapter 2

Numerical Modeling

In this chapter, the numerical modeling used in this work will be presented. The different solvers involved and their numerical implementation will be outlined, starting from a basic comprehensive analysis and gradually adding improvements by replacing certain components of the framework with more advanced solvers capable

of capturing more flow physics. Then, the coupling strategy used between the various codes will be layed out and the idea of a multi-fidelity framework introduced.

2.1 Comprehensive Analysis: UMARC

The first piece of the framework presented is a comprehensive analysis solver. It is called comprehensive because it can be used as a standalone package. It can carry out both structural and aerodynamic analysis of rotor systems, and has an algorithm to perform rotor trim.

2.1.1 Code Description

The comprehensive aero-elastic analysis is based on a finite element methodology (Ref. [7]). The four blades are modeled as second order non-linear isotropic Euler-Bernoulli beams. They are divided into 20 span-wise elements undergoing coupled flap (w), lead-lag (v), torsion (ϕ), and axial (u) degrees of freedom based on Ref. [8] and Ref. [9], resulting in a total of 15 degrees of freedom for each beam element, as schematized on Fig. 2.1. Blade deflections as a function of the spanwise location are obtained using interpolating polynomials: third order for u, v, w and second order for ϕ.

Modal reduction is limited to the first 10 dominant natural modes (5 flap, 3 lag, 2 torsion). The structural dynamic equations are integrated in time using the finite element in time Gaussian procedure which uses 12 equal temporal elements, with 6 points within each element. This results in an effective azimuthal discretization

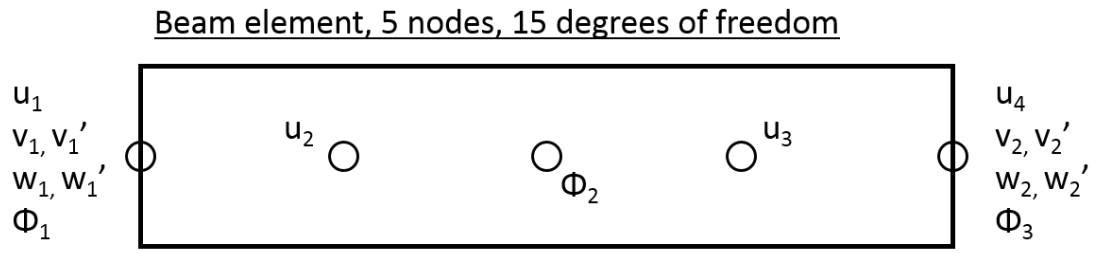

Figure 2.1: UMARC model beam element.

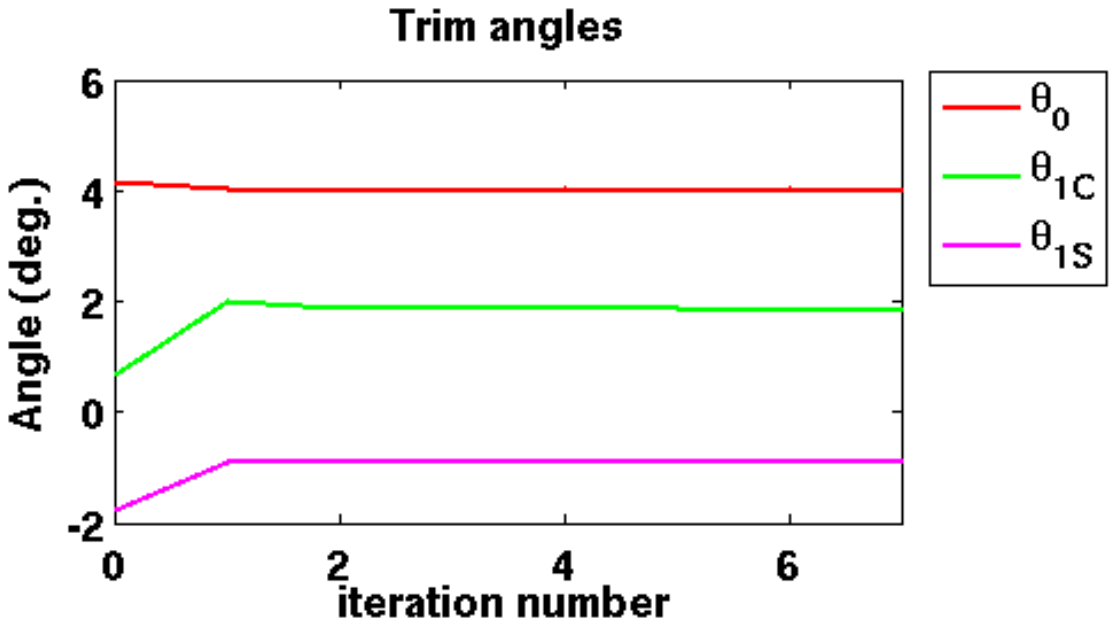

Figure 2.2: Iteration histories of the trim angles (BL case, wake coupling method).

of 5 °. Rotor trim is performed to the target thrust and hub roll/pitch moments obtained from wind tunnel measurements. A wind-tunnel trim algorithm is used (Ref. [10]) which means that only the three equations corresponding to this force and the two moments are solved, as opposed to a free-flight or propulsive trim method which solves all six equations of motion. Iteration histories for the different trimmed control angles predicted by the code are plotted in Fig. 2.2. θ_0 is the collective pitch angle, θ_{1C} is the lateral cyclic pitch, and θ_{1S} is the longitudinal cyclic. It can be seen that good converge was achieved after a few coupling cycles.

A force summation method is used to compute bending moments. It was shown in Ref. [2] that this approach yields better results than the modal or curvature method for the same number of terms. UMARC has its own linearized aerodynamics solver which, for these results, uses a uniform or linear inflow assumption. Once a converged aerodynamic solution is obtained, the new airloads are sent to the structural dynamics solver. The steady integrated loads are computed at the hub and compared to the target thrust and moments (delta method), leading to re-trim of the aircraft and updated values of the control angles and blade deflections. It should be noted that some the results shown in later chapters, especially for the fuselage model validation study, were obtained using prescribed deflections and control angles. It was decided to use this approach instead of the fully coupled simulation to concentrate on the aerodynamic results (airloads, flow visualization), which should reflect the influence of the fuselage and the difference between the different modeling methods. These prescribed deflections were obtained by the HART-II AFDD team and were found to be very close to experimental data at available stations. Figure2.3 shows a comparison of the normal force coefficient, unfiltered and filtered (f>10/rev) at 87% radius, for a fully coupled simulation and using prescribed blade deformations. It is clearly seen that the lower frequency content from the blade motion is better correlated with the experimental data when prescribed deformations are used, which results in a slight improvement in the predicted higher frequency content as well. The coupled results were obtained using the wake coupling approach which, as will be shown below, is known to have predictive deficiencies compared to the more advanced wake capturing technique used by AFDD to get the set of

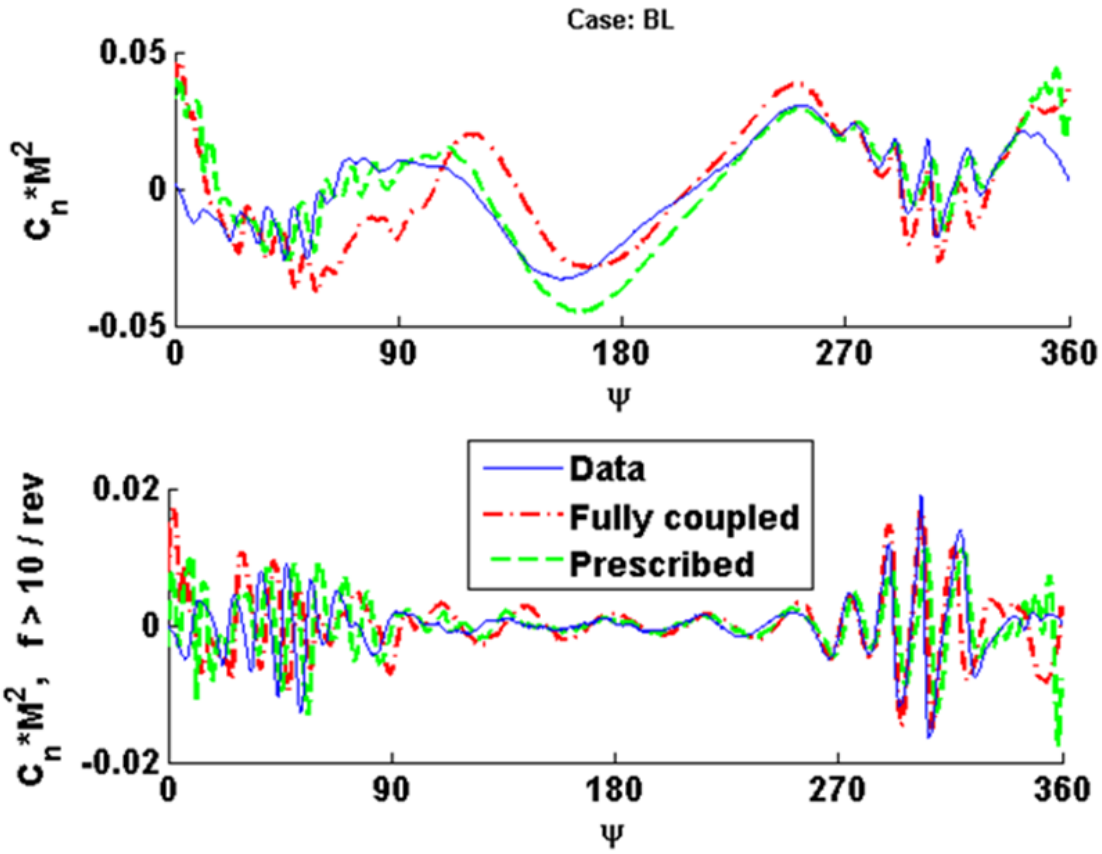

Figure 2.3: Fully coupled vs. prescribed deflections, $C_l M^2$ unfiltered and 10/rev filtered, at 87%R

prescribed deflections. It should be noted that, since no coupling with CSD is performed when using the AFFD deflections, there is no guarantee that rotor trim is obtained. The simulations with the prescribed deformation are less expensive numerically than performing CSD coupling since the number of revolutions to obtain periodic flow is reduced due to the disturbances to the wake needing to settle down after each coupling cycle.

Label	Organization	CSD Code
US	AFDD and NASA, USA	CAMRAD-II
KU	Konkuk University, Korea	DYMORE 2.0
Onera	Onera, France	HMMAP
DLR	German Aerospace Center, Germany	S4
UM	University of Maryland, USA	UMARC
GIT	Georgia Institute of Technology, USA	DYMORE 4.0

Table 2.1: List of the CSD codes used by different organizations.

2.1.2 Code Validation

The structural model has been validated for various rotors and flight conditions by diverse researchers at UMD. The HART-II collaborative papers (Ref. [2] and Ref. [3]) allowed for more direct comparisons with other well established CSD codes. The different predicted modes of the HART-II rotor blades were examined, both in terms of frequency and shape. The first five modes in flap, first three modes in lead-lag, and first two modes in torsion were plotted. Figure 2.4 is a fan plot of the HART-II rotor and compares results obtained by different research teams. It is a representation of the modal frequencies as a function of the rotor's rotational speed. Figure 2.5 shows the predicted modes shapes. As can be seen, good agreement was found between the different codes. Slightly more disparity can be noticed for the higher frequency modes, especially the 5^{th} flap, 3^{rd} lag, and 2^{nd} torsion. Table 2.1.2 gives the name of the CSD solvers used by the different organizations.

2.2 Free-Wake Model: PWAM

As mentioned in the previous chapter, BVI is highly dependent on the correct representation of the rotor wake and trailed vortices. However, the linearized aero-

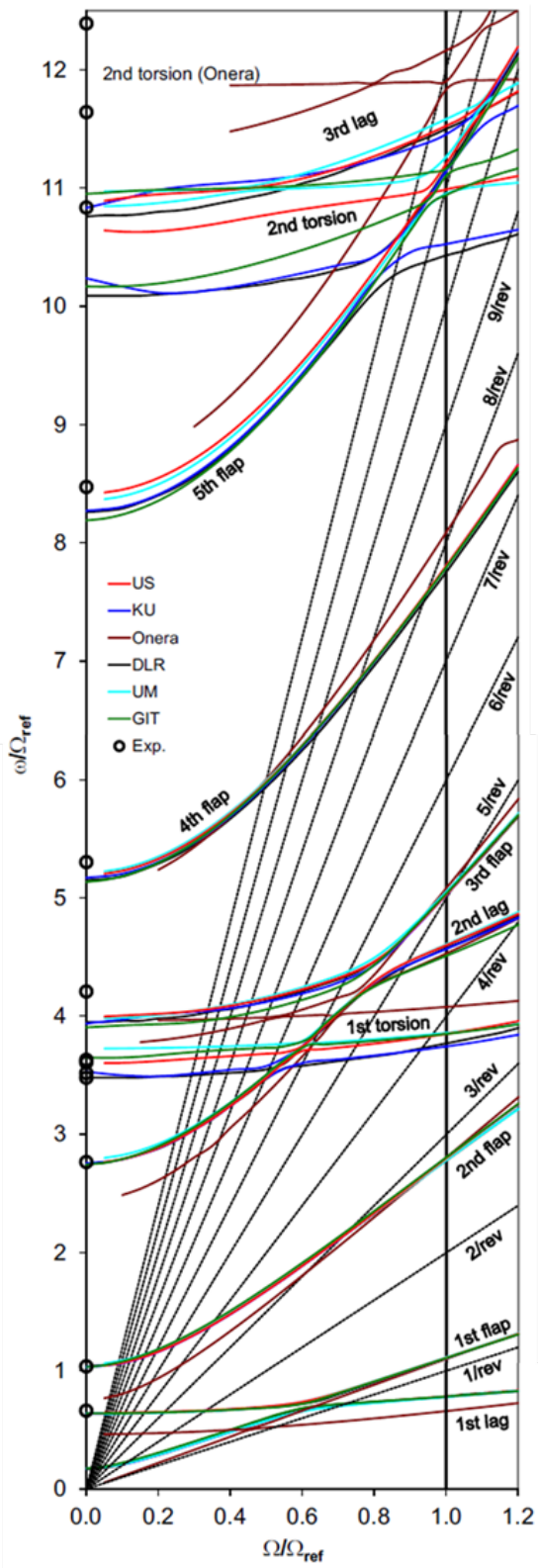

Figure 2.4: Fan plot of the HART-II rotor, comparison of State-of-the-Art CSD codes (Ref. [2])

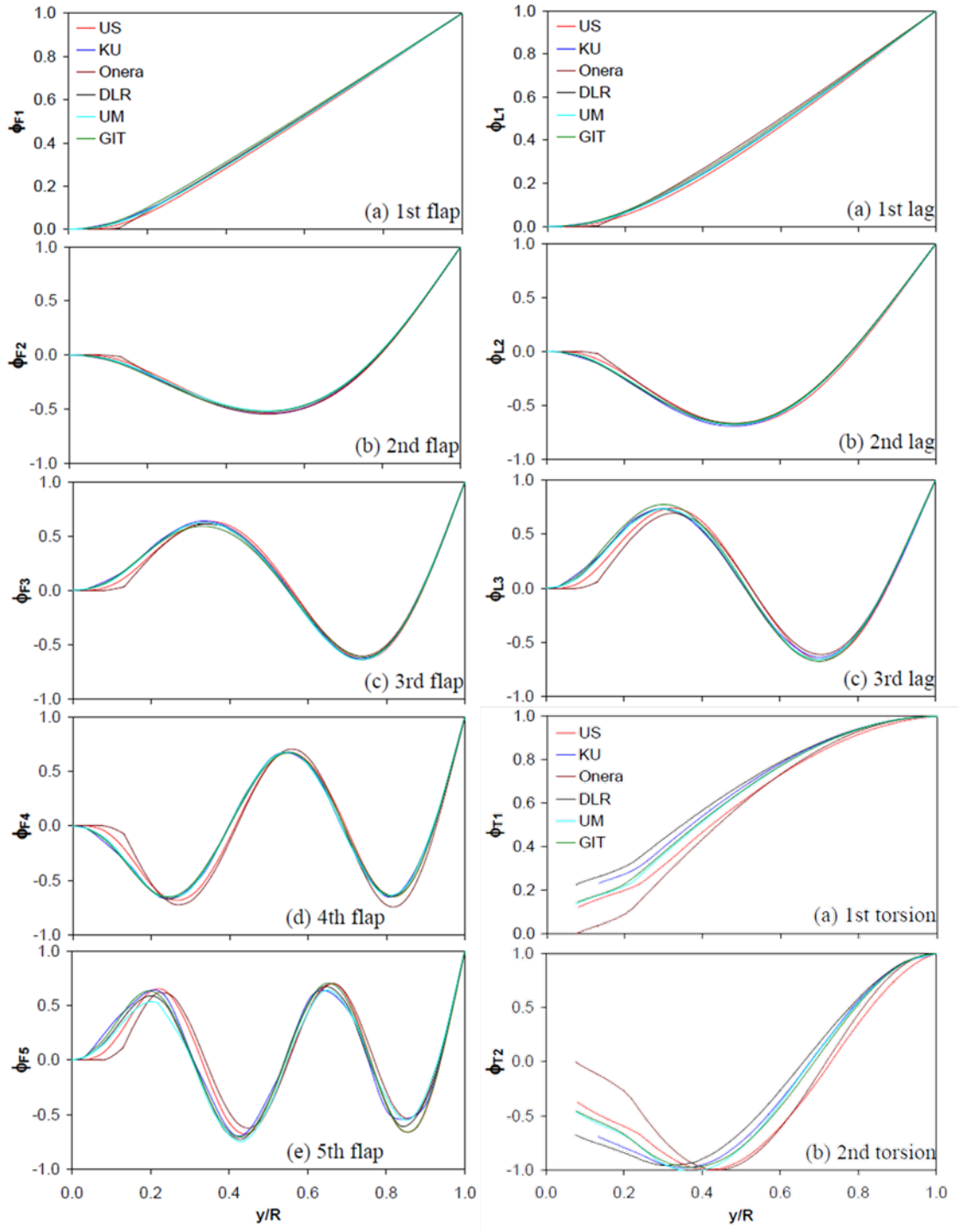

Figure 2.5: Mode shapes of the HART-II rotor, comparison of State-of-the-Art CSD codes (Ref. [2])

dynamics solver included in UMARC was only used with uniform or linear inflow to simulate the effect of the rotor wake on the blade loading. Using this configuration, it is not possible to capture BVI features. Therefore, it was decided to couple UMARC with a Free-Wake code that would carry out the task of modeling a predetermined number of independent vortex trailers in the flow field. It is a Lagrangian approach in which vortices are represented by straight line filaments and are convected under the local flow velocity and their mutual influence. It should be noted that UMARC does have an internal free-wake solver that can be used in place of the chosen inflow model, but in order to make the whole framework more modular and accessible, a different free-wake code was used. This allowed for easy modification of various modeling assumptions, such as number of trailers, initial strength and position, growth rate, extent of near-wake region, ...

2.2.1 Code Description

The free-wake module, PWAM (Parallel Wake Analysis Module) developed at the University of Maryland is a time accurate, efficient, scalable parallel implementation of the solution of the vorticity transport equations in a Lagrangian domain (Ref. [18]). The wake geometry is discretized into vortex filaments whose strengths are calculated from the provided aerodynamic forcing (Lifting-Line or RANS). The maximum value of blade bound circulation found in the outer half of the blade is chosen as filament strength. The convection velocity of each vortex filament is computed by aggregating their mutual influences, the free stream convection ve-

locity, and, if necessary, an external velocity from a panel code when modeling a fuselage. The mutual influence between the vortex filaments is computed using the Biot-Savart law:

$$d\vec{V}(P) = \frac{\Gamma d\vec{l} \times \vec{r}}{4\pi|\vec{r}|^3}$$

$\vec{V}$ is the vortex induced velocity at point P, Γ is the vortex strength or circulation, $\vec{l}$ is the vortex tangent vector, $\vec{r}$ is the vector between the vortex and P, as can be seen on Fig. 2.6(a). Therefore, the induced velocity is normal to the vortex axis. If a straight filament assumption is made, this expression can be simplified:

$$dV(P) = \frac{\Gamma(\cos(\theta_1) - \cos(\theta_2))}{4\pi(r^2 + r_c^2)}$$

This is the magnitude of the induced velocity vector, as shown in Fig.2.6(b). It is used in the free-wake approach. It can be seen that a desingularization is used by adding r_c, the vortex core radius, to the denominator. This avoid having singular values for points P very close to the vortex.

The resulting equations for wake position are integrated in time using one of the available time marching schemes: Euler-Explicit, second or fourth order Runge-Kutta. The wake azimuthal (temporal) discretization corresponds to that of the CFD solver used (Lifting-Line: 1.0 °, RANS: 0.25 °). A discretization of 5 ° is used for the filaments' length (wake age, ie spatial discretization). In the meantime, the first filament is allowed to grow to its full size before being released. This reduces the computational cost significantly. The trailed vortex system consists of a root vortex

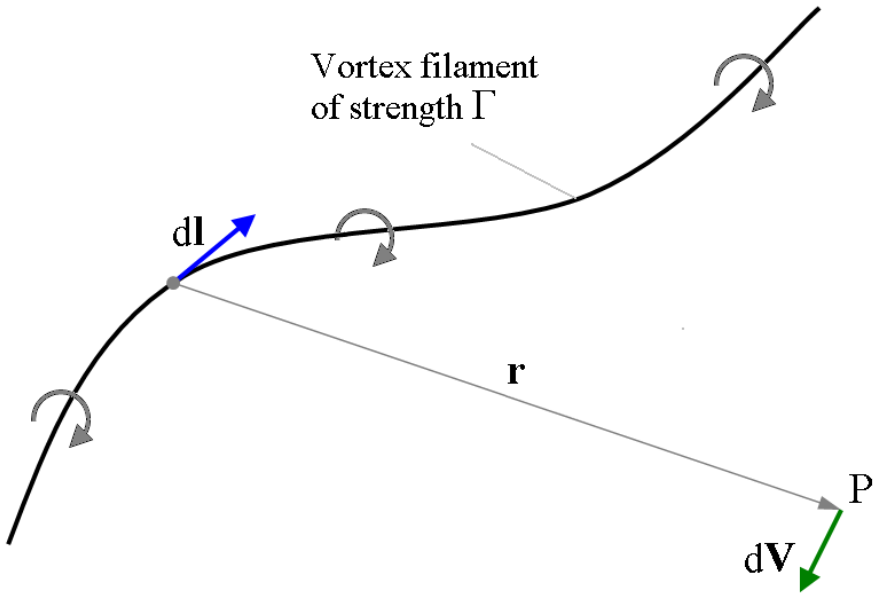

(a) Vortex induced velocity.

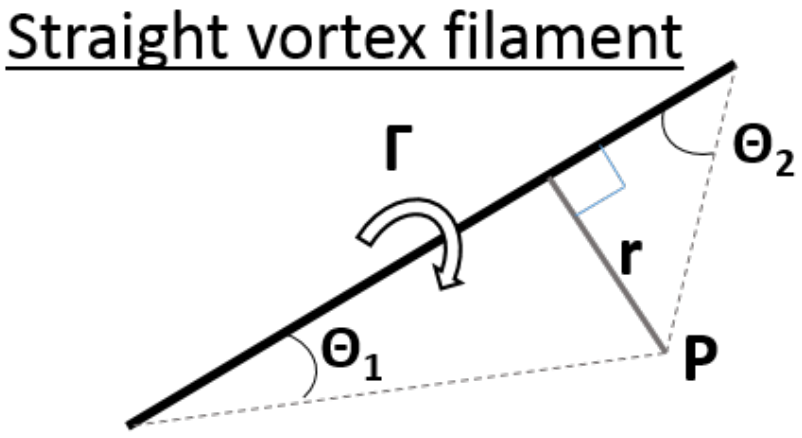

(b) Straight vortex assumption.

Figure 2.6: Vortex filament models

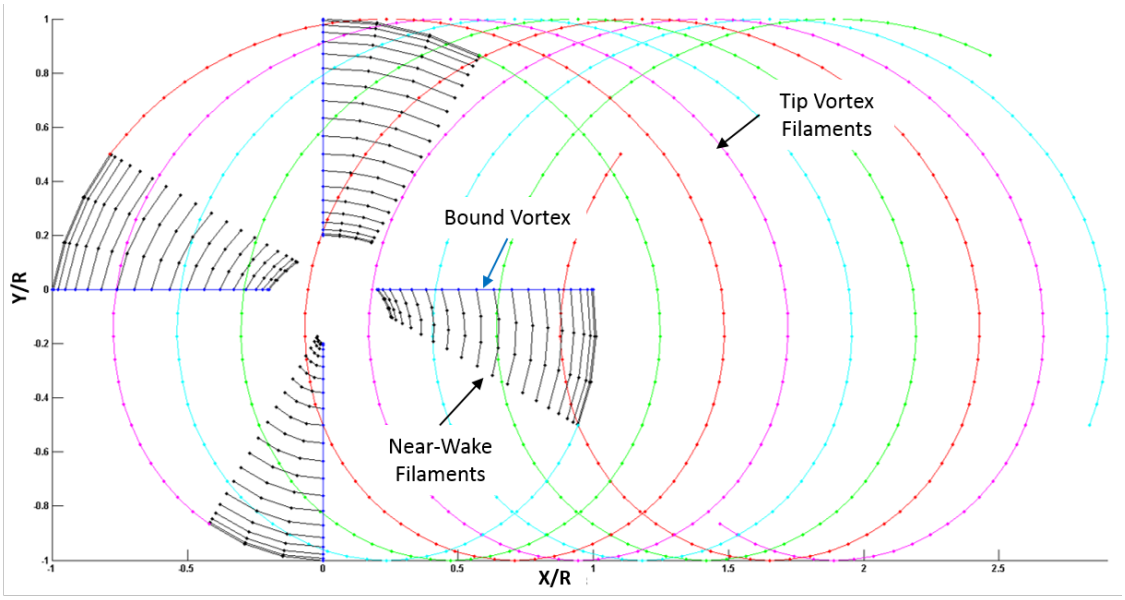

Figure 2.7: Top view of the near- and far-wake vortex filaments and blade bound vortex filaments.

and a tip vortex which convect for three revolutions. To account for the possibility of negative lift across the rotor disk and generation of two counter rotating vortices, the tip vortex release point is allowed to move to the first spanwise point of negative lift in the outer portion of the blade. The spanwise direction is discretized using 20 elements. The near wake region spans over 30 °, before rolling up into the tip/root vortices. The resulting set of vortex filaments is shown on Fig. 2.7, which is a top view of the near- and far-wake filaments, as well as the bound vortex filaments that are used in the linearized aerodynamics code, as will be seen in the next section. Vortex aging follows Squire's law (Ref. [25]):

$$r_c(\phi) = \sqrt{r_0^2 + \frac{4\alpha\delta\nu\phi}{\Omega}}$$

where r_c is the vortex core radius, ϕ is the wake age, r_0 is the initial core size, α is a constant equal to 1.25643, δ is the vortex growth rate, ν is the kinematic viscosity,

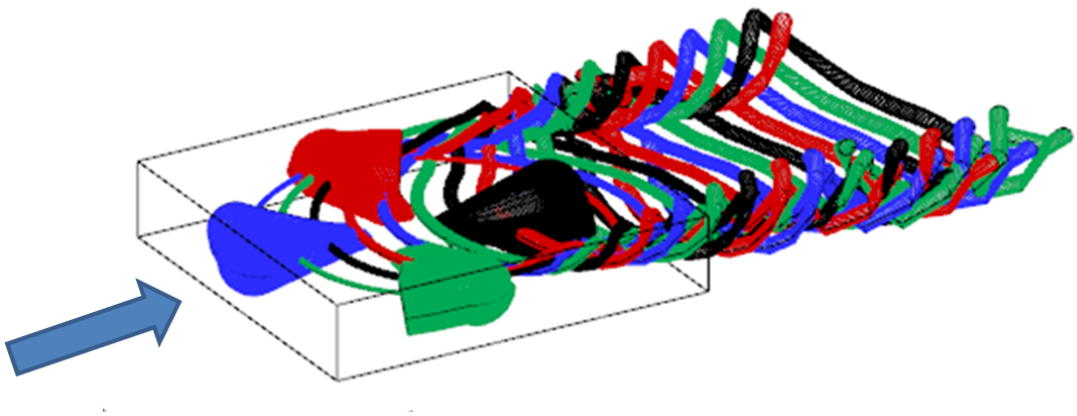

Figure 2.8: Computational domain of the wake coupling methodology

Ω is the rotor rotational velocity. The value of the initial core size, α, and δ were chosen to best correlate experimental data. Typically, the initial core size of the root vortex is set to 10 times that of the tip vortex. The swirl velocity model is due to Scully's formulation (Ref. [26]). Figure 2.8 shows the computational domain used for the wake coupling methodology. The blade meshes are shown along with the free-wake filaments, which are represented with their actual core radii. It should be noted that the box shown is only displayed to give a size comparison with the computational domain used in the wake capturing approach. A parametric study was conducted to determine the optimal number of wake trailers and the number of revolutions needed for accurate BVI prediction. This is presented in the next chapter.

2.3 Unsteady Linearized Aerodynamics

In addition to the free-wake solver, the framework was extended to use an improved linearized-aerodynamics module in place of the one included in UMARC. As

will be explained below, the improvements made to the code proved to be critical for accurate BVI predictions, especially for pitching moments. However, it was decided to keep using UMARC's aerodynamic solver, with the uniform inflow assumption, to perform rotor trim, as it is fast and generally enough for structural dynamics, which doesn't require higher frequency loads to be precisely captured, due to the lower response time of the blade structures.

2.3.1 Code Description

A multi-bladed lifting-line linearized compressible unsteady aerodynamic model was used. In this method, a rotor blade is modeled as a 3-dimensional bound vortex positioned along the quarter chord line of the blade. No-penetration is enforced at the $\frac{3}{4}$ chord location. The sectional blade lift, drag, and moment coefficients are obtained using 2-dimensional airfoil lookup tables, which give the different coefficients as a function of Mach number and Reynolds number. To account for the effects of the wake shed by the blade, the Weissinger-L near-wake model (Ref. [11]) is used. This is the "Horseshoe" wake model in which vortex filaments are trailed behind the blade to simulate the reduction in effective angle of attack seem when a vortex sheet is shed from a blade, as well as other 3D effects. Figure 2.9 is the representation of this trailed wake. As can be seen, each bound vortex filament is given an average value of the blade bound circulation as strength. The trailed vortices' strengths are the difference in bound circulation of the neighbor bound filaments, such that overall, Kelvin's circulation theorem is respected. To find the blade bound circulation

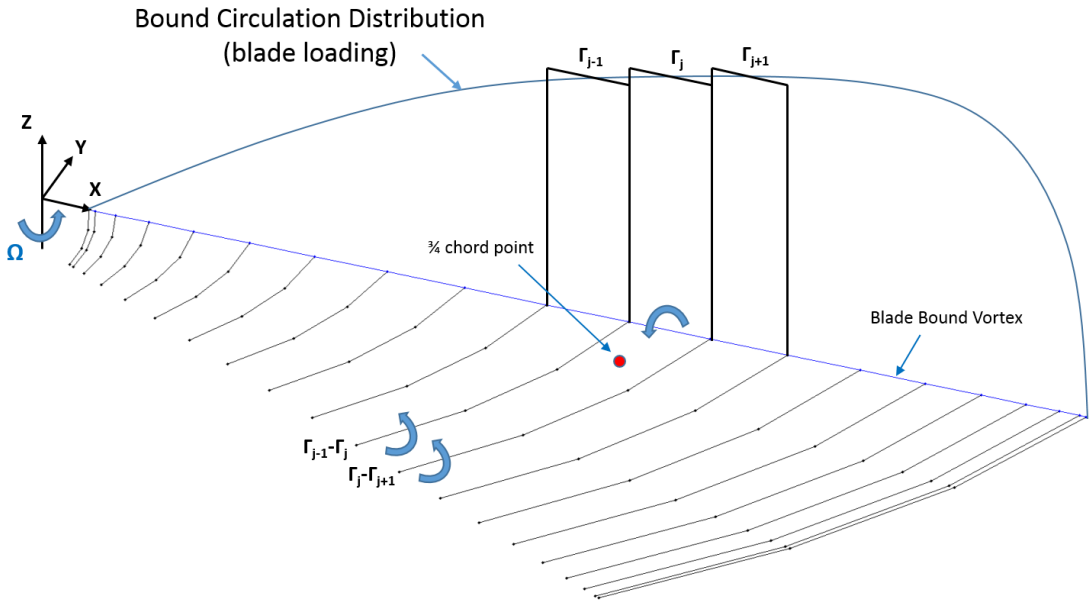

Figure 2.9: The Weissinger-L near-wake model.

distribution, the following linear system of equation has to be solved:

$$(\mathbf{A}_{bound} + \mathbf{A}_{near-wake})\vec{\Gamma}_{bound} = \vec{V}_{ext} \tag{2.1}$$

where A_{bound} is the influence matrix of all bound vortex filaments on the $\frac{3}{4}$ chord points, $A_{near-wake}$ is the influence matrix of all near-wake vortex filaments on the $\frac{3}{4}$ chord points, Γ_{bound} is the bound circulation vector, and V_{ext} is the vector of external velocity at the $\frac{3}{4}$ chord points. This external velocity includes freestream, blade inflow (from uniform/linear model, or free-wake), and the velocities due to blade motion and deformation. It should be noted that, since only the normal component of the external velocity has to be canceled at the no-penetration point ($\frac{3}{4}$ chord point), only the normal component of each equation is solved. This is done by inverting the system. If the near-wake and blade are assumed to be rigid, this

is done only once, which saves on computational time. Once the bound circulation has been found, the blade effective angle of attack can be calculated and the airload coefficients found by table lookup are used to determine the lift, drag, and pitching moment. Additional models can be added to simulate more advanced effects, such as dynamic stall using the Leishman-Beddoes model (Ref. [12]). Unsteady effects can also be added, as will be seen in the next section. Finally, the azimuthal discretization used in the code was 1 ° with 120 spanwise elements. This time-step size was determined to be sufficient by parametric study, which is presented in the next chapter. The near-wake region spanned over 30 degrees.

2.3.2 Unsteady Modeling

For rotorcraft applications, unsteady effects for lifting-line methods are often introduced using indicial response theory. This is required by the fact that the reduced frequency of rotors changes continuously, as the blades rotate around the hub. Therefore, Theodorsen's model had to be modified to obtain a representation of unsteady effects in time domain, and use the principle of superposition to combine indicial responses. In addition, the wake shed by rotor blade is not planar, which is one of the assumptions in Theodorsen's theory. Two unsteady models were developed over the years: the Wagner model, which provides the indicial response of a blade to a step change in angle of attack, and the Kussner model, which gives the indicial response to a sharp-edged vertical gust. The most commonly used model is the Wagner model, as most aerodynamic and structural effects can be approxi-

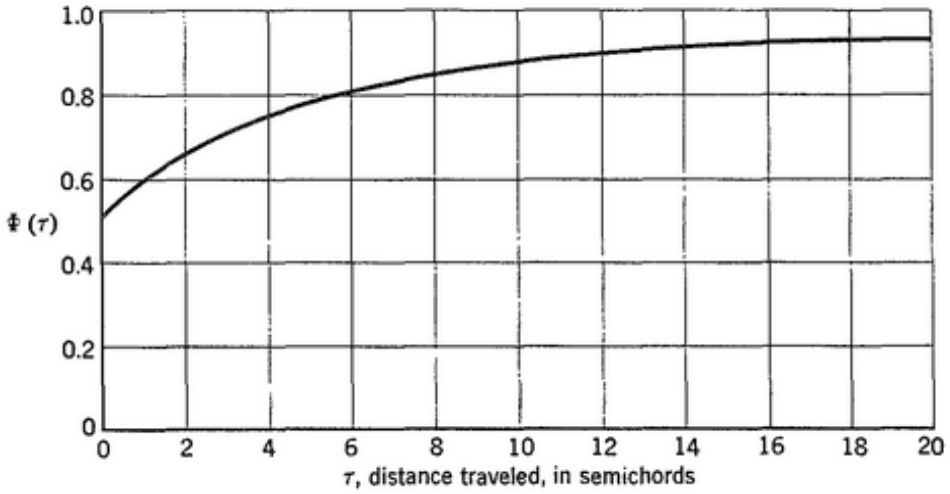

(a) Wagner function.

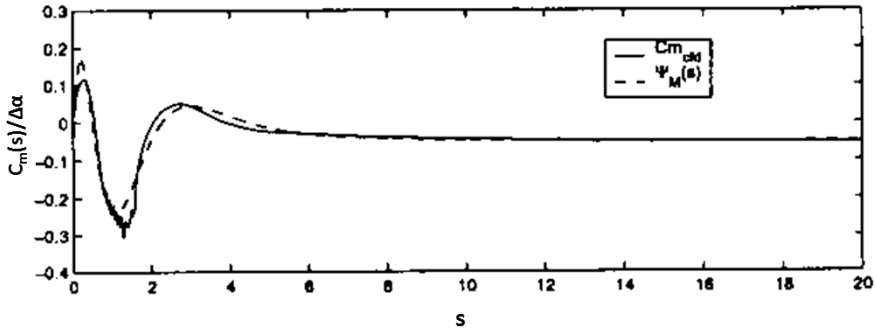

(b) Kussner function for pitching moment.

Figure 2.10: Rotorcraft indicial unsteady models (Ref. [28])

mated as step changes in angle of attack. Using this model, the formulation of the lift coefficient becomes:

$$Cl = 2\pi\alpha\Phi(s) + \frac{\pi c}{2V}\delta(t) \tag{2.2}$$

where α is the effective angle of attack, Φ is the Wagner function, s is the distance traveled in semi-chord, c is the blade chord, V is the local velocity, δ is the Diract function, and t the time. As can be seen, the quasy-steady term is scaled by the Wagner function, which is plotted on Fig. 2.10(a). This is used to represent the circulatory effects, which are due to the creation of circulation around airfoils and

the shedding of a wake sheet. As was mentioned above, a reduction in effective angle of attack results from circulatory effects, which is what the Wagner function effectively does, by scaling α in half initially and letting its full value be restored after a certain time. The second term in the above equation is the non-circulatory term, which models the "apparent mass" effect due to the acceleration of the flow around a moving airfoil. Although the Wagner function is defined analytically, an exponential approximation is often used, as it is easier to use when superposing different indicial responses with what is known as the Duhamel integral.

Modifications were made to the unsteady indicial model present in the current implementation of the linearized aerodynamics code, to better represent the specific case at hand. Unsteady computations used to be based on the Wagner indicial model, with the Prandtl-Glauert correction to take into account compressibility effects. However, for the HART-II case, a major contribution to the changing angles of attack and pitch rates come from the strong vertical gusts that appear in the vicinity of each blade, due to the passing vortices. Therefore, it was decided to modify the unsteady modeling, keeping the compressible Wagner formulation to compute the unsteady effects due to the rotor kinematics, and adding a compressible Kussner formulation for the unsteadiness due to the rotor inflow. Using the Kussner function, the lift coefficient can be formulated as follows:

$$Cl = 2\pi \frac{\omega_0}{V} \Psi(s) \tag{2.3}$$

where ω_0 is the vertical component of the gust velocity and Ψ is the Kussner function.

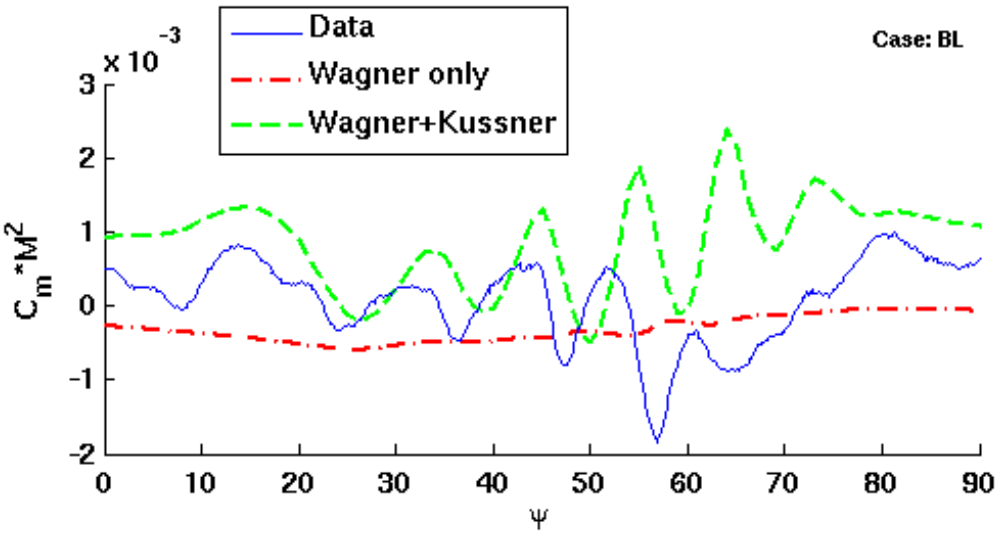

Figure 2.11: Influence of the unsteady model on pitching moment.

This unsteady modeling can be critical for accurate airloads predictions, especially for the pitching moments. A generalized moving gust function was developed by Sitaraman et al (Ref. [28]) as an exponential approximation of the Kussner function. The various required constants were derived from CFD simulations. Figure 2.10(b) shows the Kussner function and the generalized moving gust function for pitching moments plotted versus time in semi-chord (s). Although the values are close to zero for the smallest times and go to zero for higher times, it can be seen that a significant portion is non-zero with a large negative peak. This has a big impact on the pitching moments, as shown in Fig. 2.11, were $C_m M^2$ predictions using both formulations are compared to experimental values on the advancing side. It is clear that the hybrid Wagner-Kussner formulation does a better job of capturing the high frequency content due to BVI events. This is due to the fact that vortices do not produce a step change in angle of attack but have a progressive influence on the blade, as the gust penetrates the airfoil. Again, the Duhamel integral is used to

apply the superposition principle and get the response to an arbitrary gust.

2.4 Navier-Stokes Model

To further improve modeling capabilities, a first-principles based approach was used, replacing the Lagrangian solvers by Eulerian alternatives. First, the lifting-line code used to calculate blade loading is replaced by a 3D unsteady RANS-based approach which uses structured, curvilinear, body-fitted CFD meshes around the rotor blades. Then, the free-wake module that was used to represent the vortices in the flow field is replaced by the URANS method and multiple overset background grids. This introduces the concepts of wake coupling and wake capturing. In wake coupling approach, also called hybrid method, the rotor wake is modeled using a simple Lagrangian method, such as the free-wake methods, whereas in the wake capturing method, the flow field is captured by CFD grids and a first principles based solver.

2.4.1 Governing Equations

The governing equations used in the RANS solver are the three-dimensional Navier-Stokes equations [44]. They are the combined formulation of the three conservation laws of physics:

- Conservation of Mass
- Conservation of Momentum

- Conservation of Energy

Together they create a system of partial differential equations that models an unsteady, compressible, viscous fluid system. Additional equations, such as the equation of state or a turbulence closure model, are required to ensure that the system is fully determined. The general formulation in Cartesian coordinates is given below:

$$\frac{\partial \mathbf{Q}}{\partial t} + \frac{\partial \mathbf{F}_i}{\partial x} + \frac{\partial \mathbf{G}_i}{\partial y} + \frac{\partial \mathbf{H}_i}{\partial z} = \frac{\partial \mathbf{F}_v}{\partial x} + \frac{\partial \mathbf{G}_v}{\partial y} + \frac{\partial \mathbf{H}_v}{\partial z} + S \tag{2.4}$$

where $\mathbf{Q}$ is the vector of conserved variables, $\mathbf{F}_i$, $\mathbf{G}_i$, and $\mathbf{H}_i$ are the inviscid convective flux vectors, $\mathbf{F}_v$, $\mathbf{G}_v$, and $\mathbf{H}_v$ are the viscous flux vectors and S is the body-force source term. The vectors in the above equations are further developed below. The terms used are: ρ, the density, (u, v, w), the velocity components in Cartesian coordinates, e, the total energy, and p, the pressure.

The conserved variables are expressed as:

$$\mathbf{Q} = \begin{bmatrix} \rho \\ \rho u \\ \rho v \\ \rho w \\ e \end{bmatrix} \tag{2.5}$$

The inviscid fluxes are expressed as:

$$\mathbf{F}_i = \begin{bmatrix} \rho u \\ \rho u^2 + p \\ \rho uv \\ \rho uw \\ (e+p)u \end{bmatrix} \tag{2.6}$$

$$\mathbf{G}_i = \begin{bmatrix} \rho v \\ \rho uv \\ \rho v^2 + p \\ \rho vw \\ (e+p)v \end{bmatrix} \tag{2.7}$$

$$\mathbf{H}_i = \begin{bmatrix} \rho w \\ \rho uw \\ \rho vw \\ \rho w^2 + p \\ (e+p)w \end{bmatrix} \tag{2.8}$$

The viscous fluxes are expressed as:

$$\mathbf{F}_v = \begin{bmatrix} 0 \\ \tau_{xx} \\ \tau_{yx} \\ \tau_{zx} \\ u\tau_{xx} + v\tau_{yx} + w\tau_{zx} - q_x \end{bmatrix} \tag{2.9}$$

$$\mathbf{G}_v = \begin{bmatrix} 0 \\ \tau_{xy} \\ \tau_{yy} \\ \tau_{zy} \\ u\tau_{xy} + v\tau_{yy} + w\tau_{zy} - q_y \end{bmatrix} \tag{2.10}$$

$$\mathbf{H}_v = \begin{bmatrix} 0 \\ \tau_{xz} \\ \tau_{yz} \\ \tau_{zz} \\ u\tau_{xz} + v\tau_{yz} + w\tau_{zz} - q_z \end{bmatrix} \tag{2.11}$$

where q_x, q_y, q_z are the thermal conduction terms and can be expressed as a function of temperature, following Fourier's law:

$$q_i = -k\frac{\partial T}{\partial x_i} \tag{2.12}$$

with k as the thermal conductivity and T as the temperature. The equation of state for a perfect gas can be used to derive the pressure p from the different flow quantities:

$$p = (\gamma - 1)(e - \frac{1}{2}\rho(u^2 + v^2 + w^2)) \tag{2.13}$$

with γ, the ratio of specific heats (ratio of C_p: specific heat at constant pressure, and C_v: specific heat at constant volume). In all simulations carried out in this work, γ is set to 1.4, which is the recognized value for air. The temperature can be obtained from density and pressure:

$$T = \frac{p}{\rho R} \tag{2.14}$$

where R is the gas constant. Finally, the mean stresses are expressed following Stokes' hypothesis, in which μ is the laminar viscosity obtained from Sutherland's law:

$$\tau_{ij} = \mu \left[\left(\frac{\partial u_i}{\partial x_j} + \frac{\partial u_j}{\partial x_i} \right) - \frac{2}{3} \frac{\partial u_k}{\partial x_k} \delta_{ij} \right] \tag{2.15}$$

2.4.2 Non-Dimensionalization

These equations are solved in their non-dimensional form using the following non-dimensionalized variables:

$$\begin{gathered} t^* = \frac{t a_\infty}{L},\ (x^*, y^*, z^*) = \frac{(x, y, z)}{L},\ (u^*, v^*, w^*) = \frac{(u, v, w)}{a_\infty}, \\ \rho^* = \frac{\rho}{\rho_\infty},\ T^* = \frac{T}{T_\infty},\ p^* = \frac{p}{\rho a_\infty^2},\ e^* = \frac{e}{\rho a_\infty^2},\ \mu^* = \frac{\mu}{\mu_\infty} \end{gathered} \tag{2.16}$$

where the superscript $*$ is used for the non-dimensionalized quantities, the subscript ∞ represents freestream variables, $a = \sqrt{\gamma p/\rho}$ is the speed of sound, and L is a reference length scale of the flow. Additional non-dimensional parameters are defined as:

$$\text{Reynolds number :} \qquad Re_\infty = \frac{\rho_\infty u_\infty L}{\mu_\infty} \tag{2.17}$$

$$\text{Mach number :} \qquad M_\infty = \frac{u_\infty}{a_\infty} \tag{2.18}$$

$$\text{Prandtl number :} \qquad Pr_\infty = \frac{\mu C_p}{k} \tag{2.19}$$

In the current work, the Prandtl number used is set to 0.72. V_∞ is the magnitude of the freestream velocity vector. When non-dimensionalized, the mean stresses and thermal conduction terms can be expressed as:

$$\tau_{ij} = \frac{\mu M_\infty}{Re_\infty}\left[\left(\frac{\partial u_i}{\partial x_j} + \frac{\partial u_j}{\partial x_i}\right) - \frac{2}{3}\frac{\partial u_k}{\partial x_k}\delta_{ij}\right] \tag{2.20}$$

$$q_i = -\frac{\mu M_\infty}{Re_\infty Pr(\gamma - 1)}\frac{\partial T}{\partial x_i} \tag{2.21}$$

It should be noted that the superscript $*$ is omitted here to simplify the notation.

2.4.3 RANS Model

Obtaining satisfactory flow simulation by directly solving these equations (DNS, Direct Numerical Simulation) requires prohibitive number of grid points, especially for high Reynolds number flows. This is due to the fact that the smallest scales of turbulence need fine grid spacings to be accurately captured. Large Eddy Simulation (LES) is an approach in which only the largest scales of turbulence are captured through the grids, whereas the smallest scales are numerically modeled. This method has shown to be adequate for low Reynolds number flows, but certainly not feasible for rotorcraft applications, at least with todays computational technology level. Therefore, the Reynolds-Average Navier Stokes (RANS) equations were introduced. The idea is to separate the flow quantities, ϕ, into their mean value, $\overline{\phi}$, and a fluctuating part, ϕ':

$$\phi = \overline{\phi} + \phi' \tag{2.22}$$

Doing so was found to be appropriate for simulations were only mean quantities are of importance. Deriving the Navier-Stokes equation (Eqn. 2.4) using this approach introduces an additional tensor: the Reynolds stress tensor:

$$\tau_{ij}^{R} = -\rho \overline{u_i' u_j'} \tag{2.23}$$

This means that an additional set of equations is required to solve the system. They are formulated in the turbulence model, of which many variations exist, with different levels of assumption and complexity.

$$Q = -\frac{1}{2}\frac{\partial u_i}{\partial x_j}\frac{\partial u_j}{\partial x_i}$$

$$Q = -\frac{1}{2}\sum_{j=1}^{3}\sum_{i=1}^{3}\nabla\vec{u}(i,j)\cdot\nabla\vec{u}(j,i)$$

$$\nabla\vec{u} = \begin{bmatrix} \frac{\partial u}{\partial x} & \frac{\partial u}{\partial y} & \frac{\partial u}{\partial z} \\ \frac{\partial v}{\partial x} & \frac{\partial v}{\partial y} & \frac{\partial v}{\partial z} \\ \frac{\partial w}{\partial x} & \frac{\partial w}{\partial y} & \frac{\partial w}{\partial z} \end{bmatrix}$$

$$Q = -\frac{1}{2}\left[\left(\frac{\partial u}{\partial x}\right)^2 + \left(\frac{\partial v}{\partial y}\right)^2 + \left(\frac{\partial w}{\partial z}\right)^2 + 2\frac{\partial u}{\partial y}\frac{\partial v}{\partial x} + 2\frac{\partial u}{\partial z}\frac{\partial w}{\partial x} + 2\frac{\partial v}{\partial z}\frac{\partial w}{\partial y}\right]$$

Figure 2.12: Definition of the "Q-Criterion"

2.4.4 Q-Criterion

A commonly used flow variables is introduced here: the "Q-Criterion". It was developed by Hunt, Wray, and Moin in 1988 and has shown to be very useful to identify regions of strong vorticity and highlight vortical structures. The formulation is given below on Fig. 2.12. It is the 2^{nd} invariant of the velocity gradient tensor.

2.5 URANS-Based Blade Model: TURNS

As mentioned above, an incremental improvement over the use of linearized aerodynamics is to use a RANS solver to capture the flow in the vicinity of the rotor blades and predict airloads. This is an Eulerian approach in which a CFD grid is generated around the blades and a finite volume code compute the flow solution.

2.5.1 Code Description

The University of Maryland Transonic Unsteady Reynolds-averaged Navier Stokes (UMTURNS, Ref. [14]) code is an unsteady 3D RANS solver. It uses a second-order backward difference method using Lower-Upper Symmetric Gauss Seidel (LUSGS) (Ref. [15]) for time integration with dual time-stepping. Up to 15 Newton sub-iterations are used to remove factorization errors and recover time accuracy for unsteady computations (Ref. [16]). The inviscid fluxes are computed using a third order upwind scheme that uses Roes flux differencing with MUSCL type limiting. The viscous fluxes are computed using second-order central differencing. The algebraic Baldwin-Lomax turbulence model is utilized for RANS closure, since the flow is mostly attached and doesn't require a more expensive model, such as the 1-equation Spalart-Allmaras model. A time-step of 0.25 ° was used. This value, along with the number of sub-iterations was found to be optimal, as will be seen below and as was shown in Ref. [4]. For the near-field domain, the solver uses four identical body-fitted C-O blade meshes consisting of 129 points in the wraparound direction (of which 97 points are on the blade surface), 129 points in the spanwise direction, and 65 points in the normal direction, which extends up to 3 chords at 70% radius. Clustering is applied at the tip and root of the blade, as well as near the leading and trailing edges and in the normal direction. The value of y+ is kept to 1.0 with 20 to 30 points inside the boundary layer at 70% radius. The spacing at the wall is 10^{-5} chord, which allows accurate capturing of the wall-bounded viscous effects. The treatment of the far-field is described in the next section.

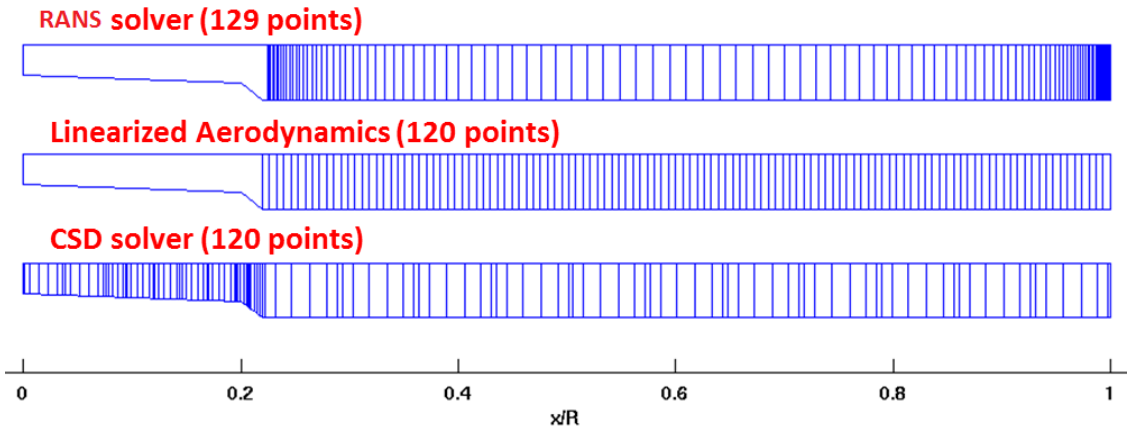

Figure 2.13: Spanwise distributions used by the different solvers.

Figure 2.13 shows the different spanwise discretizations used by the different codes. While all use almost the same number of points (129 for RANS, 120 for the structural solver and linearized aerodynamics), different levels of clustering are applied. As expected, the structural solver has a refined distribution near the root to better capture the blade structural deformations. The RANS solver has refinement both at the root and at the tip to help preserve the forming vortical structures. However, the linearized aerodynamics solvers has a uniform spanwise distribution of points.

2.6 URANS-Based Far-Field Model: OVERTURNS

The final improvement made to the framework is to switch to an all-Eulerian model to capture the entire flow field. In this approach, the free-wake solver used so far is replaced by overset meshes in the far-field, while the near-field solution is computed using the model introduced in the previous section.

2.6.1 Code Description

The wake capturing approach uses multiple overset rectangular Cartesian meshes for the far-field, each grid level having a different spacing and adequate stretching between them. Although this methodology is much more computationally expensive than wake coupling, it usually shows the highest level of accuracy and correlation with experimental data. OVERTURNS is the version of TURNS designed for overset grid topologies. An Implicit Hole Cutting (IHC) strategy (Ref. [19]) is used to determine connectivity between the different overlapping grids. In the present work, two levels of Cartesian background meshes are used. The finer level consists of a mesh with a spacing of 0.1 chords and extending 1.1R in front of the rotor and 1.5R behind, 1.2R on each side, and 0.25R above and below the rotor. The spacing extends up to 0.8 chords in an overlap region with the coarser background mesh. This second mesh extends up to 6 rotor radii behind the rotor, 3.5R in front and on each side, and 0.7R above and below. It has a spacing of 0.8 chords extending up to 1.6 chords at the far-field boundary. Figure 2.14 shows this computational domain. The same body-fitted grids as described above are used to capture the near-field in this approach. Figure 2.15 shows the relative spacing used for the blade meshes and the finer level of Cartesian background grid. It should be noted that, although a turbulence model is used to compute the flow solution on the blade meshes, it has been turned off in the background grids. This was done to avoid excessive numerical dissipation of the vortical structures, which some turbulence models are known to produce. Therefore, this approach is effectively a hybrid

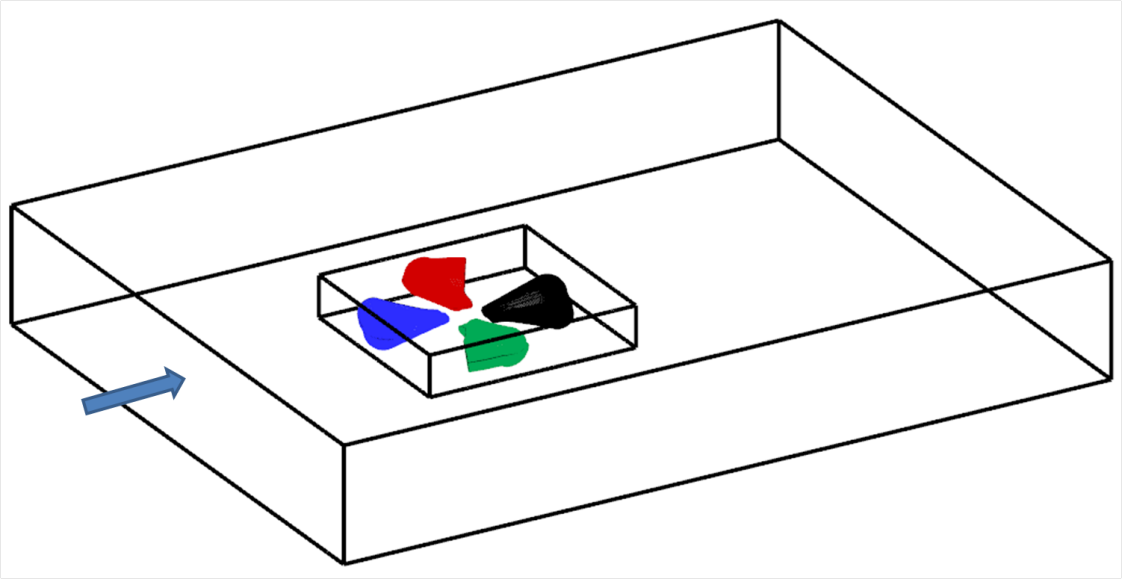

Figure 2.14: Computational domain of the wake capturing methodology

Grid	Type	Points	Spacing (finest)
Blade (1)	Structured, Curvilinear	1.08M	10^{-5}c
First background	Structured, Cartesian	8.5M	0.1c
Second background	Structured, Cartesian	1.1M	0.8c

Table 2.2: Computational grids details (wake capturing).

RANS-LES simulation. In addition, this saves computational time by avoiding the need to calculate wall distances for the background meshes, which can be expensive without an advanced search algorithm and has to be done at every time step, due to the fact that the blades are rotating in fixed background meshes. As will be explained in the next chapter, a higher order space marching scheme than the one used in TURNS was employed for this overset mesh setup, going from 3^{rd} order to 5^{th}. This proved to be one of the keys to achieving high levels of experimental correlation.

Table 1 summarizes the types and sizes of the different grids that are used in this study for wake capturing.

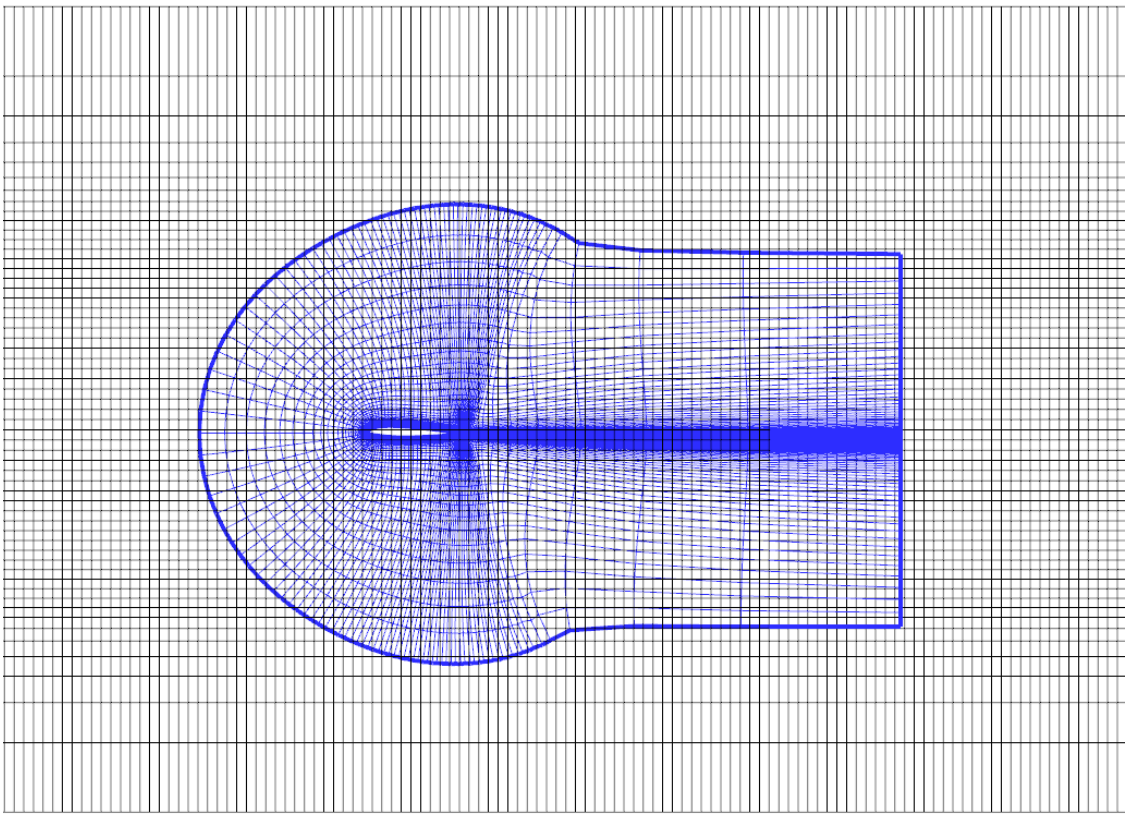

Figure 2.15: Visualization of one of the blade grids and the finer level of background mesh.

2.7 Multi-Fidelity Framework and Coupling Strategy

The previous sections introduced the main computational components used in the framework:

- Comprehensive analysis:
  - Structural dynamics
  - Simple linearized aerodynamics with uniform or linear inflow models
  - Rotor trim algorithm
- Free-Wake solver
- Improved linearized aerodynamics
- RANS blade model
- Overset RANS to capture the entire computational domain

This ensemble creates a multi-fidelity framework in which the various components can easily be switched and consistently compared.

Two different approaches were presented: wake coupling and wake capturing. In the first approach, the flow solution in the domain around the rotor blades (near-field) is obtained using either the lifting-line based method or the full 3D URANS CFD solver. The far-field domain is represented using the free-wake code, which models the tip and root vortices shed from the rotor blades as Lagrangian vortex filaments. To compute the influence of these vortices on the blades, a field-velocity method is used, in which velocities induced by the free-vortex filaments are computed

at each grid points using the Biot-Savart law. These velocities are added to the grid velocities, which include components due to the rotation of the blades, grid deformation, and velocities due to other solvers, such as a panel code to model a fuselage. This process is done at each time step.

In the wake capturing approach, the entire computational domain is captured using the RANS solver and multiple levels of overset grids. These aerodynamic modules are loosely coupled to the structural solver using the method developed by Tung, Caradonna, and Johnson (Ref. [5]). In this approach, data is exchanged between the different codes at every rotor revolution, unlike the tight coupling approach in which data is transferred after every time step. At the start of the simulation, the CSD code is given the rotor's thrust coefficient, advance ratio, and shaft tilt angle, which are required by the aerodynamic solver and the inflow models. All blade structural properties are also sent to the code to compute the blade deflections. This includes the blade mass per unit length, torsional and bending stiffness as a function of span, moments of inertia, and geometrical offsets between the center of gravity, aerodynamic center, and elastic axis. In addition, the rotor target thrust and pitching and rolling moments required by the wind tunnel trim algorithm is set. The initial CSD solution uses linearized aerodynamics with uniform inflow to obtain the trimmed blade deflections and control angles. This data is then sent to either aerodynamic solver and several rotor revolutions are performed to obtain a converged and periodic solution. In the CFD solvers, the blade grids (or blade markers) are deformed to reflect these deflections. When using the wake coupling approach, the wake geometry and strength is sent to the aerodynamic solvers in

which vortex induced velocities are computed, using the Biot Savart law. It should be noted that to avoid double bookkeeping and over-prediction of near-wake effects, the first 30 *degrees* of the vortex filaments sent to the two flow solvers were trimmed off. This is due to the fact that the lifting-line solver has its own near-wake region to account for the induced reduction in effective angle of attack, and the RANS-based model captures the near-wake region using blade meshes. The resulting airloads computed by either CFD solvers are transferred back to the CSD code through "delta coupling": after every rotor revolutions, delta values of normal force, chord force, and pitching moments are computed as the difference between the CFD and CSD lifting-line airloads. This difference is applied to the CSD airloads to obtain new trimmed blade deformations and control angles. The mathematical formulation of "delta coupling" is outlined on Fig. 2.16. This coupling cycle goes on until a converged solution is reached, typically after 5 to 7 rotor revolutions.

Overall, three modeling levels will be compared: wake coupling using linearized aerodynamics, wake coupling using RANS for the blade solution, and wake capturing. Table 2.7 shows the number of coupling cycles performed for each of the three modeling levels, as well as the number of degrees of azimuth each solver is run for each coupling cycle. The linearized aerodynamics only takes 5 coupling cycles to converge whereas wake coupling and wake capturing run for 7. From the CFD solution, airloads are obtained by keeping the last 90 ° of solution from each blade and splicing them together. It should be noted that the wake capturing method requires more rotor revolutions to be performed within each cycle, especially for the first few cycles as the wake needs to develop and settle in the computational domain, keeping

Iteration number	Lifting-Line	FW-RANS	Wake Capturing
1	5 revs	360 °	1080 °
2	5 revs	270 °	1080 °
3	5 revs	180 °	1080 °
4	5 revs	180 °	1080 °
5	5 revs	180 °	-
6	-	180 °	-
7	-	180 °	-
Run-time	2 hours	9 days	50 days

Table 2.3: Coupling cycles required by the different solvers.

in mind that the most intense BVI interaction occurs for wake ages between two and three rotor revolutions. Table 2.7 also shows the average total run-time of each code using 32 3.2 GHz Intel Xeon cores for the RANS based methods and 4 cores for linearized aerodynamics. Clearly, the wake capturing method takes the longest time to run, while the linearized aerodynamics based method is the fastest. This is very useful as this code can therefore be used for quick debugging and testing purposes, while still maintaining satisfactory levels of accuracy, as will be shown below and as was demonstrated in Ref. [2].

A schematic of the framework and the coupling strategy is shown in Fig. 2.16. The three methodologies presented are clearly highlighted: Wake Coupling with Lifting-Line, Wake Coupling with RANS solver, Wake Capturing. The different data transfers are shown, as well as the delta coupling scheme. The stars represent the inclusion of a fuselage model in the framework. Coupling between the various solvers is implemented using Python scripts. For each solver, a Python class interface is created, which interacts with the Fortran modules using Fortran to Python Interface generator (F2PY). Parallelization of the code is achieved using pyMPI. The

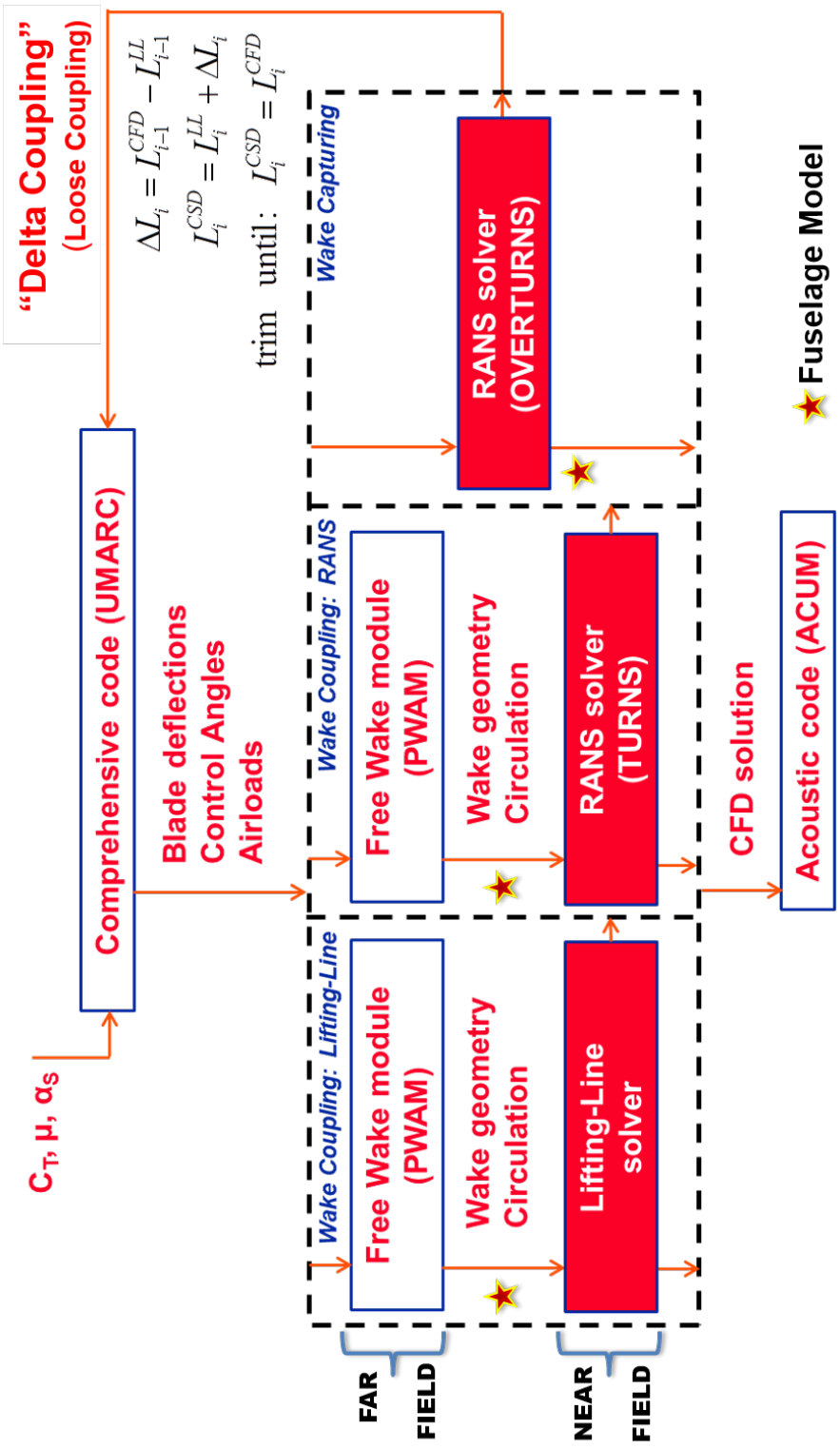

Figure 2.16: Multi-fidelity coupled CFD/CSD framework

different computational grids are split into blocks, each running on a separate processor, with an algorithm designed to achieve near load-balanced simulations. The Python NumPy library is used for array manipulation and data exchange between the solvers. Data from the different codes is interpolated using spectral interpolation in the azimuthal direction and cubic spline interpolation in the radial direction.

As will be seen in a later chapter, the effect of the fuselage on the flow field around the rotor was modeled using three different methods: a high resolution panel method, a curvilinear fuselage grid, and an Immersed Boundary Condition (IBC). The first method is used with the wake coupling approach and either CFD solver (Lifting-Line or RANS). The other two methods are implemented for the wake capturing solver. The solution accuracy and computational expense of each method is compared and put in perspective of the numerical framework.

2.8 Acoustic Model: ACUM

The last code introduced here is the acoustic solver, which was developed at the University of Maryland (Ref. [27]). It is based on the Ffwocs-Williams and Hawkings (FWH) equation using Formulation 1A (Ref. [21]). It has both on- and off-surface capabilities, and includes the near-field and far-field terms for both loading and thickness noise calculations. In addition, the code can handle either distributed pressures on CFD meshes, from the RANS model, or chordwise compact blade loads, from the lifting-line approach, as inputs. To speed up acoustic computations, the code was re-written in CUDA-C and optimized for running on a GPU, where

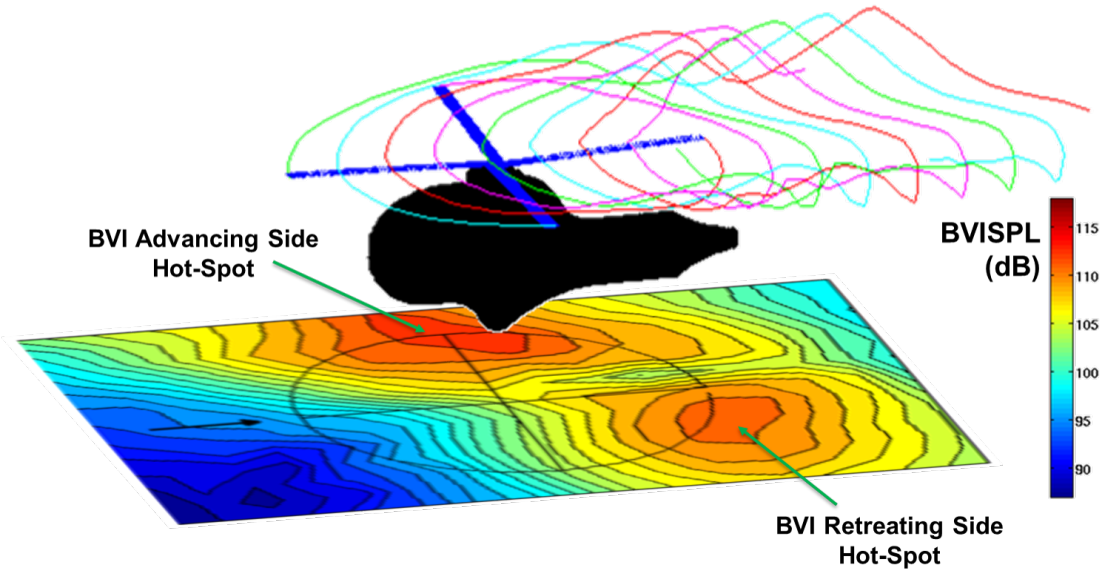

Figure 2.17: Representative view of the HART-II rotor acoustic signature.

each GPU thread calculates the noise created by all sources at a single observer location. A representative view of the acoustic signature predicted by the code for the HART-II rotor is shown on Fig. 2.17.

2.9 GPU Computation

One of the newest additions in the computational world came through the use of Graphic Processing Units (GPU) to tackle fluid dynamics problems. The unique architecture of GPUs offer great potential speed-ups to developers, thanks to the massively parallel organization of their cores. Thousands of threads are simultaneously available to carry out computational tasks on a single graphics card, whereas it takes hundreds of high-end nodes on computational clusters to reach the same level of parallelism. Therefore, an important objective of this doctoral work was to take advantage of this promising technology and develop codes that could

run on GPUs. The programming language used for NVIDIA hardware is CUDA-C. However, GPU computing still has some limitations. A major one is that the amount of memory available on Graphics cars is limited, reaching a few Gigabits for higher-end models. Also, there seems to be an important numerical cost penalty when excessive memory transfers between CPU and GPU are performed. It was found by Thomas et al in Ref. [41] that porting parts of a CPU-based code to GPU was usually not beneficial as the memory transfer overhead greatly reduces the overall efficiency of the solver. Therefore, an additional effort was made to have as many parts of the framework run on the GPU. The free-wake solver was re-written in CUDA-C and the panel method that will be presented in a later chapter was entirely developed with this consideration in mind. To complete this all-GPU framework, a 3D URANS solver was developed by Thomas et al at UMD (Ref. [41]).

2.10 Summary

In this chapter, the main numerical components of the framework developed in this doctoral work to tackle the simulation of helicopter BVI were presented. Going from comprehensive analysis to a full 3D URANS solver, with incremental improvements in between, both in near-field and far-field modeling, an advanced multi-fidelity computational environment was created. The specific coupling strategies employed to exchange data between the codes were also highlighted. The resulting three different aerodynamic simulation approaches will be compared, both in terms

of solution accuracy and experimental correlation, and computational efficiency.

Chapter 3

Parametric Studies

In this chapter, different parametric studies are presented. This follows the previous chapter in which the various solvers used in this work were introduced. The goal here is to determine optimal numerical and physical parameters for these codes and ensure that the highest levels of solution accuracy are achieved. The study includes time step refinements for both the lifting-line linearized aerodynamics solver and the RANS method, tuning of diverse geometrical and physical variables in the free-wake model, and assessment of the ideal grid topology and size for the problem at hand.

3.1 Linearized Aerodynamics

3.1.1 Temporal Discretization

The influence of temporal discretization on solution fidelity was determined by running the code with different time step sizes, ranging from 5.0 ° to 0.25 °. This study helped determine the minimum time step required to capture BVI events as accurately and efficiently as possible. Figure 3.1 shows the normal force and pitching moment coefficients, as well as their time derivatives as a function of azimuth on the advancing side of the rotor and for the baseline case. It can be seen that for a time step above 2.5 °, the sharp BVI peaks are not well captured in magnitude because

not enough points in the azimuthal direction are being used. The coarser time discretization leads to clipping of these peaks and the miss-prediction of BVI intensity, which has a large impact on acoustic predictions. However, the low frequency content of these airloads remains satisfactory. For a time step of 1.0 °, which is what is used for the rest of this work, the difference with the next two lower values of $d\psi$ is minimal, as only a small fraction of the magnitude is missing for the sharpest peaks. In addition, avoiding unnecessarily low time step sizes ensured that computational costs remained acceptable for this lower fidelity approach, which is its main advantage over more advanced and expensive methods. In fact, as one of the most time consuming procedures within each time step is the calculation of vortex induced velocities on the blade, reducing the number of operation per rotor revolution was critical. It should be noted that the structural deformations and structural loads are not affected by the value of $d\psi$ used in the aerodynamics solver, as only the lower frequency content of the airloads is of importance since the blade's response time is generally low. This explains why the time step used in the structural solver is only 5.0 °.

3.1.2 Spatial Discretization

Furthermore, the influence of the number of spanwise blade markers used in the lifting-line approach was observed. Although the spanwise loading doesn't display unreasonably sharp gradients or peaks as the blade rotates, it was decided to use a rather fine spatial discretization (120 points along the span), close to that used

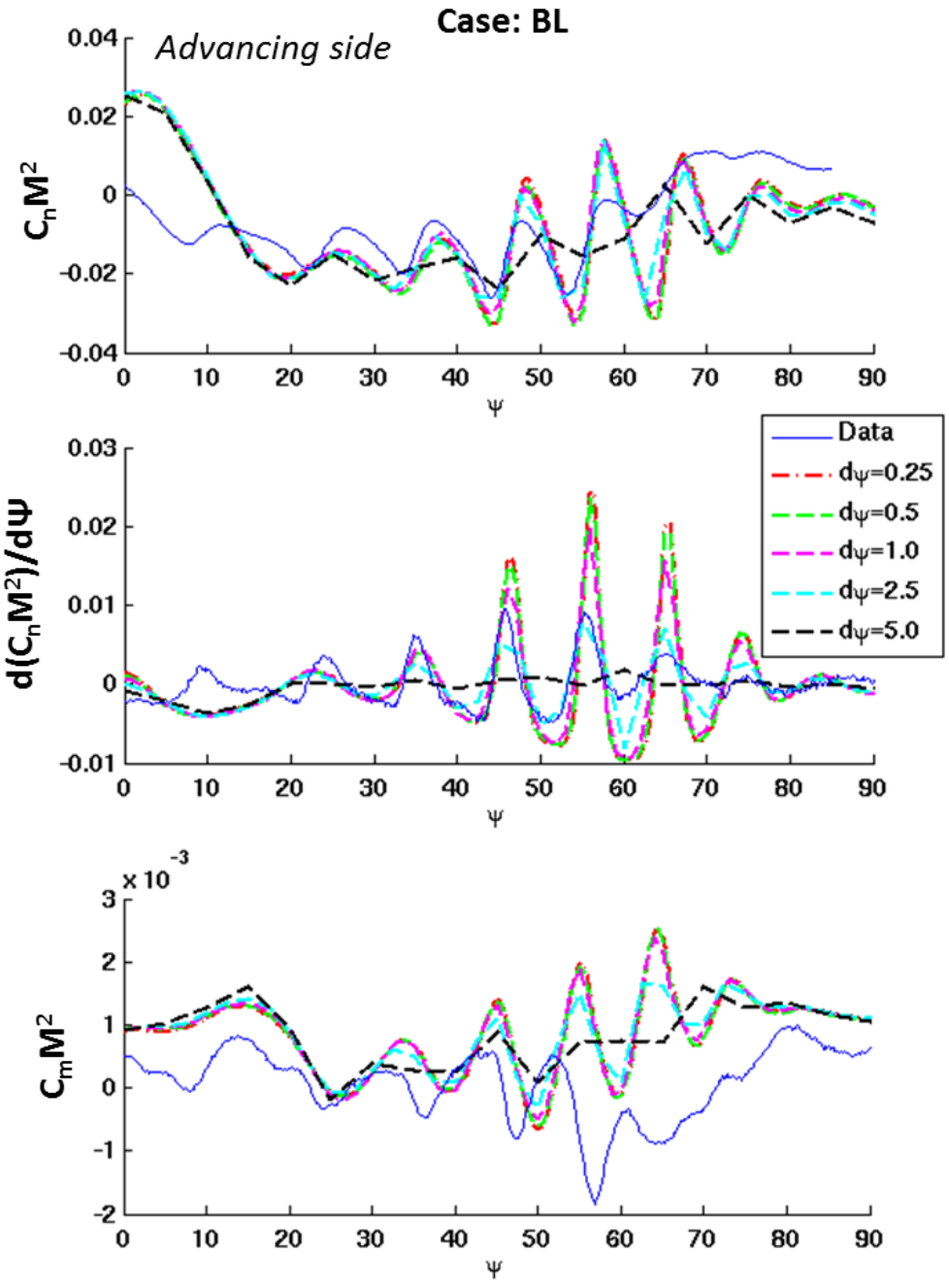

Figure 3.1: Influence of the time step size on BVI peaks predictions.

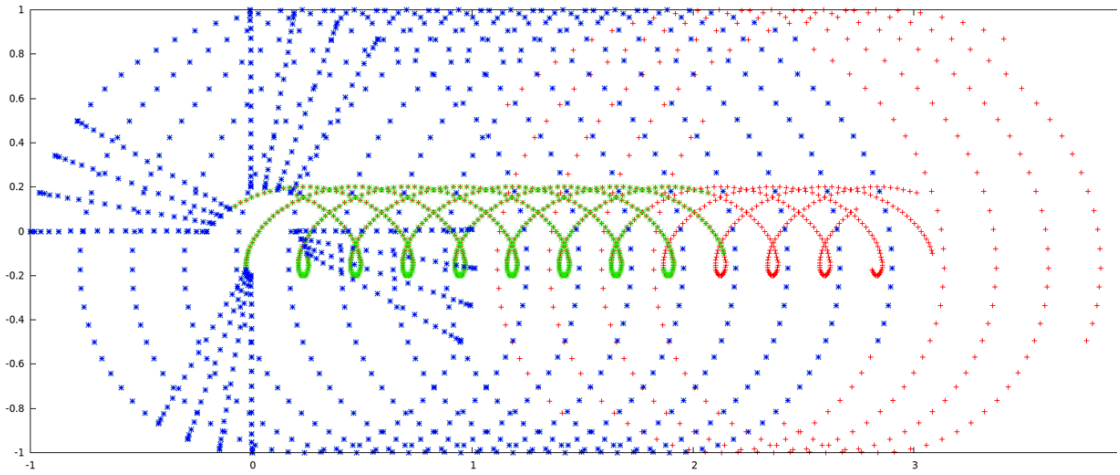

Figure 3.2: Initial free-wake: tip/root vortex modeling for various wake lengths.

in the RANS method (129 points). The potential time saving that could have been achieved with a lower resolution, especially by reducing the number of points at which induced velocities need to be computed, was deemed minimal, thanks to the parallel implementation of the code.

3.2 Free-Wake Model

3.2.1 Wake Geometry: number of trailed vortices and wake age

First, the inclusion of root vortices, in addition to those released at the tip of the blade, and the number of revolutions each vortex is free to convect for was varied. Between two and five revolutions were considered, remembering that nearly all BVI events occur for wake ages lower than three rotor revolutions. Figure 3.2 shows a top view of the initial wake representation for a few of these configurations: tip-only - 2 revolutions, tip+root - 2 and 3 revolutions.

Figure 3.3 shows the impact on the normal force coefficient. While adding

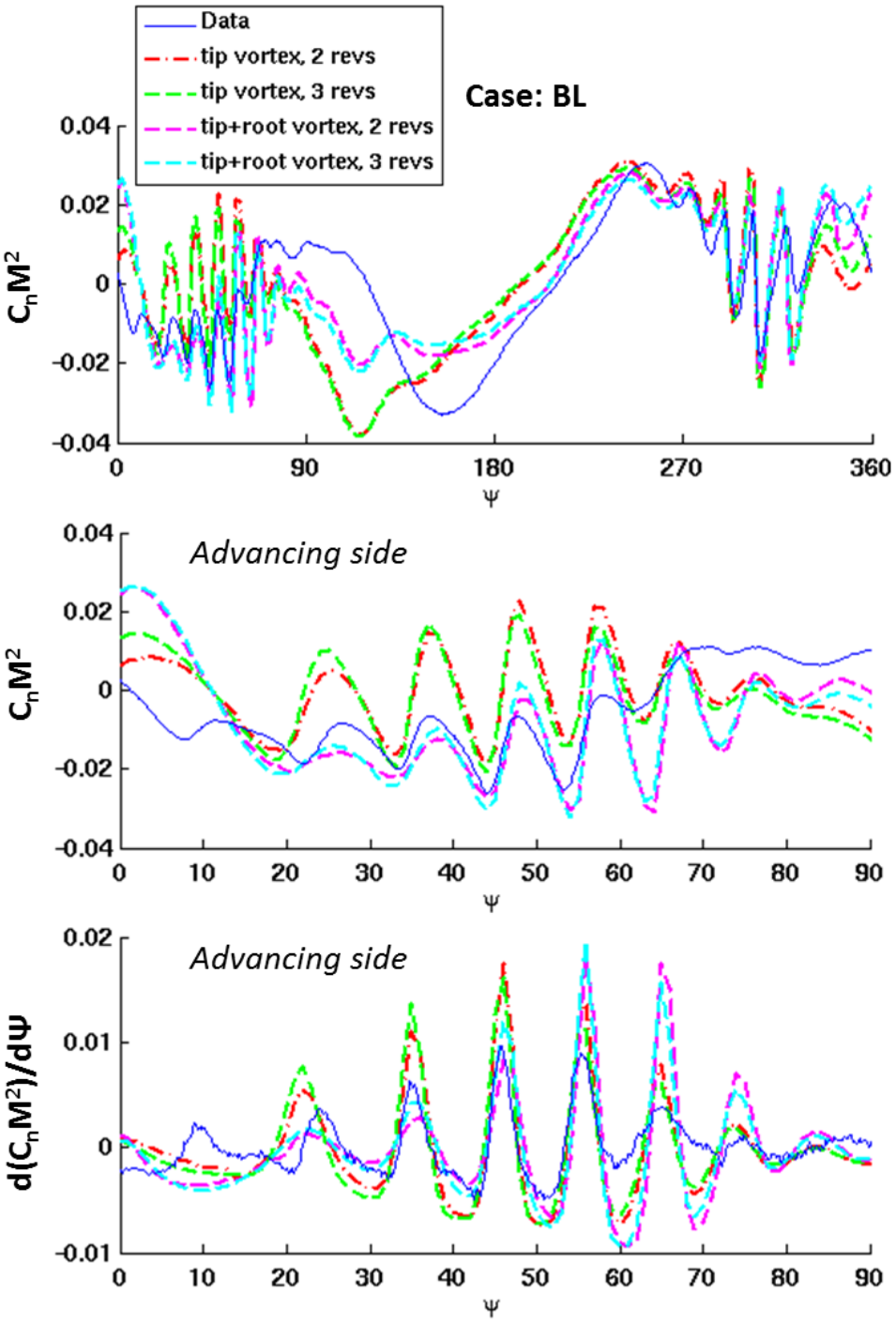

Figure 3.3: Influence of Free-Wake geometry.

root vortices in the simulation made an important difference, as had been noted by Lim et al in [29], the number of revolutions only had a minor influence. Four and five revolutions had no improvement over three revolutions, but greatly increased the computational cost, as the number source filaments is increased in the vortex induced velocity calculations. The addition of root vortices reduced the magnitude of BVI events to acceptable levels, compared to the tip-only simulation which clearly over-estimates BVI peaks. In addition, improvements in the low frequency content of the normal force is observed. However, no noticeable difference is seen in terms of phase, although the phase of the BVI signal of maximum intensity is shifted by 10 *degrees* when including root vortices, which actually leads to decreased fidelity on the advancing side. It should also be noted that the normal force on the retreating side and the pitching moment are not affected as much by this modeling change. The blade deflections are mildly affected by these parameters, with both vortices modeled and more revolutions being slightly beneficial. Obviously, the addition of root vortices in the free-wake representation doubles the computational time, as the number of trailed filaments is twice that of the tip-only approach. However, the observed improvements justified the increased cost. This parametric study was done using the lifting-line solver but the findings were found to be applicable to the RANS-based wake coupling methodology, as the free-wake module used is the same. The fact that the lifting-line code runs much faster than the RANS blade model made it easier to conduct.

The length of each vortex filament modeled here was kept to 5 *degrees*. This was deemed sufficient has the near-field vortices are not subject to high distortion

rates under the current flight conditions (advance ratio and tilt angle). Increased resolution is often necessary to accurately simulate filaments impinging on structures, such as a fuselage or even a ground plane.

3.2.2 Near-Wake Discretization

Another study was performed on the number of trailers used in the near-wake model, both for the free-wake code and the lifting-line solver. A combination of 20 to 120 trailed near-wake vortex filaments were tested. Figure 3.4 clearly shows that this parameter does not have a large influence on airloads predictions as they are very similar to each other. The impact on numerical cost was minimal when using more near-wake trailers, as in the modeling assumption used here, the near-wake filaments are not distorted by the far-wake vortices, which means that no induced velocities are computed. However, it was decided to use the lower number of markers.

3.2.3 Core Radius Study

Further studies have been carried out to determine the optimal initial core radii and vortex core growth rates to be used for both the tip and root vortices. In addition, the strength given to the filaments was also varied, the idea being that a percentage between 70% and 90% of the blade bound circulation should be transferred to the free-wake vortices to account for lost vorticity. This study was done by trying to match the available swirl velocity levels seen in experimental PIV

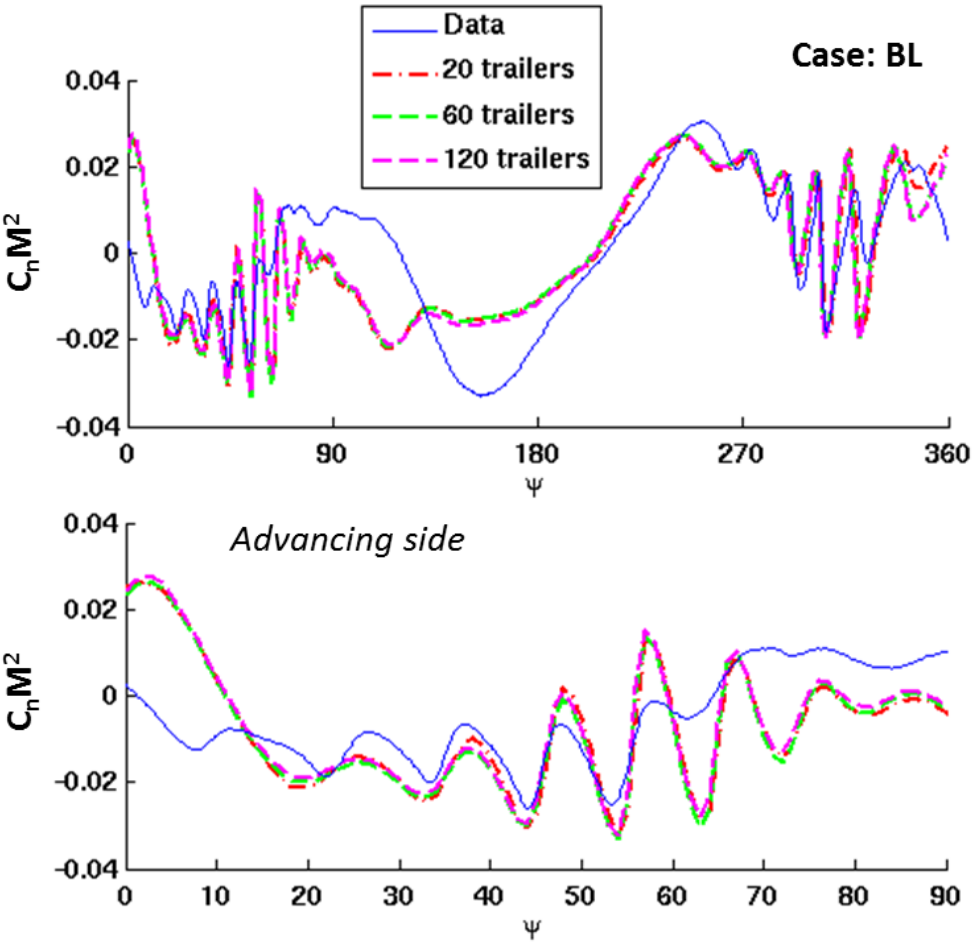

Figure 3.4: Influence of the number of trailers in the near-wake.

maps and the extracted core radii, for the tip vortices. Figure 3.5 shows core radius as a function of wake age for multiple values of the growth parameter δ used in Squire's model. Extracted experimental data is also plotted, both using conditional averaging and simple averaging (label "paper"). Results using a more advanced core growth model in which the growth parameter is calculated from the vortex Reynolds number are displayed as well. As can be seen, it appears to be difficult to match experimental data for both low and large wake ages. Figure 3.6 shows PIV maps from the HART-II wind tunnel measurements. The extracted (white circle) and free-wake (purple circle) core radii are plotted on top for each wake age location. The growth parameter used in these plots is $\delta = 250$. Finally, numerical results from the highest fidelity approach were also observed and the predicted vortex structures compared. Figure 3.7 has two views showing the free-wake vortices, represented with their actual core sizes, and the RANS solution. As can be seen, the correlation is good for low wake ages but fluctuates more for older vortices. Also, there seems to be more scatter in the prediction of the root vortices' location.

3.2.4 Temporal Integration Scheme

Finally, the influence of the numerical scheme used to integrate the wake motion equation was accessed. It was found that, although a higher order scheme like the 4^{th} order Runge-Kutta method yields slightly better precision and stability in the wake geometry predictions, the added cost over the RK-2 scheme was not justified. This is especially true in the context of the lifting-line wake coupling approach

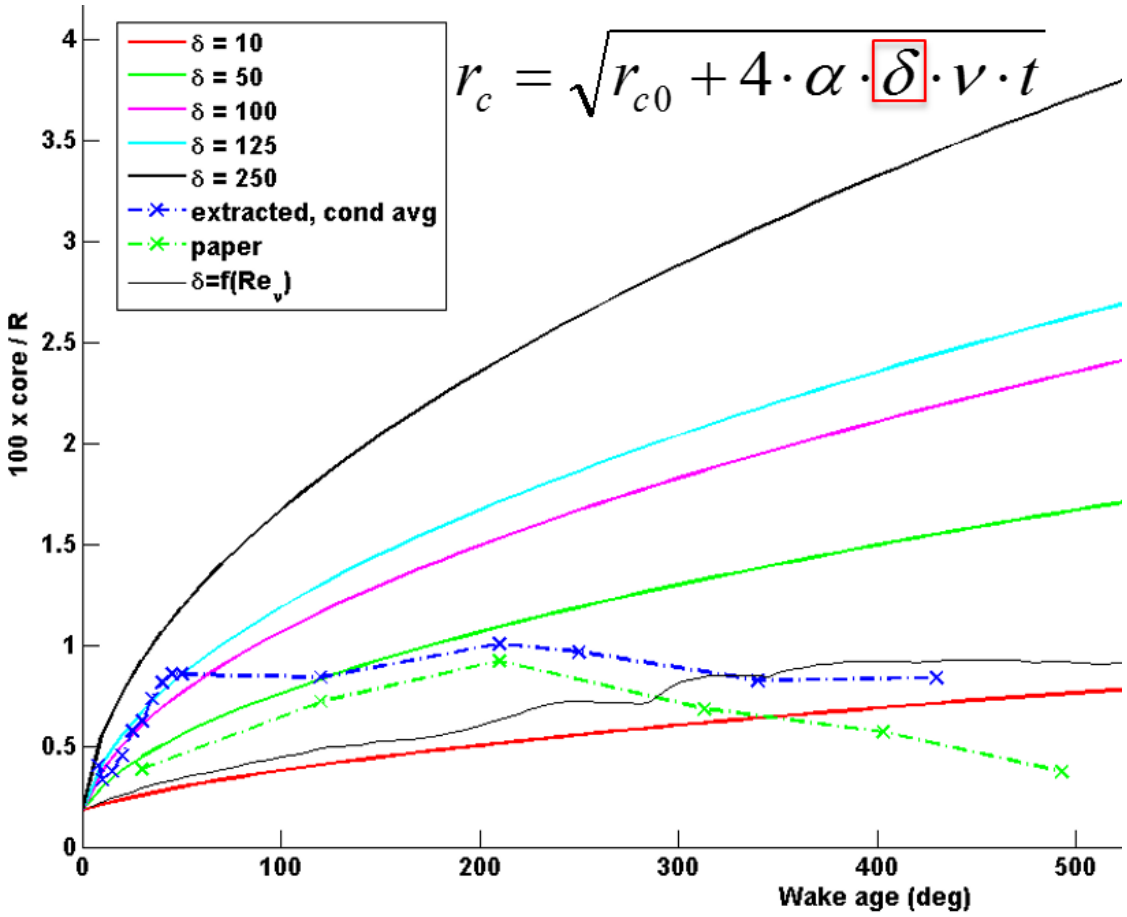

Figure 3.5: Comparison of free-wake predicted and experimental core radius.

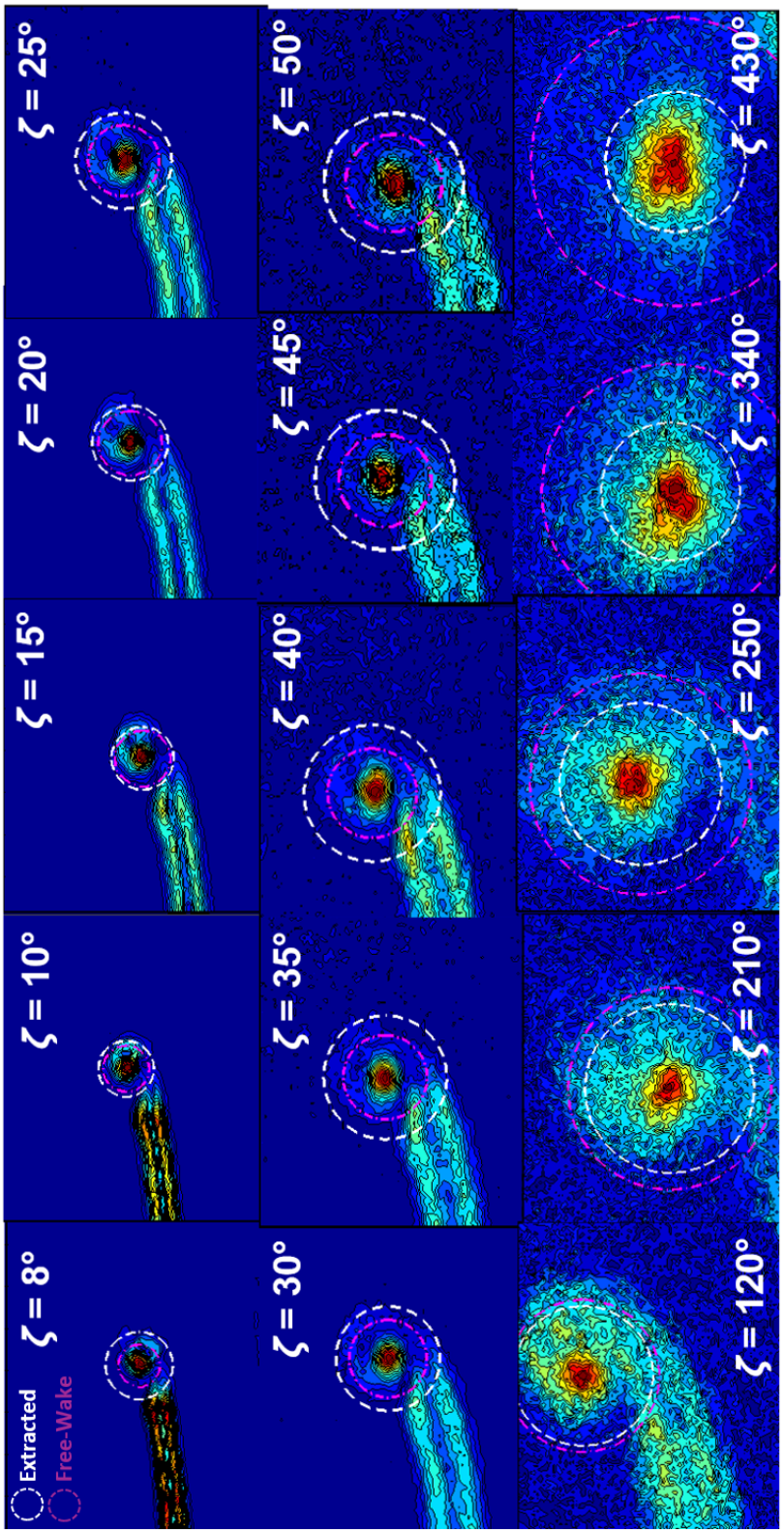

Figure 3.6: Core radius evolution: experimental PIV maps.

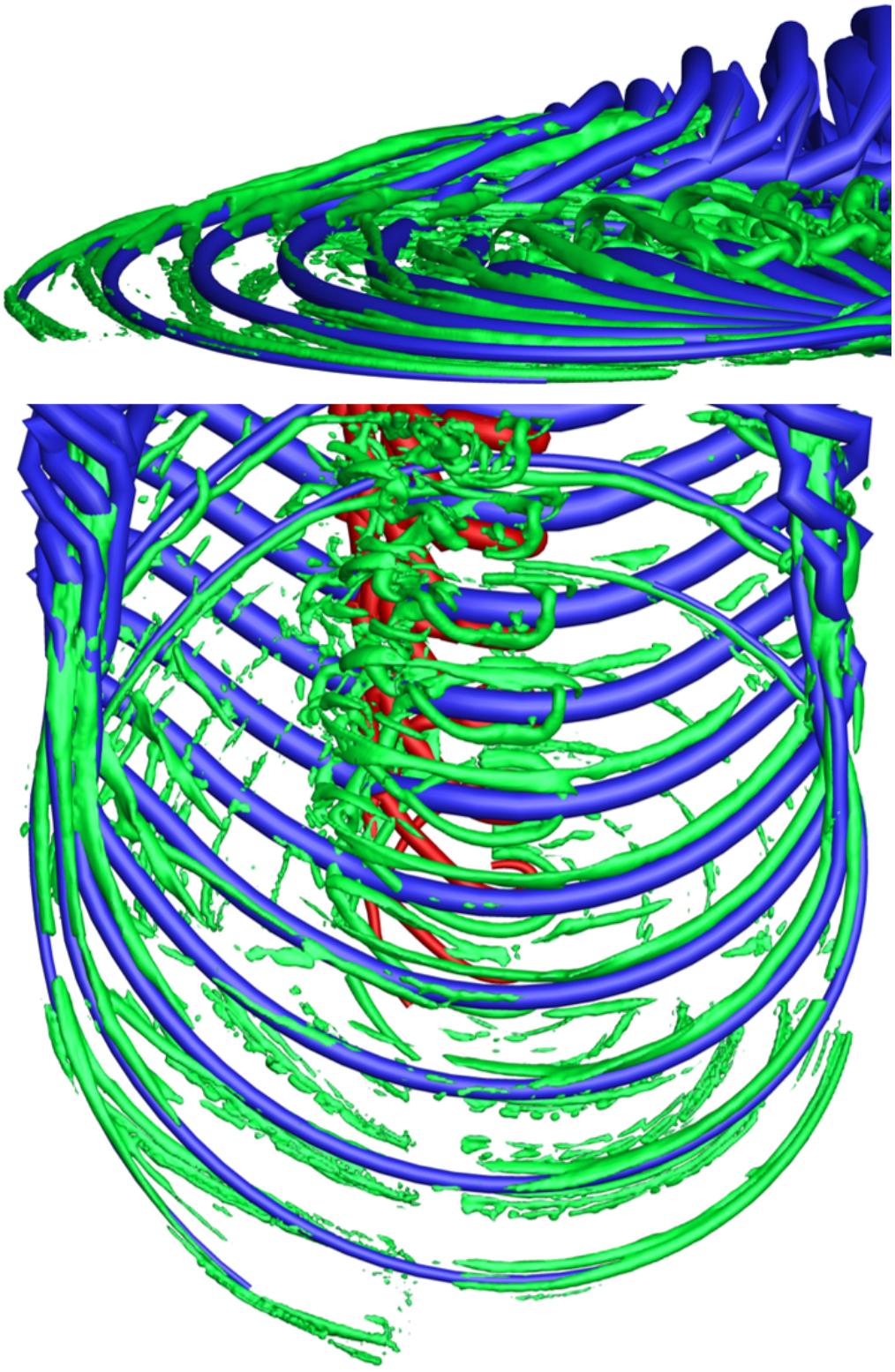

Figure 3.7: Superposition of vortex structures predicted by Free-Wake and RANS.

which is only attractive over higher fidelity alternatives if its run-time remains low.

3.3 URANS Solver

3.3.1 Temporal Discretization and Optimal Number of Sub-Iterations

Early numerical simulations using the wake coupling approach showed large over-predictions of BVI peaks in the pitching moments, especially for the minimum vibration case. It was determined that this was due to the relatively low number of sub-iterations used, six, and that more sub-iterations were required to better resolve the pitching moments and obtain more convergence within every time step. Further testing was done using 10 and 15 sub-iterations and the impact on $C_m M^2$ is shown in Fig. 3.8. The influence of the time step size on this issue was also examined, going from 0.25 ° to 0.125 ° with 10 sub-iterations. It can be seen that with more sub-iterations, the over-prediction of the pitching moment decreases. Going to a smaller time step size of 0.125 ° with 10 sub-iterations, which is equivalent to running 20 sub-iterations at 0.25 °, does not present any clear improvement compared to 15 sub-iterations at the larger time step. In addition, no real difference was noticed in the normal force. Therefore, 15 sub-iterations were used in the present work with $d\psi = 0.25$.

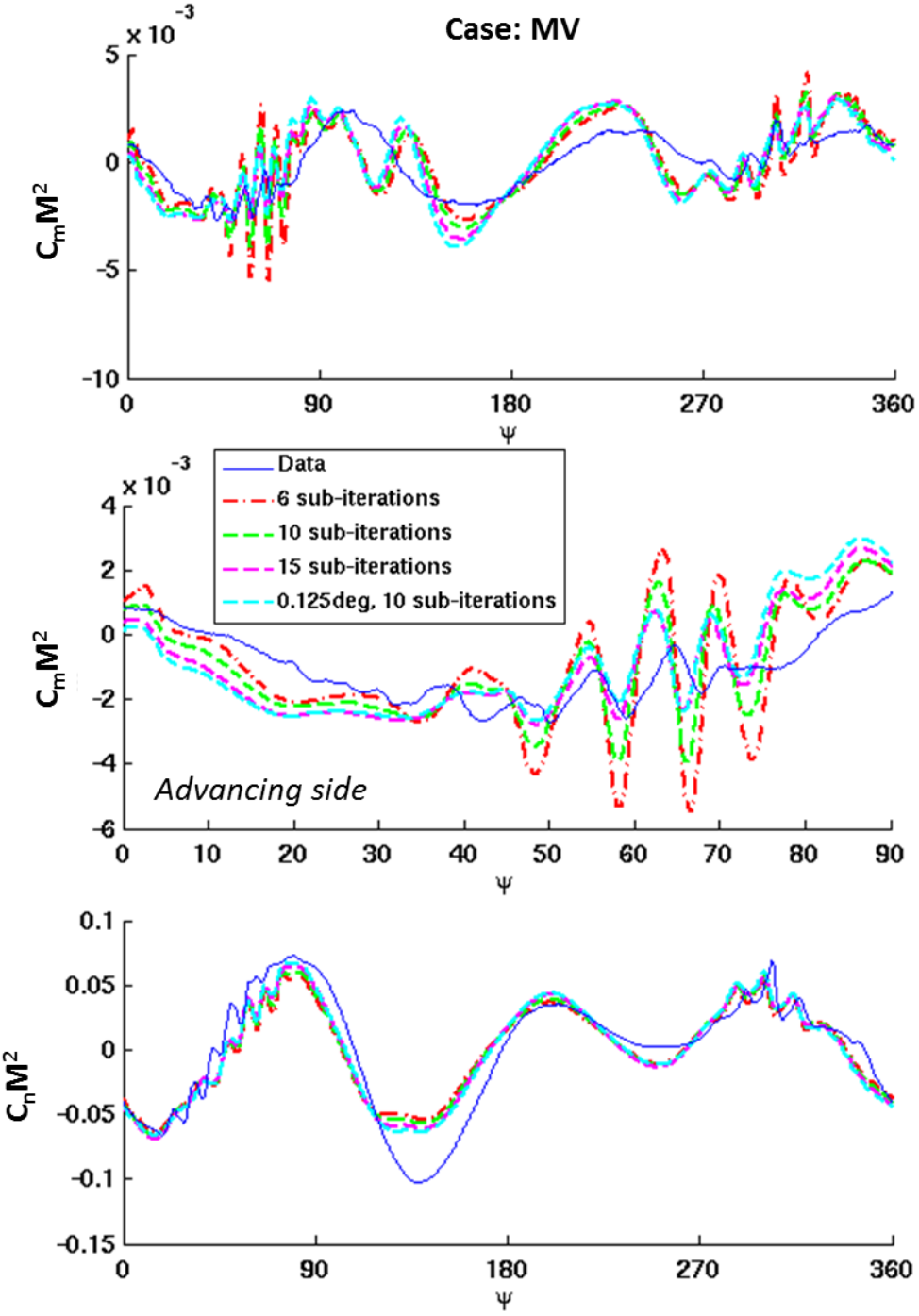

Figure 3.8: Influence of the number of sub-iterations on the pitching moments.

3.4 Wake Capturing Method

3.4.1 Mesh Topology

This study was conducted to determine the ideal mesh setup to best simulate the HART-II flight condition. Although initial computations were made using cylindrical background meshes, it was found that rectangular Cartesian meshes were more appropriate for low speed, descending flight conditions, and in general for forward flight. This is due to the fact that, when using a cylindrical mesh centered around the rotor hub, a large extent of it is "wasted" at the front of the rotor, although a large radius is necessary to capture all trailed vortices behind the rotor. The reduction in mesh size and number of grid points achieved when using Cartesian meshes is significant. It actually outweighs the potential gains obtained by being able to split the cylindrical computational domain into four 90 *degrees* mesh partitions, which reduces connectivity computations by restricting the implicit hole cutting search to each blade mesh and its quarter of cylindrical grid. Figure 3.9 shows the cylindrical mesh setup, along with the four blade meshes used in the simulation. It should be noted that an additional cylindrical mesh of much larger radius is overset on top of these grids to capture the entire flow field and make sure no undesired boundary reflections are created. The figure also highlights the clustering used on the cylindrical mesh, both in the azimuthal and vertical directions, to refine the mesh spacing around the blade and its outboard region. The lower image on this figures displays an additional Cartesian mesh that was positioned on the advancing side of the rotor disk to try to better capture vortices in that region. This was done to

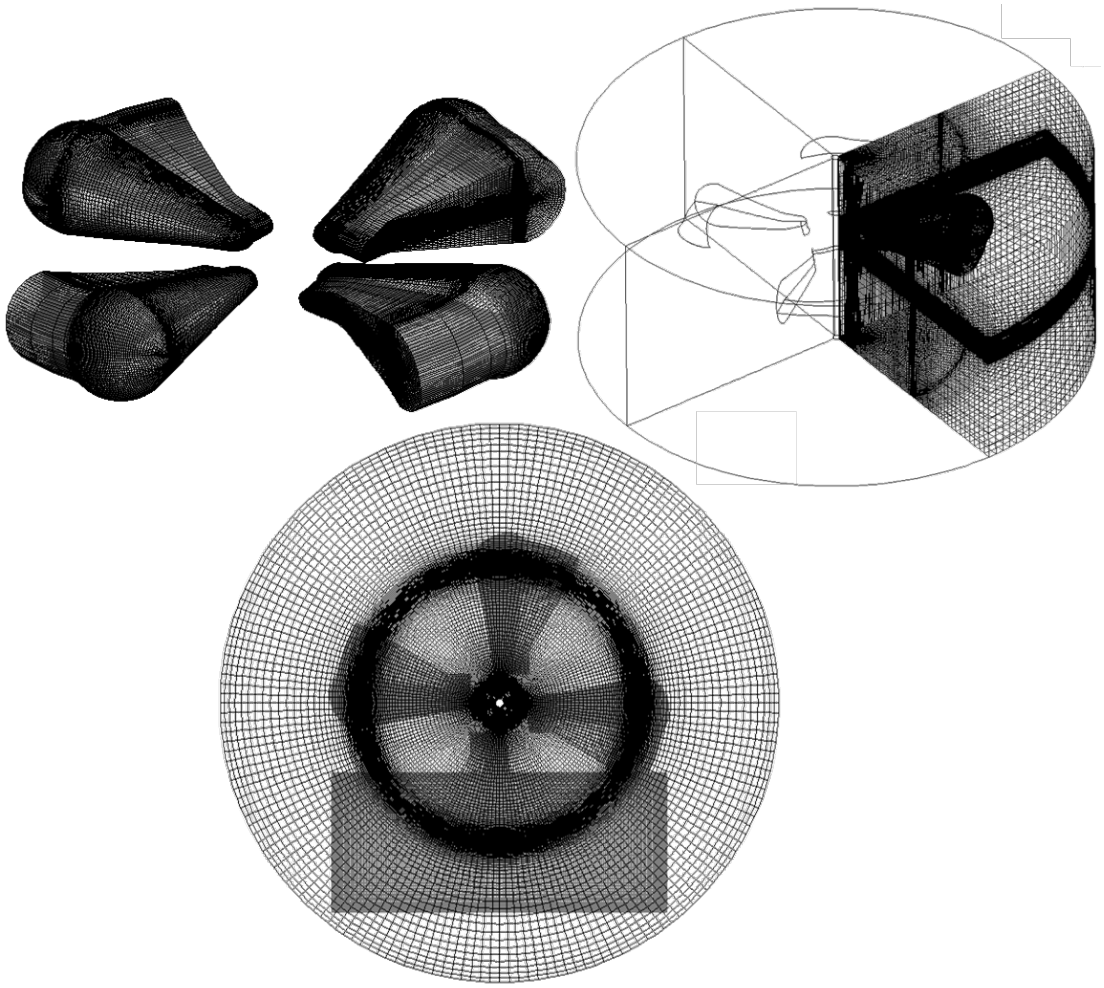

Figure 3.9: Cylindrical mesh setup tested initially.

improve BVI predictions, which are known to be predominant in the first quadrant and more difficult to capture due to the older wake ages of the vortices that interact with the blades there. However, as mentioned above, this setup was dropped to use Cartesian grids in the background (far-field). Figure 3.10 shows this setup, which was already presented earlier.

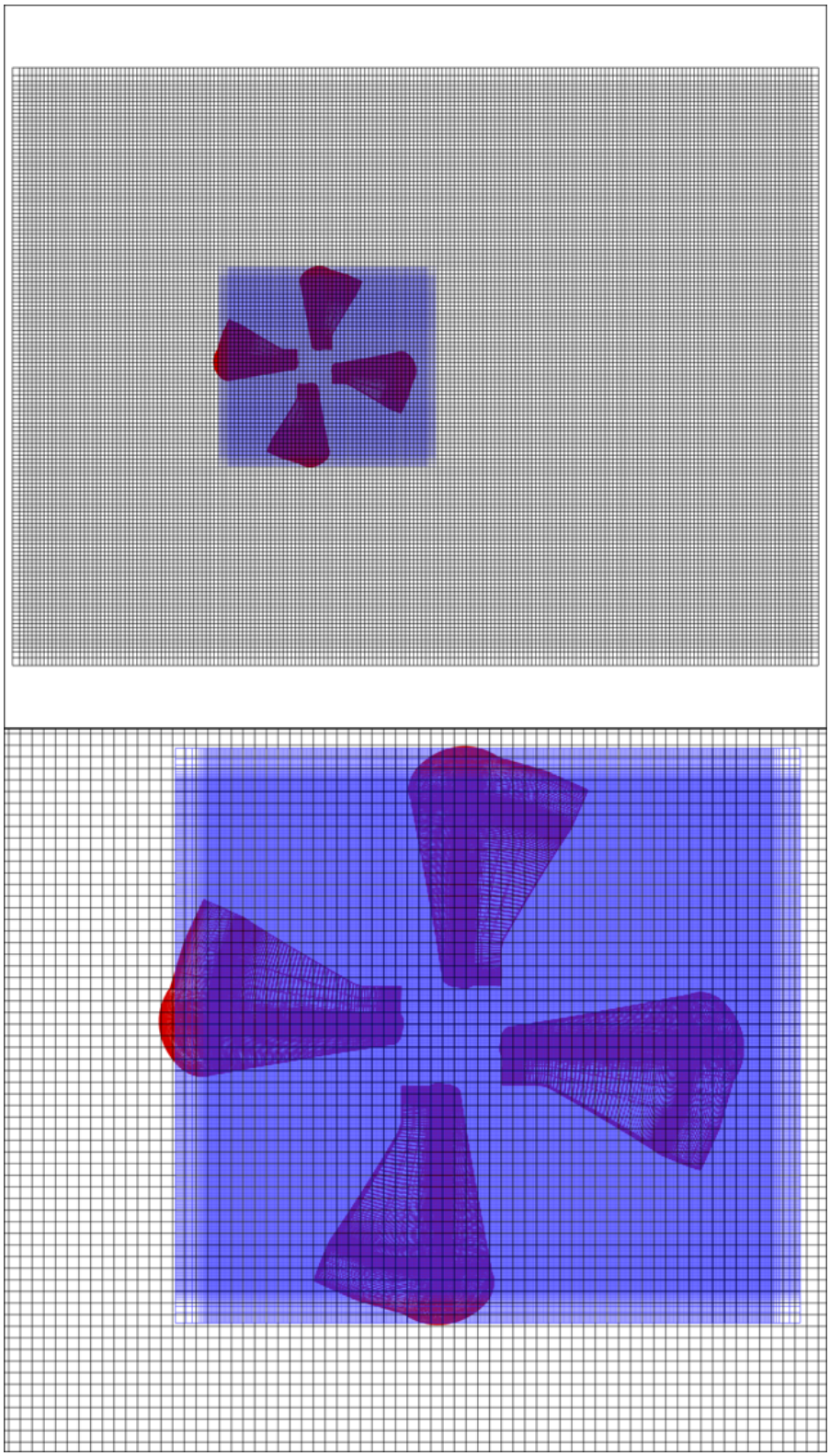

Figure 3.10: Cartesian mesh setup with adequate resolution and stretching between the grids.

3.4.2 Spatial Discretization and Mesh Stretching

The mesh spacing used in both background meshes was carefully chosen to avoid excessive numerical diffusion. In addition, the stretching used between these two grids was designed to have a smooth transition by limiting the cell growth ratio to 1.2 and matching cell sizes at the edge of the smaller background mesh. This proved to be crucial to make sure the hole cutting algorithm would perform as expected and transfer information between the grids without dissipation.

3.4.3 Spatial Integration Scheme

In order to correctly capture and preserve the vortical structures present in the flow field, it was decided to use a higher order scheme for spatial discretization of the inviscid terms, namely a fifth order Compact-Reconstruction Weighted Essentially Non-Oscillatory (CRWENO). This scheme was recently developed at UMD (Ref. [42]). It uses a non-linear, solution-dependent combination of lower-order compact interpolation schemes to yield a higher-order non-oscillatory compact scheme. The CRWENO scheme has significantly higher accuracy and spectral resolution compared to the WENO scheme of the same order of convergence. This scheme has been validated for steady and unsteady flows around airfoils (Ref. [43]) and result in the improved resolution and preservation of small-length-scale flow structures in the near-blade region, as well as the wake. Using this scheme helped limit numerical diffusion of the vortices and led to improved BVI loading prediction. Figure 3.11 shows the vorticity magnitude in a plane cutting vertically through the rotor, the

reference blade being at $\psi = 0\ ^\circ$. It can be seen that the CRWENO scheme is able to preserve the vortices better and for longer wake ages. Similarly on Fig. 3.12, which shows iso-surfaces of Q-criterion (level = 0.05, colored by vorticity magnitude: scale = 0.0 to 1.0), the CRWENO scheme captures more details in the flow field and the vortices appear tighter and stronger. This is critical to obtain good BVI predictions. As was seen in previous chapters, in the case of the HART-II rotor, BVI occurs both on the advancing and retreating sides and manifests itself as impulsive loading. Figure 3.13 shows filtered $C_l M^2$ data on the advancing side at 87% radius, as well as the first derivative. This is a good way to compare the magnitude and phase of the BVI events. It can been seen that the CRWENO scheme predicts the full magnitude of most of those peaks. The phase appears to be offset but this will be improved by modeling the fuselage. A similar trend is observed for the pitching moments. However, it should be noted that the lower frequency content predicted by the different schemes was very close.

3.5 Summary

In this chapters, the optimal values of numerous numerical as well as physical variables were determined through parametric studies. It was shown that certain aspects of the simulation are sensitive to spatial and temporal refinements, whereas others aren't. The choice of the best parameters was made as a compromise between improvements in solution accuracy and reasonable computational cost increases. The best integration schemes for both space and time were also chosen by following

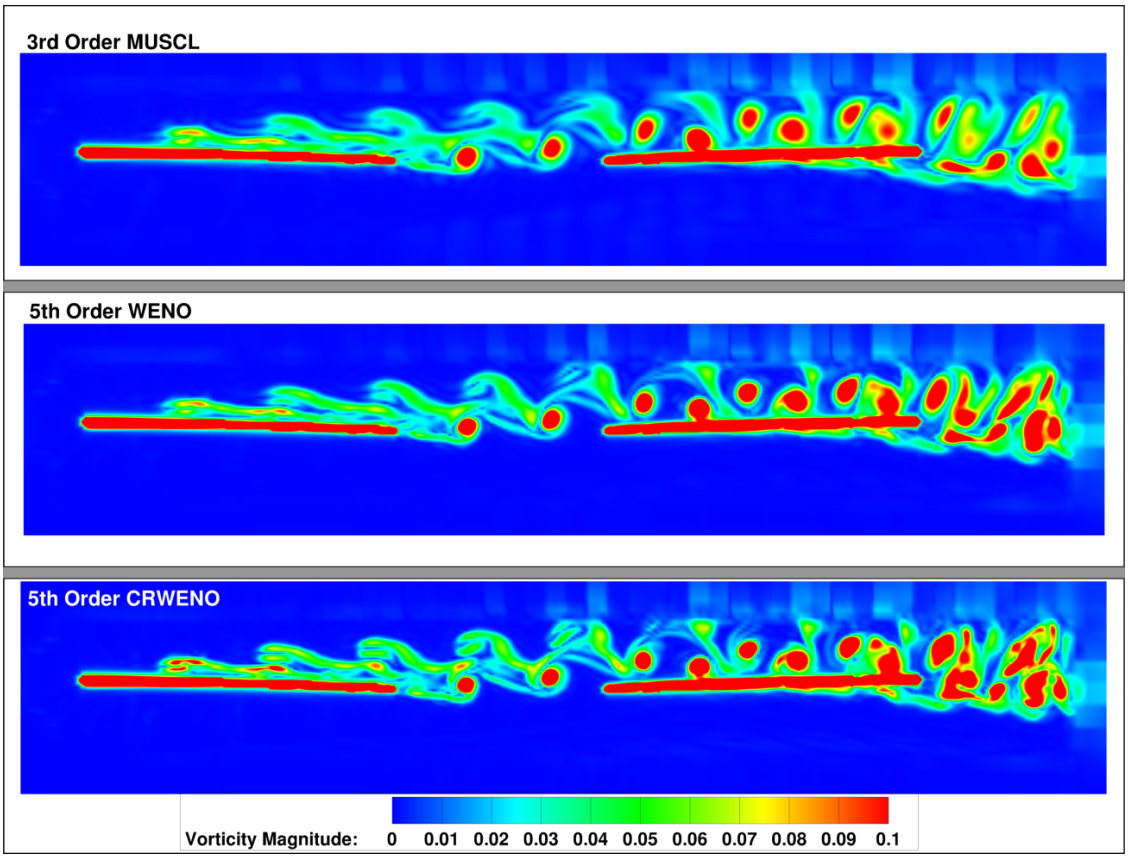

Figure 3.11: Vorticity magnitude at center plane, $\psi = 0$ °, scheme comparison

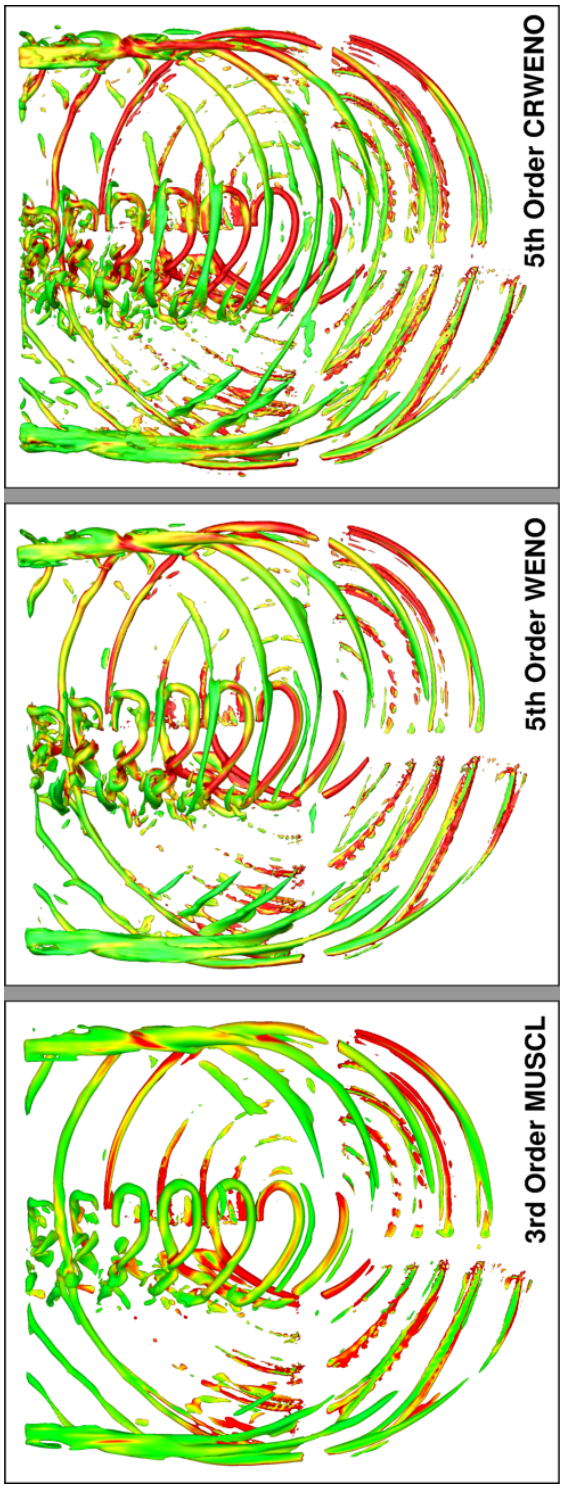

Figure 3.12: Iso-surface of Q-criterion, colored by vorticity magnitude, scheme comparison

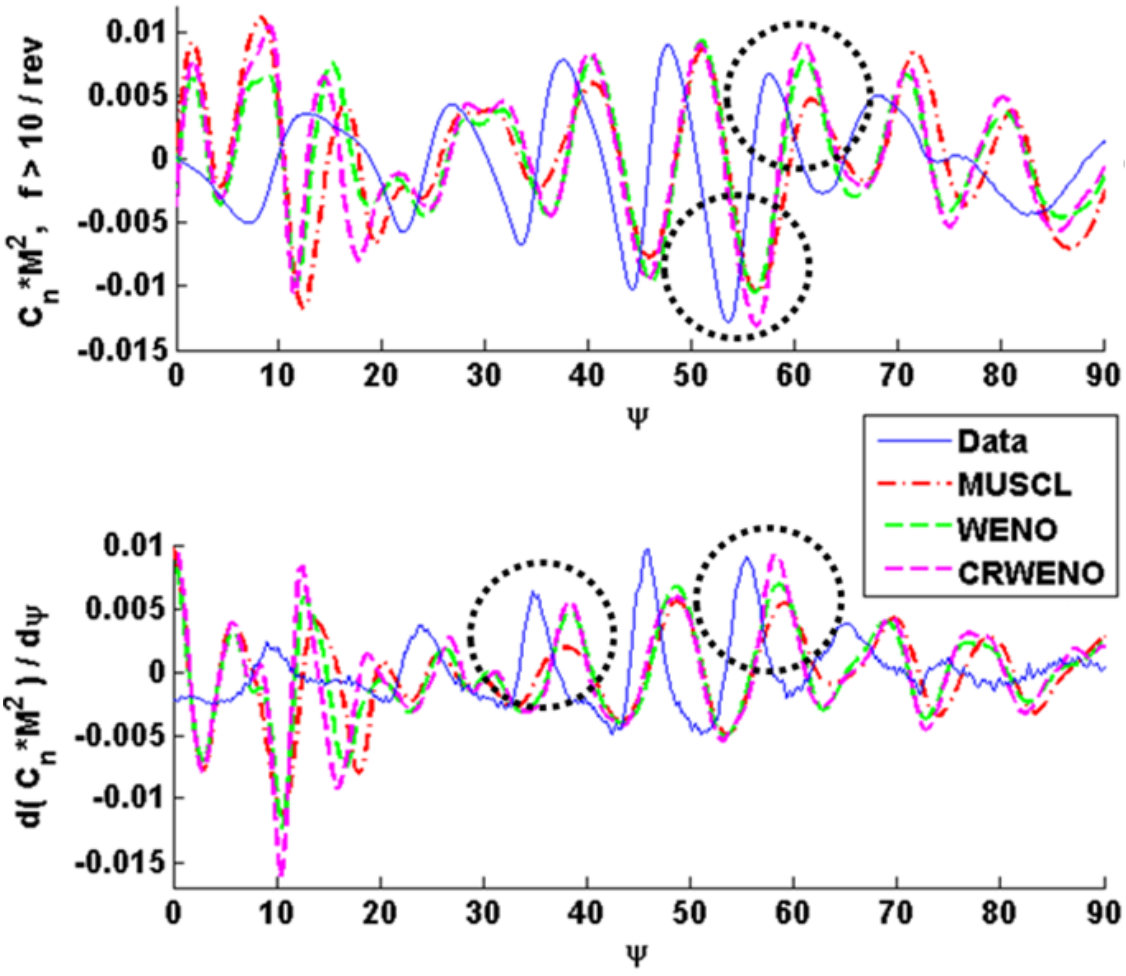

Figure 3.13: $C_l M^2$ filtered and derivative on advancing side, 87%R, scheme comparison

this dichotomy. As a vital component of BVI simulation is the adequate modeling of the rotor wake, various geometrical and numerical assumptions were evaluated in the free-wake model. For the wake capturing approach, a study of the trade-offs between different mesh topologies was conducted to obtain an optimal setup which ensures that relevant vortical structures are correctly captured and preserved through the computational domain.

Chapter 4

Fuselage Modeling

As was seen in previous chapters, the HART-II wind tunnel testing was conducted using a generic fuselage shape to obtain a more representative BVI flight condition. Since then, it has been shown by different research groups (Ref. [36] - Ref. [37]) that the addition of a fuselage model in CFD could lead to higher levels of accuracy in BVI loading predictions In fact, they saw that the influence of the fuselage on the rotor and its surrounding flow field was not negligible. Therefore, it was decided to investigate and implement different fuselage modeling techniques that could be used in the multi-fidelity framework.

The most commonly used approach chosen by modern CFD codes is to add a fuselage specific mesh in the simulation. If a structured grid topology is used in the flow solver, the new mesh is curvilinear and body-fitted around the simplified helicopter shape. It is embedded in the overset group and a connectivity module takes care of data transfer between the grids. When using unstructured meshes,

the grid generator adds the fuselage surface as an additional wall boundary. This grid-based approach usually gives the best levels of solution accuracy, although the computational time can be greatly increased by the added mesh points and refined density around the body surface. In addition, the grid generation process can be quite complex to create a satisfactory mesh around helicopters body when a detailed representation is used, although an unstructured method wouldn't require as much effort as a structured one.

On the other side of the complexity scale, simpler models have been implemented. For example, in their comprehensive code S4, DLR included the effect of the fuselage through a potential flow formulation. A one-time representation of the flow around the HART-II fuselage was obtained using a panel method with 1700 constant strength panels. It was used to compute the velocities at the rotor disk, which then were described by polynomials in radial direction and a Fourier series in azimuthal direction. From this, an analytic description of fuselage velocities at every radial and azimuthal position of the blades was obtained and used in subsequent simulations. Obviously, once an analytical formulation has been established and validated, this approach is much less expensive than the one above.

In the present work, three methods have been developed and coupled to the various levels of aerodynamic modeling. First, the potential flow approach proposed by DLR was extended to use a panel method within the framework. Although more costly, doing so avoids having to developed new formulations for different flight conditions and provides a more dynamic response of the fuselage on the entire flow field. Then, a grid-based technique using an overset structured fuselage mesh was

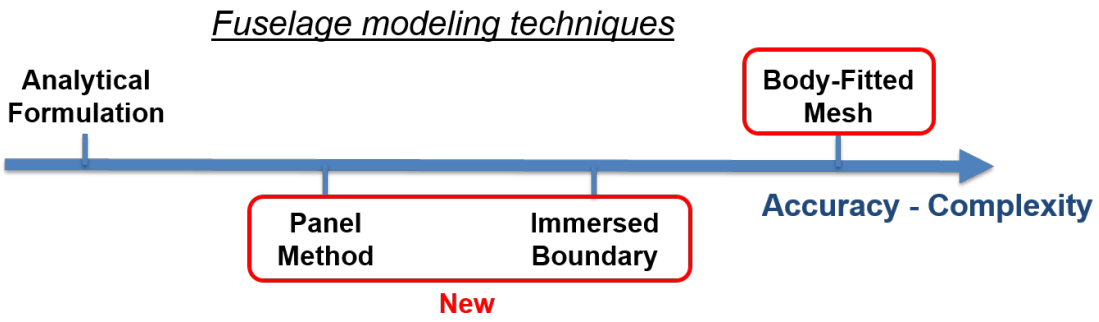

Figure 4.1: Fuselage models ordered by accuracy and complexity.

implemented. This required the development of a new grid generation code, as will be seen below. Finally, an intermediate solution was tested. It is also grid-based but relies on an Immersed Boundary Condition (IBC). These methods are presented in the following sections. Figure 4.1 shows the various techniques presented above on a virtual accuracy / complexity scale.

4.1 High Resolution 3D Vortex Panel Method

In the wake coupling approach, the far-field domain is not modeled using CFD grids but rather Lagrangian vortex filaments. Therefore, it was decided to use a similar concept to model the fuselage: a vortex panel method.

4.1.1 Code Description

This method is based on the solution of the Laplace equation for the velocity potential ϕ:

$$\nabla^2 \phi = 0 \tag{4.1}$$

In this method, a body of arbitrary shape is represented and discretized by

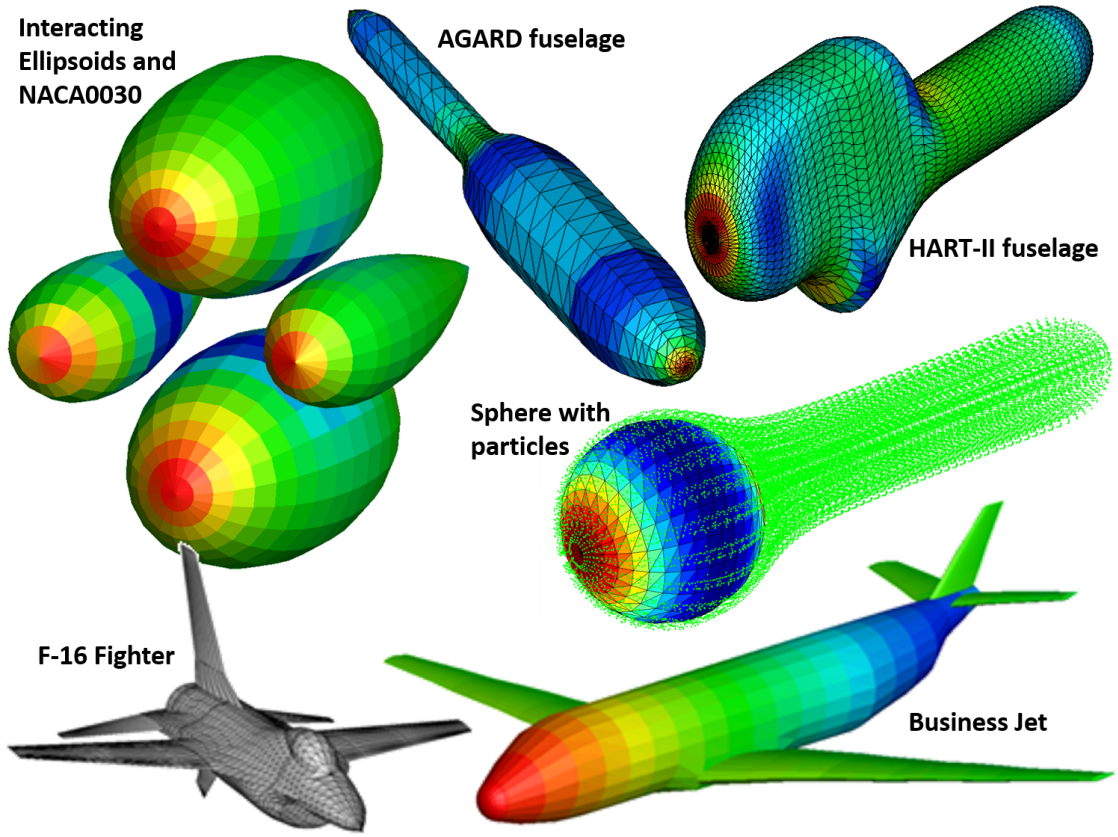

Figure 4.2: Example of geometries modeled with the panel code.

a set of polygonal panels (Fig. 4.2, each made of a certain number of constant strength vortex filaments. Complex geometries with concave corners can easily be modeled, as seen in the Fig. 4.2, which is a big advantage of this method. The idea behind the code is to enforce flow tangency at the surface of the body by giving a specific strength γ to the panels to cancel out the component of velocity normal to the surface. The code can handle multiple interacting bodies, which can either be fixed or move. Different formats for the input geometries are supported, such as STL or quadrilateral definitions, for which a toolkit was developed to check and fix surface holes, overlapping elements, bad quality cells, ... At the body surface, the no-penetration condition, or flow tangency, is enforced by solving a set of linear

equations: the product of the influence matrix $\mathbf{A}$, which combines the influence of all panels on each other, by the filament strength vector $\vec{\Gamma}$ must be equal and opposite to the local normal component of velocity. The system of equations is given by:

$$\mathbf{A}\vec{\Gamma} = -\vec{V}_i.\vec{n}_i \tag{4.2}$$

where $\mathbf{A} = A_{i,j} = \vec{\nabla}\phi_i.\vec{n}_j$ and $\vec{\Gamma} = \gamma_j$, (i, j) being panel indices. $\vec{n}_i$ is the surface normal vector at panel i and $\vec{V}_i$ is the local velocity. This velocity combines any free-stream velocity, displacement velocity due to body motion and/or deflection, and any external velocity, from the free-wake solver for example. The Biot-Savart law is used extensively in these computations, as it gives the velocities induced by vortex filaments at arbitrary points in space. The resulting system is linear and square and contains N equations for N unknowns, N being the number of panels. The unknowns are the panel strengths γ_i. Solving it requires the inversion of matrix $\mathbf{A}$, which is often more expensive than the Biot-Savart calculations. Overall, the cost of this method is on the order of N^3 operations. A recurrent issue with such a system of equations is that it is often ill-conditioned and singular, and therefore can not be inverted. To overcome this problem, an additional equation is added to the system, making it over-determined but solvable. A least square solution algorithm is used in the present work. The additional equation can be used to ensure that the total circulation over the entire surface remains zero, for non-lifting bodies. This is analog to the Kutta condition used in 2D panel methods. For lifting bodies, trailing wake panels can be used to model the circulation change around the body. Although

this panel method was derived from potential flow theory and it is only applicable to flows that are steady, incompressible, inviscid, and irrotational, it was found to be capable of predicting the rough effect of a fuselage shape on the rotor disk with acceptable accuracy. Pressure at the body surface is computed using Bernoulli's formula:

$$P = 1 - \left(\frac{V}{V_\infty}\right)^2 \tag{4.3}$$

The code was extended to model rotating and deforming rotor blades, but this feature was not preferred over the lifting-line approach. Its advantage would have been the ability to fully represent the geometry of the blades, which the lifting-line code only approximates. However, this is an inviscid method whereas the linearized aerodynamics alternative includes some viscous effect through the use of airfoil tables derived from unsteady, compressible, viscous flow solvers.

4.1.2 GPU Implementation

This panel method was implemented in CUDA-C to take advantage of the high potential speed up offered by GPU computations. High surface resolutions are possible thanks to CUDA's massively parallel coding environment. Calculation of the terms of the influence matrix and the normal component of velocity at each panel greatly benefit from the high level of parallelization available. Each GPU thread is mapped to a specific panel where the influence of all other panels is evaluated, as well as a single normal velocity value. The linear system of equations is solved using the CUDA-optimized linear algebra library CULA (culaDeviceDgels: solution

of over-determined linear systems of equations), which brings an additional speed up to the code. To further increase the numerical efficiency to the code, a GPU-optimized Fast Multipole Method (FMM) could be used to speed up the Biot-Savart computations.

4.1.3 Coupling Strategy

The panel code is "tightly" coupled to either near-body CFD solver (Lifting-Line or RANS) and to the free-wake code, as seen on Fig. 4.3. At each time-step, the influence of the free-wake filaments and the fuselage panels, which are made of vortex filaments as well, on the CFD near-body points (blade markers or grid points) is computed, using the Biot-Savart law. However, it should be noted that, although the free-wake filaments are directly influenced by both the blade solution, through the blade airloads (or blade bound circulation), and the panel code, the fuselage is only affected by the free-vortex filaments.

4.2 Curvilinear Body-Fitted CFD Mesh

In the wake capturing method, the far-field domain is modeled using CFD computational grids. Therefore, it was decided to use a grid-based approach to model the fuselage. Two different methods were implemented and compared.

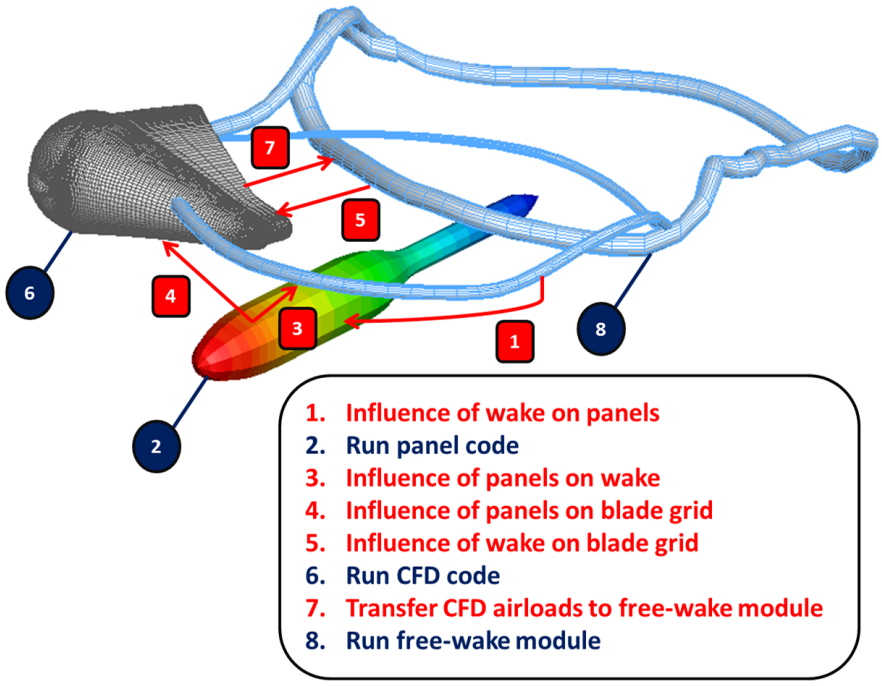

Figure 4.3: Interaction between the different modules, influence of the fuselage (single blade showed, agard fuselage)

4.2.1 Code Description

A 3-D algebraic mesh generator for structured, curvilinear, body-fitted CFD grids was developed at UMD. Structured surface definitions can be used as input geometries, or mathematical formulations for different body shapes are also available. Additional smoothing and clustering of the surface definition in the lengthwise and radial directions can be done by the code, as seen on Fig. 4.4. This clustering was obtained using a 2D Poisson solver, on which more details are given below and the mathematical formulation can be found in the appendix. The volume mesh is generated using a multi-surface algebraic mesh generation procedure with one intermediate surface between the wall and the outer boundary. Initially, wall normal vectors are calculated at each point on the body surface. Then, smoothening is

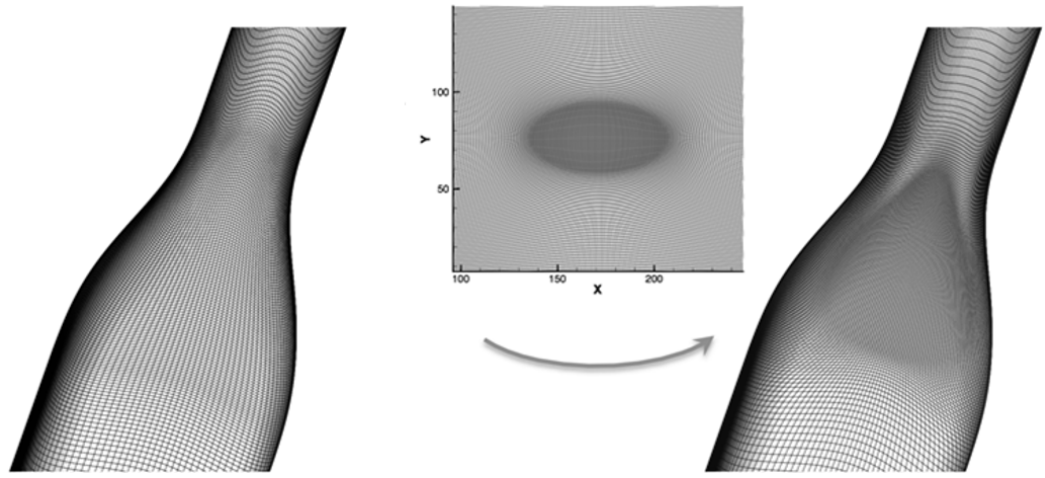

Figure 4.4: Surface clustering of the input geometry for the O-O mesh generator.

applied to the normals using nearby neighbors in all four directions. This helps avoid the creation of negative volumes, especially in region of high curvatures or for concave shapes. The smoothened wall normals are projected outward from the body surface by a fixed distance to form an intermediate surface. Finally, points on the three surfaces (wall, intermediate and outer) are used to define quadratic lines. Mesh points are created by quadratic interpolation using user-defined point distributions and the quadratic lines defined previously. A high density of points is used at the wall to capture viscous effects accurately and stretching is applied in the normal direction. The resulting mesh has an O-O topology. This code has been used for various bodies including simplified helicopter fuselages like AGARD, Robin mod-7 (Fig. 4.5), and HART-II. Meshes for rotor blades and insect wings (Fig. 4.5) were also created as an alternative to the C-O topology used previously. For a fuselage mesh, the total number of grid points created nears 4 million.

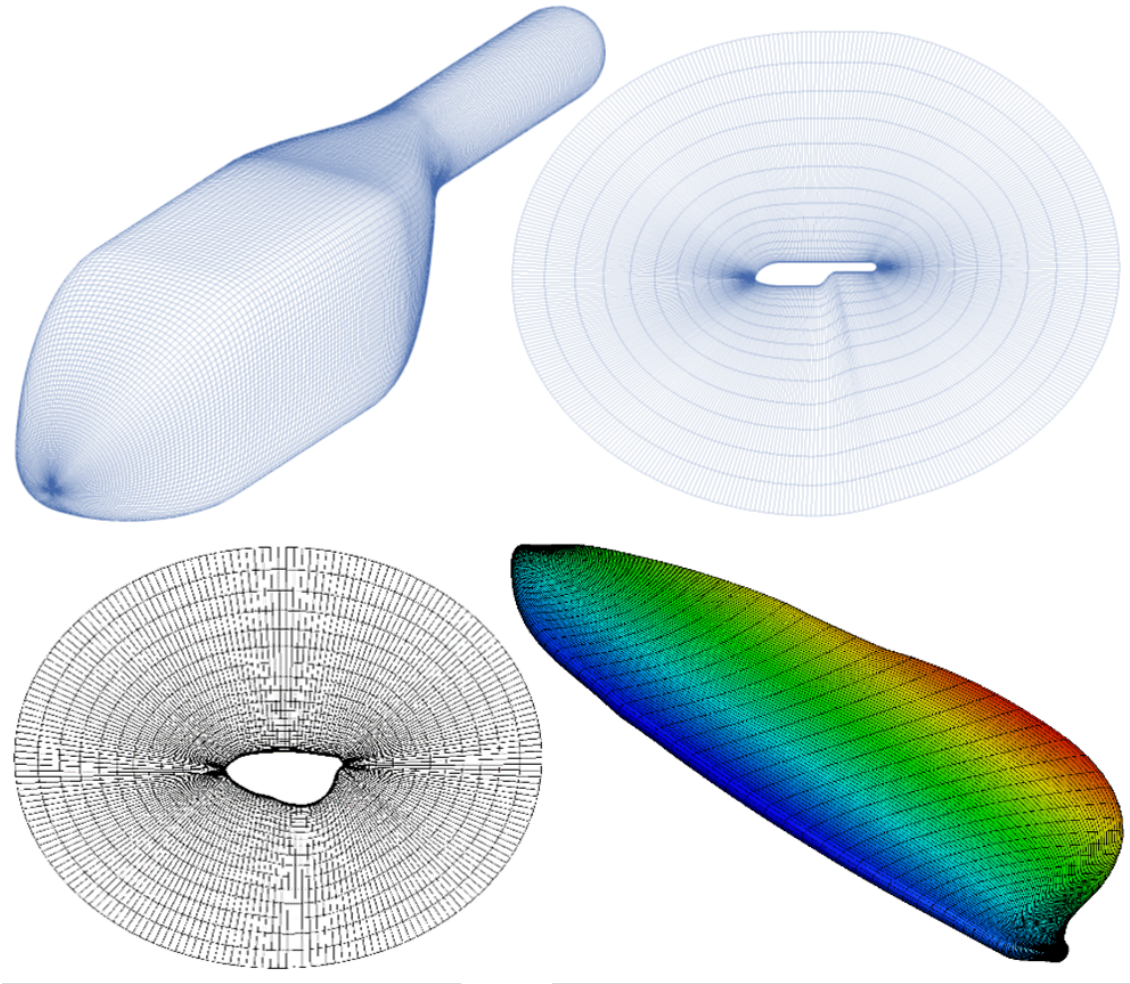

Figure 4.5: O-O mesh for the Robin mod-7 fuselage and an insect wing.

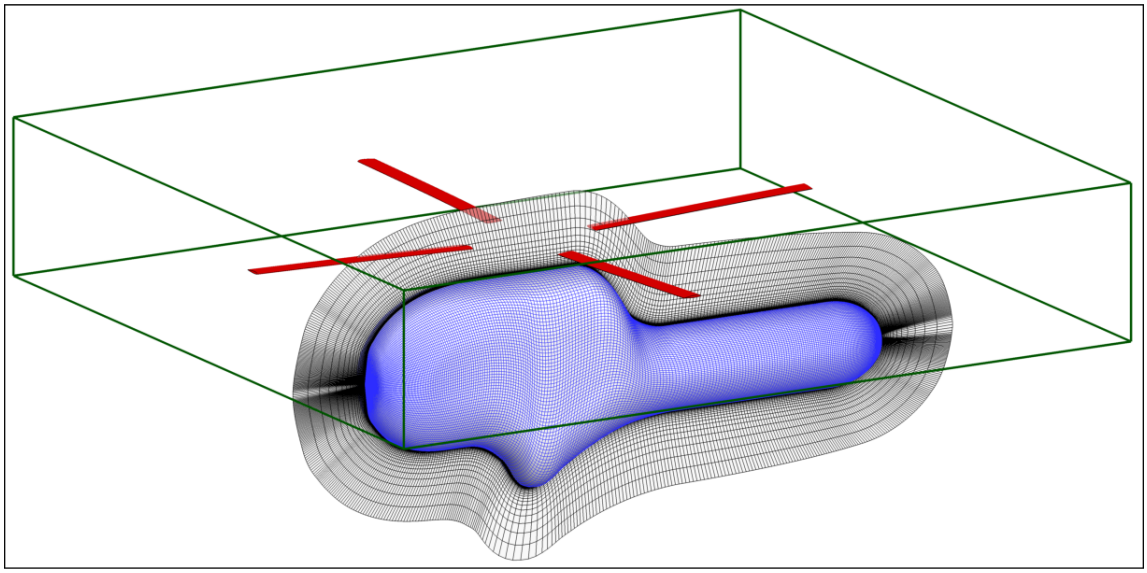

Figure 4.6: HART-II fuselage mesh: overset group

4.2.2 Coupling Strategy

As mentioned above, this model is used with the wake capturing approach. The new mesh is included in the overset group with the near-body blade grids and the Cartesian background grids. The implicit hole cutting algorithm is used to determine the connectivity information between them. Figure 4.6 shows the surface definition and a slice of the mesh used for the HART-II fuselage inside the overset group (largest background mesh not shown).

Validation of this fuselage modeling technique is shown in the next section for the Robin mod-7 fuselage.

4.3 Immersed Boundary Condition

4.3.1 Code Description

Another way of modeling a body of arbitrary shape using CFD meshes is the immersed boundary method. The idea is to impose no-penetration and no-slip conditions at the surface of the given geometry through local modification of the flow variables, to reflect the presence of a wall boundary. The present implementation uses a rectangular Cartesian grid, in which the body shape is embedded. First, a hole cutting algorithm using ray-tracing is employed to blank out the body interior points. Then, points that are inside the body but within a few cells of the surface are flagged as immersed boundary nodes. Finally, interpolation coefficients are computed using the closest 8 unblanked grid points (body exterior points). For fixed geometries, this process is only done once at the beginning of the computation. However, hole cutting would have to be performed at every time steps for moving or deforming immersed bodies. Then, flow primitive variables are updated at every time instants using tri-linear interpolation with the boundary nodes. Similarly to the previous method, this mesh is embedded into the overset group and IHC is used to obtained connectivity information between the participating grids. Figure 4.7 summarizes this process. Validations were also performed for the Robin-mod 7 fuselage and are showed below. An advantage of this method over the structured body-fitted mesh approach is that complex shapes with concave corners can easily be modeled, as long as an efficient hole cutting algorithm is used.

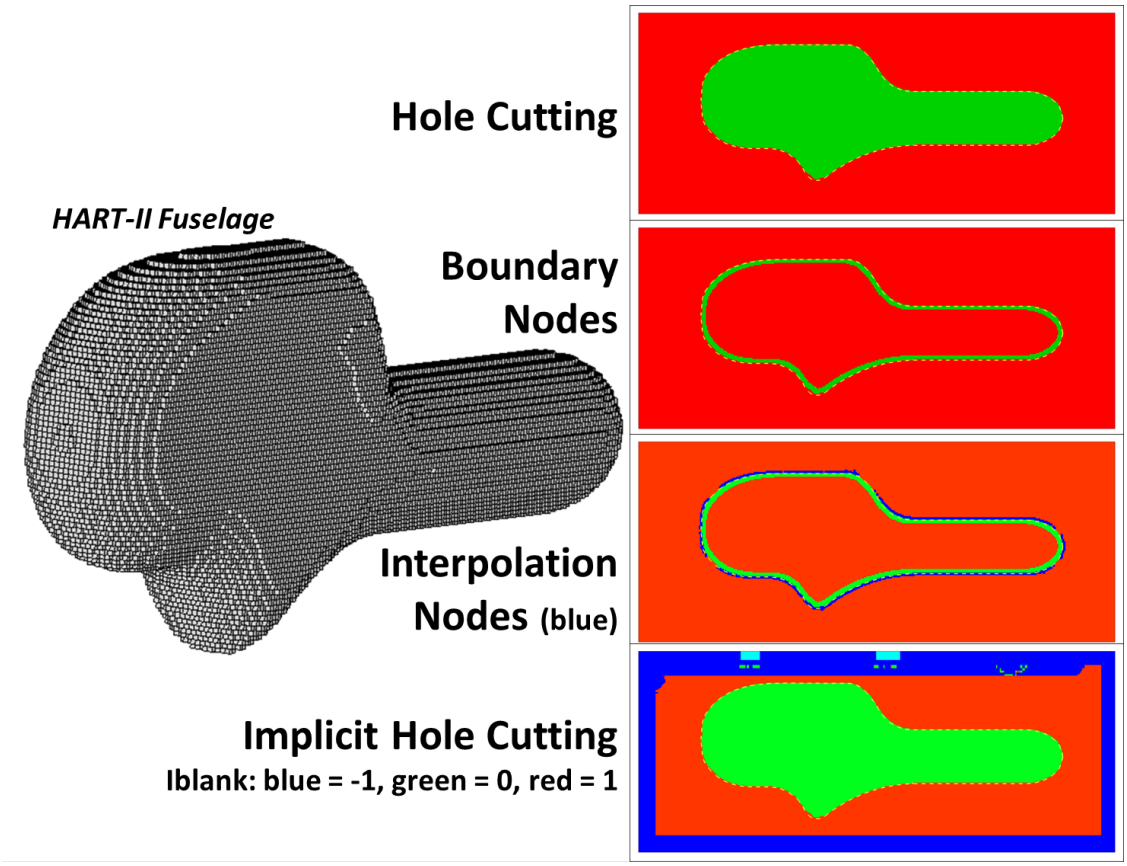

Figure 4.7: Steps of Immersed Boundary Condition process

4.3.2 Volume Refinement using 3D Elliptic Grid Generation

One drawback of this method is that viscous effects at the wall cannot be captured precisely since the required high density of points inside the boundary layer would make the computation too expensive. In addition, the grid points near the fuselage surface do not conform to the body shape, which also degrades the quality of the numerical solution. To help increase the mesh resolution in the boundary layer, an additional set of nested Cartesian grids with refined grid density could be used. However, doing so would increase the computational as the total number of mesh points is increased and more work is required to determine connectivity information in IHC. Therefore, an alternate method was develop. The idea was to keep the number of points the same but cluster the mesh around the body surface to better capture the wall bounded flow. To do so, a 3D elliptic grid generation algorithm was developed. It is based on solving a 3D Poisson equation with source terms. These source terms define regions where the grid needs to be refined. The user can prescribe a radius of adaption which sets the extent of the clustering around the source points, as shown in Fig. 4.8. Additionally, a skew angle can be introduced for each cell, which would allow for the grid to conform more with a geometry, such as a fuselage for example. The numerical implementation of the solver is shown in the appendix, both for 2D and 3D. First, the mesh adaption is carried out on the computational domain. Then, tri-cubic interpolation is used to obtain the adapted physical mesh from the baseline curvilinear mesh. This is schematized on Fig. 4.9. The Laplacian nature of elliptic equations ensure that the final mesh is smooth. However, Poisson equations

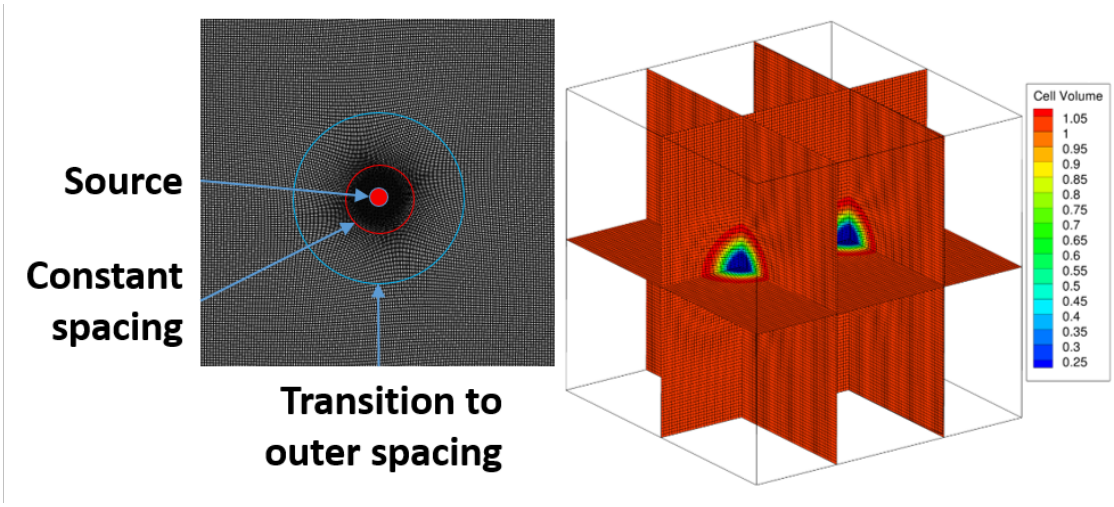

Figure 4.8: User defined refinement around source points using the 3D Poisson solver.

can be costly to solve, unless advanced numerical methods are used, although when applied to cluster point around fixed source points, like a fuselage, this process is only done once. Also, the current implementation requires that the location and strength of source points, which are virtual coordinates, be re-evaluated every few time steps because the adaption process moves them. The physical source points of adaption can either be points on a body surface, such as a fuselage, or targeted flow points based on feature extraction (Q-criterion, vorticity magnitude, ...). This is displayed on Fig. 4.10 where the adapted region is highlighted. The iso-surfaces of cell volume show that the mesh was clustered around the fuselage shape or the regions of high vorticity. Therefore, this method could replace more advanced and expensive ways of preserving blade vortices in the flow field, such as Automated Mesh Refinement (AMR) or the use of Vortex Tracking Grids (VTG). The main advantage here is that no additional mesh points are created, whereas the two methods mentioned can drive the computational cost of a simulation very high.

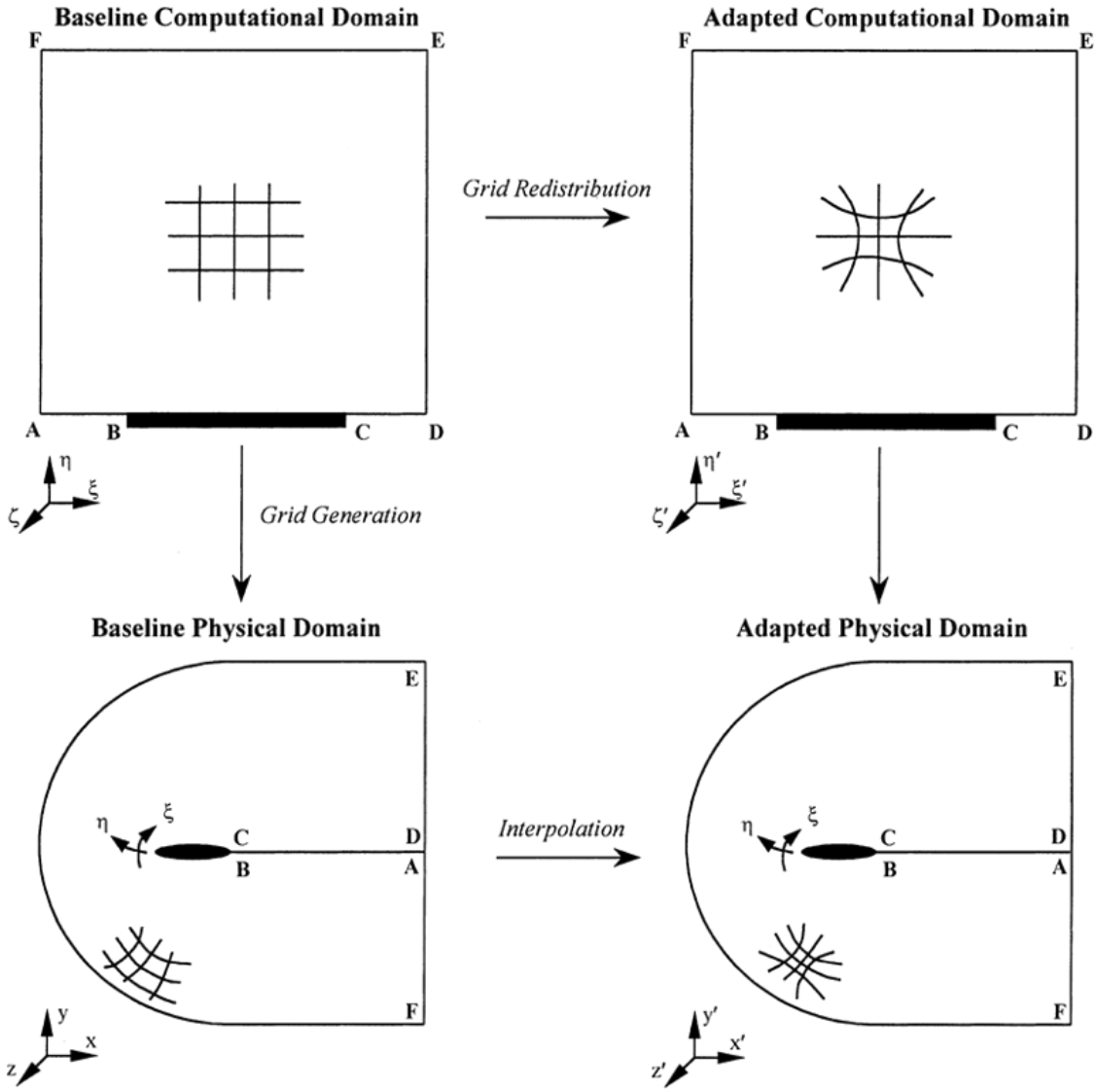

Figure 4.9: Adaption process between the computational and physical domains.

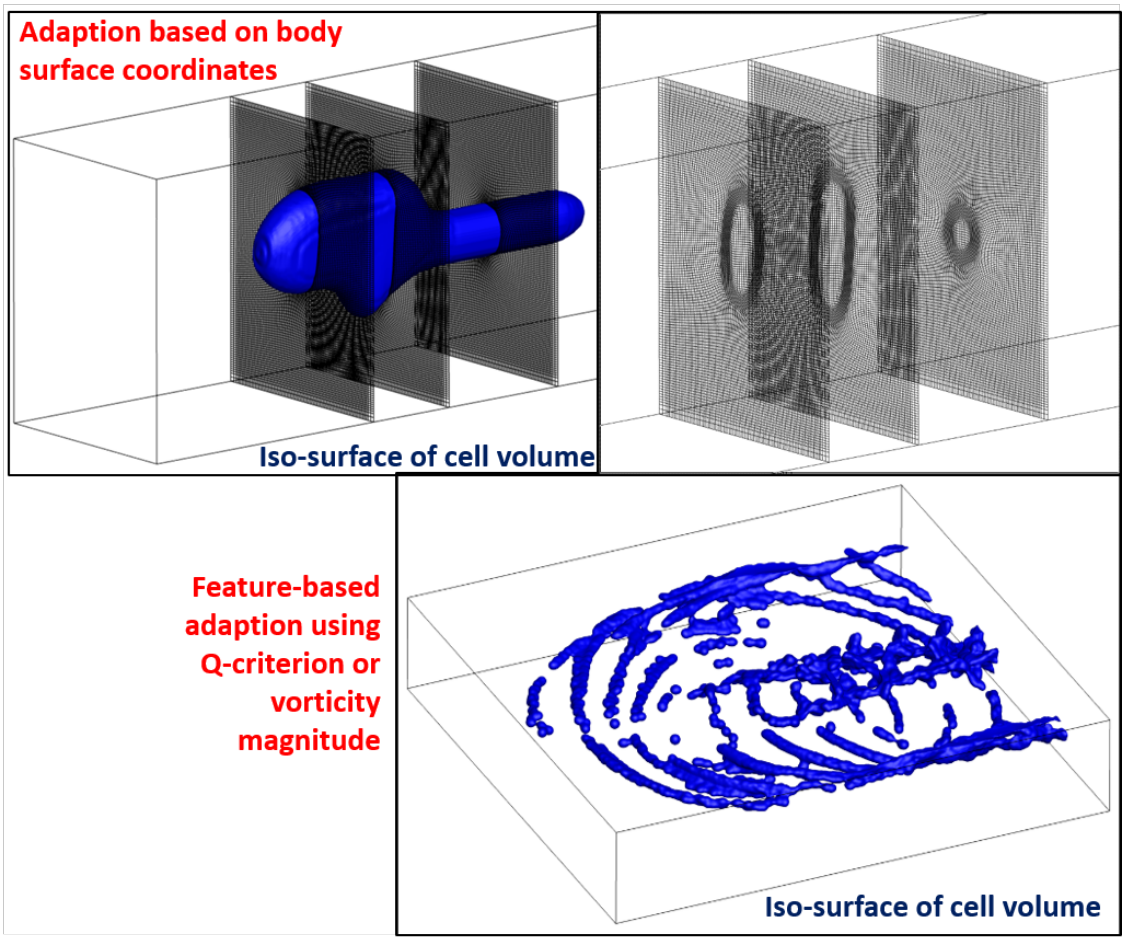

Figure 4.10: Sources of adaption: physical coordinates or feature based.

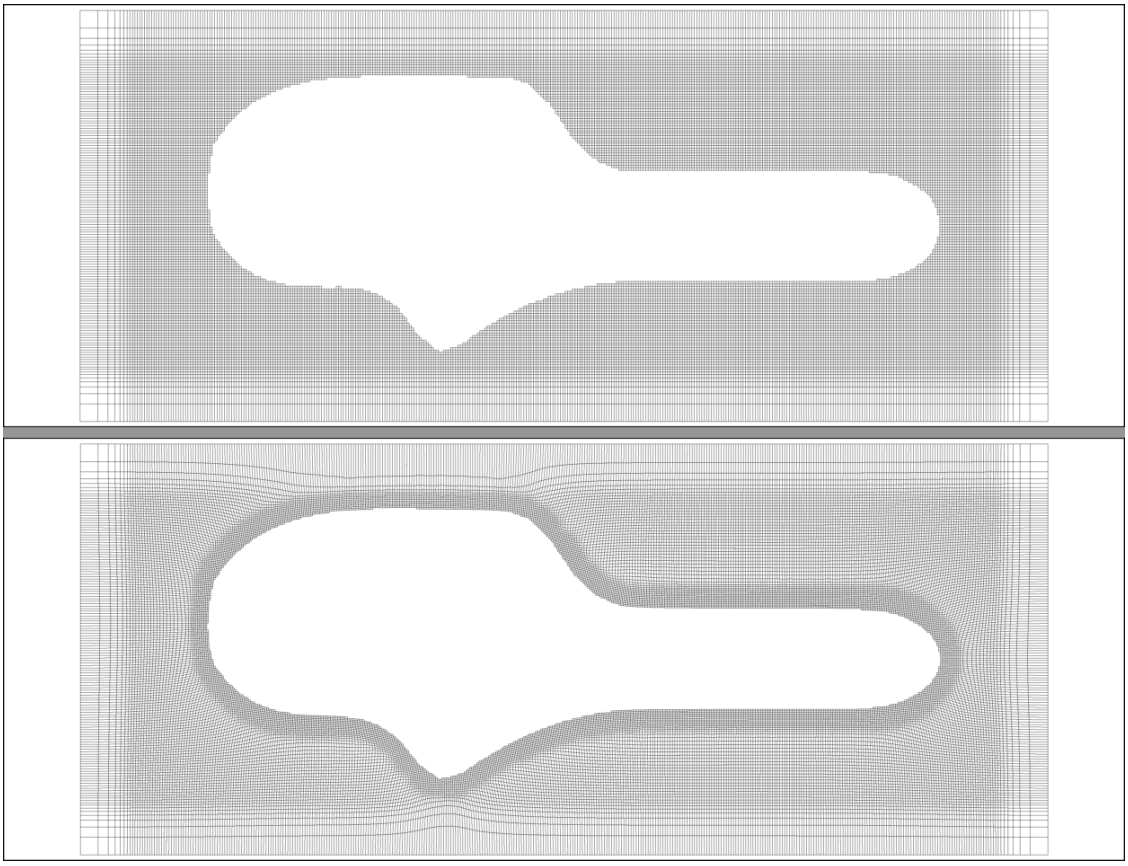

Figure 4.11: Comparison of a baseline IBC fuselage mesh and its adapted version.

Figure 4.11 compares cross-sections of a baseline mesh used with the IBC method and an adapted mesh. It appears clearly that the refined region is around the fuselage surface. This plot also highlight the need for the outer surfaces of the IBC mesh to be far enough away from the adapted region to avoid cells being stretched too much, which is starting to happen on the top and bottom surfaces. Figure 4.12 shows the vorticity magnitude predicted around the fuselage using both meshes. Although the thickness of the boundary layer is significantly decreased and the separated region near the back ramp of the fuselage reduced, it seems that more refinement would be necessary to achieve comparable results as a body-fitted mesh.

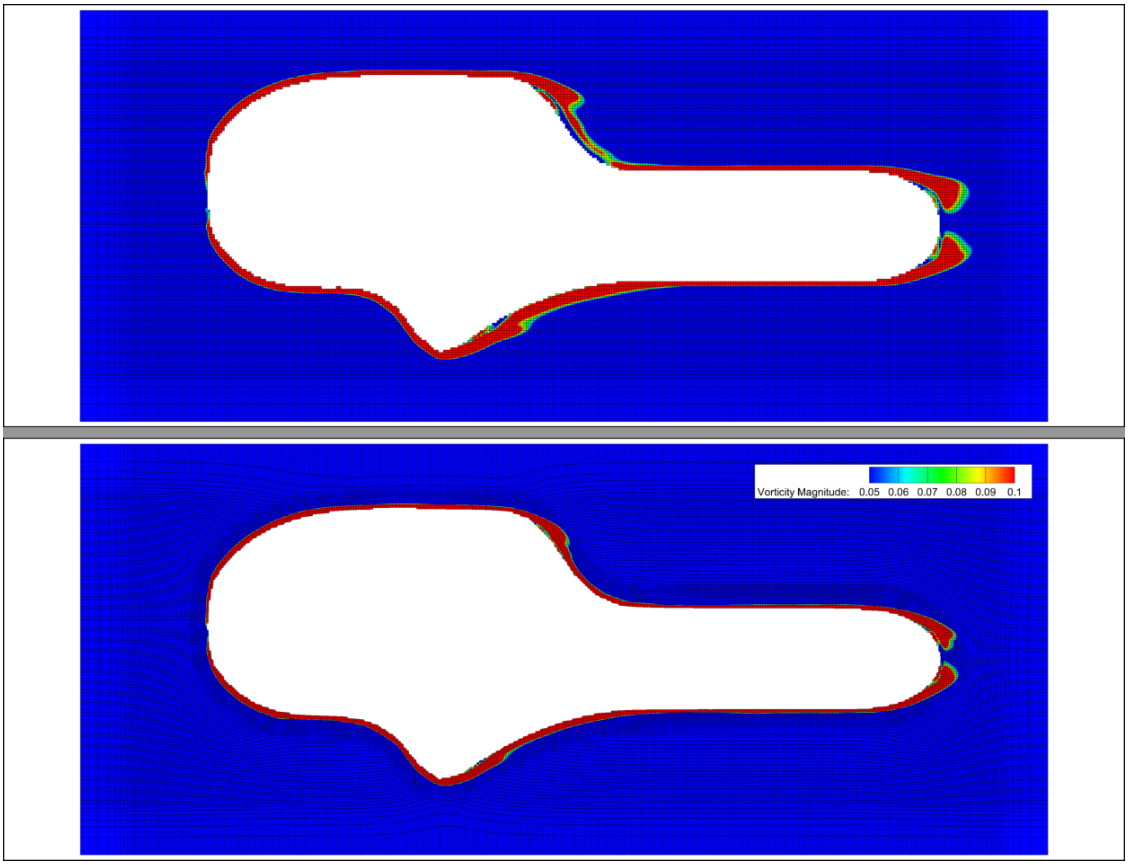

Figure 4.12: Influence of adaption on vorticity magnitude for an IBC fuselage simulation.

4.4 Validation of the Methods

4.4.1 Isolated Fuselage: Robin mod-7

Each of the three methods for modeling a fuselage has been tested and validated against experimental data, starting with a simple sphere and the isolated "Leishman" AGARD fuselage. In addition, a more realistic fuselage shape was used: The Robin mod-7 fuselage (Ref. [40]). It is a generic helicopter fuselage developed in the 1970s by NASA. The main purpose of this work was to access the predictive capabilities of CFD codes to simulate rotorcraft flows. Wind tunnel measurements were made to serve as experimental correlation data, as seen on Fig. 4.13. The mod-7 shape is more rectangular than the original one and has a steeper ramp section and higher tail boom.

Comparisons between the numerical solution obtained with the three solvers and experimental data for the Robin mod-7 fuselage are shown below. Plotted on Fig. 4.14 are the pressure coefficients across the upper and lower surfaces, comparing the results from the three methods, as well as predictions obtained using OVERFLOW, against experimental data. The fuselage mesh was ran with and without viscous terms, the later comparing well with the inviscid panel results. Good correlation is achieve with experimental results, especially for the viscous codes. The inviscid simulations do not capture flow separation at the back ramp of the fuselage. The immersed boundary method does well at the front of the fuselage but doesn't predict separation correctly either. This is most likely due to the fact that the grid spacing at the wall is too coarse, as mentioned above, and cannot capture

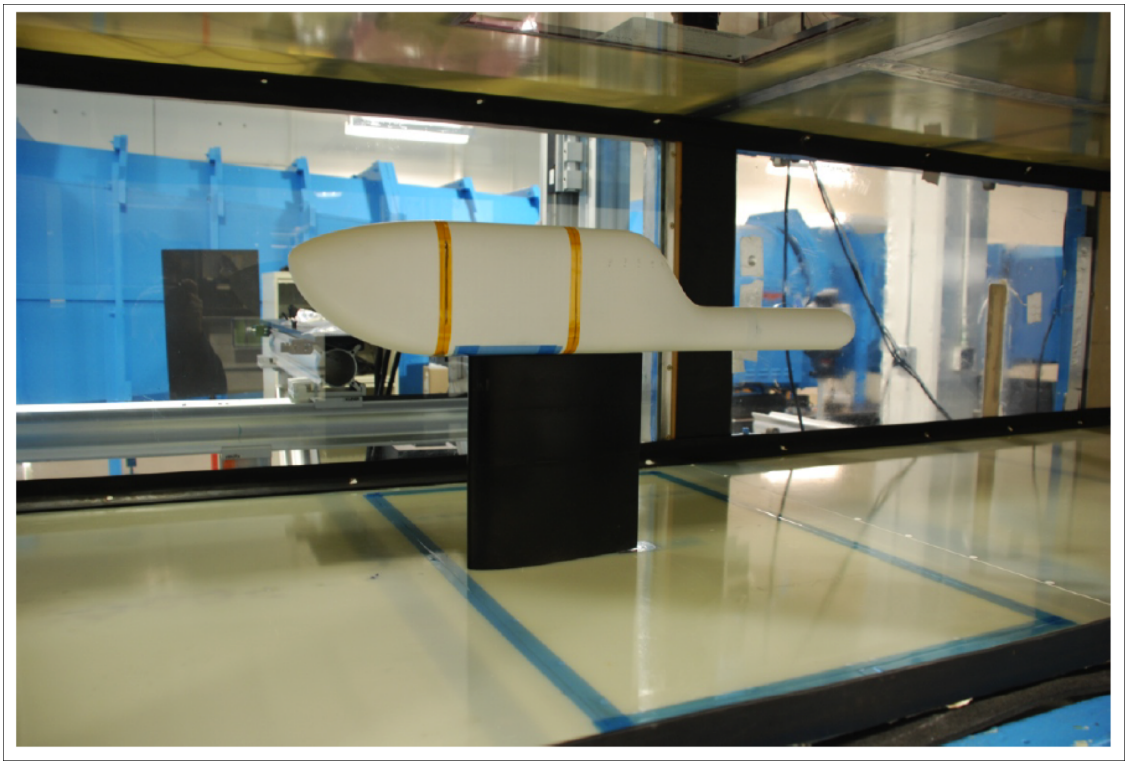

Figure 4.13: Robin mod-7 fuselage during wind tunnel measurements (Ref. [40])

the boundary layer accurately. Pressure coefficients are also shown at the fuselage surface on Fig. 4.15. Good agreement is found between the different codes, although the panel code seems to under-predict the pressure at the front. This could be due to the lower surface refinement used for the panels' definition in this region, which avoids having too small panels and large size ratios between them. The surface pressure plot for the IBC method was obtained by interpolating the flow quantities of the Cartesian grid back onto the initial polygonal surface definition.

4.4.2 Inflow at Rotor Plane

Another way of comparing the three methods and to check the influence of the fuselage on the rotor blades is to look at the inflow across the rotor plane. This is

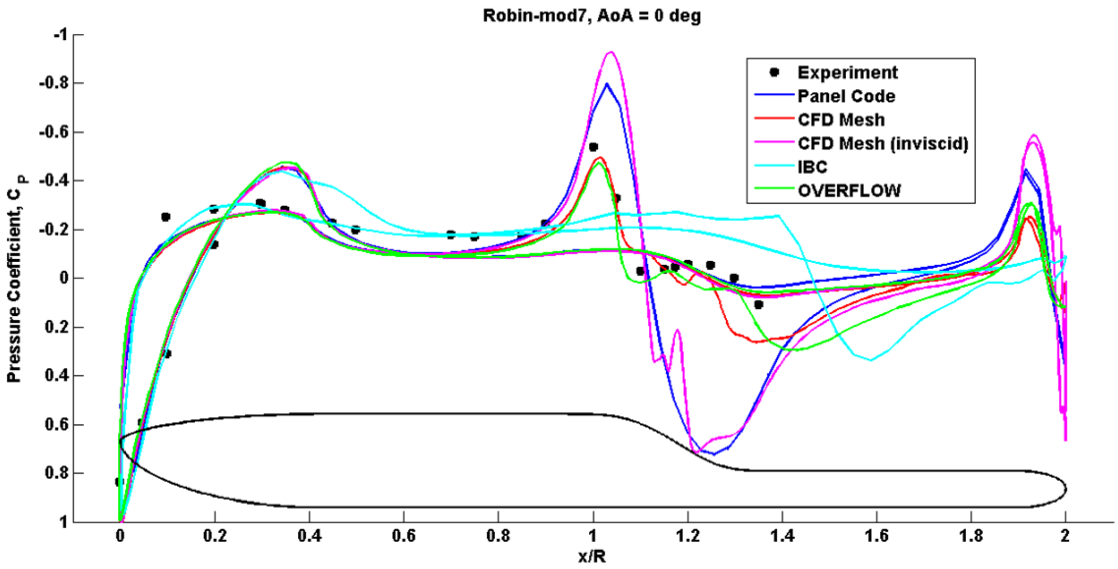

Figure 4.14: Surface pressure coefficient, upper and lower surface

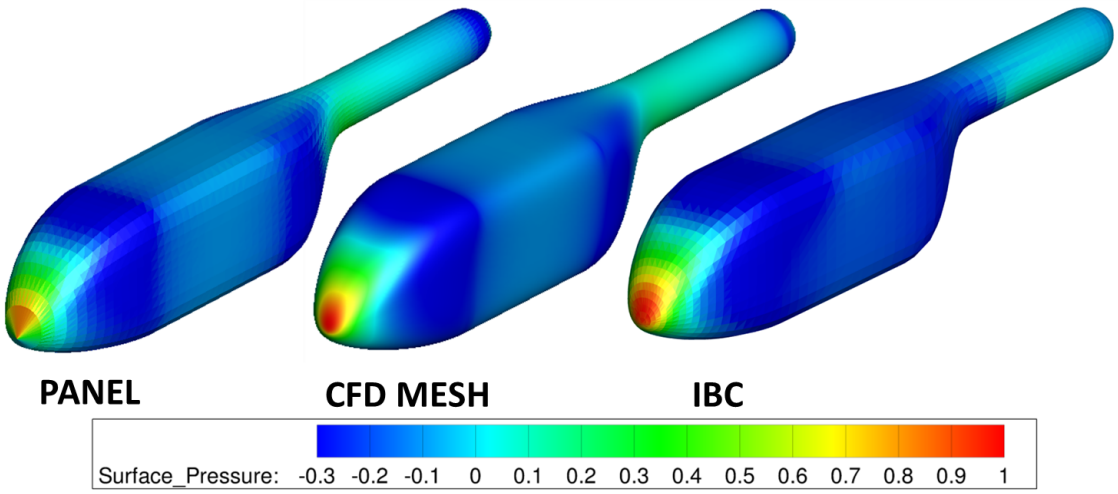

Figure 4.15: Robin-mod 7 surface Cp

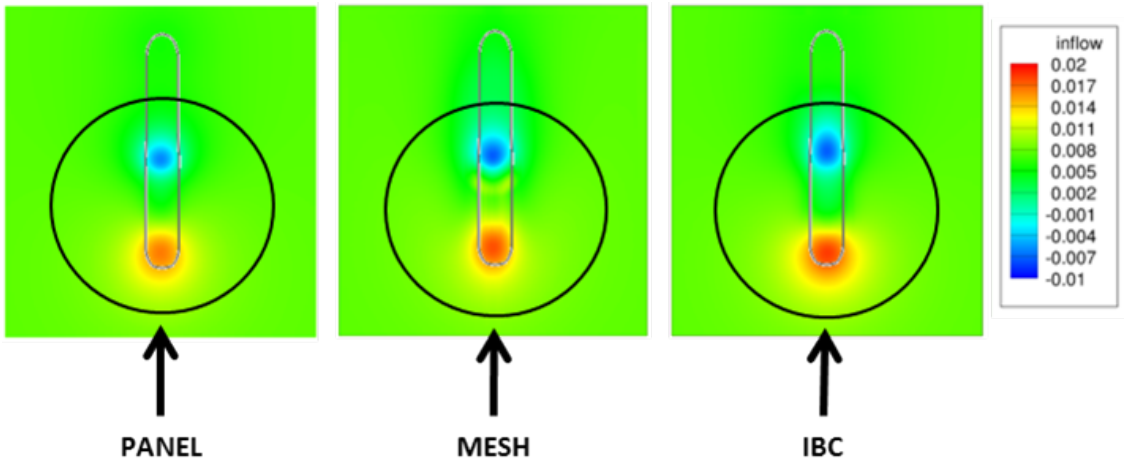

Figure 4.16: Inflow at rotor plane (Mach number), HART-II fuselage

done for the HART-II fuselage, which has a double ramp, upward then downward, on the upper surface. The expected effect is an upwash at the front of the fuselage where the flow is accelerated and pushed up, and similarly a downwash at the back ramp. Figure 4.16 does show this trend. All three methods match in magnitude and location of the upwash/downwash. The panel code predicts slightly lower inflow at the front, as indicated earlier. It should be noted that the free-stream inflow value is non-zero and upward because of the 4.5° angle of attack.

4.5 HART-II Simulation Results

To investigate the effect of a fuselage of a helicopter rotor, the three methods evoked above are applied to the HART-II baseline condition (BL, no HHC). Prescribed blade deflections and control angles were used instead of doing a fully coupled simulation in order to concentrate on the aerodynamic results (airloads, flow visualization). This was done to better understand the influence of the fuse-

lage and the difference between the different modeling techniques. These prescribed deflections were obtained by the HART-II AFDD team and were found to be very close to experimental data. It should be noted that the fuselage used in the wind tunnel experiments had a fairing around the hub that is not modeled by any of the method in this study. Therefore, further improvement in numerical correlation can be expected by taking this into account in future work.

4.5.1 Aerodynamic Loading at 87% Radius

As explained above, the fuselage creates an upwash at the front of the rotor and a downwash at the back. This should lead to higher and lower effective angles of attack respectively, which means that the normal force should be higher for azimuths around 180° and lower around 0°. Figure 4.17 compares the normal force coefficient with and without fuselage for both the wake coupling and the wake capturing approaches, at 87% span. It can be seen that the expected effect is achieved, leading to closer correlation with experimental data. The influence of the panel code is slightly lower, especially at the back of the rotor (around 0°). It is interesting to notice that the fuselage mesh and the IBC method predict almost identical loadings despite their approach to this problem being quite different and, as seen above, the flow physics not being modeled as well by the IBC method (fuselage boundary layer). In addition, the magnitude of the point of minimum lift at the front of the rotor is improved when using one of the fuselage models, compared to a simulation without fuselage model. The lower plot on Fig. 4.17 compares the three fuselage

models. It is difficult to compare the panel method to the other two because of the intrinsic differences of the wake coupling and wake capturing approaches. As will be seen in the next chapter, the wake coupling approach with Lifting-Line over-predicts the BVI events both on the advancing and retreating sides and does not capture the full peak to peak magnitude of the normal force at the front of the rotor. It should also be noted that the fuselage models do not influence the pitching moment predictions, as seen on Fig. 4.18.

A close-up view of the normal force coefficient on the advancing side (Fig. 4.19) displays another benefit of modeling the fuselage. The BVI peaks phasing is improved and appears closer to the experimental data, although this is not as pronounced for the panel method. Also, the effect on the BVI phasing is not as strong on the retreating side.

4.5.2 Flow Visualization

To observe the influence of the fuselage on the flow field, it is interesting to look at a centered longitudinal plane cutting across the fuselage. Fig. 4.20 shows vorticity magnitude contours and displays details of the wake system. It can be seen that the IBC method captures a thicker boundary layer at the upper surface of the fuselage. In addition, more separated flow is present behind the back ramp. This can be explained by the fact that, due to the coarse and non-body-conforming distribution of points used in the IBC based method, it does not capture the wall-bounded viscosity accurately and the flow fails to remain attached. Using the elliptic mesh

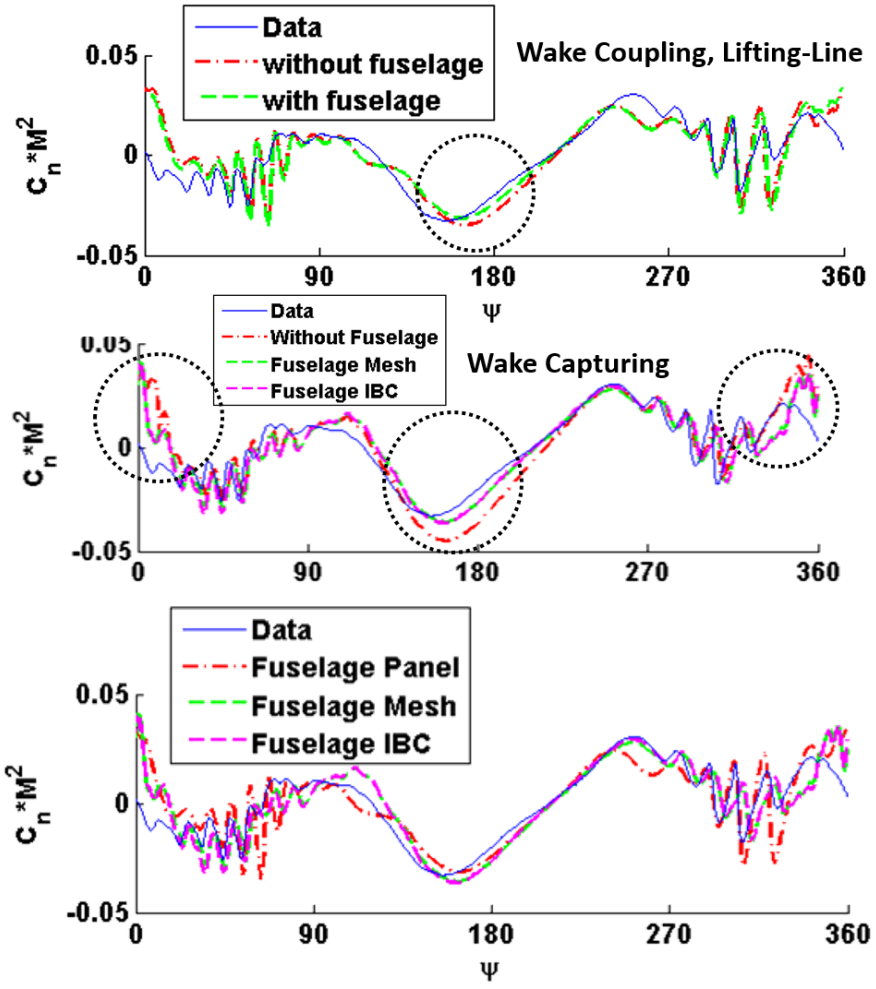

Figure 4.17: Normal force coefficient comparison, 87%R

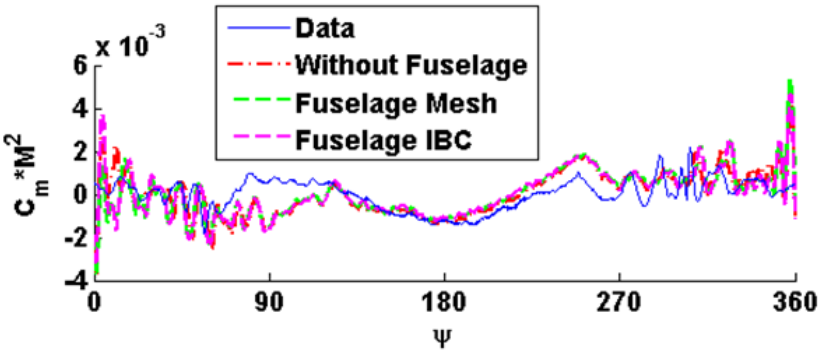

Figure 4.18: Pitching moment coefficient comparison, 87%R

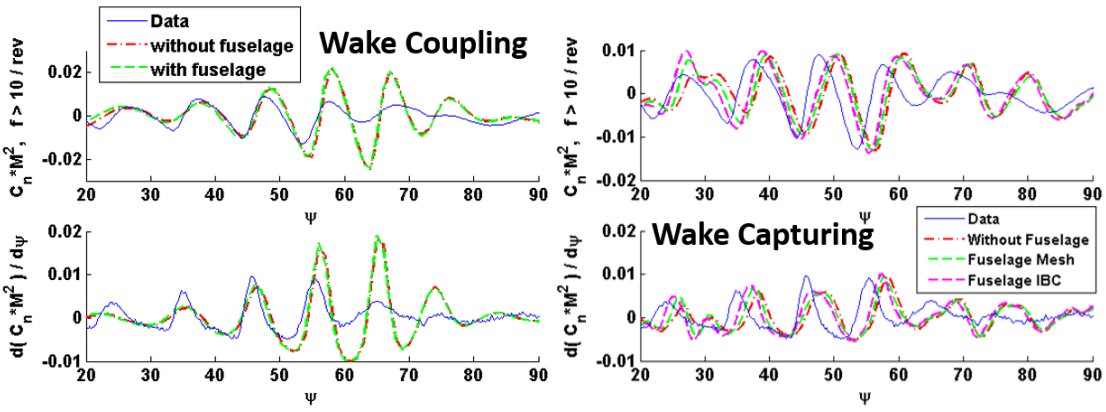

Figure 4.19: $C_l M^2$ filtered and derivative on advancing side, 87%R

refinement technique presented in previous sections, the local grid clustering around the fuselage surface does help reduce these undesirable effects, as seen in the last contour plot. Although the thickness of the boundary layer as greatly reduced, the amount of separated flow behind the fuselage is still excessive and, while promising, this method requires more development. Vortex positions at this center plane have been extracted for the different methods and plotted on Fig. 4.21. It can be seen that, as expected, the wake system is being pushed up at the front of the fuselage and down at the back, when using fuselage models. The root vortices, which are released close to the center of the fuselage, are only affected by the downwash. The limitation of the wake coupling approach (with lifting-line) is clearly displayed in these plots as the vortex system does not convect upwards sufficiently. The same trend had been pointed out in Ref. [4]. However, the panel method is able to influence the free-vortex filaments to an acceptable degree, although slightly less at the back of the fuselage. The HART-II experimental database contains flow visualization data. Vortex positions were captured using PIV on two longitudinal

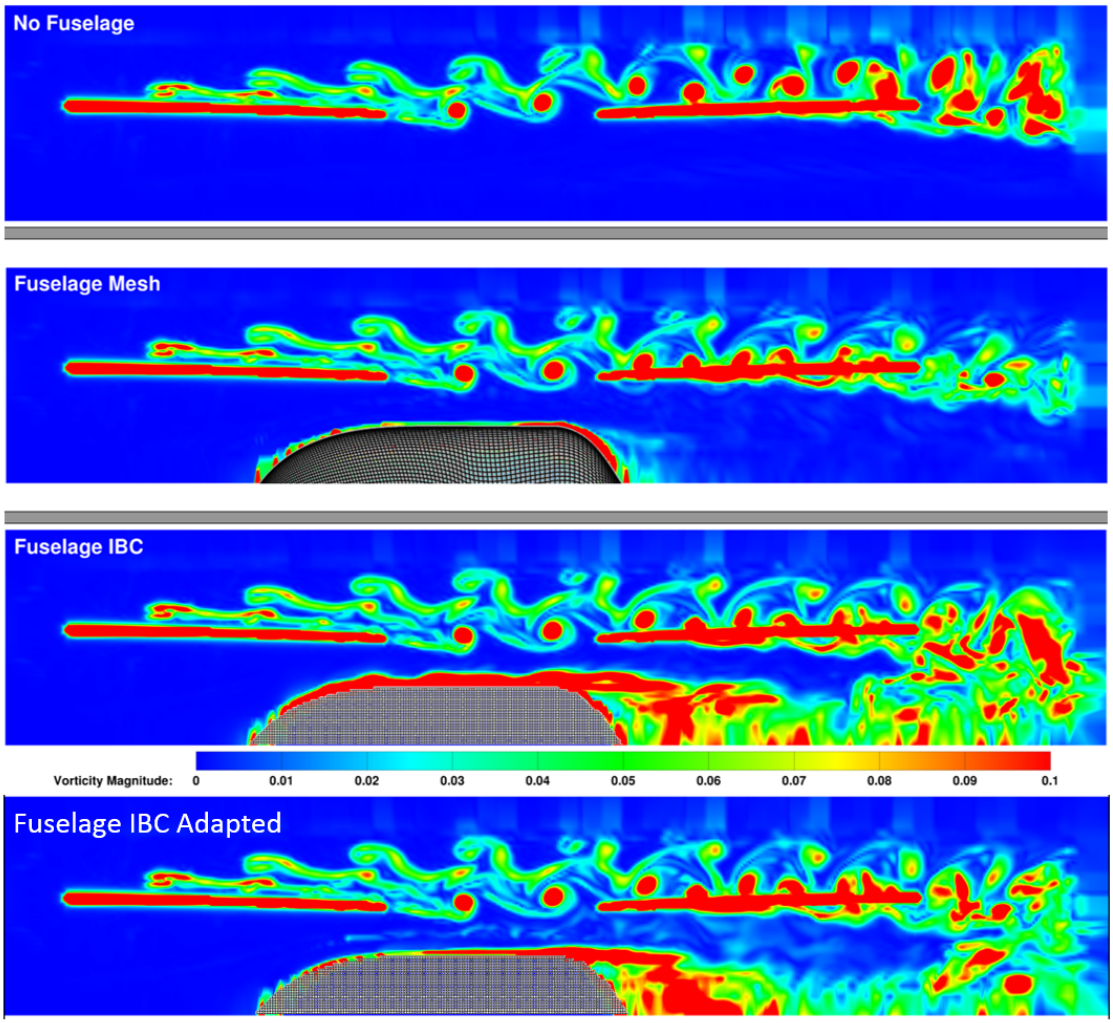

Figure 4.20: Effect of fuselage at center plane, vorticity magnitude, $\psi = 0\ ^\circ$

planes at $\pm 70\%$ radius. However, at these outboard stations, the effect of the fuselage is minimal and comparisons are not shown here. Finally, as noted above, the fairing around the hub that was used in the experimental setup was not modeled. It could potentially improve these results further.

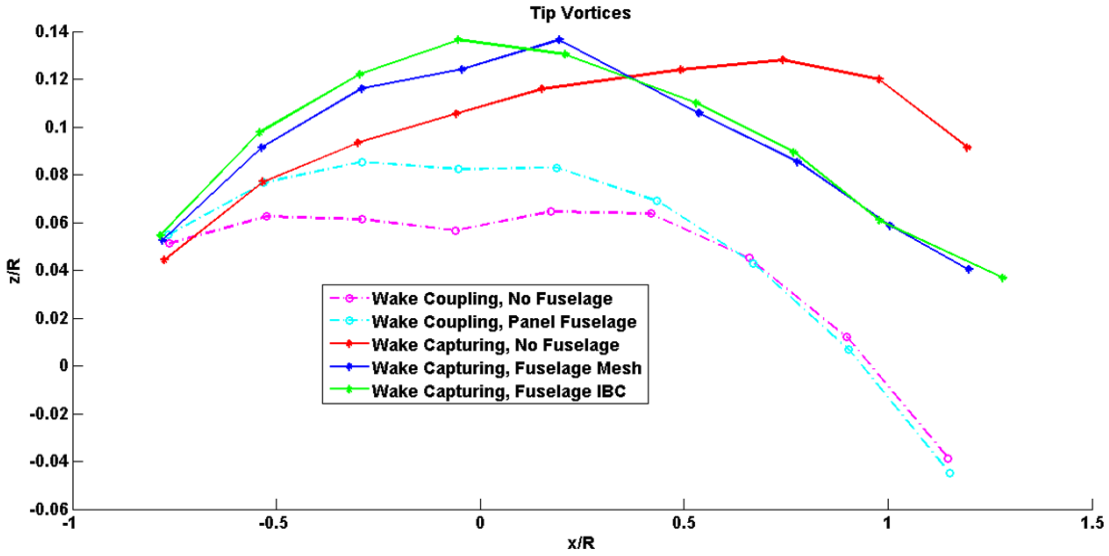

(a) Tip vortices

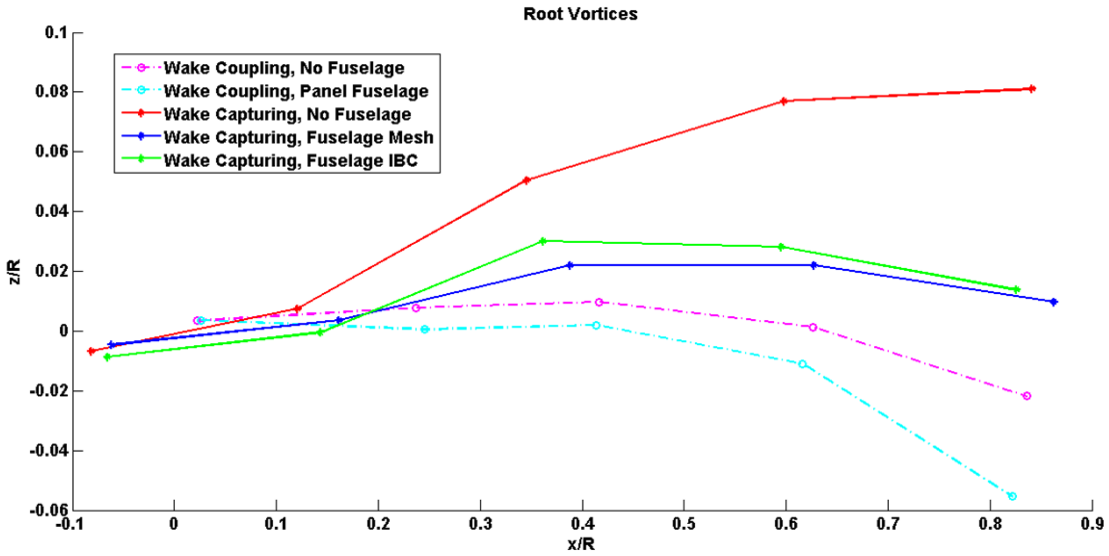

(b) Root vortices

Figure 4.21: Vortex position at center plane, $\psi = 0$ °

4.6 Summary

In this chapter, three fuselage modeling techniques were presented: a panel code, a body-fitted curvilinear CFD mesh, and an immersed boundary method. They are to be used in the multi-fidelity framework to improve solution accuracy by bringing the effect of a fuselage shape on the flow field. Each required specific algorithms to be developed. Validation and comparison with experimental data was also carried out for a simple fuselage geometry, the Robin mod-7 fuselage. Good correlation was found when using the body-fitted mesh and a viscous flow solver. However, limitations were shown for inviscid computations, although the overall effect on the rotor disk was found to be very comparable for all methods. The three techniques were then applied to the HART-II rotor to get a better understanding of the effect on blade vortices and blade airloads. Prescribed blade deflections were used to simplify the problem and number of varying parameters. The two methods used with the wake capturing approach gave significant improvements, both in terms of magnitude and phase of blade normal force. However, the effect modeled by the panel code was not as strong. In the next chapter, the numerical results presented all use a fuselage model: the panel code for both wake coupling approaches, and the

fuselage mesh for wake capturing.

Chapter 5

HART-II Numerical Simulations

In this chapter, numerical simulation results of the HART-II rotor are presented. The three methodologies introduced in previous chapters have been used and are compared here: wake coupling with lifting-line, wake coupling with RANS, wake capturing. In addition, the fuselage models detailed in the previous chapter are included: panel code for the wake coupling approaches, body-fitted fuselage mesh for wake capturing. The three HART-II flight conditions are shown: baseline, minimum noise, and the minimum vibration, which include 3/rev higher harmonic blade pitch control. Comparisons are made with the experimental measurements obtained during the wind tunnel test campaign. The data presented includes:

- Blade airloads mean values
- $C_n M^2$: normal force coefficients time histories, at 87% spanwise location, unfiltered, 10/rev filtered, time derivative, mean removed, with emphasis on the advancing and retreating sides.
- $C_m M^2$: pitching moment coefficients time histories, at 87% spanwise location, unfiltered, 10/rev filtered, time derivative, mean removed, with emphasis on the advancing and retreating sides.
- Blade tip flap deflection

- Blade tip lead-lag motion
- Blade tip torsion
- Rotor control angles: $theta_0$, $theta_{1C}$, $theta_{1S}$
- Structural flap bending moments
- Structural lag bending moments
- Structural torsion bending moments
- Structural pitch-link loads
- Wake geometry: vortex positions on longitudinal planes at $\pm 70\% R$
- Acoustic pressure at two microphone locations (advancing and retreating sides)
- Noise carpet on plane $1.1R$ below the rotor
- BVISPL minimum/maximum levels

5.1 Blade Airloads

Numerical predictions of normal force and pitching moment coefficients are presented here, along with experimental results, at the 87%R spanwise location. Unfiltered data, 10/rev filtered data, and time derivatives of the data are plotted. The unfiltered airloads are shown with their mean value removed. This allows for easier comparison of magnitude and phase of the low frequency content of the data from the different solver and experiments. The filtered data helps compare

higher frequency content and BVI loading predictions. The time derivatives relate to the sharpness of the BVI peaks and are a good indication of noise levels, as they are the driving factor in sound generation and propagation. The mean values of the airloads are plotted in Fig. 5.1 and show relatively good agreement with experimental data. The wake capturing method achieves slightly lower correlation, which could be explained by the reduced number of coupling cycle between CFD and CSD, due to its prohibitive cost. It should be noted that pitching moment mean values for the minimum noise and minimum vibration cases are further, but the experimental values are thought to be offset, as explained in Ref. [2].

Figure 5.2 presents $C_n M^2$ and $C_m M^2$ for the baseline case. It can be seen that all three methods capture the low frequency content of the normal force correctly, although only the RANS based approaches, especially wake capturing, manage to predict the full peak-to-peak magnitude near the front of the rotor disk. The lifting-line based method predicts a much higher value near 180 °. As was explained in the previous chapter, the phase of the lower peak near 180 ° is improved by including a fuselage model, but it is still lagging the experimental measurement. The pitching moments lower frequency content is well captured by both RANS methods, although wake coupling shows some over-prediction. Linearized aerodynamics does not pick up all low frequency variations but proves quite satisfactory in predicting higher frequency content, thanks to the hybrid Wagner-Kussner unsteady formulation used.

Figure 5.3 is a close up view on the advancing side of the rotor disk ($\psi = 0\ ^\circ to 90\ ^\circ$) and Fig.5.4 shows the retreating side ($\psi = 270\ ^\circ to 360\ ^\circ$), for the baseline case. The unfiltered data is shown along with the 10/rev filtered data and time

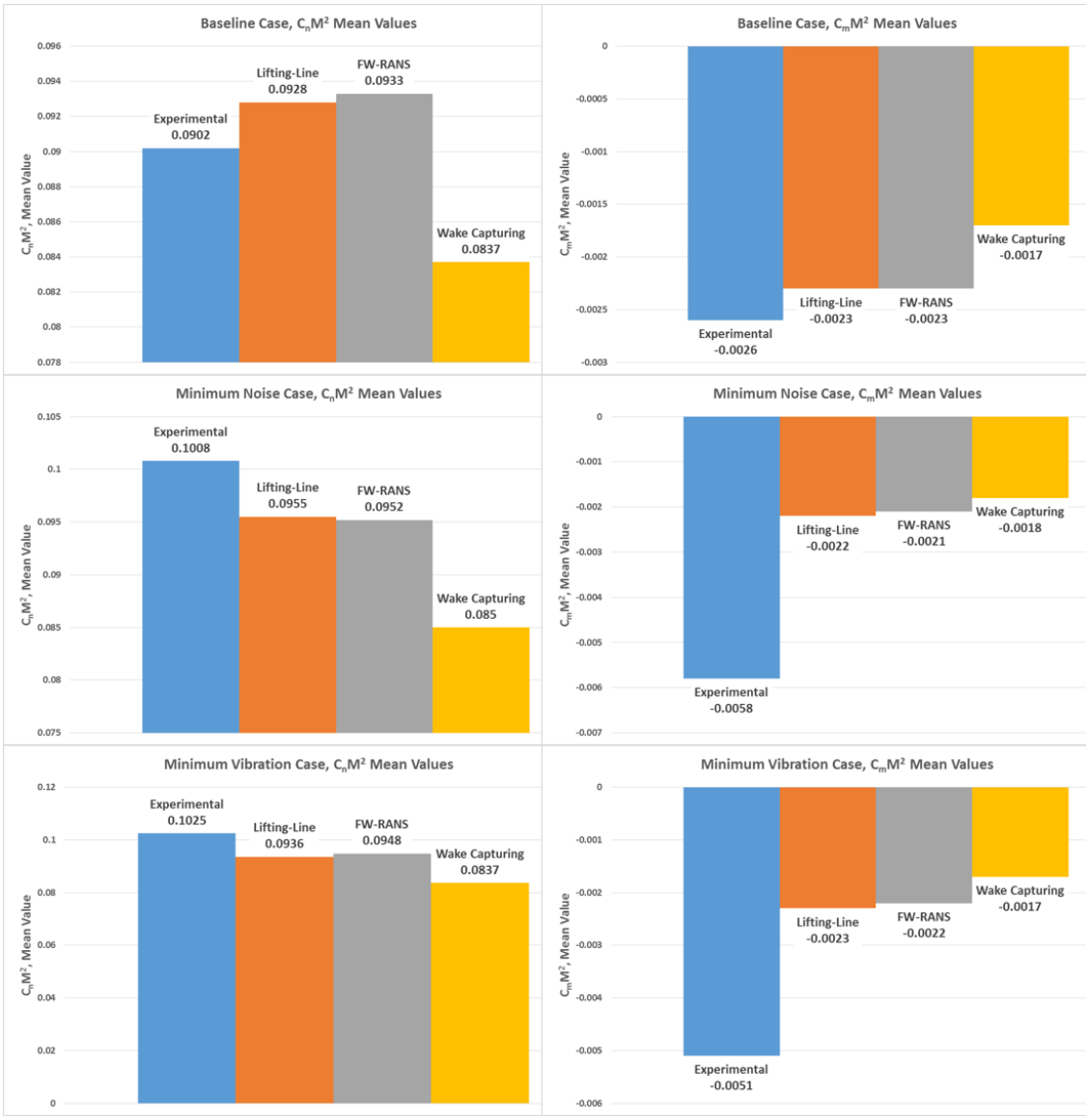

Figure 5.1: Mean values of C_nM^2 and C_mM^2 for the three HART-II cases.

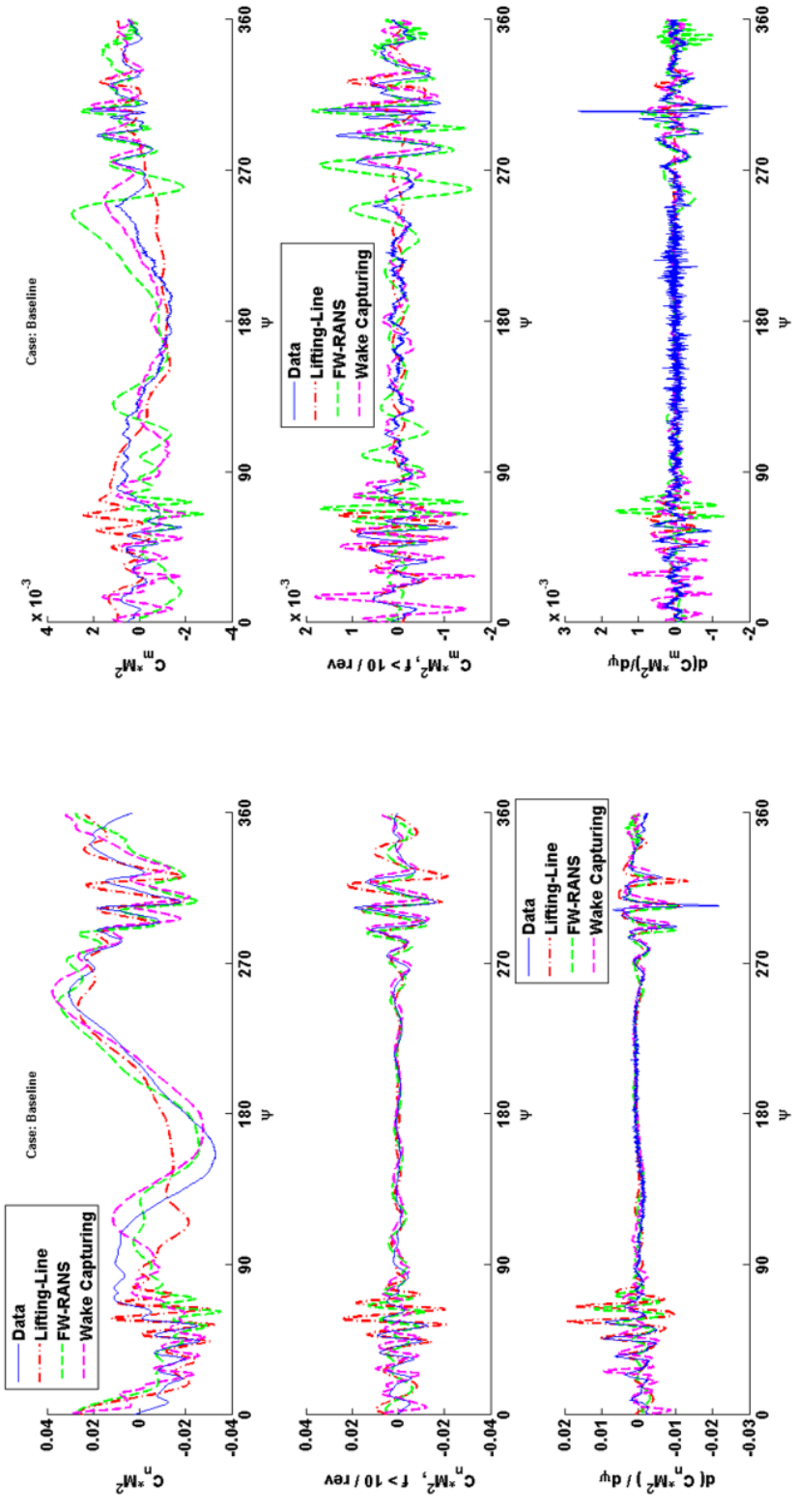

Figure 5.2: C_nM^2 and C_mM^2, Time History, Baseline Case.

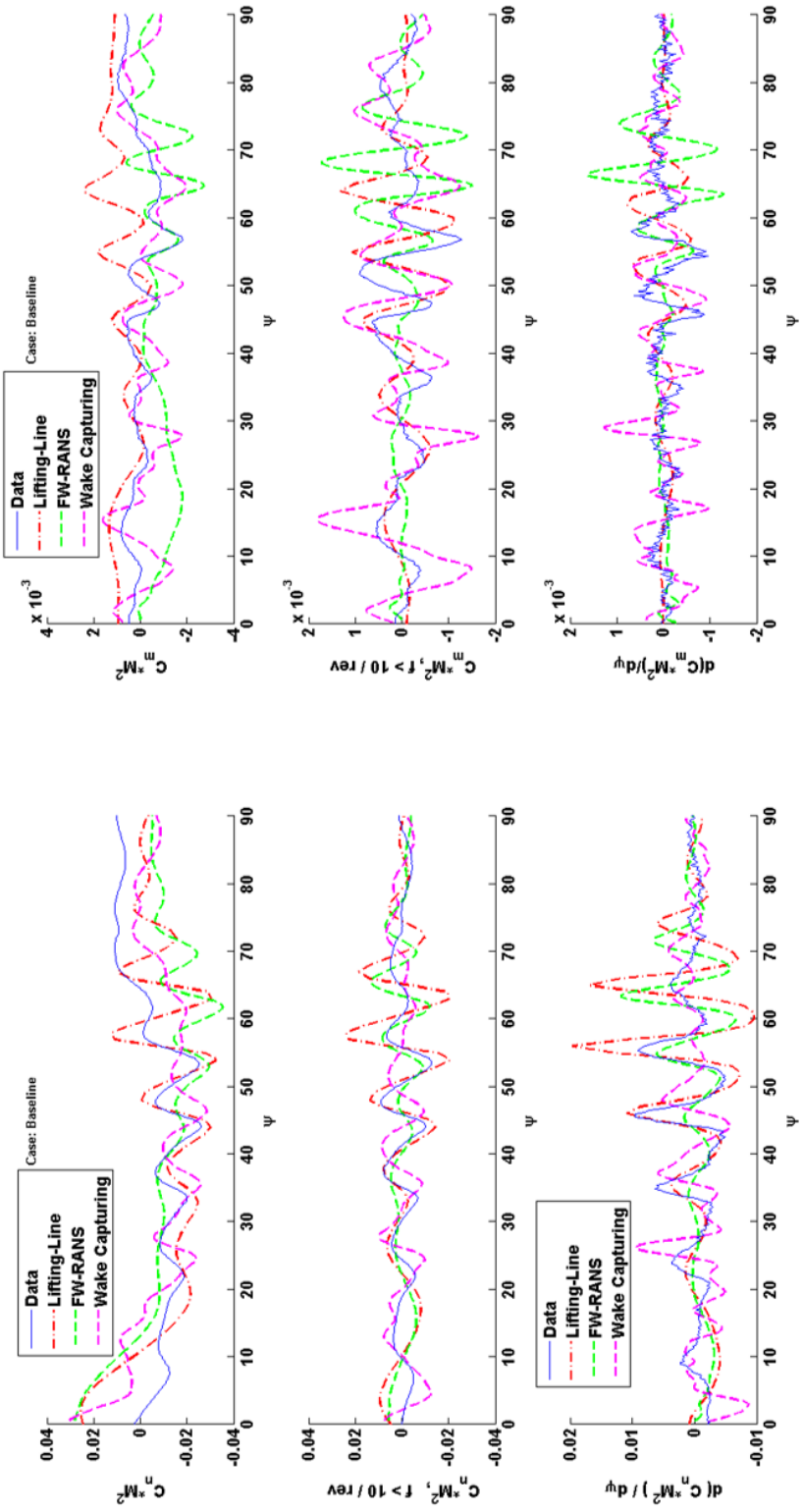

Figure 5.3: $C_n M^2$ and $C_m M^2$, Advancing Side, Baseline Case.

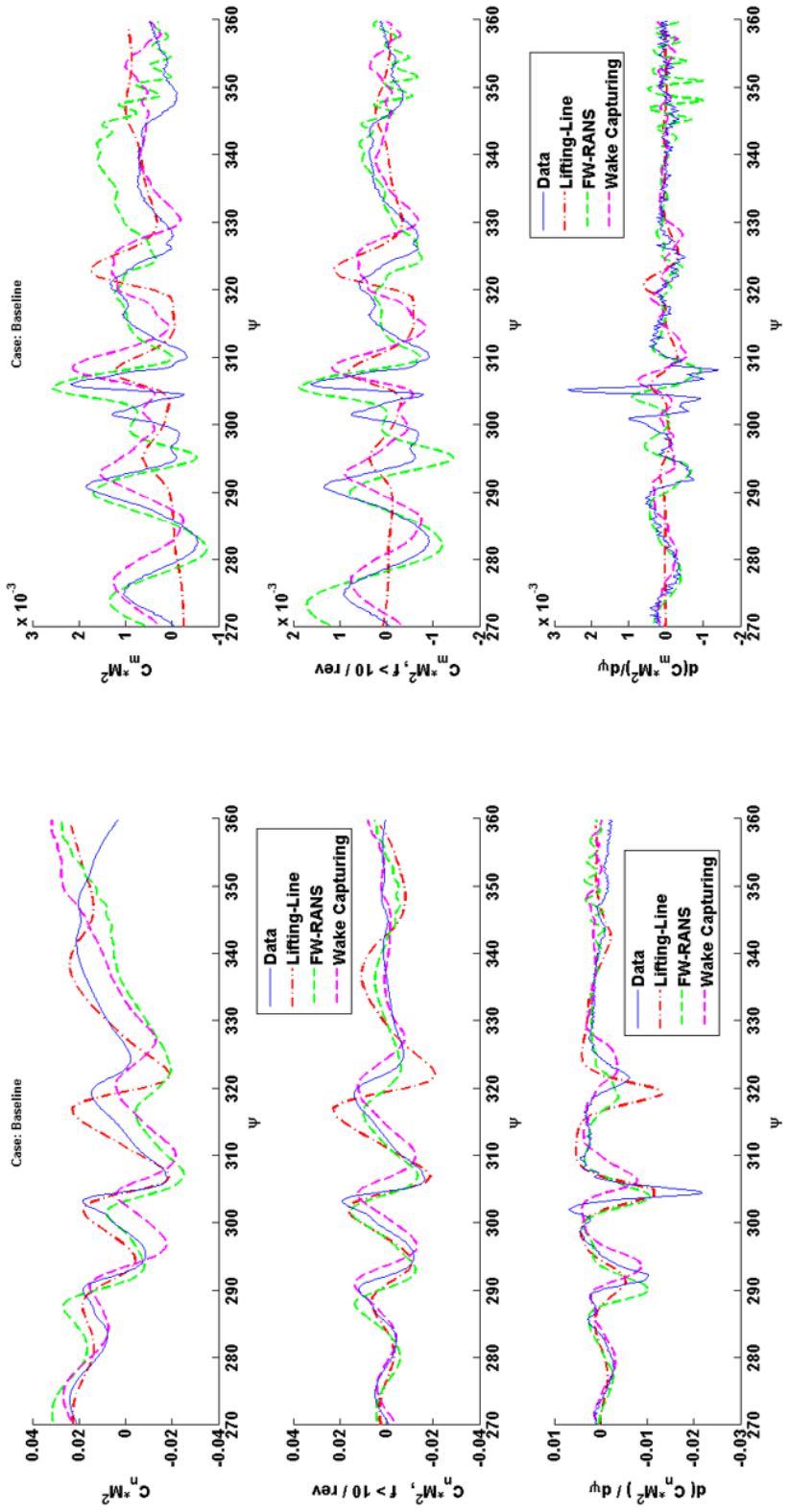

Figure 5.4: $C_n M^2$ and $C_m M^2$, Retreating Side, Baseline Case.

derivatives. It is known that the advancing side is generally more difficult to capture accurately than the retreating side, as the blades interact with older vortices that are more prone to being over-diffused and have wandered more. Here, the lifting-line approach clearly over-predicts the magnitude and sharpness of BVI peaks, although phasing appears quite good. As will be seen later, this has a negative effect on noise predictions. The free-wake/RANS method does a better job in terms of magnitude, but displays a tendency to shift the peak of highest magnitude to later azimuths, similarly to lifting-line. This can be explained by the lower vertical position of the filaments which lead to later interactions with the blades, as will be seen in the wake geometry comparison. Only the wake capturing method has the correct behavior, thanks to its more accurate wake model. However, the magnitude and phase of each peak is slightly off, indicating that the vortices might be over-diffused at the time of interaction. This suggests that a finer grid resolution might be necessary on the first level background mesh (going from 0.1c to 0.05c) to better preserve those structures. The pitching moments show more scatter. Both free-wake based approaches shows some over-prediction on the advancing side, although the use of more sub-iterations in the wake coupling approach made these levels acceptable.

As expected, on the retreating side, all three methods capture the magnitude, phase, and numbers of BVI events fairly well, both for normal force and pitching moment. The linearized aerodynamics based method tends to over-predicts the magnitude of the 3^{rd} BVI peak, giving it a higher and sharper value than the previous two peaks. All methods under-predict the 2^{nd} peak and wake capturing results shows slightly higher phase lag. The pitching moments are also better captured than on

the advancing side.

Figure 5.5, Fig 5.6, and Fig. 5.7 show the same data but for the minimum noise case. The strong 3/rev behavior due to HHC is clearly exposed here, and will also be seen in the structural deformations and moments (flap and torsion). All three methods capture the lower frequency content well for both normal force and pitching moment. The wake capturing method has a slight lag at the front of the rotor, despite using a better fuselage model. The lifting-line approach misses the full magnitude of the 2^{nd} high lift peak.

Looking at the higher frequency content, both on the advancing and retreating sides, it can be seen that, compared to the baseline case, the minimum noise case shows lesser and smaller BVI events and they are shifted upstream, near the 70 ° azimuthal location. This is due to the application of HHC and the effects explained in previous chapters. As will be seen, this results in lower levels of noise. All methods display this trend but are unable to capture the sharpness of the peak near 70 °. Again, lifting-line over-predicts the signal slightly while the other two methods show very comparable variations. The pitching moment predictions of the peaks due to BVI are difficult to judge. On the retreating side, similar comments can be made, with large overshoot and phase shift when using lifting-line. Wake capturing predicts the magnitude and phase quite well here.

Finally, the minimum vibration results are shown on Fig 5.8. The lower frequency content of normal force and pitching moment is slightly under-predicted by lifting-line, although the overall trend is well matched. On the advancing side (Fig. 5.9), only the wake capturing approach manages to show adequate phasing of

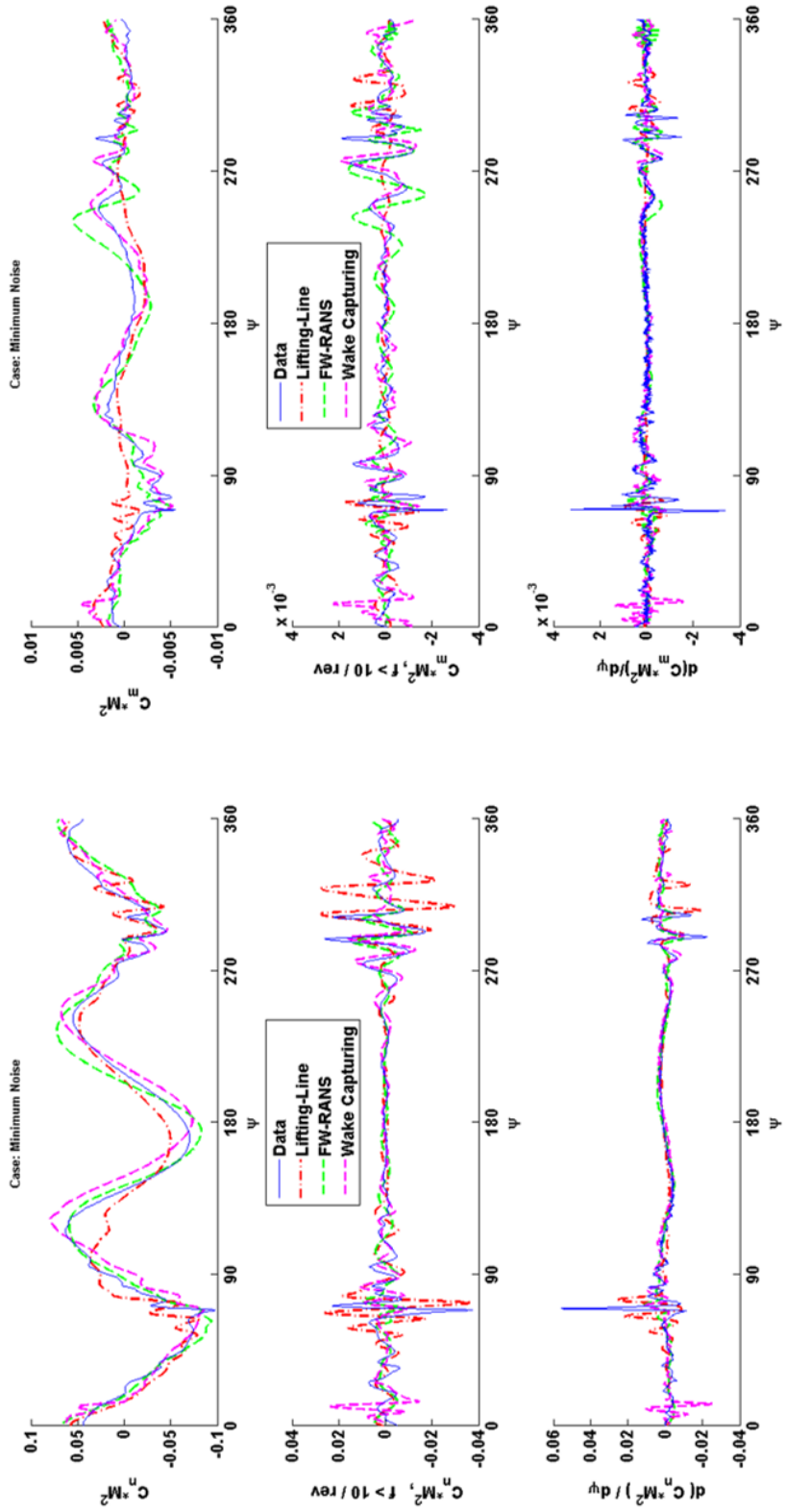

Figure 5.5: $C_n M^2$ and $C_m M^2$, Time History, Minimum Noise Case.

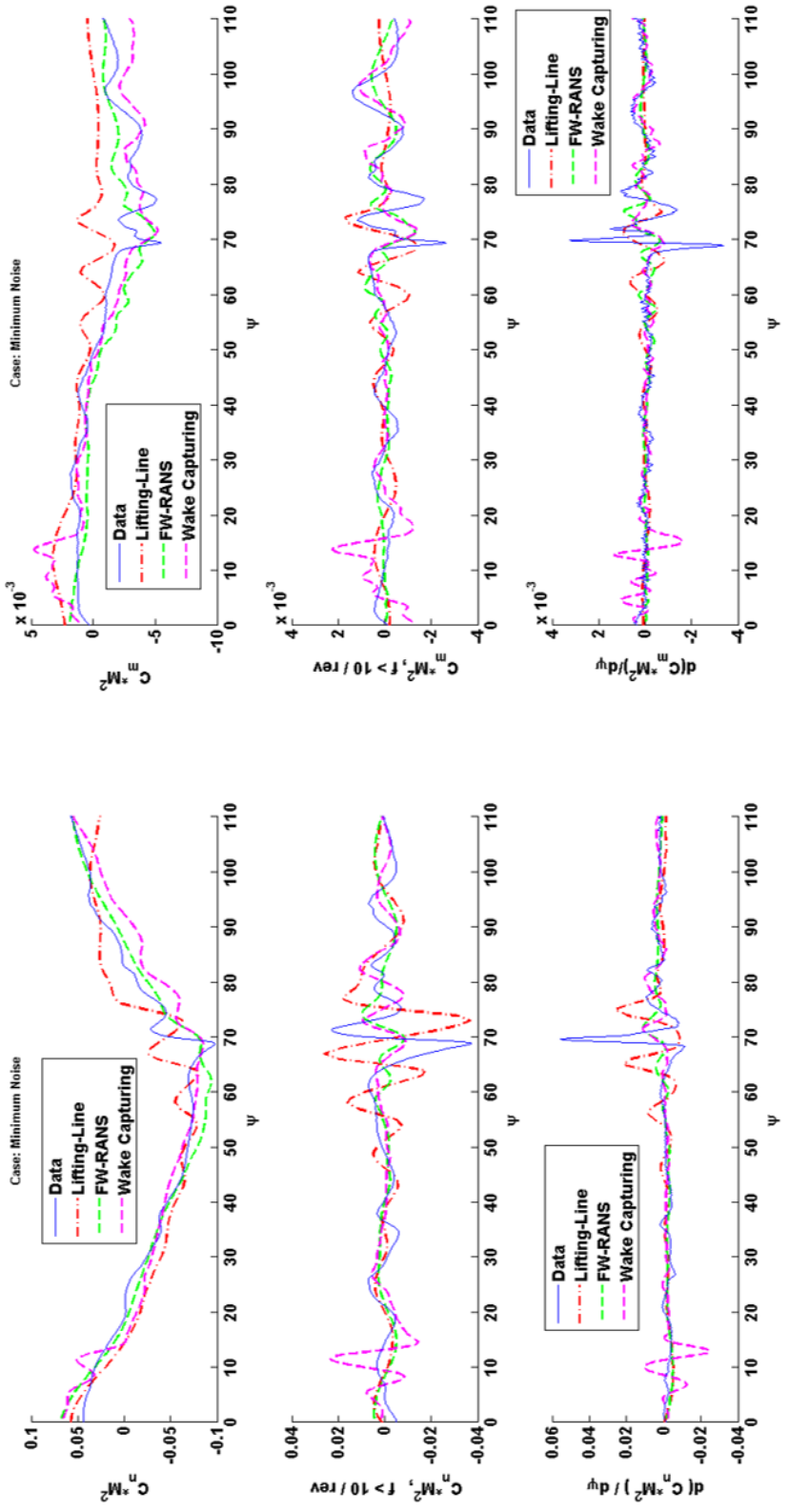

Figure 5.6: $C_n M^2$ and $C_m M^2$, Advancing Side, Minimum Noise Case.

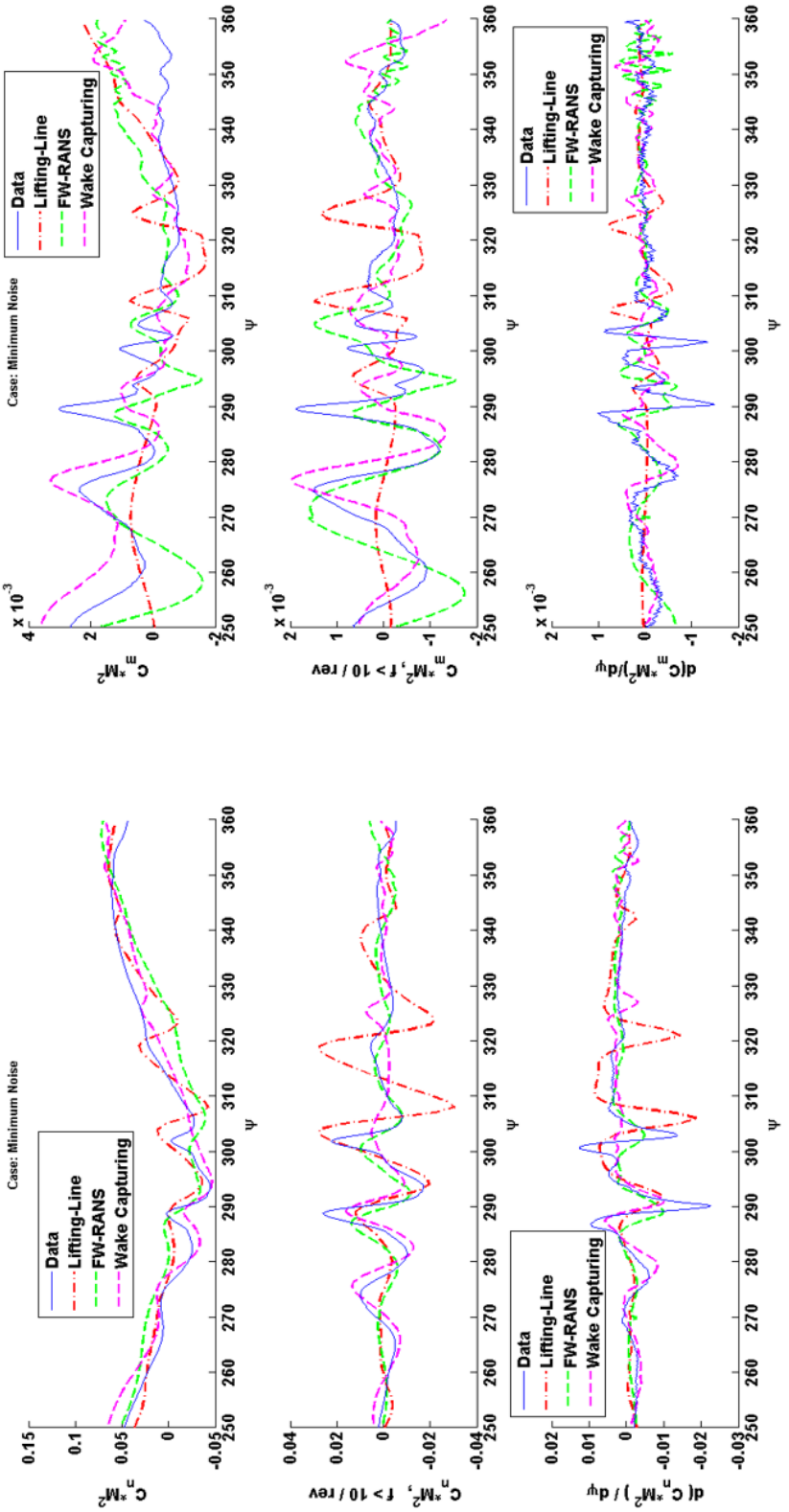

Figure 5.7: C_nM^2 and C_mM^2, Retreating Side, Minimum Noise Case.

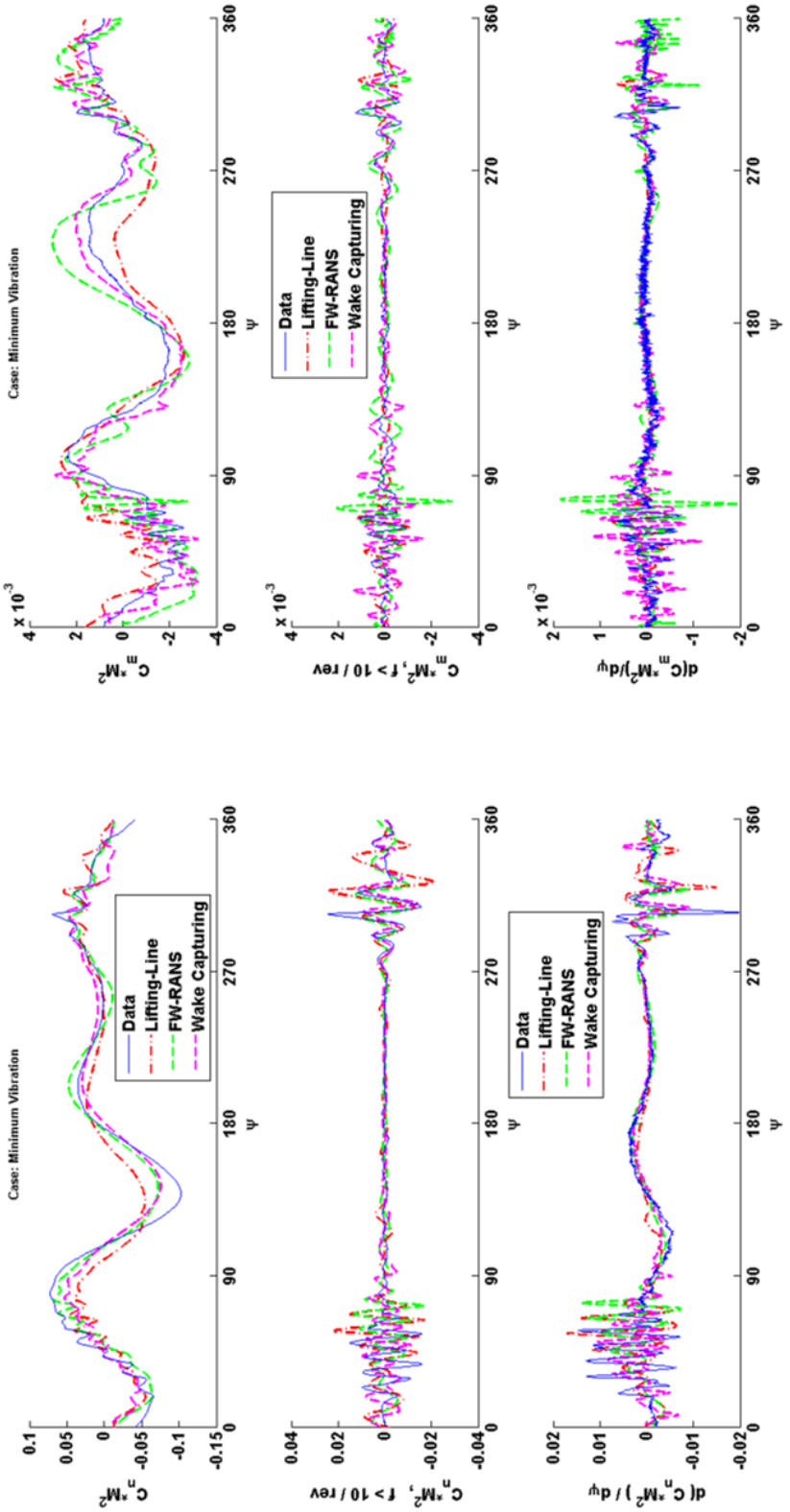

Figure 5.8: C_nM^2 and C_mM^2, Time History, Minimum Vibration Case.

the peaks, with some under-prediction in magnitude. Pitching moments are more scattered, with some over-prediction for wake coupling with RANS. On the retreating side (Fig. 5.10), good correlation is achieved, although all methods miss the 2^{nd} BVI peak on the normal force. The pitching moments are well matched. It is interesting to note that all methods seem to predict a 3^{rd} peak that is not present in the experimental data.

Overall, the lifting-line based approach had a tendency to over-predict BVI events, while clipping the peak-to-peak magnitude of the lower frequency content. But considering its much shorter run-time, its level of accuracy is very encouraging. The wake coupling approach usually showed the best level of correlation in terms of magnitude of BVI peaks. However, wake capturing proved to be the only method to accurately predict the phasing of BVI loading, although slight under-prediction was noticed, which could be resolved by a finer grid resolution.

To obtain further evidence of the differences seen so far between the three methods, and to gained a deeper understanding of the physical mechanisms involved in noise/vibration reduction through HHC, it is interesting to look at contours of time derivatives of normal force around the rotor disk. Figure 5.11 shows such contours for the three methods and the baseline case. What was seen at 87% span is confirmed on these plots: the lifting-line code predicts stronger oscillations of $\frac{dC_nM^2}{dt}$ and wake capturing lower levels, both on the advancing and retreating sides. It is interesting to note that the effect of root vortices appears in the wake capturing results at the back of the rotor. Figure 5.12 presents the same data for the minimum noise case. Although the trend between the methods remains the

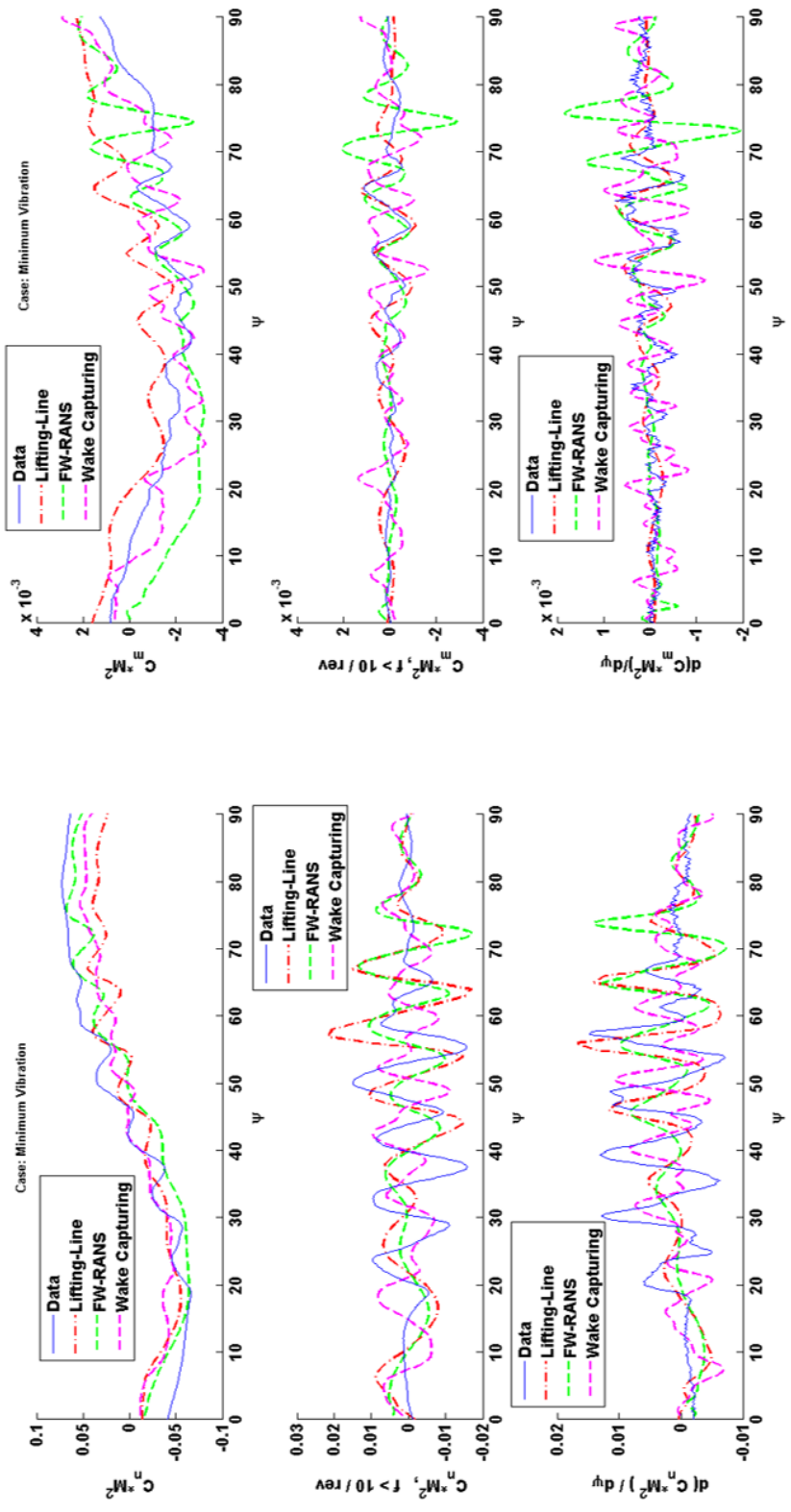

Figure 5.9: C_nM^2 and C_mM^2, Advancing Side, Minimum Vibration Case.

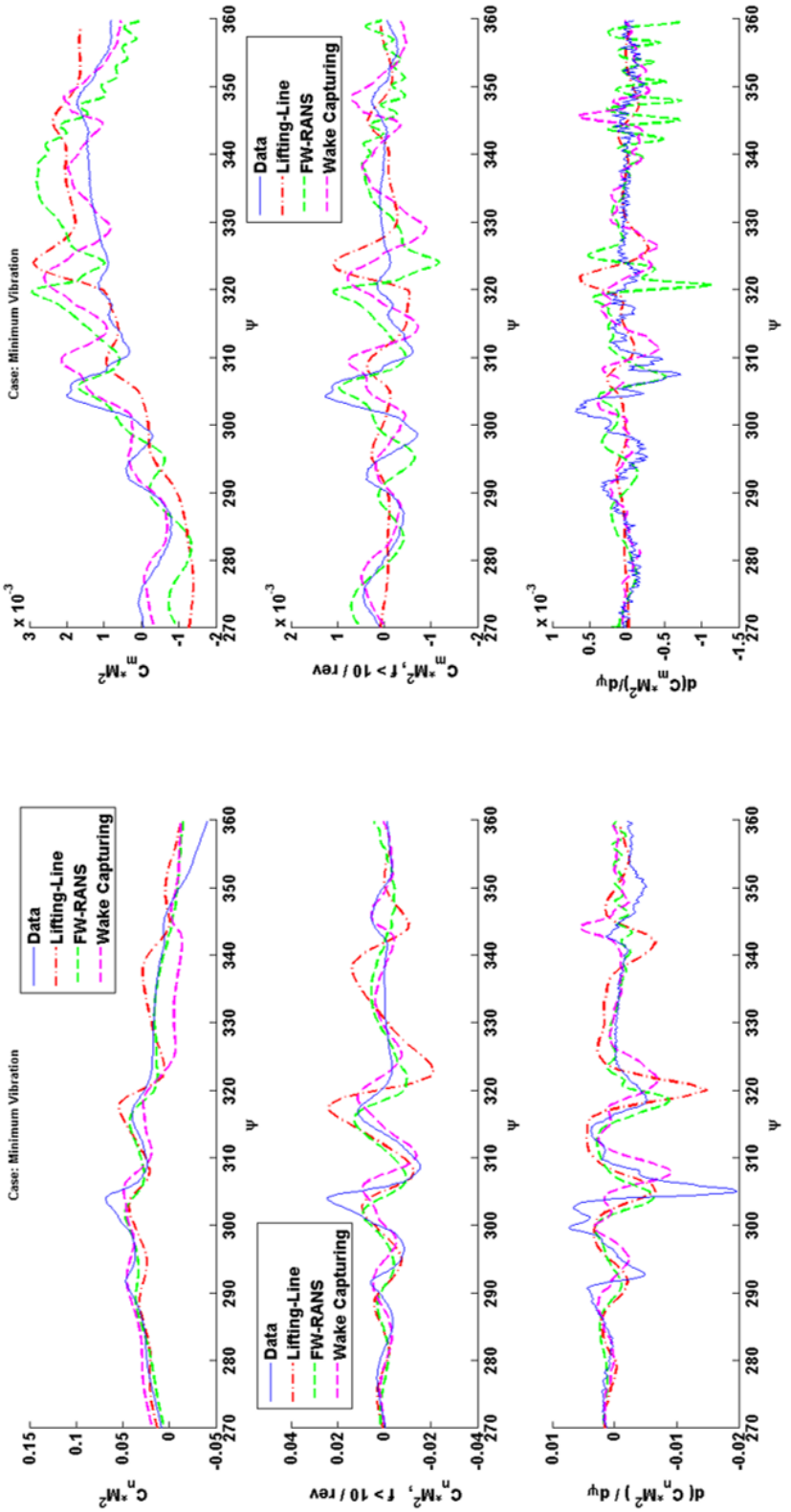

Figure 5.10: C_nM^2 and C_mM^2, Retreating Side, Minimum Vibration Case.

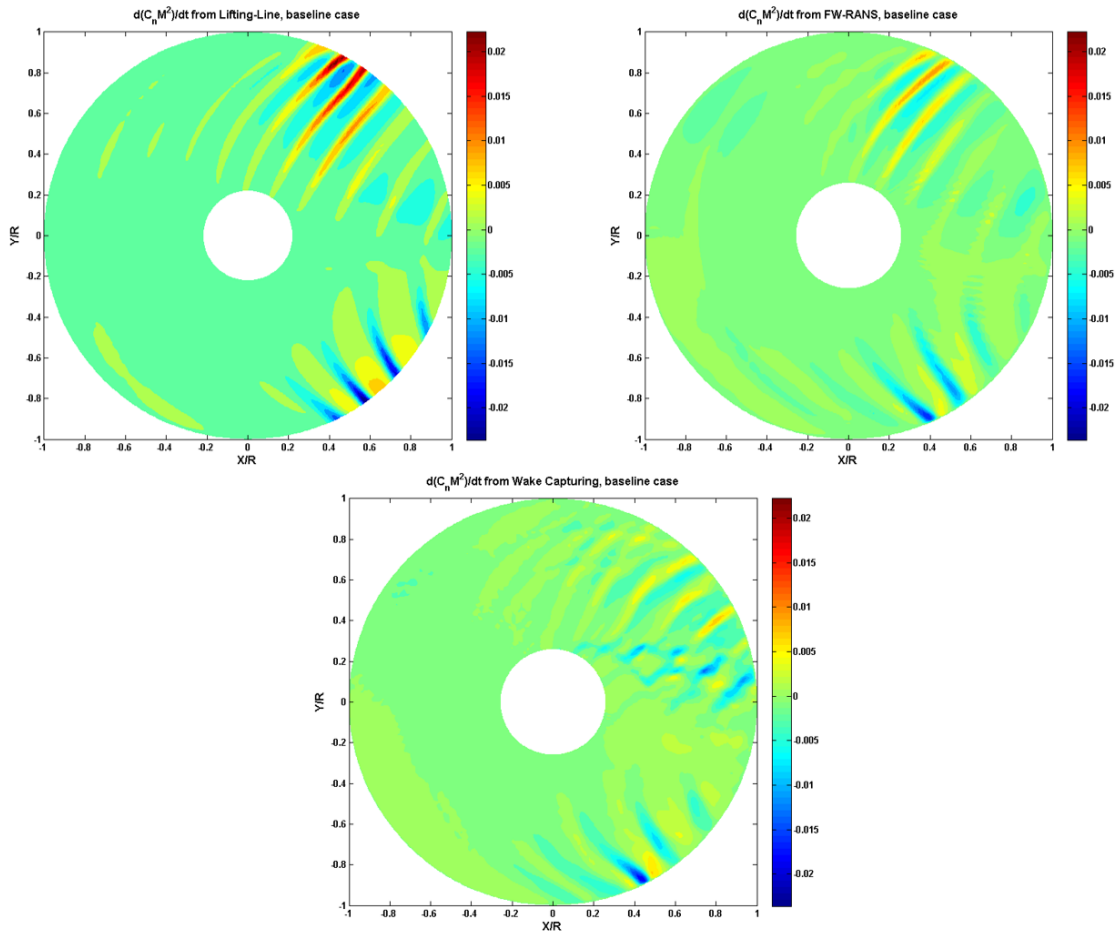

Figure 5.11: Contours of normal force time derivative, comparison between solvers, baseline case.

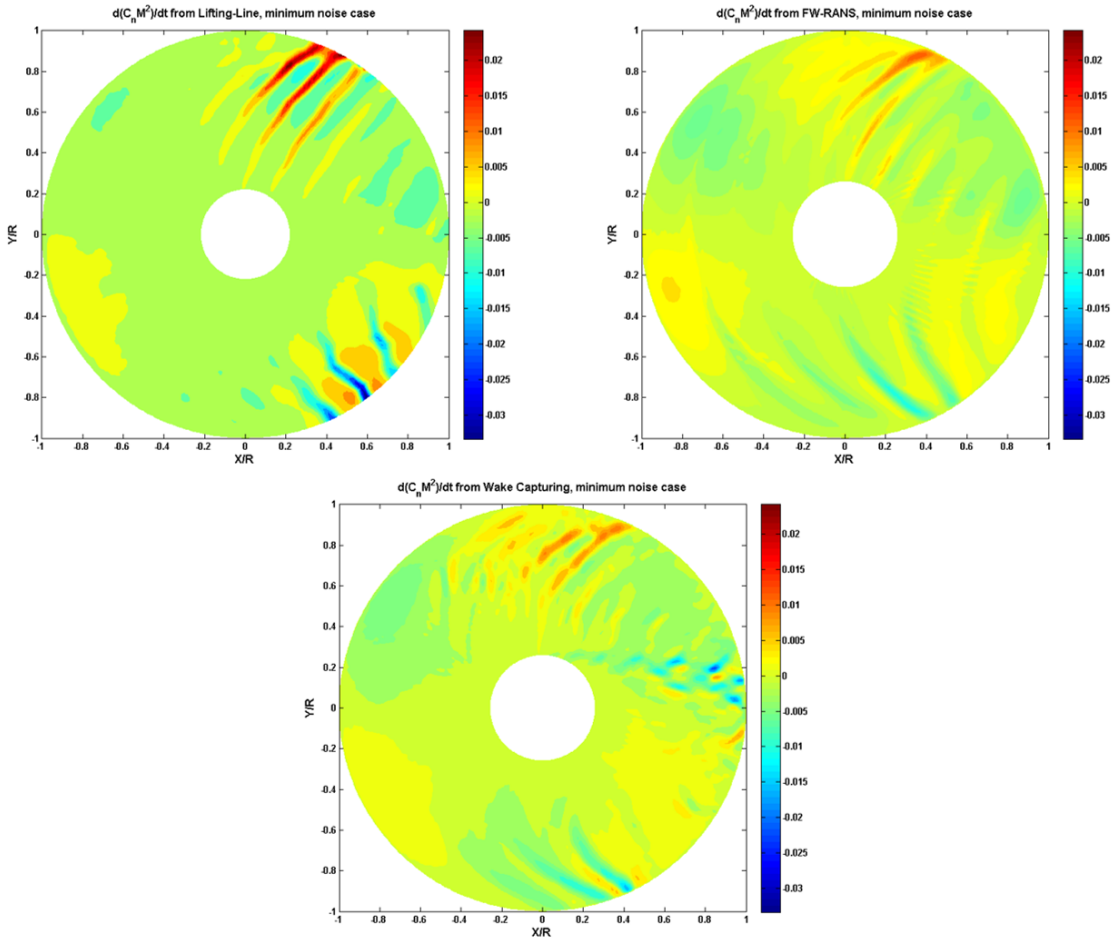

Figure 5.12: Contours of normal force time derivative, comparison between solvers, minimum noise case.

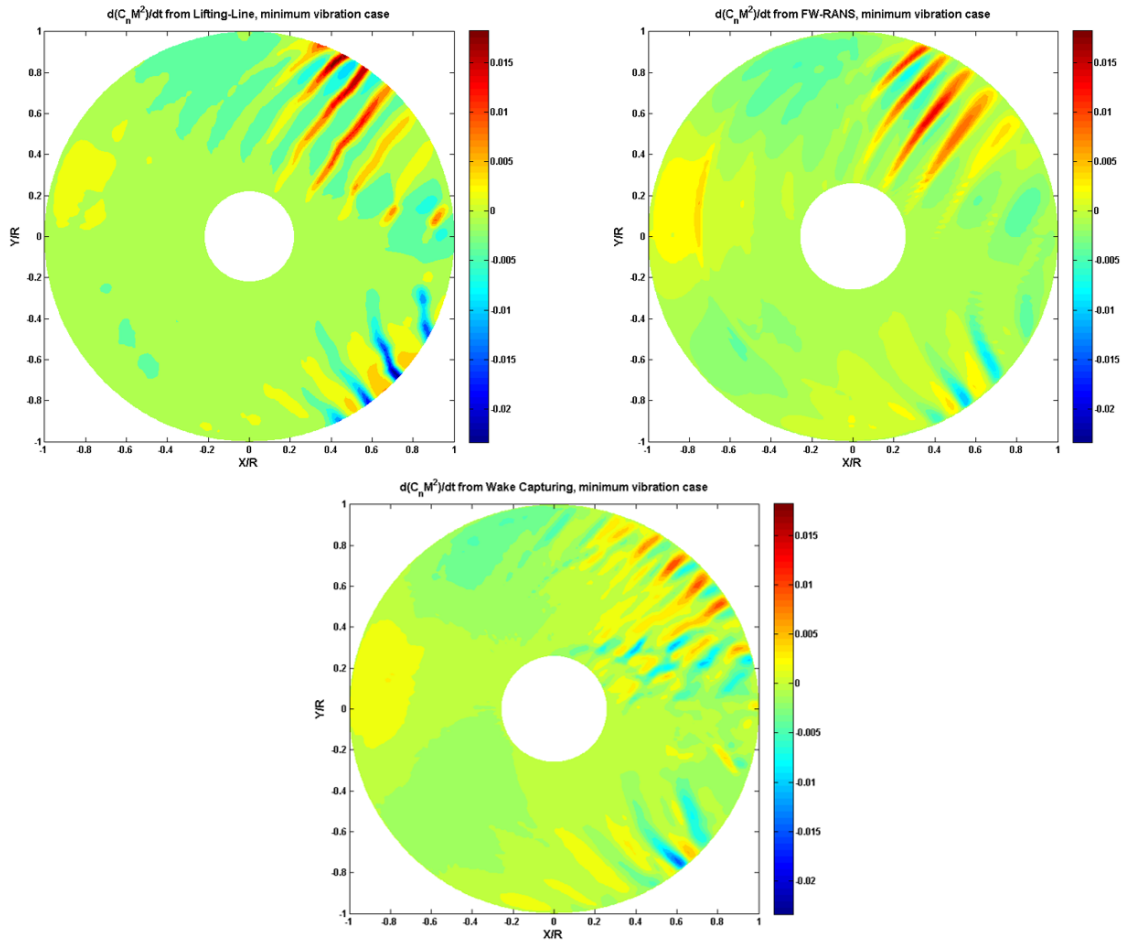

Figure 5.13: Contours of normal force time derivative, comparison between solvers, minimum vibration case.

same, the differences between BL and MN are more apparent. As was explained in earlier chapters, HHC in MN configuration has the effect of shifting the BVI events upstream compared to the baseline case. This effect is very well captured by wake capturing. On the other hand, MV HHC creates more BVI events in the first quadrant, as seen in Fig. 5.13.

5.2 Blade Elastic Motion

The second set of results shown here are the blade tip deflections. This includes elastic flapping, lead-lag, and torsion deformations predicted by the structural solvers. Figure 5.14 presents these blade displacements for the different methods versus experimental data. Error bands show the extent of scatter between blades as measured in the wind tunnel. It should be noted that flapping motion is plotted without precone, lead-lag motion is shown with mean removed, as the experimental mean levels are thought to be offset, and torsion is plotted without pitch due to control angles, higher-harmonic control, and linear built-in blade twist.

First looking at the flap motion, it can be seen that both free-wake based methods under-predict the flapping displacement (negative) at the front of the rotor, while the wake capturing approach is close to the experimental data. This trend is found for the three HART-II conditions. Some 3/rev content is seen for the the minimum noise and minimum vibration cases, as torsion and flap motions are coupled. The lead-lag deflection is well predicted by all methods, although the linearized aerodynamics approach displays a slight phase shift of the peak, which is thought to be due to the lack of unsteady modeling of the rotor drag. Finally, the elastic twist predictions are acceptable for all methods and cases. In the baseline case, it is interesting to notice that an additional oscillation is predicted by both RANS-based methods, on the advancing side. For the MN and MV cases, the strong 3/rev elastic pitching motion can be observed. Both RANS-based methods are capturing the peak-to-peak magnitudes correctly but the linearized aerodynamics method often

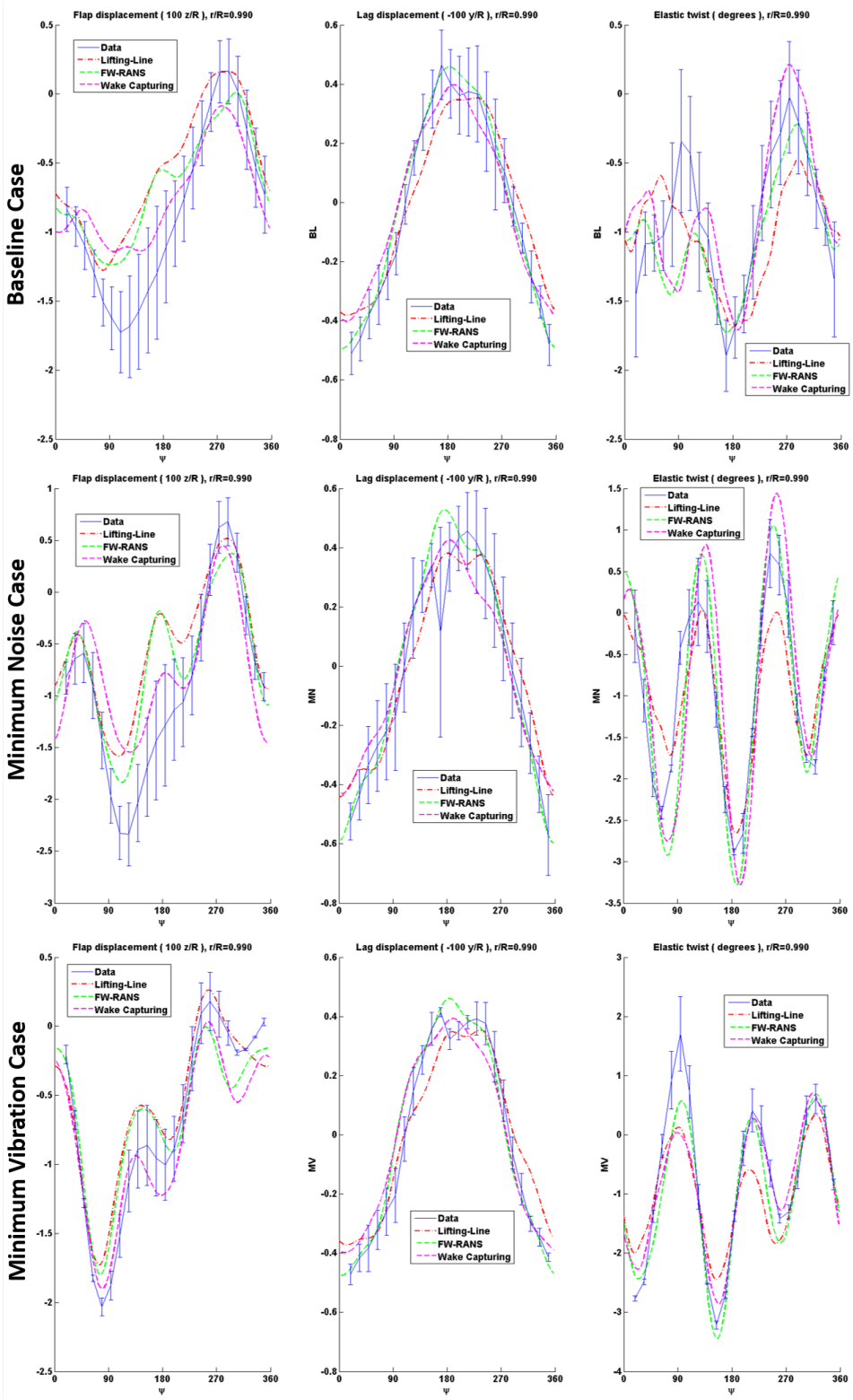

Figure 5.14: Blade elastic flap, lead-lag, and torsion displacements.

under-predicts these oscillations. Overall, the wake capturing approach gives the best levels of correlation with the experimental data, especially on flap, which is quite important for BVI predictions as seen in previous chapters. The other two methods also give very reasonable results, as higher frequency loading has little impact on the structural behavior of rotor blades.

5.3 Rotor Trim

Control angles (θ_0, θ_{1C}, θ_{1S}) obtained by performing rotor trim in the structural solver are plotted in Fig. 5.15 for all three cases. It can be seen that the wake coupling approach gives better predictions than the other two methods, although the offset is usually less than 0.5 °. The longitudinal cyclic pitch (θ_{1S}) is slightly under-estimated by both RANS-based methods, as was noticed in Ref. [2], while it is over-predicted by the linearized aerodynamics. The lower correlation of the wake capturing approach could be explained by the lower number of coupling cycles performed between CFD and CSD, due to the higher computational cost of this method.

5.4 Blade Structural Moments

Blade structural bending moments have proven difficult to accurately predict as a large scatter was observed in Ref. [2] and Ref. [3] between different state-of-the-art structural solvers. In the present work, a force summation method was used in the CSD solver. This algorithm has often lead to higher levels of accuracy

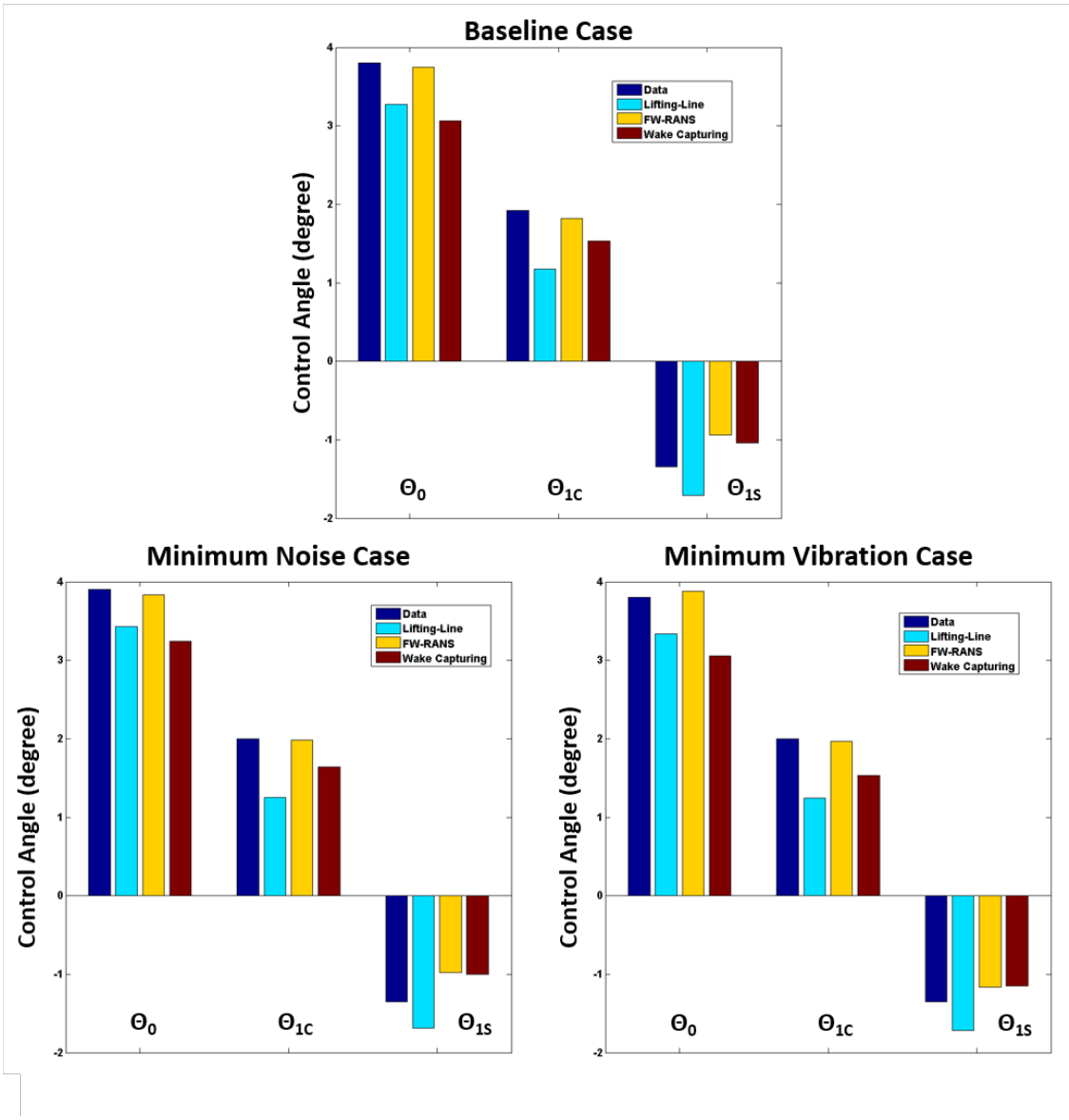

Figure 5.15: Trimmed control angles (θ_0, θ_{1C}, θ_{1S}) for the three cases.

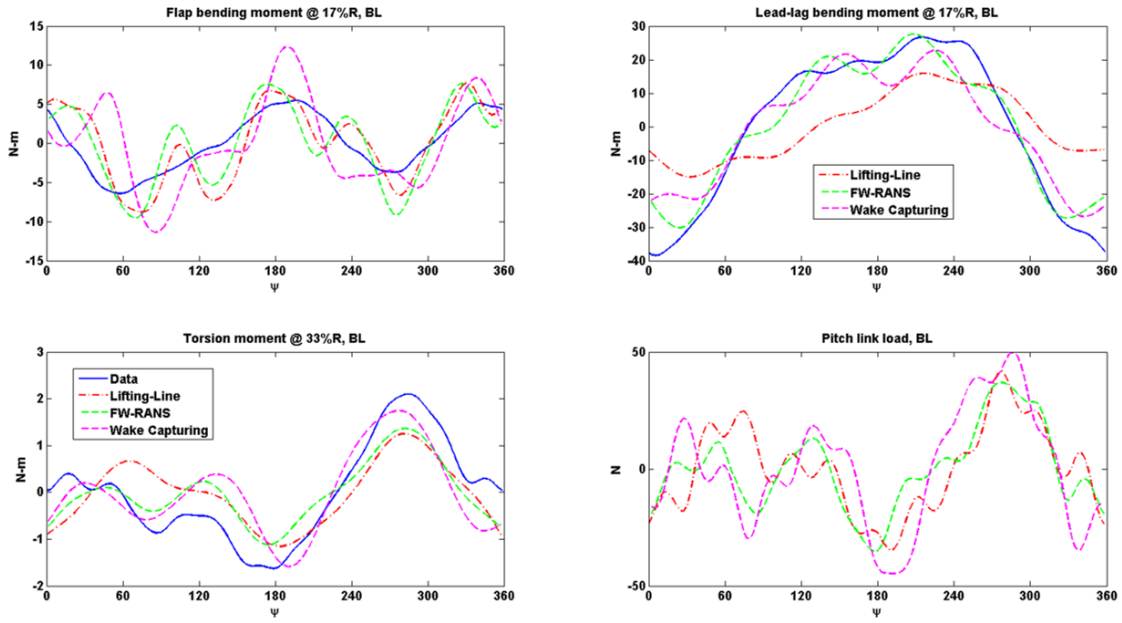

Figure 5.16: Blade structural bending moments, Baseline Case.

than a modal approach. Shown in Fig. 5.16 are the bending moments in flap at 17%R, lag at 17%R, and torsion at 33%R for the baseline case. All methods tend to predict higher frequency content, around 5/rev, that was only very mildly picked up in the wind tunnel experiments. However, the low frequency content obtained are satisfactory in flap, lag, and torsion, where the correct trend are predicted. The lag bending moment of the linearized aerodynamics method is slightly offset in phase, similarly to what was seen in the tip lead-lag results. The last plot shows pitch-link loads, although no experimental data is available. Relatively good agreement is found between the three methods, with some scatter in higher frequency content.

Figure 5.17 shows the same data for the minimum vibration case. There, flap bending moments seem over-predicted, especially by the RANS-based methods. Lifting-line under-predicts lag bending, torsional moments, and pitch-link loading as the 3/rev peak-to-peak magnitude is only completely captured by wake capturing.

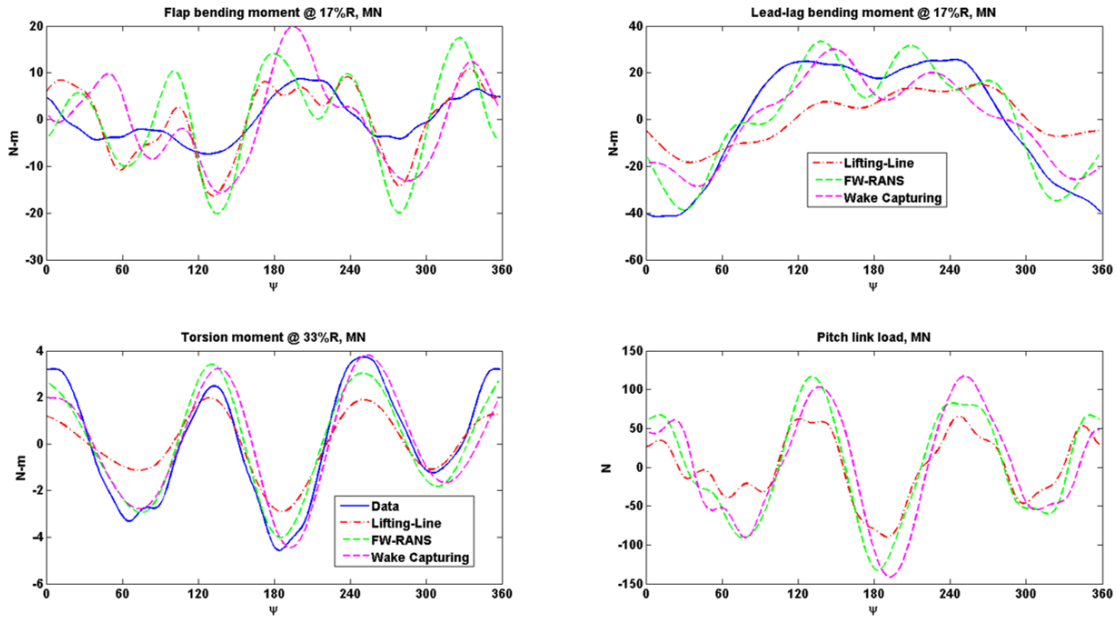

Figure 5.17: Blade structural bending moments, Minimum Noise Case.

Similar conclusions can be made about the minimum vibration results, as seen in Fig. 5.18.

5.5 Wake Geometry

As was explained before, the wake geometry is a key factor in rotorcraft BVI. Comparisons of vortex trajectories are made here. Experimental vortex center locations are known in two lateral planes on the advancing and retreating sides of the rotor at ±70%R, as shown in Fig. 5.19 for the wake capturing approach. This data was obtained from PIV measurements with the reference blade at two azimuthal locations: 20 ° and 70 ° . Predictions at those two planes using all three methods are compared in Fig. 5.20 for the Baseline case, Fig. 5.21 for the Minimum Noise case, and Fig. 5.22 for the Minimum Vibration case. It can be seen that the wake capturing method is the closest to the experimental data, although the wake cou-

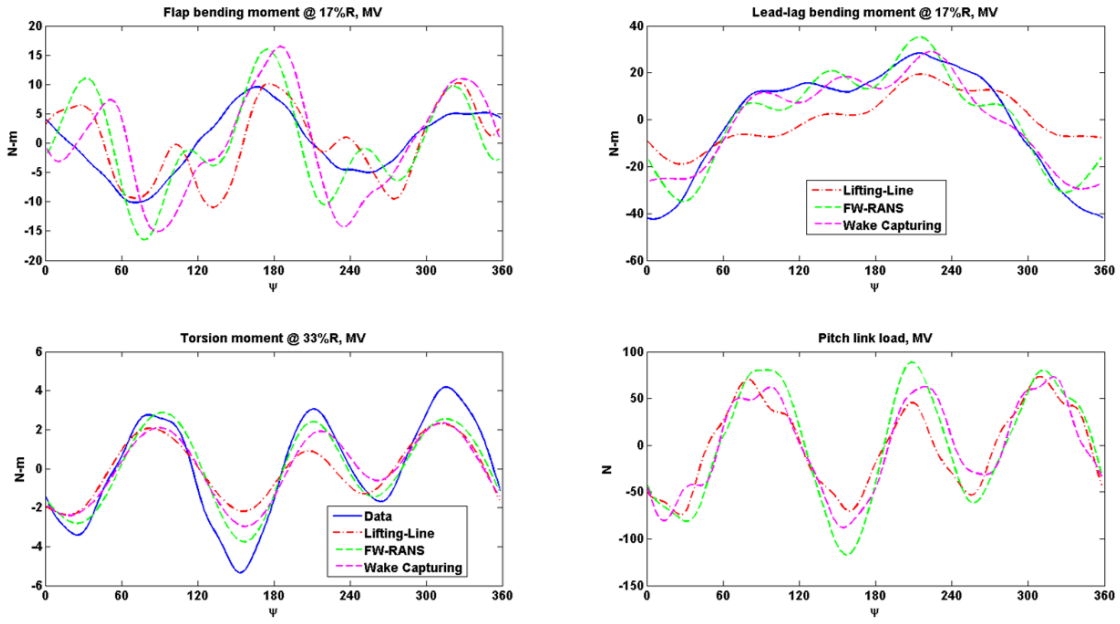

Figure 5.18: Blade structural bending moments, Minimum Vibration Case.

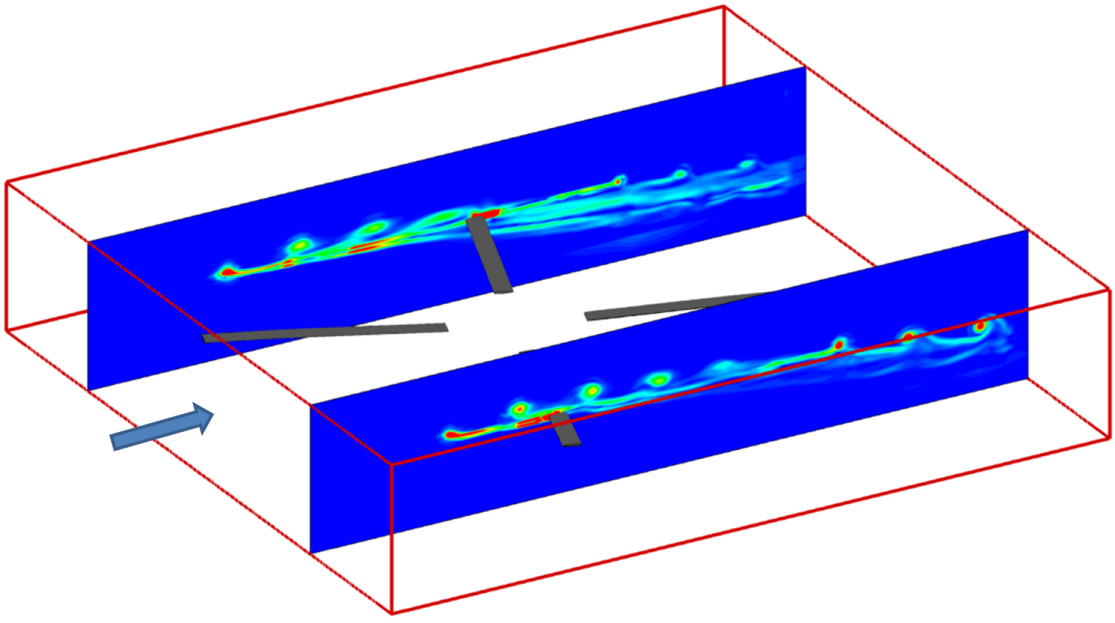

Figure 5.19: $\pm 70\%R$ planes, vorticity magnitude levels: 0.01-0.15, minimum vibration case, wake capturing.

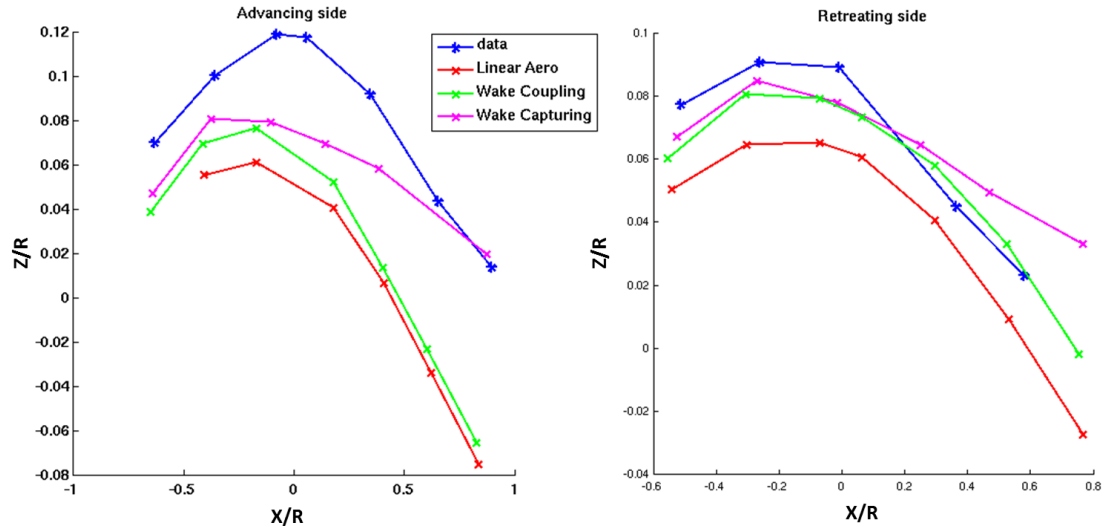

Figure 5.20: Vortex vertical position, advancing and retreating sides: baseline case

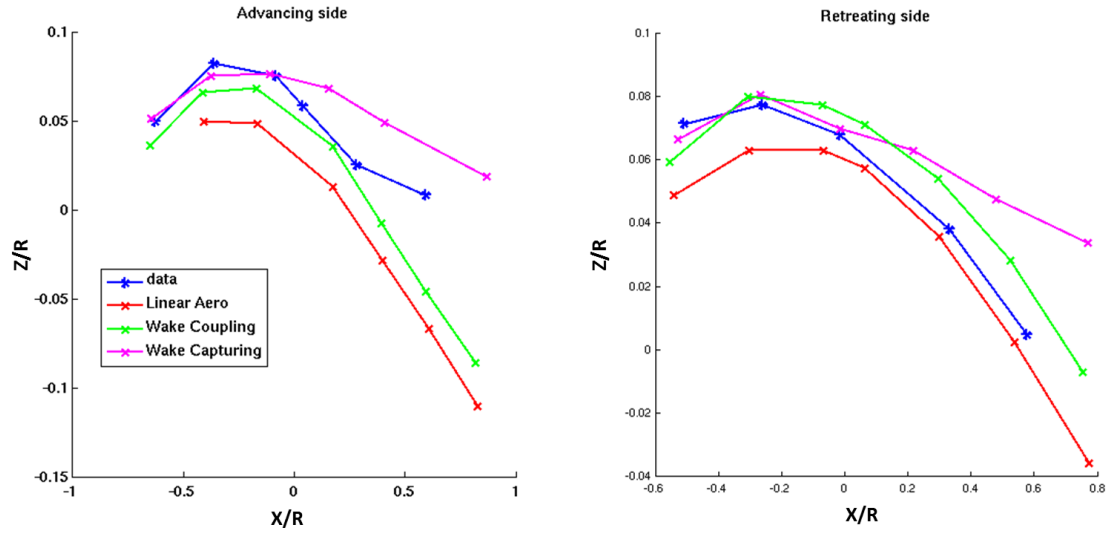

Figure 5.21: Vortex vertical position, advancing and retreating sides: minimum noise case

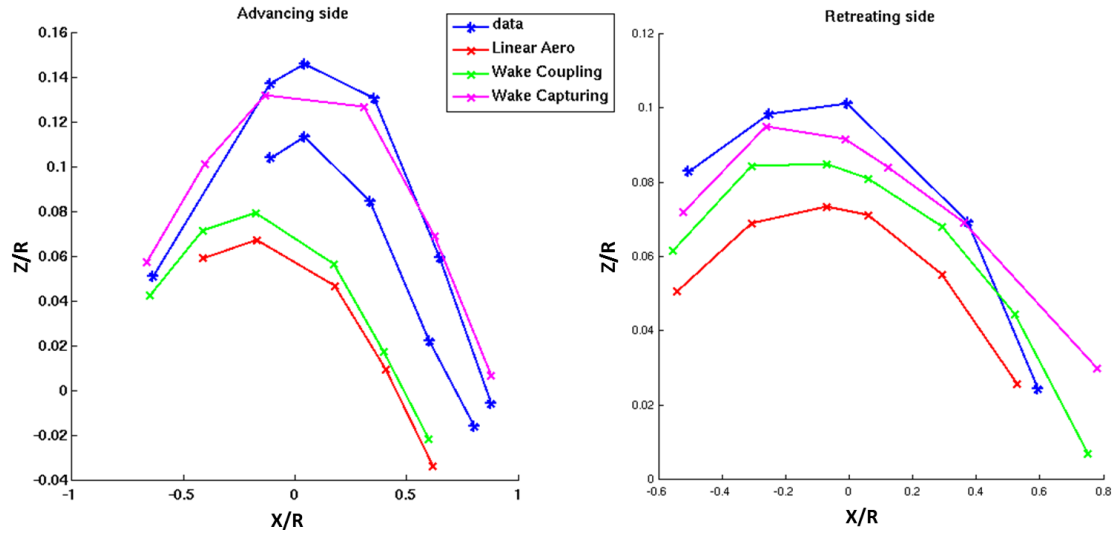

Figure 5.22: Vortex vertical position, advancing and retreating sides: minimum vibration case

pling approach gives reasonable results, especially at the back of the rotor where the wake capturing method predicts a higher wake position. This is probably due to the fact that the intermediate vortices (older vortices near the center of the rotor) that should push the vortex system down are somewhat diffused. Linearized aerodynamics gives the poorest prediction with lower overall wake positions. It should be noted that both free-wake based methods have similar wake locations in the first quarter of the rotor disk, which, as seen previously, leads to an offset of the BVI peak of maximum magnitude, as the blades hit the vortices later. Similar comments can be made about the MN case. The experimental results for the MV case show a dual-vortex system on the advancing side. This is due to a negative tip loading around azimuths of 150 ° and the formation of a counter-rotating vortex. Contours of $C_n M^2$ are plotted on Fig. 5.23 for all three methods and the MV case. It can be seen that only the wake capturing method fully predicts this region of negative

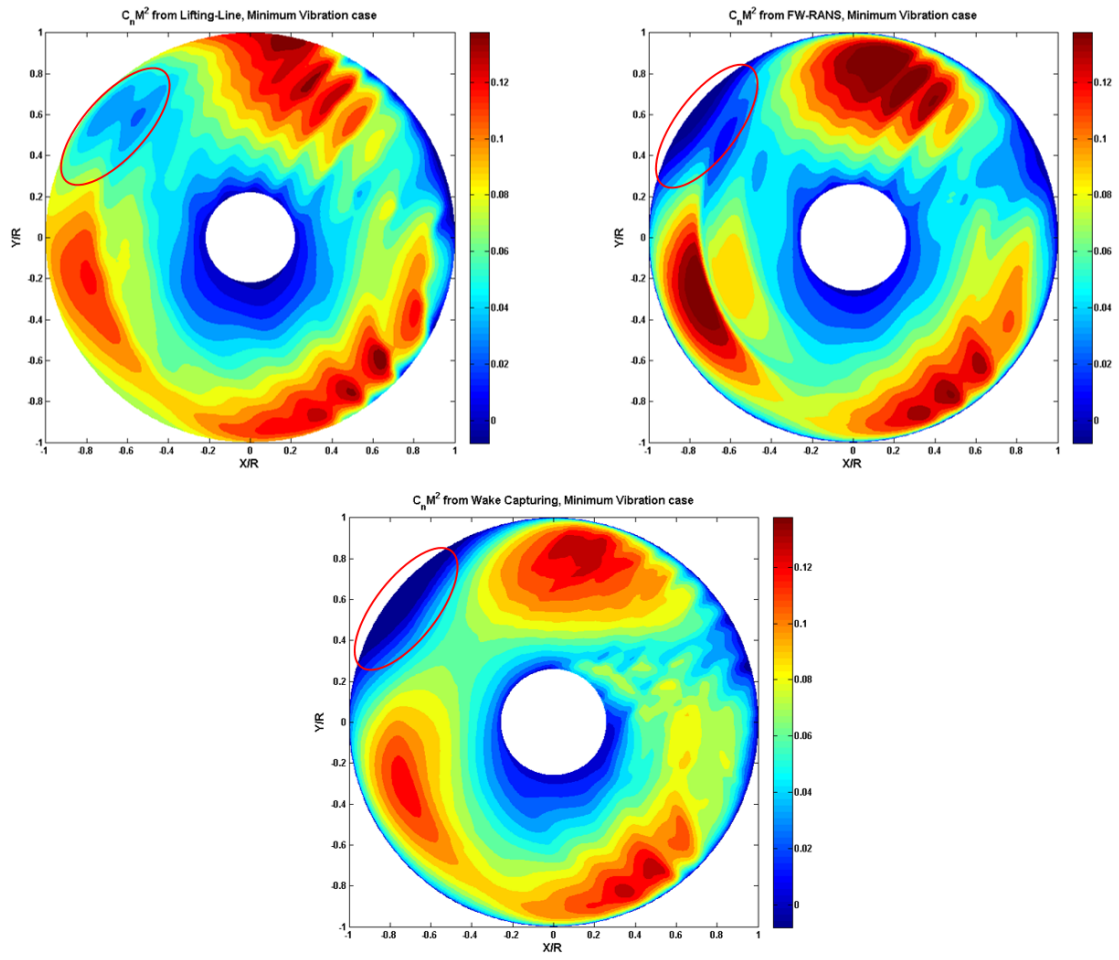

Figure 5.23: Contours of C_nM^2 obtained by all three methods for the minimum vibration case.

loading; RANS-based wake coupling only has a small negative zone at that location and lifting-line doesn't show this trend at all. Therefore, both free-wake based methods do not capture this phenomena as no, or little, negative loading is predicted. The wake capturing method was able to predict a higher wake locations on the advancing side but the counter-rotating vortex could not be extracted properly due to over-diffusion, as seen in Fig. 5.19. However, it could be captured shortly after being released and an iso-surface of Q-criterion showing the wake structure is displayed on Fig. 5.24. This clearly shows that a refinement of the free-wake model is necessary, as well as a finer discretization for the wake capturing approach.

5.6 Noise Levels

The acoustic signatures of the HART-II rotor for the three flight conditions were obtained from blade airloads using the code developed at UMD. As a first validation, time histories of acoustic pressure at two microphone locations were plotted for the three methods against experimental data. Microphone M11 is on the advancing side and microphone M4 on the retreating side, as shown on Fig. 5.25, which also has the location of the microphone array used for the noise carpet plots. Figure 5.26 displays the time history of acoustic pressure at M11, for a single blade. It can clearly be seen that lifting-line over-predicts the BVI peak, which is consistent with the remarks made above about the time derivative of normal force. The RANS wake coupling method give more reasonable magnitudes with good phasing. Wake capturing appears somewhat under-predicted and slightly offset in phase at that

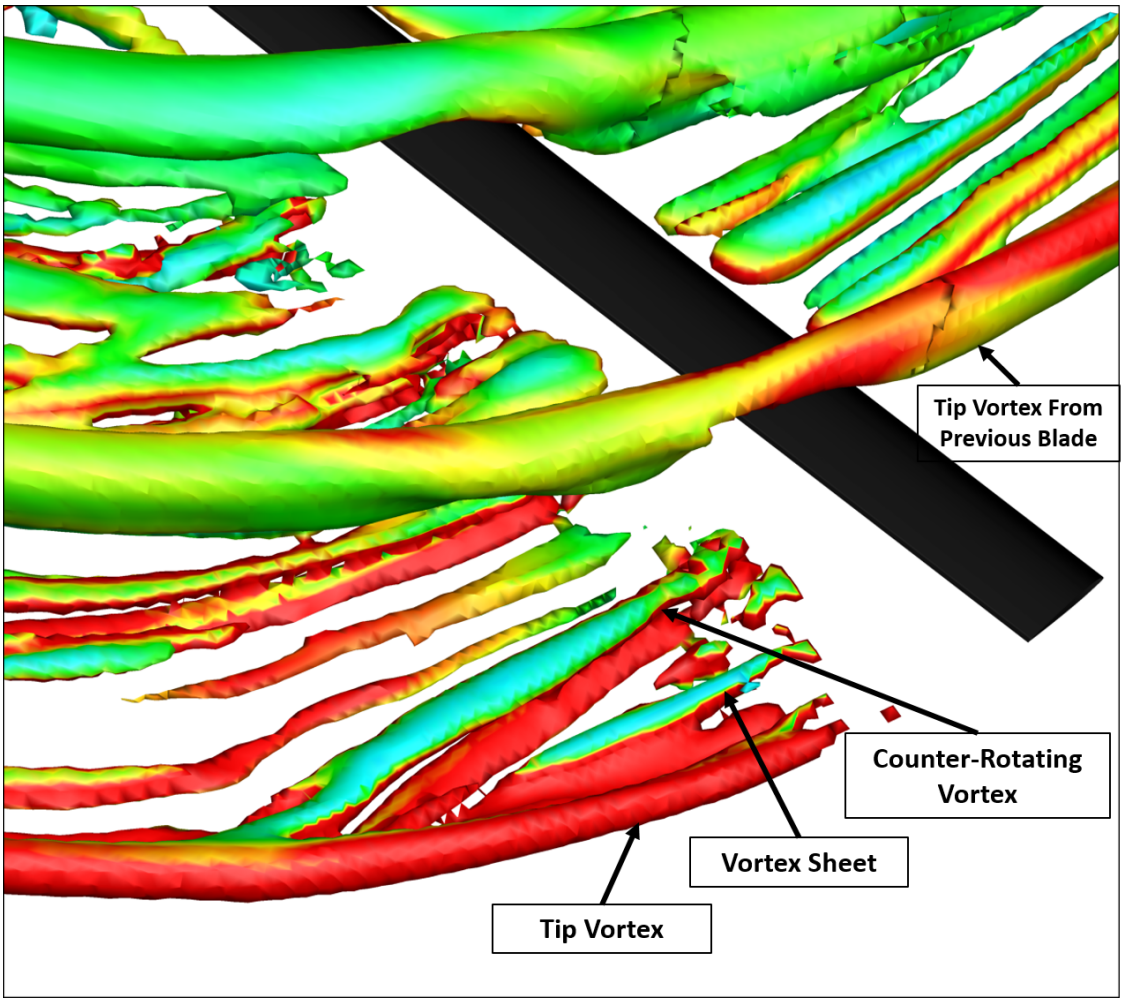

Figure 5.24: Iso-surface of Q-criterion showing the wake structure and CRV shortly after release, MV case, wake capturing.

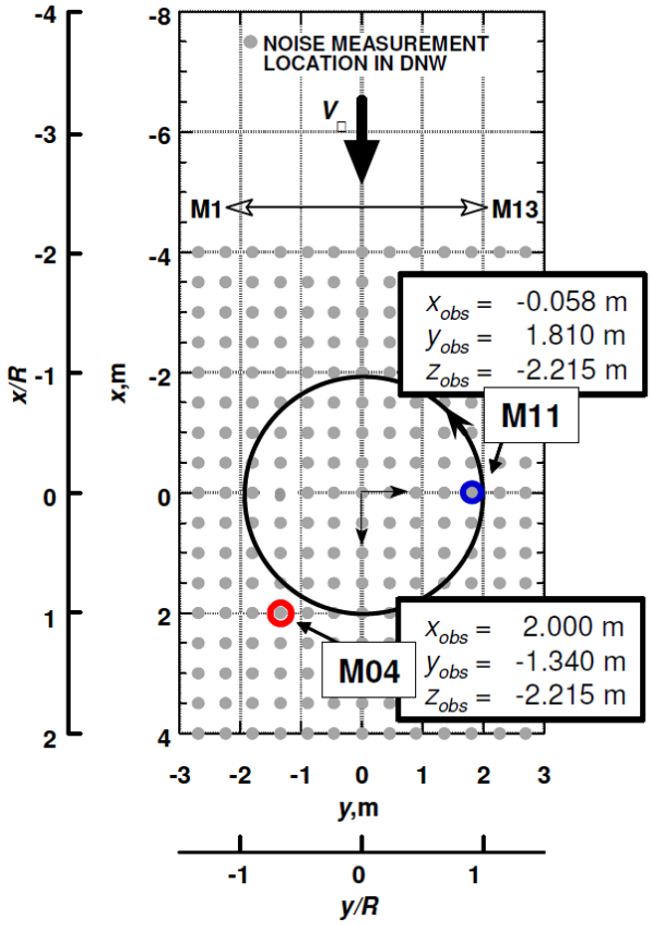

Figure 5.25: Microphone locations in DNW wind tunnel (Ref. [18])

microphone location. Similarly, results for microphone M4 are shown on Fig. 5.27. The phasing of the wake capturing results is very good, while the lifting-line peaks are again over-predicted.

The second set of acoustic results are Sound Pressure Level (SPL) contours. Experimental data was obtained from a microphone array placed 1.1R below the hub, and extending 2R in front and behind and 1.35R on each side on the rotor. BVISPL, which are 6 to 40 Blade Passage Frequency (BPF) filtered results, for this noise carpet are compared with numerical results in Fig. 5.28. It can be seen that all methods predict the right noise directivity pattern: in the minimum noise case, the advancing side hot-spot is shifted upstream and reduced in intensity, while in the minimum vibration case, the hot-spot is larger and stronger. Also, as expected due to the larger time derivatives of BVI loading, the linearized aerodynamics based method gives over-predicted levels for all three flight conditions. The RANS-based approaches give good noise levels, although the MN levels are slightly lower. In addition, the dual hot-spot that appears in the MN case is only predicted by wake capturing. To obtain a deeper comparison with experimental data, the minimum and maximum values in the noise contours are plotted in Fig. 5.29. As expected, the lifting-line levels are the highest, while wake capturing often has the best correlation.

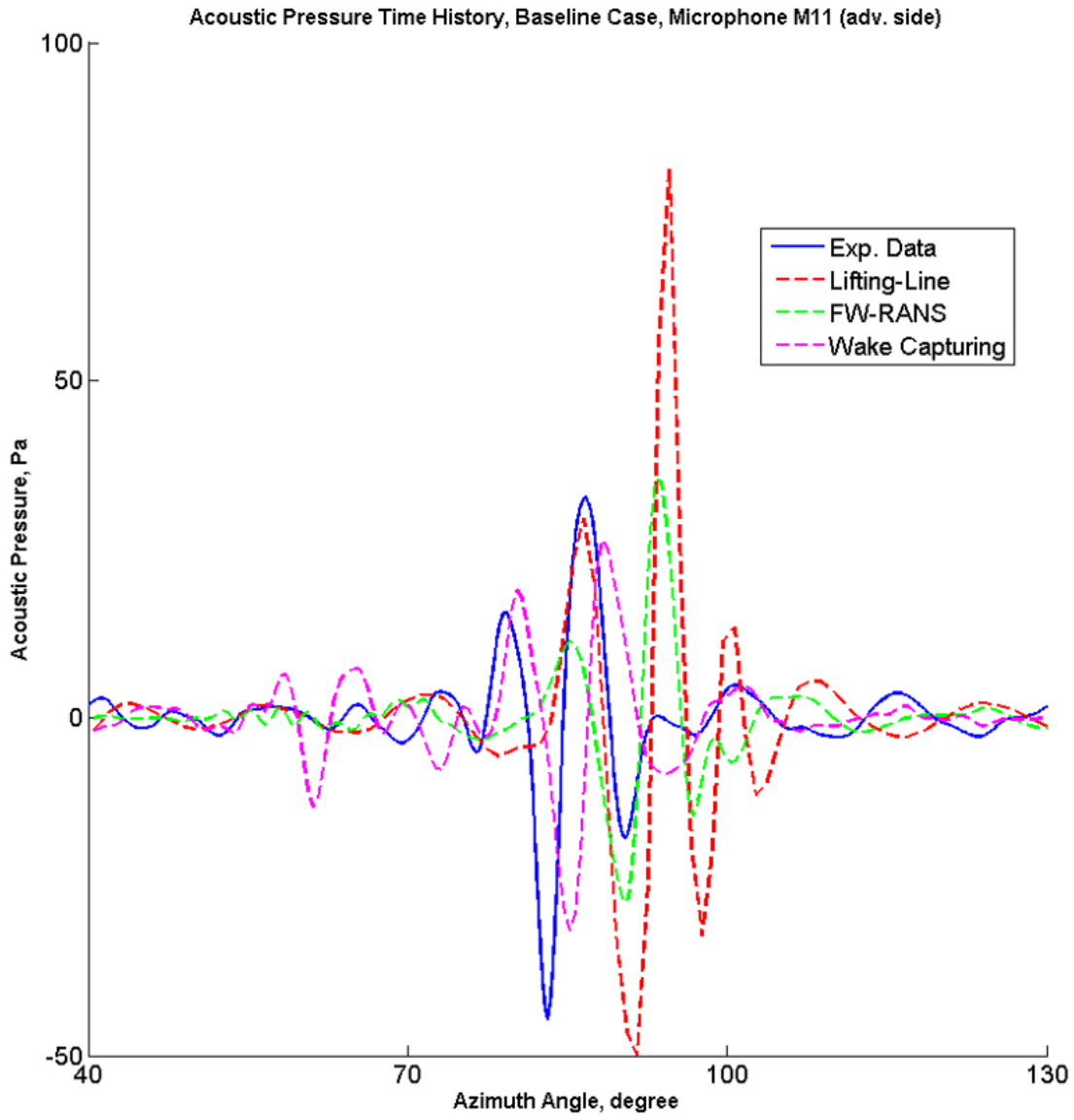

Figure 5.26: Time histories of acoustics pressure level, Microphone M11 (advancing side).

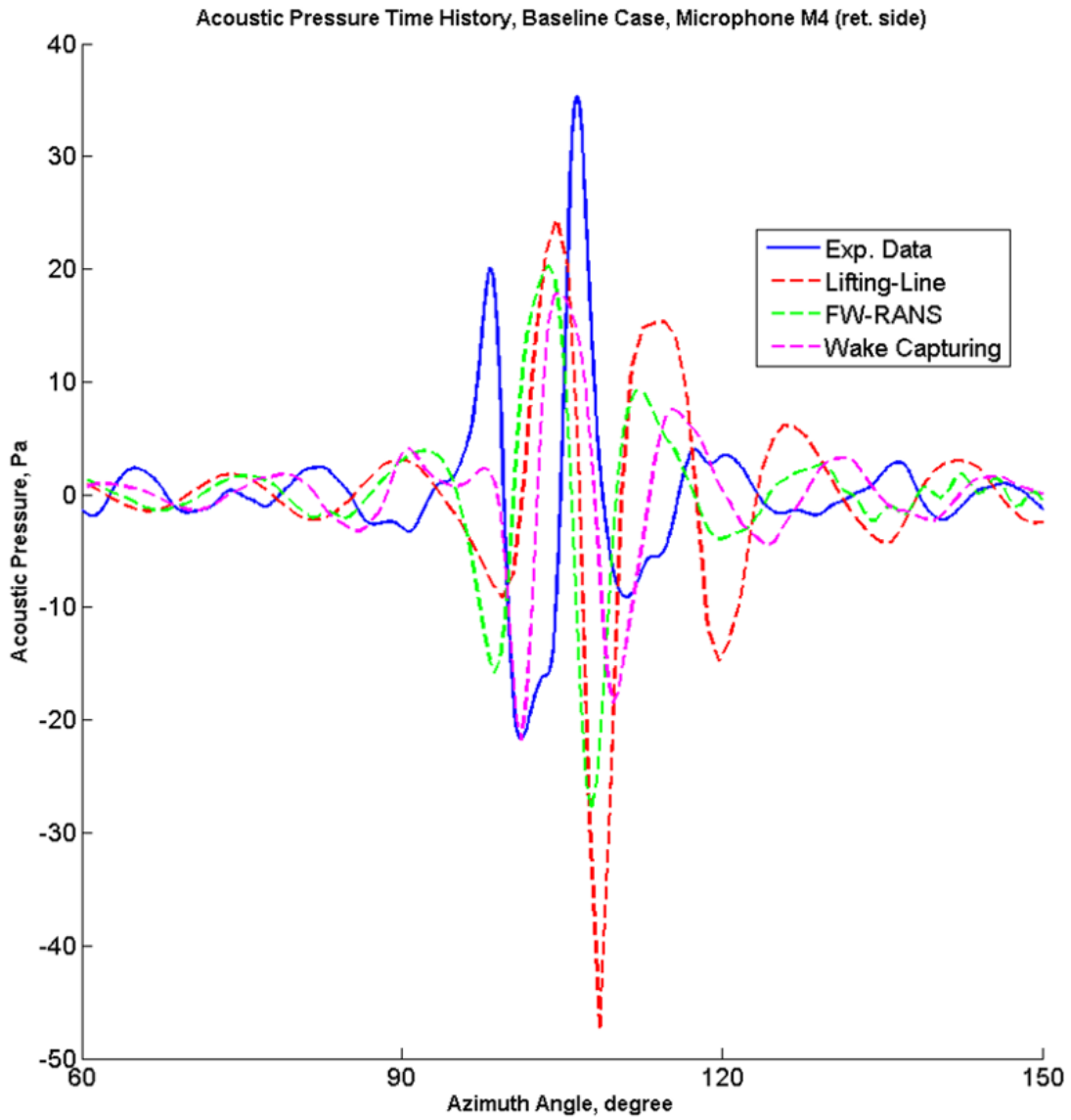

Figure 5.27: Time histories of acoustics pressure level, Microphone M4 (retreating side).

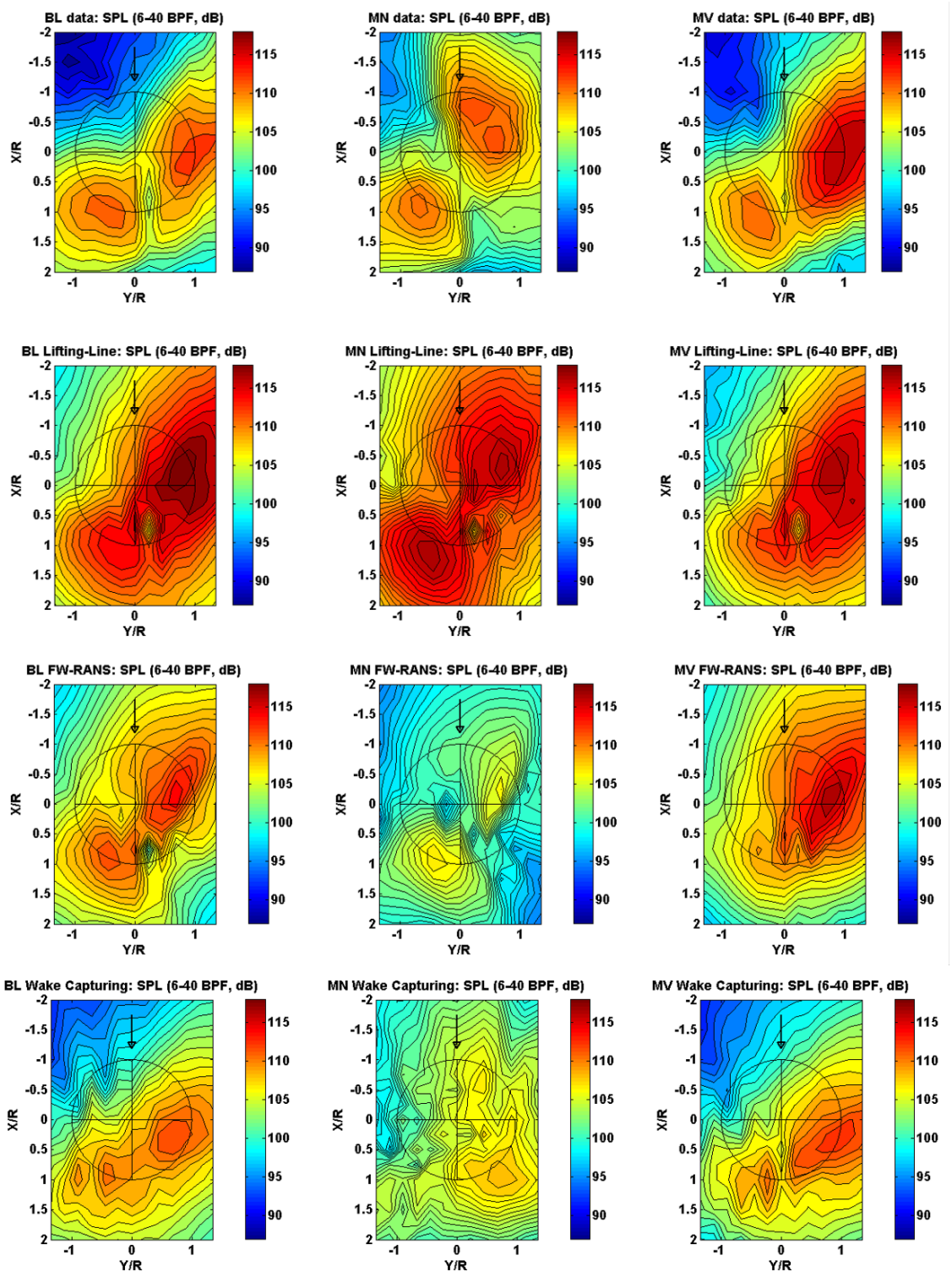

Figure 5.28: BVISPL contours, 6-40 BPF filtered.

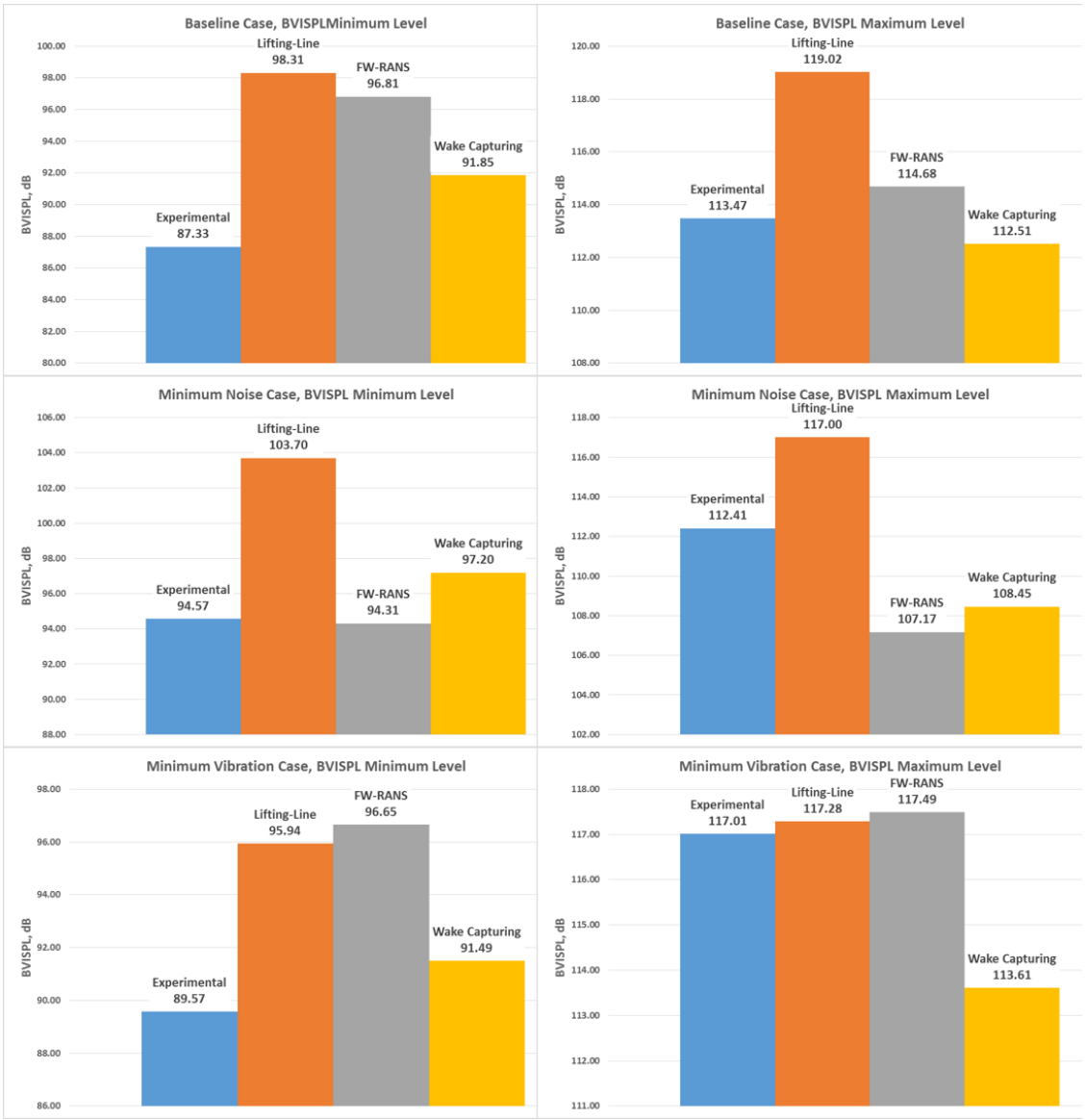

Figure 5.29: Minimum and maximum levels of BVISPL on acoustic contours.

5.7 Computational Efficiency

The previous sections compared the different modeling techniques in terms of numerical accuracy. In this section, the computational cost of each method is put into perspective. Although it often gave the best level of predictions, the wake capturing approach is known to be much more expensive in terms of CPU time and numerical resources required than the other two approaches. Using either fuselage model (body-fitted mesh or IBC), the total number of grid points was close to 18 million. With 32 3.2 GHz Intel Xeon cores, these computations took 315 hours (13 days) to perform one CFD-CSD coupling cycle, with the three rotor revolutions required to let the wake develop and settle in the flow field. The total simulation lasted for almost 50 days and was limited to 4 coupling cycles. The use of more CPUs could help reduce this computational time, but as was seen in the previous sections, more mesh refinement is also needed to better preserve tip vortices, which would drive the cost higher. Using the other RANS-based approach, with Free-Wake, it was seen that the time taken to perform a single rotor revolution was slightly less than half the time taken by wake capturing. In addition, this method does not require as many rotor revolutions to obtain a converge solution. On average, the overall CPU time of wake coupling with RANS was 9 days, for 7 coupling cycles, using the same number of processors. In its original Fortran implementation, the wake coupling method with lifting-line was already much faster than both other solvers, where a satisfactory converged solution could be obtained in a few hours on 4 processors. Going to GPU computing using CUDA-C, this approach ended up

taking only a few minutes to run on a single NVIDIA GeForce GTX 480. This is a considerable gain, which has to be put in perspective of the lower fidelity results obtained. For applications such as rotorcraft initial design and optimization, this is a very interesting approach, as it allows fast parametric studies to be conducted. Further improvements and optimization of the GPU implementation, along with the use of speedier higher end GPU cards, would allow close to real-time simulations, which could be used in on-board flight systems. However, when higher levels of fidelity are required, or for flight conditions involving more separated flow, blade stall, or transonic effects, this method is not appropriate. It should be noted that a RANS-based GPU solver was also developed at UMD by Thomas et al (Ref. [41] to be used in a wake coupling framework. Reductions in cost up to 50 times were observed, but the GPU implementation was not used in this study.

5.8 Summary

In this chapter, all numerical results computed for the HART-II rotor and its three flight conditions were presented. Comparisons were made between the three numerical techniques developed in the current framework and experimental data. The results included blade airloads, structural deformations and moments, control angles, wake geometry, noise radiation, and computational time. Overall, the wake capturing approach had the best correlation in terms of phase of BVI events, but was still lacking accurate magnitudes, which is thought to be due to over-dissipation of vortices. The wake coupling method with RANS solver had

very good magnitude predictions and somewhat offset BVI events. The lifting-line wake coupling technique however often had over-predicted levels, due to the level of empiricism and assumptions used. In terms of numerical cost, wake capturing proved to be very expensive, while the other two methods were more reasonable. Using GPU technology, the computational cost of wake coupling can be greatly decreased, down to a few minutes for the lifting-line solver.

Chapter 6

Conclusion

6.1 Summary

This doctoral dissertation presented the application of a multi-fidelity coupled CFD/CSD framework to the HART-II rotor test and the problem of helicopter BVI.

In the first chapter, the Rotorcraft Blade-Vortex Interaction was introduced. Key factors and physical mechanisms involved with BVI were presented. The impact of wake geometry, and especially that of the tip-released vortices, was shown to be important, as their location and strength is a driving factor of BVI intensity and directivity. The levels of noise and vibration induced by BVI are highly dependent on these parameters. From a computational standpoint, these considerations were used to define minimum levels of numerical modeling required to yield accurate simulation results. Then, the HART-II wind tunnel test and its database were presented. It is one of the most extensive aerodynamic, structural, and acoustic dataset available for the rotorcraft research community. A large portion of this data

was used for this doctoral work to validate the various numerical results shown. The impact of Higher-Harmonic Control, which was used in the HART-II test campaign to mitigate rotor noise and vibration, was analyzed as well. HHC was included in this research to correlate the wind tunnel findings. In addition, some of the most notable past computational work on HART and rotorcraft BVI were highlighted, which showed the great interest in this problem and the large variety of methods employed to address it. Key conclusions and important modeling assumptions were surveyed and carried over to the current work.

In the second chapter, the proposed computational strategy was presented. The main numerical components of the framework developed in this doctoral work to tackle the simulation of helicopter BVI were detailed. Going from a lifting-line based comprehensive analysis to a full 3D URANS solver, with incremental improvements both in near-field and far-field modeling, an advanced multi-fidelity computational environment was created. The various aerodynamic modules were coupled to a structural solver to predict blade deflections and perform rotor trim. An acoustic solver was also included to obtain and compare the rotor's noise signature. The specific coupling strategies employed to exchange data between the codes were also explained. Overall, three different numerical paradigms were developed and compared: wake coupling with free-wake and lifting-line, wake coupling with free-wake and RANS, and wake capturing with RANS. While achieving and maintaining greater solution accuracy was a driving factor in this research, computational efficiency was also made a priority. In that regard, a number of the codes involved in the framework were re-written in CUDA-C and optimized to run

on Graphics Processing Units. Their massively parallel computational environment helped increase the overall performance of the solvers, while greatly reducing the required numerical resources.

In the following chapter, optimal values of numerous numerical as well as physical variables were determined through parametric studies. It was shown that certain aspects of the simulation are sensitive to spatial and temporal refinements, whereas others are not. The choice of the best parameters was made as a compromise between improvements in solution accuracy and reasonable computational cost increase. The best integration schemes for both space and time were also chosen by following this dichotomy. As a vital component of BVI simulation is the adequate modeling of the rotor wake, various geometrical and numerical assumptions were evaluated in the free-wake model. For the wake capturing approach, a study of the trade-offs between different mesh topologies was conducted to obtain an optimal setup which ensures that relevant vortical structures are correctly captured and preserved through the computational domain.

The next chapter introduced the idea of fuselage modeling as an important contributing factor to achieving higher levels of solution accuracy and experimental correlation. In this chapter, three fuselage modeling techniques were presented: a 3D GPU panel code, a body-fitted curvilinear CFD mesh, and an immersed boundary method. Each required specific algorithms to be developed and were used in the multi-fidelity framework to bring the effect of a fuselage shape to the flow field. The panel method was coupled to both wake coupling approaches, whereas the CFD mesh and IBC code were used with wake capturing. Validation and comparison with

experimental data was also carried out for a simple fuselage geometry, the Robin mod-7 fuselage. Good correlation was found when using the body-fitted mesh and a viscous flow solver. However, limitations were shown for inviscid computations, although the overall effect on the rotor disk was found to be very comparable for all methods. The three techniques were then applied to the HART-II rotor to get a better understanding of the effect on blade vortices and blade airloads. The upwash captured at the front of the fuselage led to higher values of lift for azimuths around 180°, while the rear downwash created lower lift at the back of the rotor. The two methods used with the wake capturing approach gave significant improvements, both in terms of the magnitude and phase of the blade normal force. However, the effect modeled by the panel code was not as strong. In the IBC model, the coarser grid resolution near the fuselage surface, and the fact that the grid points do not conform to its curvature, led to non-physical effects, such as larger boundary layer and excessive flow separation. Improvements were made to that method through the local refinement of the grid using a 3D elliptic solver.

The following chapter presented the numerical results computed for the HART-II rotor and its three major flight conditions (HHC). Comparisons were made between the numerical paradigms developed in the current framework and experimental data. The results included blade airloads, structural deformations and moments, control angles, wake geometry, noise radiation, and computational time. Overall, the wake capturing approach had the best correlation in terms of phase of BVI events, but was somewhat lacking accurate aerodynamic loading magnitudes, due to mild over-dissipation of vortices. However, the detailed wake structures captured

proved to be very important in order to obtain appropriate blade deflection and structural moment predictions. The wake coupling method with RANS solver had very good magnitude predictions, and therefore good acoustic intensity, but showed some offset in the BVI events. The lifting-line wake coupling technique often had over-predicted aerodynamic loading levels, due to the degree of empiricism and assumptions used in this model. As a result, higher levels of noise were predicted, despite the relatively high temporal discretization used, which is known to have a strong impact on the time derivative of lift and on acoustics. In addition, the pitching moments computed by the lifting-line code benefited greatly from the hybrid Wagner-Kussner unsteady formulation implemented.

In terms of computational efficiency, wake capturing is a very expensive approach, while the other two methods had more reasonable run-times. The use of GPU technologies in the lifting-line wake coupling solver proved to be a key to achieving impressive gains over more traditional, CPU-based methods. Therefore, the superiority of either approach cannot be determined by simple considerations. Specific applications which require low run-times, such as rotorcraft initial design, sizing, parametric study, would benefit from trading accuracy for numerical cost. However, applications that require high levels of fidelity or in which complex flow phenomena are present will have to rely on more expensive methods, such as the wake capturing approach.

6.2 Observations

This section lists some key observations and conclusion about each part of the simulation.

Blade Structural solver

- Modeling the blades as fully elastic with all degrees of freedom and the first ten dominant natural modes proved crucial for accurate airloads predictions.
- Bending moments benefited from the use of a force summation method, compared to the modal method.

Free-vortex wake modeling

- Modeling root vortices, in addition to the traditional tip vortices, has a large impact on the lower frequency content of the blade loading.
- Using the 4^{th} order Runge-Kuta scheme for temporal integration helps the wake converge better. This is especially true for hover cases in which the vortex filaments have trouble convecting downward.
- Implementing a GPU version of the free-wake code led to a large decrease in computational time, mainly due to the increased parallelization of the Biot-Savart Kernel, which is the most expensive part.

Lifting-line linearized aerodynamics

- The use of a hybrid Wagner-Kussner compressible unsteady model was critical for the correct prediction of pitching moments.

- A time-step of 1° was necessary to fully capture BVI events.

3D URANS solver

- The use of compact reconstruction in the space marching scheme (CRWENO) helped improve spatial accuracy. This was especially important to reduce the numerical diffusion of vortices in the background computational domain. Achieving similar levels of wake capturing with the regular WENO scheme would have required a much finer grid resolution and therefore increased computational time.

Acoustic solver

- The combination of near-field and far-field terms for both loading and thickness noise led to accurate predictions of the rotor acoustic signature.

- The GPU implementation of the code helped decrease the overall computational time by parallelizing the calculations between all observer locations (microphones).

High resolution 3D panel method

- The use of GPU technology was especially important for the panel method used to model the fuselage. It allowed for the large parallelization of the most time consuming parts of the code.

- The access to GPU optimized linear algebra libraries increased the code's efficiency further, especially for the inversion and solution of the over-determined linear system.

- As a result of the low run-time of the code, a fine discretization could be used for the fuselage's surface definition.

3D, algebraic, curvilinear mesh generation

- The flexibility of algebraic mesh generation allowed for fast and easy gridding of the fuselage geometry. Obtaining a body-fitted mesh using the hyperbolic solver used for blade meshes would have been a lot more involved.

- Clustering of the surface definition near regions of separated flow (fuselage back ramp) was done using a 2D elliptic solver and proved to be important.

Immersed boundary method for fuselage modeling

- The immersed boundary method was able to predict the influence of the fuselage at the rotor plane. The use of tri-cubic interpolation to prescribe flow variables at the fuselage surface was necessary to ensure higher accuracy.

- The lower grid resolution at the surface of the fuselage led to increased flow separation near the back ramp. The use of local volume grid refinement helped mitigate this effect.

Volume refinement using 3D elliptic grid generation

- Local volume grid refinement was obtained using a 3D elliptic solver.

- User inputs were limited to source locations, radius of adaption, and level of adaption to make this approach simple and efficient.

- The refinement obtained proved to be helpful for the IBC method, although additional adaption and better orientation of the cells near the fuselage surface might be necessary.

Wake coupling

- The use of a loose coupling strategy with delta method was sufficient to simulate the steady HART-II flight conditions. Tight coupling did not seem to be required, which helped save on computational time.

Wake capturing

- The use of rectangular (Cartesian) background meshes to capture the far-field domain proved quite adequate for forward flight simulations. Using nested grids allowed for locally refining the computational domain where needed. Compared to cylindrical grids, typically used for hover cases, it avoided wasting grid points in front of the rotor. In addition, this approach doesn't require the calculation of the grid metrics necessary for curvilinear domains, which could decrease the overall simulation run-time, although this is not implemented in the current version of the code.

- Implicit Hole Cutting proved to be a powerful tool to handle grid connectivity. It ensured the correct transfer of data between the various grids without excessive user input.

6.3 Contributions

As was seen in the first chapter, many different numerical methods were used by various research teams around the world to model helicopter BVI and the HART-II rotor. The main objective of this thesis was to pursue this effort and to implement a numerical framework with multiple levels of fidelity capable of accurately simulating BVI. All aspects of the simulation were covered creating a multi-fidelity and multi-physic framework including: finite element structural dynamics, multiple Lagrangian and Eulerian flow solvers, acoustics modeling, and advanced meshing tools. The combination and systematic comparison of a broad range of CFD methods helped gained a deeper understanding of the required components to perform BVI simulations and achieve high experimental correlation. To further develop the framework and improve initial BVI predictions, three techniques were implemented to include fuselage effects into the CFD codes: a 3D GPU panel code, a body-fitted curvilinear fuselage mesh, and an immersed boundary based method. In addition, numerical efficiency was a key aspect, along with solution accuracy, of the proposed framework, such that computational time and required resources would remain reasonable. Therefore, various improvements and optimizations were made, and GPU computing technologies were used for some of the numerical codes developed, which greatly reduced the simulation run-times. Diverse grid generation techniques were employed for specific parts of the computational domain: Cartesian for the far-field, hyperbolic for the near-field (blade grids), algebraic for the fuselage mesh, and 2D and 3D elliptic for grid clustering and local refinement. Validation of the frame-

work was carried out using the HART-II experimental database. Various metrics were used, such as blade loading and deformations, wake geometry, and acoustic signature to assess the level of fidelity. Comparisons were also made with numerical results from other research teams which used different solvers (Ref. [2], Ref. [3]).

6.4 Recommendations

In this doctoral work, many numerical methods and solvers were developed. The level of accuracy obtained by the various methods was satisfactory but further improvements and optimization can be made by future researchers:

- The wake coupling approach could be modified to include a characteristic boundary condition instead of the field velocity method for calculating the effect of vortices on the grid points. This avoids the computation of the Biot-Savart law at every grid point, which can be expensive if not using a Fast Multipole Method (FMM). Grid velocities would only be modified at the mesh boundary, along with density, using isentropic relations, and pressure, using Bernoulli's principle. The vortices would then be free to convect inside the computational domain.

- The level of grid refinement used in the wake capturing approach should probably be increased to further capture and preserve the vortices present in the flow field. The use of Vortex Tracking Grids (VTG) or Automated Mesh Refinement (AMR) can be considered, if the finer grid discretization required drives the numerical cost too high for the available resources.

- Airloads predictions could potentially be improved by integrating the chordwise pressure distribution only where pressure sensors where positioned in the experiments. Good levels of improvement can be expected from such a method, especially for pitching moments, as shown by Biedron et al. (Ref. [38]) for the UH-60 and by Park et al. (Ref. [39]) for the HART-II rotor.

- Further fuselage simulations should be performed with more complex and representative fuselage shapes, for which the flow does not follow the laws of potential theory anymore. For the HART-II case, the addition of the hub could benefit the solution as it appears to be a significant source of disturbance in the flow field. To do so, improvements need to be made to the methods: in the panel code, vortex blobs could be release at the body surface to simulate viscous effects; the IBC-based method showed promising results when local grid refinement was applied in boundary layers, which needs to be further developed and made more efficient.

- With the rapid progress of GPU technologies, it will soon be possible to run an all-GPU simulation using the proposed framework, including wake capturing, which should provide considerable gains in efficiency and lead the way for future rotorcraft development.

Elliptic Grid Generation

2D Grid Metrics

$$\text{Jacobian Matrix: } \mathbf{J} = \begin{bmatrix} x_\xi & x_\eta \\ y_\xi & y_\eta \end{bmatrix}$$

$$\text{Inverse Jacobian Matrix: } \mathbf{J}^{-1} = \begin{bmatrix} \xi_x & \xi_y \\ \eta_x & \eta_y \end{bmatrix}$$

$$\det(\mathbf{J}) = j^{-1} = x_\xi y_\eta - x_\eta y_\xi \text{ (cell surface)}$$

$$\text{with: } \begin{vmatrix} \xi_x = j y_\eta & \xi_y = -j x_\eta \\ \eta_x = -j y_\xi & \eta_y = j x_\xi \\ \xi_t = j(-x_\tau y_\eta + y_\tau x_\eta & \eta_t = j(x_\tau y_\xi - y_\tau x_\xi) \end{vmatrix}$$

$$\text{Metric Tensor: } \mathbf{G} = \mathbf{J}^T\mathbf{J} = \mathrm{g}_{ij} = \mathbf{x}_{\xi i}.\mathbf{x}_{\xi j}$$

$$\text{ie: } \begin{vmatrix} g_{11} = x_\xi^2 + y_\xi^2 \\ g_{22} = x_\eta^2 + y_\eta^2 \\ g_{12} = g_{21} = x_\xi x_\eta + y_\xi y_\eta \end{vmatrix}$$

$$\mathrm{g} = \det(\mathbf{G}) = j^2$$

$$\text{Inverse Metric Tensor: } \mathbf{G}^{-1} = \mathrm{g}^{ij} = \nabla_{\mathbf{x}}\xi_i.\nabla_{\mathbf{x}}\xi_j$$

$$\text{ie:} \left| \begin{array}{c} g^{11} = g g_{22} \\ g^{22} = g g_{11} \\ g^{12} = g^{21} = -g g_{12} \end{array} \right|$$

2D Elliptic Grid Generation

Based on Laplace Equation on computational coordinates (ξ, η):

$$\xi_{xx} + \xi_{yy} = 0 \text{ and } \eta_{xx} + \eta_{yy} = 0$$

To be more convenient to use in a numerical algorithm, these equations are inverted (if the mapping is invertible: $g \neq 0$):

$$g^{11}\mathbf{x}_{\xi\xi} + 2g^{12}\mathbf{x}_{\xi\eta} + g^{22}\mathbf{x}_{\eta\eta} = 0$$

or, using g_{ij}:

$$g_{22}\mathbf{x}_{\xi\xi} - 2g_{12}\mathbf{x}_{\xi\eta} + g_{11}\mathbf{x}_{\eta\eta} = 0$$

This is the Winslow equation. It can be written using the Winslow operator $Q_w\mathbf{x} = 0$ To control the grid spacing, add clustering, change cell orientation,... a source term can be added to this equation, making it a Poisson Equation. The idea is to have the inverse Jacobian matrix be as close as possible to a prescribed weight matrix $\mathbf{S}$ such that: $div_x(J^{-1}$ - $\mathbf{S}) = 0$

Then, the Winslow equation with source terms can be derived:

using $\mathbf{C} = \sqrt{\mathbf{g}}\mathbf{J}^{-T}$:

$$div_{\vec{x}} J^{-1} = div_x \mathbf{S}$$

$$div_\xi J^{-1} C = div_\xi \mathbf{SC}$$

$$div_\xi \sqrt{g} G^{-1} = [\nabla_\xi \mathbf{S}]\mathbf{C}$$

$$-\sqrt{g}\mathbf{J} div_\xi \sqrt{g} G^{-1} = -\sqrt{g}\mathbf{J}[\nabla_\xi \mathbf{S}]\mathbf{C}$$

$$\mathrm{g}[\nabla_\xi \mathbf{J}]G^{-1} = -\sqrt{g}\mathbf{J}[\nabla_\xi \mathbf{S}]\mathbf{C}$$

$$\mathbf{Q}_w \mathbf{x} = -\sqrt{g}\mathbf{J}[\nabla_\xi \mathbf{S}]\mathbf{C}$$

ie: $g_{22}\mathbf{x}_{\xi\xi} - 2g_{12}\mathbf{x}_{\xi\eta} + g_{11}\mathbf{x}_{\eta\eta} = -\sqrt{g}\mathbf{JR}$

ie: $g_{22}\mathbf{x}_{\xi\xi} - 2g_{12}\mathbf{x}_{\xi\eta} + g_{11}\mathbf{x}_{\eta\eta} + g_{22}P\mathbf{x}_\xi + g_{11}Q\mathbf{x}_\eta = 0$

$\mathbf{R}$ is the source term: $\mathbf{R} = [\nabla_\xi \mathbf{S}]\mathbf{C}$, $\mathbf{S}$ being a weight matrix

$$\text{and } \mathbf{R} = \begin{bmatrix} (S_{11})_\xi y_\eta - (S_{12})_\xi x_\eta - (S_{11})_\eta y_\xi + (S_{12})_\eta x_\xi \\ \\ (S_{21})_\xi y_\eta - (S_{22})_\xi x_\eta - (S_{21})_\eta y_\xi + (S_{22})_\eta x_\xi \end{bmatrix}$$

The weight matrix S is based on a length scale l and a cell rotation angle θ.

The length scale is:

$$l = \begin{Bmatrix} 1 - A & r \leq R_1 \\ 1 - A + A\left(3 - 2\frac{r-R_1}{R_2-R_1}\right)\left(\frac{r-R_1}{R_2-R_1}\right)^2 & R_1 < R_2 \\ 1 & r \geq R_2 \end{Bmatrix}$$

$$\text{And } S = \begin{bmatrix} \frac{cos(\theta)}{l} & \frac{sin(\theta)}{l} \\ -\frac{sin(\theta)}{l} & \frac{cos(\theta)}{l} \end{bmatrix}$$

3D Grid Metrics

$$\text{Jacobian Matrix: } \mathbf{J} = \begin{bmatrix} x_\xi & x_\eta & x_\zeta \\ y_\xi & y_\eta & y_\zeta \\ z_\xi & z_\eta & z_\zeta \end{bmatrix}$$

$$\text{Inverse Jacobian Matrix: } \mathbf{J}^{-1} = \begin{bmatrix} \xi_x & \xi_y & \xi_z \\ \eta_x & \eta_y & \eta_z \\ \zeta_x & \zeta_y & \zeta_z \end{bmatrix}$$

$\det(\mathbf{J}) = j^{-1} = x_\xi y_\eta z_\zeta + x_\zeta y_\xi z_\eta + x_\eta y_\zeta z_\xi - x_\xi y_\zeta z_\eta - x_\eta y_\xi z_\zeta - x_\zeta y_\eta z_\xi$ (cell volume)

with:

$$\left|\begin{array}{lll} \xi_x = j(y_\eta z_\zeta - y_\zeta z_\eta) & \xi_y = j(z_\eta x_\zeta - z_\zeta x_\eta) & \xi_z = j(x_\eta y_\zeta - y_\eta z_\zeta) \\ \eta_x = j(z_\xi y_\zeta - y_\xi z_\zeta & \eta_y = j(x_\xi z_\zeta - z_\xi x_\zeta) & \eta_z = j(y_\xi x_\zeta - x_\xi y_\zeta) \\ \zeta_x = j(y_\xi z_\eta - z_\xi y_\eta) & \zeta_y = j(z_\xi x_\eta - x_\xi z_\eta) & \zeta_z = j(x_\xi y_\eta - y_\xi x_\eta) \\ \xi_t = -x_\tau \xi_x - y_\tau \xi_y - z_\tau \xi_z & \eta_t = -x_\tau \eta_x - y_\tau \eta_y - z_\tau \eta_z & \zeta_t = -x_\tau \zeta_x - y_\tau \zeta_y - z_\tau \zeta_z \end{array}\right|$$

Metric Tensor: $\mathbf{G} = \mathbf{J}^T\mathbf{J} = \mathrm{g}_{ij} = \mathbf{x}_{\xi i}.\mathbf{x}_{\xi j}$

ie:
$$\left|\begin{array}{c} g_{11} = x_\xi^2 + y_\xi^2 + z_\xi^2 \\ g_{22} = x_\eta^2 + y_\eta^2 + z_\eta^2 \\ g_{33} = x_\zeta^2 + y_\zeta^2 + z_\zeta^2 \\ g_{12} = g_{21} = x_\xi x_\eta + y_\xi y_\eta + z_\xi z_\eta \\ g_{13} = g_{31} = x_\xi x_\zeta + y_\xi y_\zeta + z_\xi z_\zeta \\ g_{23} = g_{32} = x_\eta x_\zeta + y_\eta y_\zeta + z_\eta z_\zeta \end{array}\right|$$

$$\mathrm{g} = \det(\mathbf{G}) = j^2$$

Inverse Metric Tensor: $\mathbf{G}^{-1} = \mathrm{g}^{ij} = \nabla_{\mathbf{x}}\xi_i.\nabla_{\mathbf{x}}\xi_j$

In 3D we have: $g^{ij} = \frac{1}{g}[g_{jm}g_{kn} - g_{jn}g_{km}]$ with cyclic permutation on (i,j,k) and

(l,m,n) such that:

$$\text{ie:} \left| \begin{array}{c} g^{11} = \frac{1}{g}[g_{22}g_{33} - g_{23}^2] \\ g^{12} = g^{21} = \frac{1}{g}[g_{23}g_{13} - g_{33}g_{12}] \\ g^{13} = g^{31} = \frac{1}{g}[g_{12}g_{23} - g_{22}g_{13}] \\ g^{23} = g^{32} = \frac{1}{g}[g_{13}g_{12} - g_{11}g_{23}] \\ g^{22} = \frac{1}{g}[g_{11}g_{33} - g_{13}^2] \\ g^{33} = \frac{1}{g}[g_{11}g_{22} - g_{12}^2] \end{array} \right.$$

3D Elliptic Grid Generation

The Laplace Equation is used on the computational coordinates (ξ, η, ζ):

$$\xi_{xx} + \xi_{yy} + \xi_{zz} = 0$$

$$\eta_{xx} + \eta_{yy} + \eta_{zz} = 0$$

$$\zeta_{xx} + \zeta_{yy} + \zeta_{zz} = 0$$

Similarly to the 2D case, these equations are inverted (if the mapping is invertible: $g \neq 0$) and source terms are added:

$$g^{11}\mathbf{x}_{\xi\xi} + g^{22}\mathbf{x}_{\eta\eta} + g^{33}\mathbf{x}_{\zeta\zeta} + 2g^{12}\mathbf{x}_{\xi\eta} + 2g^{13}\mathbf{x}_{\xi\zeta} + 2g^{23}\mathbf{x}_{\eta\zeta} + g^{11}P\mathbf{x}_{\xi} + g^{22}Q\mathbf{x}_{\eta} + g^{33}R\mathbf{x}_{\zeta} = 0$$

with the source terms [P Q R] = $[\nabla_{\xi}\mathbf{S}]\mathbf{C}$, ie:

$$P = (S_{11})_\xi \xi_x + (S_{12})_\xi \xi_y + (S_{13})_\xi \xi_z + (S_{11})_\eta \eta_x + (S_{12})_\eta \eta_y + (S_{13})_\eta \eta_z + (S_{11})_\zeta \zeta_x +$$

$$(S_{12})_\zeta \zeta_y + (S_{13})_\zeta \zeta_z$$

$$Q = (S_{21})_\xi \xi_x + (S_{22})_\xi \xi_y + (S_{23})_\xi \xi_z + (S_{21})_\eta \eta_x + (S_{22})_\eta \eta_y + (S_{23})_\eta \eta_z + (S_{21})_\zeta \zeta_x +$$

$$(S_{22})_\zeta \zeta_y + (S_{23})_\zeta \zeta_z$$

$$R = (S_{31})_\xi \xi_x + (S_{32})_\xi \xi_y + (S_{33})_\xi \xi_z + (S_{31})_\eta \eta_x + (S_{32})_\eta \eta_y + (S_{33})_\eta \eta_z + (S_{31})_\zeta \zeta_x +$$

$$(S_{32})_\zeta \zeta_y + (S_{33})_\zeta \zeta_z$$

The metrics can be replaced by their expression given above.

Bibliography

[1] van der Wall, B.G., Burley, C.L., Yu, Y.H., Pengel, K., Beaumier, P., *The HART II Test - Measurement of Helicopter Rotor Wakes,* Aerospace Science and Technology, Vol. 8, (4), June 2004, pp. 273-284.

[2] van der Wall, B. G., Lim, J. W., Smith, M. J., Jung, S. N., Bailly, J., Baeder, J. D., and Boyd, Jr., D. D., *An Assessment of Comprehensive Code Prediction State-of-the-Art Using the HART II International Workshop Data,* Presented at the 68^{th} Annual AHS Forum, Fort Worth, TX, USA, May 1-3 2012.

[3] Smith, M. J., Lim, J. W., van der Wall, B. G., Baeder, J. D., Biedron, R., Boyd, Jr., D. D., Jayaraman, B., Jung, S. N., and Min, B.-Y., *An Assessment of CFD/CSD Prediction State-of-the-Art Using the HART II International Workshop Data,* Presented at the 68^{th} Annual AHS Forum, Fort Worth, TX, USA, May 1-3 2012.

[4] Amiraux, M., Baeder, J. D., Koushik, S. N., *Improved correlation with the HART-II rotor test data using coupled CSD/CFD and three levels of numerical modelization,* Presented at the 38^{th} European Rotorcraft Forum, Paper 149, Amsterdam, Netherlands, September 2012.

[5] Tung, C., Caradonna, F. X., and Johnson, W. R., *The Prediction of Transonic Flows on an Advancing Rotor,* Presented at the American Helicopter Society 40^{th} Annual Forum, Arlington, VA, USA, May 1984.

[6] Ananthan, S., Baeder, J. D., and Sitaraman, J., *Hybrid Unsteady Simulation of Helicopters: HUSH,* Presented at the 26^{th} AIAA Applied Aerodynamics Conference, Honolulu, HI, USA, August 2008.

[7] Chopra, I., and Bir, G., *University of Maryland Advanced Rotor Code: UMARC,* American Helicopter Society Aeromechanics Specialists Conference, San Franscisco, CA, USA, January 1994.

[8] Hodges, D.H., and Dowell, E. H., *Nonlinear Equations of Motion for the Elastic Bending and Torsion of Twisted Nonuniform Rotor Blades,* NASA TN D7818.

[9] Ormiston, R. A., Hodges, D. H., and Peters, D. A., *On the Nonlinear Deformation Geometry of Euler-Bernoulli Beams,* NASA Technical Paper 1566.

[10] Datta, A., *Understanding, Prediction and Validation of Rotor Vibratory Loads in Steady Level Flight,* Doctoral Dissertation, University of Maryland, MD, USA, 2004.

[11] Weissinger, J., *The Lift Distribution of Swept-Back Wings,* NACA TM 1120, 1947.

[12] Leishman, J. G., Beddoes, T. S., *A Semi-Empirical Model for Dynamic Stall,* Journal of the American Helicopter Society, Vol. 34, No. 3, July 1989, pp. 3-17.

[13] Beddoes, T. S., *A Wake Model for High Resolution Airloads,* Second International Conference on Basic Rotorcraft Research, Research triangle Park, North Carolina, 1985.

[14] Sitaraman, J., Baeder, J., and Chopra, I., *Validation of UH-60 Rotor Blade Aerodynamic Characteristics Using CFD,* Presented at the 59^{th} Annual Forum of the American Helicopter Society International, Phoenix, AZ, USA, May 2003.

[15] Yoon, S., and Jameson, A., *Lower-Upper Symmetric-Gauss-Seidel Method for Euler and Navier-Stokes equations,* AIAA Journal, Vol. 26, 1988, pp. 1025-1026.

[16] Pulliam, T., *Time Accuracy and the use of Implicit Methods,* American Institute of Aeronautics and Astronautics 1993-3360, 1993.

[17] Jeong, J., Hussain, F., *On the Identification of a Vortex,* Journal of Fluid Mechanics, Vol. 285, 1995, pp. 69-94.

[18] Gopalan, G., Sitaraman, J., Baeder, J. D. and Schmitz, F., H., *Aerodynamic and Aeroacoustic Prediction Methodologies With Application to the HART-II Model Rotor,* Presented at the 62^{nd} Forum of the American Helicopter Society, Phoenix, Arizona, USA, May 9-11, 2006.

[19] Lee, Y., and Baeder, J. D., *Implicit Hole Cutting - A New Approach to Overset Grid Connectivity,* Presented at the 16^{th} AIAA Computational Fluid Dynamics Conference, Orlando, FL, USA, June 2003.

[20] Ffowcs Williams, J. E. and Hawkins, D. L., *Sound Generated by Turbulence and Surfaces in Arbitrary Motion,* Philosophical Transactions of the Royal Society, Series A, Vol. 264, 1969, pp. 321-342.

[21] Farassat, F., *Linear Acoustic Formulas for Calculation of Rotating Blade Noise,* Journal of the American Institute of Aeronautics and Astronautics, Vol. 19, No. 9, September 1981, pp. 1122-1130.

[22] Brentner, K. S., Farassat, F., *Modelling Aerodynamically Generated Sound of Helicopter Rotors,* Progress in Aerospace Sciences, 2003.

[23] Koushik, S. and Schmitz, F.H., *Understanding In-Plane Helicopter Blade-Vortex Interaction (BVI) Noise,* Presented at the 68^{th} Forum of the American Helicopter Society,Fort Worth, TX, USA, May 2012.

[24] Koushik, S. N., *A New Experimental Approach to Study Helicopter Blade-Vortex Interaction Noise,* Doctoral Dissertation, University of Maryland, 2007.

[25] Leishman, J. G., Bhagwat, M. J. and Ananthan, S., *Free-Vortex Wake Predictions of the Vortex Ring State for Single-Rotor and Multi-Rotor Configurations,* Presented at the 58^{th} Forum of the American Helicopter Society, Montreal, Canada, June 2002.

[26] Bhagwat, M. J., Leishman, J. G., *Generalized Viscous Vortex Model for Application to Free-Vortex Wake and Aeroacoustic Calculations,* Presented at the 58^{th} Forum of the American Helicopter Society, Montreal, Canada, June 2002.

[27] Chen, P., Baeder, J. D., Evans, R. A., Niemczuk, J., and Ross P., *Active Twist Smart Rotor Technology for Blade-Vortex Interaction Noise Reduction,* Proc. SPIE 3668, 37, 1999.

[28] Sitaraman, J., Baeder, J. B., *Enhanced Unsteady Airload Models Using CFD,* AIAA Paper 2000-2465, Denver, CO, USA, June, 2000.

[29] Lim, J. W., van der Wall, B. G., *Investigation of the Effect of a Multiple Trailer Wake Model for Descending Flights,* Presented at the 61^{st} Forum of the American Helicopter Society, Grapevine, TX, USA, June 2005.

[30] Sim, B. W., Lim, J. W., *BLADE-VORTEX INTERACTION (BVI) NOISE and AIRLOAD PREDICTION USING LOOSE AERODYNAMIC/STRUCTURAL COUPLING,* Presented at the 62^{st} Annual Forum of the American Helicopter Society, Phoenix, Arizona, May 2006

[31] Dietz, M., Kramer, E., Wagner, S., *Tip vortex conservation on a main rotor in slow descent flight using vortex-adapted Chimera grids,* Presented at the 24^{th} AIAA Applied Aerodynamics Conference, San Fransisco, California, June 5-8, 2006

[32] Kelly, M. E., Brown, R. E., *The effect of blade aerodynamic modelling on the prediction of high-frequency rotor airloads,* Presented at the 65^{st} Annual Forum of the American Helicopter Society, Grapevine, Texas, May 27-29, 2009

[33] Anusonti-Inthra, P., *VALIDATIONS OF COUPLED CSD/CFD AND PARTICLE VORTEX TRANSPORT METHOD FOR ROTORCRAFT APPLICATIONS: HOVER, TRANSITION, AND HIGH SPEED FLIGHTS,* Presented

at the 66^{st} Annual Forum of the American Helicopter Society, Phoenix, Arizona, May 11-13, 2010

[34] van der Wall, B. G., Yin, J., *DLR's S4 Rotor Code Validation With HART II Data: The Baseline Case,* Presented at the International Forum on Rotorcraft Multidisciplinary Technology, Seoul, Korea, October 15-17, 2007

[35] Yu, D. O., Jung, M. S., Kwon, O. J., Yu, Y. H., *Predicting Blade Loading and Wake Structure of the HART II Rotor using Adaptive Unstructured Meshes,* 2^{nd} International Forum on Rotorcraft Multidisciplinary Technology, Seoul, Korea, October 19-20, 2009

[36] Lim, J.W., *The Effect of Fuselage and Rotor Hub on Blade-Vortex Interactions Airloads and Rotor Wakes,* Presented at the 36^{th} European Rotorcraft Forum, Paris, France, Sept. 2010.

[37] Sa, J. H., You, Y.-H., Park, J.-S., Jung, S.N., Park, S. H., and, Yu, Y. H., *Assessment of CFD/CSD Coupled Aeroelastic Analysis Solution for HART II Rotor Incorporating Fuselage Effects,* Presented at the 67^{th} Forum of the American Helicopter Society, Virginia Beach, VA, USA, May 2011.

[38] Biedron, R. T., Lee-Rausch, E. M., *An Examination of Unsteady Airloads on a UH-60A Rotor: Computation versus Measurement,* Presented at the 68^{th} Forum of the American Helicopter Society,Fort Worth, TX, USA, May 2012.

[39] Park, J.-S., You, Y.-H., Sa, J. H., Park, S. H., and, Jung, S.N., *Extensive Validation of CFD/CSD Aeroelastic Simulations for a Helicopter in Descending Flight,* Presented at the 68^{th} Forum of the American Helicopter Society,Fort Worth, TX, USA, May 2012.

[40] Shaeffler, N. W., Allan, B. G., Lienard, C., Le Pape, A., *Progress Towards Fuselage Drag Reduction via Active Flow Control: A Combined CFD and Experimental Effort,* Presented at the 36^{th} European Rotorcraft Forum, Paper 064, Paris, France, September 2010

[41] Thomas, S., Amiraux, M., Baeder, J. D., *GPU-accelerated FVM-RANS Hybrid Solver for Simulating Two-phase Flow beneath a Hovering Rotor,* Presented at the 69^{th} Forum of the American Helicopter Society, Phoenix, AZ, USA, May 2013

[42] Ghosh, D., Baeder, J.D., *Compact Reconstruction Schemes with Weighted ENO Limiting for Hyperbolic Conservation Laws,* SIAM Journal on Scientific Computing, 34(3), 2012, pp. A1678-A1706

[43] Ghosh, D., Medida, S., Baeder, J.D., *Compact-Reconstruction Weighted Essentially Non-Oscillatory Schemes for Unsteady Euler/Navier-Stokes Equations,* AIAA 2012-2832, 42nd AIAA Fluid Dynamics Conference and Exhibit, New Orleans, LA, USA, June 25-28, 2012

[44] Hirsch, C., *Numerical computation of internal and external flows,* Volumes 1 and 2, Wiley Publishers, 1988.

[45] Spalart, P. R., Allmaras, S. R., *One-equation turbulence model for aerodynamic flows,* Proceedings of the 30th AIAA Aerospace Sciences Meeting and Exhibit, Reno, NV, Jan 6-9 1992.

[46] Dacles-Mariani, J., Zilliac, G. G., Chow, J. S., Bradshaw, P., *Numerical and experimental study of a wingtip vortex in the near field,* AIAA Journal 33 (9), 1561, 1995.